

Illumination Planning for Photometric Measurements

Fredric Joel Solomon

CMU-RI-TR-96-21

Submitted in partial fulfillment of the requirements for the degree of  
Doctor of Philosophy in the field of Robotics

The Robotics Institute  
Carnegie Mellon University  
Pittsburgh, Pennsylvania 15213-3890

June 3, 1996

© 1996 Carnegie Mellon University

This work was sponsored by the Advanced Research Projects Agency under the Department of the Army, Army Research Office under grant number DAAH04-94-G-0006. Views and conclusions contained in this document are those of the authors and should not be interpreted as necessarily representing official policies or endorsements, either expressed or implied, of the United States Government.





# Robotics

Thesis

## Illumination Planning for Photometric Measurements

Fredric Joel Solomon

Submitted in Partial Fulfillment of the Requirements  
for the Degree of  
Doctor of Philosophy  
in the field of Robotics

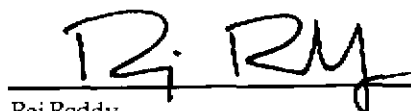
ACCEPTED:

  
Katsushi Ikeuchi Thesis Committee Chair

June 14, 1996  
Date

  
Matthew T. Mason Program Chair

July 10, 1996  
Date

  
Raj Reddy Dean

7/11/96  
Date

APPROVED:

  
Paul Christiano Provost

12 July 1996  
Date



## Abstract

Illumination is one of the basic factors that influence the quality of all intensity images in computer vision. Surprisingly, very few researchers have studied how illumination planning can make a difference in the quality of a computer vision method. Almost all intensity based computer vision techniques, including edge based methods, segmentation methods, and photometric methods, are affected by illumination. Since photometric methods directly model intensity, photometric measurements may be the intensity based computer vision technique which is most sensitive to illumination.

Photometric techniques use physically based reflectance models to model image brightness based on lighting geometry, imaging geometry, local shape, and reflectance. If we can control imaging geometry and illumination geometry, we can use a reflectance model in conjunction with measured image brightness to determine local shape and reflectance parameters.

In photometric stereo, which is one class of photometric techniques, multiple images of an object are taken from the same viewpoint, using different light source directions, in order to determine local shape. The position of the light sources affects what parts of the object are illuminated and the accuracy with which you can recover the object's local shape.

This thesis explores how illumination affects the reliability of the photometric measurement of surface orientation. We discuss the determination of surface orientation in the presence of intensity noise for the following: lambertian surfaces, rough diffuse surfaces, specular spike surfaces, and specular lobe surfaces. In addition to discussing how illumination affects the reliability of the photometric measurement of surface orientation, we also discuss how illumination affects the reliability of reflectance parameter measurements for specular lobe surfaces, and we discuss how to illuminate hybrid (specular lobe + lambertian) surfaces.

There are two basic types of errors in photometric measurements: random errors (noise) and fixed errors. Random errors are due to the variance of the camera and digitizer. These are the errors that we try to predict with our planner. Fixed errors include: errors in light source direction, errors in light source radiance, and errors in the photometric function. Fixed errors can be accounted for by a careful calibration procedure.



## Acknowledgments

I would like to thank my advisor, Katsushi Ikeuchi, for teaching me how to do research and for introducing me to computer vision. Katsu was great to work with. My committee, Takeo Kanade, Eric Krotkov, and Shree Nayar were also very helpful. Eric Krotkov introduced me to error propagation, statistical analysis, and camera calibration. He also had many helpful suggestions during my eye/hand calibration work. Takeo Kanade made my degree possible by directing the Robotics Institute and the VASC group. These two organizations provided a very nurturing environment in which to grow as a graduate student. Takeo also had many insightful comments and suggestions throughout the period of my thesis work. Shree Nayar conducted a lot of the research that is the foundation for my work. He had many constructively critical suggestions about the direction and details of my work throughout the course of the thesis research.

I am indebted to Reg Wilson who implemented Tsai's camera calibration algorithm, and provided this code to me. Reg was a big help during the hand/eye calibration work and had many suggestions about lenses and cameras. Martial Hebert provided code for implementing his 3D transformation algorithm and for generated tessellated icosahedrons. Carol Novak provided camera linearization routines and had many useful suggestions during my four light photometric stereo work.

Srinivas Akella was a great office mate, and was a big help with numerous "stupid" questions during the approximately 7 years that we sat across from each other. Dafna Talmor was my other great, long term, office mate. If I ever needed to know anything about algorithms, Dafna was very helpful. Scott Crowder made the first couple of years at CMU much brighter than they would otherwise have been, and Marco Zaghera introduced the office to the infamous "Snyder's of Hanover Creative Pretzel Eaters Club". Roland Luthi and Doug Beeferman also made the office unique.

My "Task Oriented Vision Lab" group mates: Yoichi Sato, Harry Shum, Mark Wheeler, George Paul, Prem Janardhan and Sing Bing Kang were all very helpful and supportive during my research. We also had many fun nights out together.

My parents, Gustave and Ethel Solomon, were always there for me. I have more to thank them for than words can express. My brother David and sister-in-law, Janet, also helped immensely. Finally, to my wife Randee, who showed me that there really is more to life than work.



# Table of Contents

## Chapter 1

Introduction	1
1.1 Previous Work	3
1.1.1 Visibility and Camera Viewpoint Planning	4
1.1.2 Illumination Planning	5
1.1.3 Photometric Methods	7
1.1.4 Photometric Stereo Error Analysis	8
1.1.5 Summary/Conclusions	8
1.2 Thesis Organization	9

## Chapter 2

Illumination of Lambertian Surfaces	11
2.1 Lambertian Model	11
2.2 2D Convex Lambertian Illumination	12
2.2.1 2D Visibility Regions	12
2.2.2 2D Exact Covers	14
2.2.3 2D Orientation Error	14
2.3 3D Convex Illumination Covers	21
2.3.1 3D Aspect Generation	21
2.3.2 3D Exact Coverage	23
2.4 3D Convex Lambertian Illumination	25
2.4.1 3D Orientation Error	25
2.4.2 Light Intensity Variance	29
2.4.3 Camera Viewpoint Selection	29
2.4.4 Object Pose Errors	30
2.5 3D Convex Lambertian Implementation	31
2.5.1 Measurement of Light Intensity Variance	31
2.6 3D Convex Lambertian Experiments	32
2.6.1 Chalk Cube	33
2.7 2D Concave Lambertian Illumination	40
2.8 3D Concave Lambertian Illumination	48
2.8.1 Implementation	49
2.9 3D Concave Lambertian Illumination Experiments	49
2.9.1 Chalk Concavity	49
2.10 2D Lambertian Source Error	55
2.10.1 2D Lambertian Source Error	55
2.10.2 3D Lambertian Source Error	62
2.11 Summary	63

## Chapter 3

Illumination of Rough Diffuse Surfaces	65
3.1 Oren-Nayar Rough Diffuse Model	65

3.2 Surface Orientation Calculation	67
3.3 2D Rough Diffuse Error Surfaces	69
3.4 Experiments	78
3.4.1 Experimental Setup	78
3.4.2 Rough Painted Sandpaper	79
3.5 Summary	83
<b>Chapter 4</b>	
Illumination of Specular Spike Surfaces	85
4.1 Specular Spike Model	85
4.2 Extended Light Sources	85
4.3 Surface Spike Orientation Calculation	89
4.4 2D Specular Spike Error Surfaces	90
4.5 Experiments	99
4.5.1 Extended Light Source Model	99
4.5.2 Polished Aluminum Plate	101
4.5.3 Polished Aluminum Cylinder	102
4.6 Summary	106
<b>Chapter 5</b>	
Illumination of Specular Lobe Surfaces	107
5.1 Introduction	107
5.2 Specular Lobe Model	107
5.3 Surface Orientation Calculation	110
5.4 2D Specular Lobe Error Surfaces	110
5.5 Estimation of B and K	119
5.6 2D B and K Error Surfaces	120
5.7 Summary	129
<b>Chapter 6</b>	
Illumination of Hybrid Surfaces	131
6.1 Introduction	131
6.2 Shape and Segmentation using Four Light Photometric Stereo	131
6.2.1 Assumptions	133
6.2.2 Shape and Segmentation in the Four Light Region	133
6.2.3 Shape and Segmentation in the Three Light Region	135
6.2.4 Shape and Segmentation in the Two Light Region	138
6.2.5 Consistent Segmentation	139
6.3 Extracting Specular Intensity and Specular Sharpness	139
6.3.1 Simplified Torrance-Sparrow Model	139
6.3.2 Determination of Specular Intensity and Specular Sharpness	141
6.4 Results	142
6.4.1 Simulations:	142
6.4.2 Experimental Results	145
6.5 Conclusions	155

**Chapter 7**

Conclusions	157
7.1 Summary	157
7.1.1 Illumination of Lambertian Surfaces	157
7.1.2 Illumination of Rough Diffuse Surfaces	158
7.1.3 Illumination of Specular Spike Surfaces	158
7.1.4 Illumination of Specular Lobe Surfaces	158
7.1.5 Illumination of Hybrid Surfaces	158
7.2 Contributions	159
7.3 Future Directions	

**Appendix A**

Light Source Direction and Normalization	161
A.0.1 Light Source Directions	161
A.0.2 Image Intensity Normalization	162

**Appendix B**

Frames and Transformations for Puma, Camera, and Light Source Array	165
Bibliography	167



## List of Figures

Fig. 1-1. Experimental setup	2
Fig. 1-2. Illumination planning data flow	3
Fig. 1-3. Cowan's Separating Support Plane	4
Fig. 2-1. Lambertian geometry	11
Fig. 2-2. Visibility ranges	13
Fig. 2-3. Visibility range/region diagram	13
Fig. 2-4. Noisy normal distribution: N at 90°, S1 at 100°, S2 at 80°.	15
Fig. 2-5. Normalized noisy normal distribution: N at 90°, S1 at 100°, S2 at 80°	16
Fig. 2-6. Normalized noisy normal distribution: N at 90°, S1 at 10°, S2 at 170°	16
Fig. 2-7. Source/viewer frame of reference coordinate system	17
Fig. 2-8. Error surface: N=90, $\delta I=0.01$	17
Fig. 2-9. 2D Lambertian error surface cross sections, N=90, $\delta I=0.01$	18
Fig. 2-10. Lambertian intensity function	18
Fig. 2-11.  Derivative  of Lambertian intensity function.	19
Fig. 2-12. Source matrix condition number.	19
Fig. 2-13. Angular error versus source intensity. N = 90°. ( $\pm 3\sigma$ noise model from section 2.5.1)	20
Fig. 2-14. 2D angular orientation error surface	21
Fig. 2-15. Convex polyhedra used for exact cover tests.	24
Fig. 2-16. 3D Normalized noisy normals	26
Fig. 2-17. Experimental setup	31
Fig. 2-18. Camera calibration target. Scale is approximately 2X.	31
Fig. 2-19. Intensity histogram	32
Fig. 2-20. Plot of $\sigma_i$	32
Fig. 2-21. Geometric model of chalk cube	33
Fig. 2-22. Intensity images: faces 3 and 4 of cube	37
Fig. 2-23. Needle map: faces 3 and 4 of cube	37
Fig. 2-24. Intensity images: faces 6, 7, and 15 of cube	38
Fig. 2-25. Needle map faces: 6, 7, and 15 of cube	38
Fig. 2-26. Illumination aspects from the 1, 1, 1 viewing direction	39
Fig. 2-27. Illumination aspects from the -1, 1, 1 viewing direction	39
Fig. 2-28. Illumination aspects from the 0, 0, 1 viewing direction	40
Fig. 2-29. Concave visibility region	40
Fig. 2-30. Interreflection geometry	42
Fig. 2-31. 140° 2D concavity	44
Fig. 2-32. 140° 2D concavity shape and pseudo shape	44
Fig. 2-33. 140° 2D concavity error surface for center of face A	44
Fig. 2-34. 90° 2D concavity	45
Fig. 2-35. 90° 2D Concavity shape and pseudo shape	45
Fig. 2-36. 90° 2D concavity error surface for center of face A	45
Fig. 2-37. 45° 2D concavity	46
Fig. 2-38. 45° 2D concavity shape and pseudo shape	46
Fig. 2-39. 45° 2D concavity error surface for center of face A	46
Fig. 2-40. Error across face A and Face B for 140° concavity	47
Fig. 2-41. Error across face A and Face B for 90° concavity	47
Fig. 2-42. Error across face A and Face B for 45° concavity	48
Fig. 2-43. Interreflection geometry	48
Fig. 2-44. 90° Chalk concavity	50
Fig. 2-45. Chalk: Intensity versus viewing angle. (incident angle = 0°)	52
Fig. 2-46. Best plan error surface, face B, 90° chalk concavity, sources: 1, 12, 5	54
Fig. 2-47. Best plan intensity, face B, 90° chalk concavity, sources: 1, 12, 5	54
Fig. 2-48. Worst plan error surface, face B, 90° chalk concavity, sources: 2, 11, 5	54

Fig. 2-49. Worst plan intensity, face B, 90° chalk concavity, sources: 2, 11, 5	54
Fig. 2-50. Intensity image from source 1, and needle map from sources: 1, 12, 5	55
Fig. 2-51. Orientation error surface: $\delta S=2^\circ$ , $N=90^\circ$ .	56
Fig. 2-52. Ratio function diagram: $S1=45^\circ$ , $S2=135^\circ$	57
Fig. 2-53. Ratio function diagram: $S1=50^\circ$ , $S2=130^\circ$	57
Fig. 2-54. Ratio function diagram: $S1=40^\circ$ , $S2=140^\circ$	58
Fig. 2-55. Ratio function diagram: $S1=40^\circ$ , $S2=130^\circ$	58
Fig. 2-56. Ratio function diagram: $S1=50^\circ$ , $S2=140^\circ$	59
Fig. 2-57. Ratio function diagram: $S1=45^\circ$ , $S2=135^\circ$	59
Fig. 2-58. Ratio Function Diagram: $S1=150^\circ$ , $S2=170^\circ$	60
Fig. 2-59. Ratio function diagram: $S1=155^\circ$ , $S2=175^\circ$	60
Fig. 2-60. Ratio function diagram: $S1=145^\circ$ , $S2=165^\circ$	61
Fig. 2-61. Ratio function diagram: $S1=145^\circ$ , $S2=175^\circ$	61
Fig. 2-62. Ratio function diagram: $S1=155^\circ$ , $S2=165^\circ$	61
Fig. 2-63. Ratio function diagram: $S1=150^\circ$ , $S2=170^\circ$	62
Fig. 3-1. V cavity facet geometry	65
Fig. 3-2. Surface patch geometry	66
Fig. 3-3. 2D Lambertian geometry	67
Fig. 3-4. Global coordinate system	68
Fig. 3-5. Global and local coordinate system spherical triangles	69
Fig. 3-6. Source/viewer frame of reference coordinate system	69
Fig. 3-7. Rough diffuse intensity surface, $\sigma = 10^\circ$ , $\theta_N = 90^\circ$ , $\rho = 0.9$ , $E_o = 314$ .	70
Fig. 3-8. Rough diffuse intensity versus viewing angle, $\sigma = 10^\circ$ , $\theta_N = 90^\circ$ , $\rho = 0.9$ , $E_o = 314$ .	70
Fig. 3-9. Rough diffuse intensity versus source direction, $\sigma = 10^\circ$ , $\theta_N = 90^\circ$ , $\rho = 0.9$ , $E_o = 314$	71
Fig. 3-10. Rough diffuse error surface, $\sigma = 10^\circ$ , $\theta_V = 10^\circ$ , $\theta_N = 90^\circ$ , $\rho = 0.9$ , $E_o = 314$ .	71
Fig. 3-11. Rough diffuse error surface, $\sigma = 10^\circ$ , $\theta_V = 45^\circ$ , $\theta_N = 90^\circ$ , $\rho = 0.9$ , $E_o = 314$ .	72
Fig. 3-12. Rough diffuse error surface, $\sigma = 10^\circ$ , $\theta_V = 90^\circ$ , $\theta_N = 90^\circ$ , $\rho = 0.9$ , $E_o = 314$ .	72
Fig. 3-13. Rough diffuse error surface cross section, $\sigma = 10^\circ$ , $\theta_V = 10^\circ$ , $\theta_N = 90^\circ$ , $\rho = 0.9$ , $E_o = 314$ .	73
Fig. 3-14. Rough diffuse error surface cross section, $\sigma = 10^\circ$ , $\theta_V = 45^\circ$ , $\theta_N = 90^\circ$ , $\rho = 0.9$ , $E_o = 314$ .	73
Fig. 3-15. Rough diffuse error surface cross section, $\sigma = 10^\circ$ , $\theta_V = 90^\circ$ , $\theta_N = 90^\circ$ , $\rho = 0.9$ , $E_o = 314$	73
Fig. 3-16. Rough diffuse intensity surface, $\sigma = 30^\circ$ , $\theta_N = 90^\circ$ , $\rho = 0.9$ , $E_o = 314$ .	74
Fig. 3-17. Rough diffuse intensity versus viewing angle, $\sigma = 30^\circ$ , $\theta_N = 90^\circ$ , $\rho = 0.9$ , $E_o = 314$ .	74
Fig. 3-18. Rough diffuse intensity versus source direction, $\sigma = 30^\circ$ , $\theta_N = 90^\circ$ , $\rho = 0.9$ , $E_o = 314$	75
Fig. 3-19.  Derivative  of Rough diffuse intensity, $\sigma = 30^\circ$ , $\theta_N = 90^\circ$ , $\rho = 0.9$ , $E_o = 314$	75
Fig. 3-20. Rough diffuse error surface, $\sigma = 30^\circ$ , $\theta_V = 10^\circ$ , $\theta_N = 90^\circ$ , $\rho = 0.9$ , $E_o = 314$ .	76
Fig. 3-21. Rough diffuse error surface, $\sigma = 30^\circ$ , $\theta_V = 45^\circ$ , $\theta_N = 90^\circ$ , $\rho = 0.9$ , $E_o = 314$ .	76
Fig. 3-22. Rough diffuse error surface, $\sigma = 30^\circ$ , $\theta_V = 90^\circ$ , $\theta_N = 90^\circ$ , $\rho = 0.9$ , $E_o = 314$ .	76
Fig. 3-23. Rough diffuse error surface cross section, $\sigma = 30^\circ$ , $\theta_V = 10^\circ$ , $\theta_N = 90^\circ$ , $\rho = 0.9$ , $E_o = 314$ .	77
Fig. 3-24. Rough diffuse error surface cross section, $\sigma = 30^\circ$ , $\theta_V = 45^\circ$ , $\theta_N = 90^\circ$ , $\rho = 0.9$ , $E_o = 314$	77
Fig. 3-25. Rough diffuse error surface cross section, $\sigma = 30^\circ$ , $\theta_V = 90^\circ$ , $\theta_N = 90^\circ$ , $\rho = 0.9$ , $E_o = 314$ .	78
Fig. 3-26. 2D rough diffuse experimental setup.	78
Fig. 3-27. Measurements versus fitted Oren-Nayar model for rough painted sandpaper.	79
Fig. 3-28. Intensity surface. $S1=(30, 0)$ , $V=(20, \pi)$	80
Fig. 3-29. Intensity surface. $S2=(50, \pi)$ , $V=(20, \pi)$	81
Fig. 3-30. Intensity surface. $S2=(50, 0)$ , $V=(20, \pi)$	81
Fig. 3-31. Intensity surface. $S1=(30, 0)$ , $V=(60, 0)$	81
Fig. 3-32. Intensity surface. $S2=(50, 0)$ , $V=(60, 0)$	82
Fig. 3-33. Intensity surface. $S2=(50, \pi)$ , $V=(60, 0)$	82
Fig. 3-34. 3 $\sigma$ Error surface. $S1=(30, 0)$ , $S2=(50, \pi)$ , $V=(20, \pi)$	82
Fig. 3-35. 3 $\sigma$ Error surface. $S1=(30, 0)$ , $S2=(50, \pi)$ , $V=(60, 0)$	83
Fig. 3-36. 3 $\sigma$ Error surface. $S1=(30, 0)$ , $S2=(50, 0)$ , $V=(60, 0)$	83
Fig. 3-37. 3 $\sigma$ Error surface. $S1=(30, 0)$ , $S2=(50, 0)$ , $V=(20, \pi)$	83
Fig. 4-1. Specular geometry	85
Fig. 4-2. 2D photosampler	86

Fig. 4-3. Extended source geometry	86
Fig. 4-4. Global/local specular notation	87
Fig. 4-5. Extended light source intensity $R=30, H=10$	87
Fig. 4-6. Spherical geometry for specular point location	88
Fig. 4-7. Spherical geometry for local specular angle of extended light source.	89
Fig. 4-8. Extended light source intensity $R=30, H=20$	90
Fig. 4-9. Derivative of extended light source intensity $R=30, H=20$	91
Fig. 4-10. 2D Specular error surface. $R=30, H=20, V=80, N=90, L=102000$	92
Fig. 4-11. 2D Specular error surface cross section, $S1=101.83, R=30, H=20, V=80, N=90, L=102000$	92
Fig. 4-12. Extended light source intensity $R=30, H=10$	93
Fig. 4-13. Derivative of extended light source intensity $R=30, H=10$	93
Fig. 4-14. 2D Specular error surface $R=30, H=10, V=80, N=90, L=25500$	94
Fig. 4-15. 2D specular error surface cross section $S1=100.07, R=30, H=10, V=80, N=90, L=25500$	94
Fig. 4-16. Extended light source intensity $R=30, H=5$	95
Fig. 4-17. Derivative of extended light source intensity $R=30, H=5$	95
Fig. 4-18. 2D specular error surface $R=30, H=5, V=80, N=90, L=6375$	96
Fig. 4-19. 2D specular error surface cross section $S1=100.76, R=30, H=5, V=80, N=90, L=6375$	96
Fig. 4-20. Extended light source intensity $R=30, H=2.5$	97
Fig. 4-21. Derivative of extended light source intensity $R=30, H=2.5$	97
Fig. 4-22. 2D Specular Error Surface $R=30, H=2.5, V=80, N=90, L=1593.75$	98
Fig. 4-23. 2D Specular error surface cross section $S1=99.9, R=30, H=2.5, V=80, N=90, L=1593.75$	98
Fig. 4-24. Experimental setup	99
Fig. 4-25. Nominal experimental setup	99
Fig. 4-26. Measured and model intensity for S1. $R=8, \theta_{SGC}=60.8, \phi_{SGC}=0, H=2.2, L=1047.1$	100
Fig. 4-27. Measured and model intensity for S2. $R=8, \theta_{SGC}=47.2, \phi_{SGC}=0, H=2.2, L=888.5$	100
Fig. 4-28. Measured and model intensity for S3. $R=8, \theta_{SGC}=32.1, \phi_{SGC}=0, H=2.2, L=943.7$	100
Fig. 4-29. Images of plate. a) S1. b) S2. c) S3	101
Fig. 4-30. Intensity surfaces. a) S1. b) S2. c) S3	102
Fig. 4-31. Error surfaces. a) S1, S2. b) S1, S3. c) S2, S3	102
Fig. 4-32. Cylinder images. a) cylinder outline. b) S1. c) S2. d) S3	103
Fig. 4-33. Cylinder intensity surfaces for S1. a) plan b) measurement	103
Fig. 4-34. Cylinder intensity surfaces for S2. a) plan b) measurement	104
Fig. 4-35. Cylinder intensity surfaces for S3. a) plan b) measurement	104
Fig. 4-36. Cylinder error surface for S1, S3. a) plan b) measurement	104
Fig. 4-37. Cylinder error surface for S2, S3. a) plan b) measurement	105
Fig. 4-38. Cylinder error surface for S1, S2. a) plan b) measurement	105
Fig. 4-39. Cylinder nominal versus measured mean surface orientation, S1, S3	105
Fig. 4-40. Cylinder nominal versus measured mean surface orientation, S2, S3	106
Fig. 4-41. Cylinder nominal versus measured mean surface orientation, S1, S2	106
Fig. 5-1. Geometry for Torrance-Sparrow model	107
Fig. 5-2. Source/viewer frame of reference coordinate system	108
Fig. 5-3. Specular lobe intensity surface, $K=10.0, B=100, N=90$ .	108
Fig. 5-4. Specular lobe intensity surface, $K=20.0, B=100, N=90$ .	109
Fig. 5-5. Specular lobe intensity surface cross section, $K=10.0, B=100, N=90$ .	109
Fig. 5-6. Specular lobe intensity surface cross section, $K=20.0, B=100, N=90$ .	109
Fig. 5-7.  Derivative  of specular lobe intensity, $K=10, B=100, V=30, N=90$ .	111
Fig. 5-8. Specular lobe error surface, $K=10, B=100, V=30, N=90$ .	111
Fig. 5-9. Specular lobe error surface cross section, $S1=150, K=10, B=100, V=30, N=90$ .	112
Fig. 5-10.  Derivative  of specular lobe intensity, $K=10, B=100, V=50, N=90$ .	112
Fig. 5-11. Specular lobe error surface, $K=10, B=100, V=50, N=90$ .	113
Fig. 5-12. Specular lobe error surface cross section, $S1=130, K=10, B=100, V=50, N=90$	113
Fig. 5-13.  Derivative  of specular lobe intensity, $K=10, B=100, V=80, N=90$ .	114
Fig. 5-14. Specular lobe error surface, $K=10, B=100, V=80, N=90$ .	114
Fig. 5-15. Specular lobe error surface cross section, $S1=100, K=10, B=100, V=80, N=90$	115

Fig. 5-16.  Derivative  of specular lobe intensity, $K=20, B=100, V=30, N=90$ .	115
Fig. 5-17. Specular lobe error surface, $K=20, B=100, V=30, N=90$ .	116
Fig. 5-18. Specular lobe error surface cross section, $S1= 150, K=20, B=100, V=30, N=90$	116
Fig. 5-19.  Derivative  of specular lobe intensity, $K=20, B=100, V=50, N=90$ .	117
Fig. 5-20. Specular lobe error surface, $K=20, B=100, V=50, N=90$ .	117
Fig. 5-21. Specular lobe error surface cross section, $S1= 130, K=20, B=100, V=50, N=90$	118
Fig. 5-22. Derivative of specular lobe intensity, $K=20, B=100, V=80, N=90$ .	118
Fig. 5-23. Specular lobe error surface, $K=20, B=100, V=80, N=90$ .	119
Fig. 5-24. Specular lobe error surface cross section, $S1= 100, K=20, B=100, V=80, N=90$	119
Fig. 5-25. Intensity Plot ( $B'=100, K=0.01$ ) and $dK/dI$ plot	120
Fig. 5-26. B error surface. $B=100, K=10, V=80^\circ, N=90^\circ, K_0=15, B_0=110$ .	121
Fig. 5-27. K error surface. $B=100, K=10, V=80^\circ, N=90^\circ, K_0=15, B_0=110$ .	122
Fig. 5-28. B error surface. $B=100, K=10, V=80^\circ, N=90^\circ, N=90^\circ, K_0=20, B_0=80$ .	122
Fig. 5-29. K error surface. $B=100, K=10, V=80^\circ, N=90^\circ, K_0=20, B_0=80$ .	123
Fig. 5-30. B error surface. $B=100, K=20, V=80^\circ, N=90^\circ, K_0=25, B_0=110$ .	123
Fig. 5-31. K error surface. $B=100, K=20, V=80^\circ, N=90^\circ, K_0=25, B_0=110$ .	123
Fig. 5-32. B error surface. $B=100, K=10, V=50^\circ, N=90^\circ, K_0=15, B_0=110$ .	124
Fig. 5-33. K error surface. $B=100, K=10, V=50^\circ, N=90^\circ, K_0=15, B_0=110$ .	124
Fig. 5-34. B error surface. $B=100, K=20, V=50^\circ, N=90^\circ, K_0=25, B_0=110$ .	125
Fig. 5-35. K error surface. $B=100, K=20, V=50^\circ, N=90^\circ, K_0=25, B_0=110$ .	125
Fig. 5-36. B error surface. $B=100, K=10, V=30^\circ, N=90^\circ, K_0=15, B_0=110$ .	125
Fig. 5-37. K error surface. $B=100, K=10, V=30^\circ, N=90^\circ, K_0=15, B_0=110$ .	126
Fig. 5-38. B error surface. $B=100, K=20, V=30^\circ, N=90^\circ, K_0=25, B_0=110$ .	126
Fig. 5-39. K error surface. $B=100, K=20, V=30^\circ, N=90^\circ, K_0=25, B_0=110$ .	126
Fig. 5-40. B error surface. $B=100, K=10, V=80^\circ, N=90^\circ, K_0=15, B_0=110, \sigma(\theta_n) = 1^\circ$ .	127
Fig. 5-41. K error surface. $B=100, K=10, V=80^\circ, N=90^\circ, K_0=15, B_0=110, \sigma(\theta_n) = 1^\circ$ .	127
Fig. 5-42. B error surface. $B=100, K=10, V=80^\circ, N=90^\circ, K_0=15, B_0=110, \sigma(\theta_n) = 2^\circ$ .	128
Fig. 5-43. K error surface. $B=100, K=10, V=80^\circ, N=90^\circ, K_0=15, B_0=110, \sigma(\theta_n) = 2^\circ$ .	128
Fig. 5-44. B error surface. $B=100, K=10, V=80^\circ, N=90^\circ, K_0=15, B_0=110, \sigma(\theta_n) = 3^\circ$ .	128
Fig. 5-45. K error surface. $B=100, K=10, V=80^\circ, N=90^\circ, K_0=15, B_0=110, \sigma(\theta_n) = 3^\circ$ .	129
Fig. 6-1. a) Illuminated gaussian sphere. b) illuminated and visible gaussian sphere.	132
Fig. 6-2. Illumination regions	132
Fig. 6-3. Three light illuminated region	135
Fig. 6-4. Two light illuminated region.	138
Fig. 6-5. Geometry for Torrance-Sparrow Model	140
Fig. 6-6. Fresnel reflectance -MgO	140
Fig. 6-7. Synthetic sphere images.	143
Fig. 6-8. Segmentation for synthetic sphere.	143
Fig. 6-9. Needle map for synthetic sphere.	144
Fig. 6-10. Intensity vs. incident angle for synthetic sphere.	144
Fig. 6-11. $\alpha^2$ versus $\ln(D*Nz)$ for synthetic sphere.	145
Fig. 6-12. Experimental Setup	145
Fig. 6-13. Painted sphere images.	146
Fig. 6-15. Needle map for painted sphere	147
Fig. 6-14. Segmentation for painted sphere.	147
Fig. 6-16. Needle map for painted sphere	148
Fig. 6-17. Measured intensity vs. incident angle for painted sphere for S3	148
Fig. 6-18. Intensity vs. incident angle for painted sphere using extracted parameters for S3.	149
Fig. 6-19. Measured intensity vs. incident angle for painted sphere for S2	149
Fig. 6-20. Intensity vs. incident angle for painted sphere using extracted parameters for S2.	150
Fig. 6-21. $\alpha^2$ versus $\ln(D*Nz)$ for painted sphere.	150
Fig. 6-22. $\alpha^2$ versus $\ln[(D-Offset)*Nz]$ for painted sphere.	151
Fig. 6-23. Plastic helmet images and manually segmented plastic helmet images.	152
Fig. 6-24. Segmentation for plastic helmet.	153

Fig. 6-25. Needle map for plastic helmet	153
Fig. 6-26. $\alpha^2$ versus $\ln(D*Nz)$ for plastic helmet.	154
Fig. 6-27. Images of plastic bottle.	154
Fig. 6-28. Segmentation for plastic bottle.	155
Fig. 6-29. Needle map for plastic bottle.	155
Fig. A-1. Measured intensity and best fit cosine.	163
Fig. B-1. Frames for Puma, camera, and light source array	165



# Chapter 1

## Introduction

Illumination is one of the basic factors that influence the quality of all intensity images in computer vision. Surprisingly, very few researchers have studied how *illumination planning* can make a difference in the quality of a computer vision method. Almost all intensity based computer vision techniques including edge based methods, segmentation methods, and photometric methods are affected by illumination. Since photometric methods directly model intensity, photometric measurements may be the intensity based computer vision technique which is most sensitive to illumination. Therefore, we choose to study how illumination affects the quality of photometric measurements.

Photometric techniques use physically based reflectance models [Nayar 91a] to model image brightness based on lighting geometry, imaging geometry, local shape, and reflectance. If we can control imaging geometry and illumination geometry, we can use a reflectance model in conjunction with measured image brightness to determine local shape and reflectance parameters.

In photometric stereo, which is one class of photometric techniques, multiple images of an object are taken from the same viewpoint, using different light source directions, in order to determine local shape. The position of the light sources affects what parts of the object are illuminated and the accuracy with which you can recover the object's local shape. The problem is to determine the best light source configuration for measuring the local shape of a given object. For example, if we arrange light sources in the shape of a tessellated sphere, Fig. 1-1. , the optimal light source positions are not obvious, and the number of potential light source combinations is too large for a human operator to consider.

We investigate the illumination planning problem from two perspectives. First, we determine how to position light sources around an object so that we *illuminate* a specified set of faces in an efficient manner. In order to solve this problem, we have to determine light source visibility and we have to find some method of efficiently "covering" a specified set of object faces.

Secondly, we determine how to position the light sources so that they give us a reliable mea-

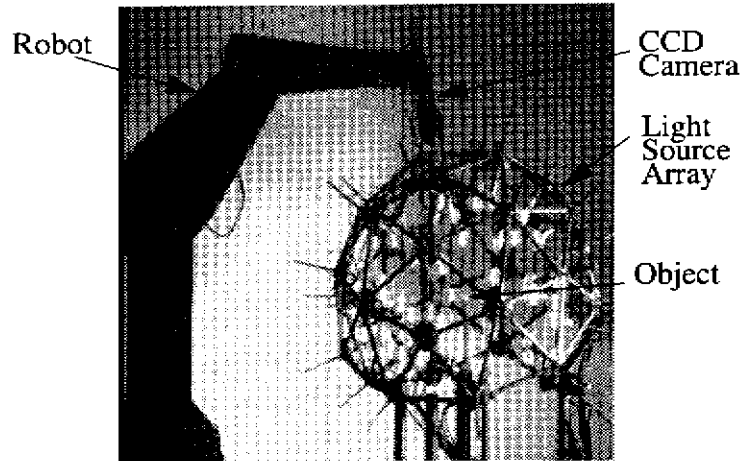


Fig. 1-1. Experimental setup

surement of local shape. There are two basic types of errors in photometric measurements: random errors (noise) and fixed errors. Random errors are due to the variance of the camera and digitizer. These are the errors that we try to predict with our planner. Fixed errors include: errors in light source direction, errors in light source radiance, and errors in the photometric function. Fixed errors can be accounted for by a careful calibration procedure.

Noise causes uncertainty in our measurement of local shape. The amount of uncertainty that this noise will create in our measurement will depend on light source positions. By using a noise model of the CCD, a CAD model of the object we are measuring, and the appropriate reflectance model, we can determine how much uncertainty we can expect in our surface orientation measurement for a given light source configuration. We can find an optimal light source configuration: one that produces a minimum amount of measurement uncertainty. Our ability to predict the uncertainty in our measurements gives us the capability to determine when a shape differs in a statistically significant amount from what we expect.

This thesis explores how illumination affects the reliability of the photometric measurement of surface orientation. We discuss the determination of surface orientation in the presence of intensity noise for: lambertian surfaces, rough diffuse surfaces, specular spike surfaces, and specular lobe surfaces. In addition to discussing how illumination affects the reliability of the photometric measurement of surface orientation, we also discuss how illumination affects the reliability of reflectance parameter measurements for specular lobe surfaces, and we discuss how to illuminate hybrid (specular lobe + lambertian) surfaces.

The environments we study are structured. We will assume that we know what we are looking at (i.e.: We have a CAD model of the object that we want to measure.) and that we know the pose of the object. Using this, we can plan our light source placement to sequentially illuminate the entire surface of the object (cover the object) that we are trying to measure, and we can also use our a priori geometric knowledge of the object to optimize our measurement of local shape. We assume orthographic projection and parallel incident light throughout this work.

We view the illumination planning problem in a model driven manner so that our illumination planners can solve different problems using similar methodologies. This allows us to

measure objects with different shapes, made of materials with different reflectances, using sensors with different noise characteristics, while using a similar solution framework. From a high level, we view our problem as having three major inputs: the CAD model of the object we are trying to illuminate, the noise model of our sensor (the noise model for our CCD camera), and the reflectance model of the object we are trying to measure. These models are used to generate an illumination plan.

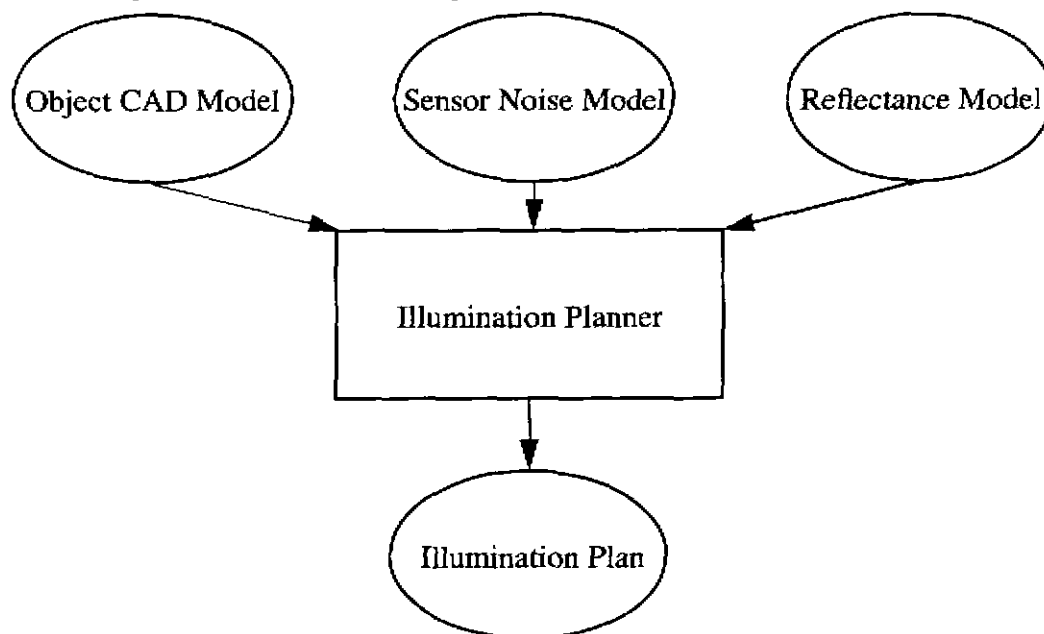


Fig. 1-2. Illumination planning data flow

In this thesis, we explore how illumination affects *one* computer vision technique, photometric methods. While photometric methods may be the intensity based computer vision technique which is most sensitive to illumination, it is hoped that this work will motivate others to study how illumination can affect *other* intensity based computer vision techniques.

## 1.1 Previous Work

Illumination planning is a subset of sensor planning. Tarabanis [Tarabanis 95] defines sensor planning as “an emerging research area that tries to understand and quantify the relationship between objects to be viewed and the sensors observing them in a model-based, task directed way.” He classifies sensor planning, by using the task to be achieved, in three categories: object feature detection, model-based object recognition and localization, and scene reconstruction. Object feature detection determines sensor parameters so that an object feature, of a known object, in a known pose, is sensed within certain requirements, such as focus and resolution. Model-based object recognition and localization determines sensing configurations for recognizing an object. The best sensor configuration is determined by using object models, sensor models, and information already obtained. Scene reconstruction determines sensor configurations for building a model of an unknown environment. Our work can be categorized in Tarabanis’s “object feature detection” classification. Below, we summarize sensor planning work that falls under this classification. We also include a brief

review of relevant photometric methods, and a summary of previous photometric stereo error analysis techniques.

### 1.1.1 Visibility and Camera Viewpoint Planning

Cowan developed the synthetic approach to determining a camera's viewpoint. In this approach, sensor locations that satisfy a task are determined directly using optimization techniques. In [Cowan 88], given a camera and lens, he develops methods for determining 3D camera locations that satisfy the following requirements: focus, field of view, visibility, view angle, and prohibited regions. For each requirement he builds a 3D region that satisfies the requirement. Then, he intersects the regions to find camera locations that satisfy all the requirements.

The visibility constraint is the most relevant constraint to our work. Cowan determines visibility using the concept of "separating support planes". Given a convex polygon "S" and an occluding convex polygon "O", a separating support plane divides space into two halves. One half space contains S and not O. The other half space contains O and not S. The half spaces are constructed by rotating a plane about each edge of S. This plane is oriented so it is between O and S, overlapping S. Then, the plane is rotated about each edge of S until it hits a vertex or an edge of O. This is repeated for each edge of S, and for each edge of O. The union of all the half spaces containing S forms the set of viewpoints where O does not occlude S. The procedure can be extended to convex polyhedral objects and obstacles.

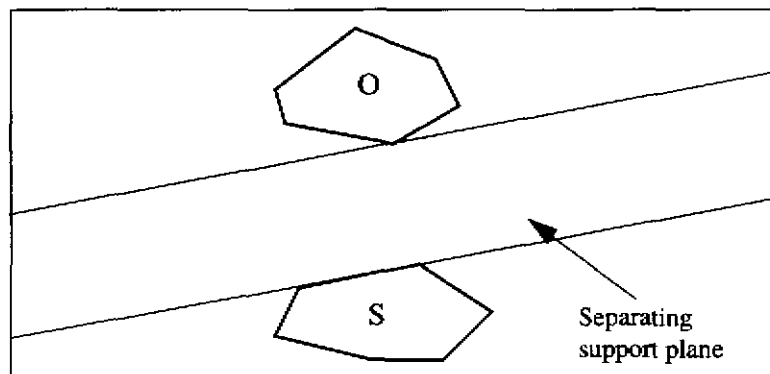


Fig. 1-3. Cowan's Separating Support Plane

In [Tsai 89], Tsai and Tarabanis develop a method for determining the visibility regions for general concave/convex polyhedral targets occluded by general concave/convex polyhedral obstacles. Their method, at its heart, is similar to Cowan's method. They have added a convex decomposition algorithm, and have improved the computational efficiency of Cowan's original algorithm. Abrams [Abrams 93] extended Tsai's work to planning a series of viewpoints for a preplanned task.

In [Tarabanis 90], Tarabanis, Tsai, and Allen use the methods of [Tsai 89] to search for visible regions where a feature can be viewed. Then, they determine the admissible camera locations where a feature can be resolved to a desired resolution. Locations are determined for orthogonal and general viewing directions.

In [Tarabanis 91], Tarabanis, Tsai, and Allen expand on their previous work. They want to determine camera pose and optical settings so that a polyhedral object is visible, in the field of view, in focus, and resolved to sufficient resolution (four constraints). They pose the problem as an optimization problem in an 8 dimensional space. The camera orientation and position contain five degrees of freedom. The distance from the back nodal point to the image plane, the lens focal length, and the aperture are the three other degrees of freedom. Visibility is determined using the method described in [Tsai 89]. The other constraints are posed as inequalities, and are merged into one optimization function with arbitrary weights assigned to each constraint. The function is then optimized using the visibility region boundaries as optimization constraints.

Tsai and Tarabanis and Cowan use a synthesis approach to sensor location. The sensor locations that satisfy a task are determined directly using optimization techniques. Sakane, Yi, and Ikeuchi use a generate and test approach. Sensor locations are generated. Then, they are evaluated against a criteria function.

In [Sakane 87], Sakane describes a system that determines camera placement on a geodesic dome, that is placed around a target's point of interest. The camera is placed so that the point of interest is not occluded by other objects in the environment or by the manipulator holding the camera. Sakane determines occlusion free regions by doing depth buffering from the center of the dome to each facet. The minimum distance is stored at each facet. If the minimum distance is less than the radius of the dome, the viewpoint is occluded. The radius of the geodesic dome is chosen to get sufficient target resolution.

Ikeuchi and Robert [Ikeuchi 91a] [Kumar 91] developed the Vantage geometric/sensor modeling system. Vantage is able to determine sensor detectability for scenes consisting of multiple objects. Vantage determines visibility and two types of occlusion: self-occlusion and cast-occlusion. Self-occlusion occurs when the angle between a surface and a sensor is greater than 90°. Cast-occlusion occurs when the visibility of a surface is blocked by another surface. Vantage has the ability to determine partial visibility of a surface. Visibility for multiple sensors can be combined using boolean operators to create higher level visibility functions.

### 1.1.2 Illumination Planning

In [Sakane 90] [Sakane 91], Sakane describes positioning light sources for a photometric stereo system. He tries to optimize the extracted surface normal and the surface coverage for lambertian surfaces. Sakane uses the method of determining occlusion free viewpoints described in [Sakane 87] to find candidate positions for the light sources. These positions provide shadow free illumination.

Sakane proposes a metric of surface orientation reliability that relies on the condition number of the source matrix to estimate the error in the surface normal vector (By definition,  $|\mathbf{N}| = 1$ ):

$$\frac{|\delta \mathbf{N}|}{|\mathbf{N}|} \leq \text{cond}(S) \cdot \frac{|\delta \mathbf{I}|}{|\mathbf{I}|}$$

The second metric Sakane uses is the size of the intersection region of the three light sources and the camera on the gaussian sphere. The three light sources will illuminate a three hemispheres of the Gaussian sphere, and the camera will be able to observe a hemisphere of the gaussian sphere. By intersecting these four hemispheres, Sakane determines the amount of the gaussian sphere that is detectable.

Sakane combines the detectability metric and the surface orientation reliability metric into a single criterion function. The relative weights of the two metrics are arbitrary. In [Sakane 91], Sakane uses a movable camera. This allows a further degree of freedom in optimizing the detectability metric. In [Niepold 87], Sakane considers lambertian edge contrast as a metric. Visibility seems to be determined using the methods described in [Sakane 87].

In [Cowan 89], Cowan discusses positioning point light sources for scene illumination. First, given a viewpoint region, Cowan finds the minimum and maximum camera apertures that bound the viewpoint region. Then, Cowan relates image irradiance to scene radiance and scene radiance to lambertian scene irradiance. Assuming a camera with a certain dynamic range, and a light source with a certain flux, he determines the minimum and maximum distance from the surface that the light source can be positioned.

In [Cowan 91] Cowan considers the edge contrast of convex lambertian surfaces. He determines the possible source orientations and distances, with respect to a given convex corner (consisting of two lambertian surfaces), that produce a required intensity difference (contrast) between the two surfaces.

In [Yi 89], Yi considers edge contrast for specular lobe objects, using a polarized light version of the Torrance Sparrow model. Yi forms a discrete spherical viewing space, with points positioned so that the arc length between viewing points is approximately equal. At discrete points along an edge Yi calculates the intensity difference. Then, he finds the “contrast distribution function” metric, which tells how much of the edge has a contrast above a certain threshold. The second metric is sensor visibility of the edge, which he defines as the ratio of the unoccluded portion of the edge to the entire edge length. Given a set of required edges, Yi searches for the light source and sensor position which maximizes the two criterion functions. Yi does not describe how he combines the two criterion functions. The results presented in the paper are for a synthetic cylinder and cube. No real results are presented.

The SPIE (Society of Photo-Optical Instrumentation Engineers) has a large literature [Batchelor 85] [Batchelor 89] [Batchelor 90] on machine vision. Their approach is to solve real industrial problems. They have realized the importance of illumination for detecting defects in surfaces. However, their approach is best described as expert experience. For each inspection task, they formulate an illumination strategy, based on their own trial and error experience [Batchelor 85]. They have even developed expert systems, which give illumination strategies based on task specifications [Batchelor 89]. For example, one application is to view bright metal surfaces without causing glinting. Their solution is to use diffuse illumination. While their techniques are useful, they tend to be ad hoc.

Murase and Nayar [Murase 94] have developed an illumination planning system for object

recognition. They take a sequence of images of a set of objects, using different light source directions and different object poses. Then, they project the image set into a universal eigenspace, which is a low dimensional representation of the image set. Each object will trace out a hypercurve in the universal eigenspace. The distance between curves can be used as a metric to distinguish objects. An illumination configuration that maximizes the distance between hypercurves can be used to discriminate between objects in an optimum way.

### 1.1.3 Photometric Methods

Woodham [Woodham 78] proposed the photometric stereo method to determine the surface shape of lambertian (diffuse) dominant surfaces by using three point light sources, and a reflectance map for each light source. Tagare and de Figueiredo [Tagare 91] developed a general theory of photometric stereo that applies to a large class of non-lambertian surfaces.

A number of methods have been developed to recover the shape of specular spike objects. Koshikawa [Koshikawa 79] used polarized light to determine the surface orientation of specular surfaces. Ikeuchi [Ikeuchi 81] used three extended sources to determine the surface orientation of specular surfaces. He determined the radiance distribution of the extended sources, and used this to predict image intensity based on surface orientation. Nayar, Weiss, Simon, and Sanderson [Nayar 90a] developed a system that used 127 point sources to determine the shape of specular objects. Nayar, Ikeuchi, and Kanade [Nayar 90b] developed a method called photometric sampling for surfaces that exhibited a specular spike and lambertian component. The method used an array of extended light sources to illuminate an object from different directions. The array of extended sources guaranteed that specular reflections were detected. In addition, they were able to determine the ratio of the specular to lambertian reflection, which is related to surface roughness. Coleman and Jain [Coleman 82] proposed using four lights to detect specularities. They assumed that points on the object were specular from at most one light source. A valid surface orientation was determined with the remaining three lights, by solving a lambertian system.

Healey and Binford [Healey 88] used a simplified version of the Torrance-Sparrow reflectance model to recover object curvature around the specular peak of objects. They assumed that the surface roughness of the object was known. Wolff [Wolff 87a] [Wolff 87b] used light polarization and the Torrance-Sparrow model to measure surface shape. [Christensen 94] developed a color photometric stereo method, which determines the shape of colored objects using white illumination. The method works for objects that follow the lambertian, Torrance-Sparrow, and dichromatic models. Kiuchi and Ikeuchi [Kiuchi 93] extended photometric sampling to specular lobe dominant objects. Surface orientation, roughness, and specular parameters were extracted. Ikeuchi and Sato [Ikeuchi 91b] developed a method to recover the shape, specular intensity, and specular sharpness of objects that follow the Torrance-Sparrow reflectance model. They took a range image using a range finder, and an intensity image using a CCD camera, using the range image to determine surface shape. Then, they used an iterative segmentation algorithm to classify pixels in the intensity image as specular or lambertian, and to determine the light source direction. Specular intensity and specular sharpness were determined by fitting specular intensity values to a simplified version of the Torrance-Sparrow reflectance model. The use of a range finder to determine surface orientation requires taking first derivatives of the range data. This makes the method

sensitive to noise.

### 1.1.4 Photometric Stereo Error Analysis

Ray, Birk, and Kelly [Ray 83] sought to analyze different sources of error in photometric stereo. They derived closed form solutions for “p” and “q” given three light source positions measured in  $\theta$  and  $\phi$ , and three intensities. Then, they derived sensitivity equations by calculating the partial derivatives of “p” and “q” with respect to intensity and source direction. Their method is valid for small disturbances, and will correctly estimate the error in surface orientation due to a given amount of intensity noise. The equations they derive are several pages long and are very cumbersome. (Jiang and Bunke [Jiang 91] re-derived the expressions for the partial derivatives in  $(\theta_n, \phi_n)$  space. Their expressions are somewhat less cumbersome.)

Ray, Birk, and Kelly's experimental images were produced by averaging 25 images, and then smoothing the image with a 3X3 averaging window. This process would virtually eliminate any intensity noise due to the CCD. They performed an error analysis of the normals for a sphere, plotting the distribution of orientation errors in  $\theta_n$  and  $\phi_n$ . Then, they determined how much error in light source position and source radiance would account for the errors in surface orientation. This part of the experimental work is hypothetical, and does not reflect what errors actually existed in their measurements.

A paper on error analysis that is worth mentioning, but is unrelated to photometric methods is [Yi 94]. In [Yi 94], Yi considers the uncertainty of edge point position (edge points found with an edge operator), and how this uncertainty propagates and affects the accuracy of: line fitting, circle fitting, ellipse fitting, corner location, distance between two points, and angle. The analysis is very extensive, and many simulations were performed. However, no real results are presented. Kemmotsu [Kemmotsu 93] integrated an uncertainty model of a light stripe range finder in recognizing the pose of a 3D object. Gremban [Gremban 92] determined multiple viewpoints which would recognize objects in intensity based images, while considering viewpoint uncertainty.

### 1.1.5 Summary/Conclusions

Cowan addressed the issues of visibility, imaging parameters, irradiance, and lambertian edge contrast. Tsai and Tarabanis addressed the issues of visibility and imaging parameters. Sakane addressed the issue of illumination in order to determine the shape of a lambertian object. Ray, Birk, and Kelly derived expressions for the sensitivity of lambertian surface orientation to different error sources. Yi addressed the issue of finding specular lobe edge contrast.

The problem of finding edge contrast is very different from that of recovering surface shape using photometric methods. In order to generate edge contrast, one only needs to achieve a high intensity difference between the two surfaces that form the edge. This is very different from using intensity to find shape.

Sakane's work is the closest to our research. There are at least three major differences

between Sakane's approach and ours. First, we propose a new metric for finding orientation error. This is developed in Chapter 2. Secondly, Sakane solves the problem of positioning lights to avoid objects in the environment or the manipulator holding the camera. We position light sources so that we illuminate a specified set of object faces in an efficient manner. Thirdly, we incorporate an accurate sensor model in our solution.

The work by Ray, Birk, and Kelly identified major sources of errors in photometric measurements of lambertian surfaces. There are at least four major differences between their work and our work. First, we propose a new metric for finding orientation error. This is developed in Chapter 2. Secondly, we incorporate an accurate sensor model in our solution. Thirdly, we explore the meaning of the sensitivity function. Our error surfaces show the locations of good and bad places to make measurements, and our experimental results give strong support to our methodology. Ray, Birk, and Kelly did not control their error sources during their experiments. Therefore, their experimental results are only casually coupled to their error models. Fourth, we derive a new way measuring the effect of light source position error on the measurement of lambertian surface orientation. This is discussed at the end of Chapter 2.

Sakane, Ray, Birk, and Kelly only examined the illumination of lambertian surfaces. We explore illumination planning for rough diffuse, specular spike, specular lobe, and hybrid surfaces.

## 1.2 Thesis Organization

The thesis is organized by reflectance model. Chapter 2 discusses the illumination of convex and concave lambertian surfaces. The concepts and techniques developed in this chapter are used throughout the remainder of the thesis. Chapter 3 discusses the illumination of rough diffuse surfaces. These surfaces follow a more general diffuse model than the pure lambertian model, allowing a wider range of surfaces to be considered. Chapter 4 discusses the illumination of specular spike surfaces. Specular spike surfaces are important because smooth metal surfaces, which are very common, follow this model. Chapter 5 discusses the illumination of specular lobe surfaces. Chapter 6 discusses the illumination of hybrid surfaces, surfaces containing both the specular lobe component and the lambertian component. Chapter 7 contains conclusions, contributions, and future directions.



## Chapter 2

# Illumination of Lambertian Surfaces

This chapter discusses the illumination of lambertian (diffuse) surfaces. We introduce concepts and techniques that are used throughout the remainder of the thesis. We discuss how illumination affects the determination of surface orientation, in the presence of intensity noise, for the following types of surfaces: 2D convex, 3D convex, 2D concave, and 3D concave. At the end of the chapter, is a brief discussion on the determination of surface orientation in the presence of light source position uncertainty.

### 2.1 Lambertian Model

For a lambertian (diffuse) surface, with surface normal,  $\mathbf{N}$ , and light source direction,  $\mathbf{S}$ ,

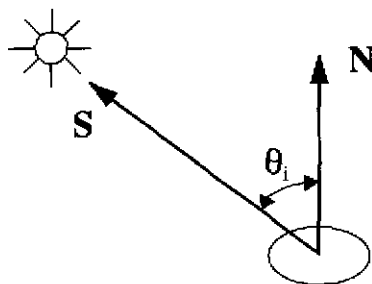


Fig. 2-1. Lambertian geometry

$$I = \rho \cos \theta_i$$

$$I = \rho (\mathbf{S} \cdot \mathbf{N})$$

$$I = \rho (S_x N_x + S_y N_y + S_z N_z)$$

where  $I$  is the measured intensity of  $\mathbf{N}$ ,  $\rho$  is the albedo,  $\theta_i$  is the incident angle.  $(S_x, S_y, S_z)$  and  $(N_x, N_y, N_z)$  are the  $x$ ,  $y$ , and  $z$  components of the unit source vector,  $\mathbf{S}$ , and unit surface normal vector,  $\mathbf{N}$ , respectively. The albedo encompasses the light source intensity and relative reflectance of the surface. So, for a lambertian surface, the intensity is dependent on the

light source direction, surface normal, and the albedo. The intensity is independent of the viewing direction.

## 2.2 2D Convex Lambertian Illumination

We begin the discussion of illumination planning by discussing the illumination of discrete 2D lambertian normals. In some sense, the illumination of all surfaces reduces to the illumination of a set of normals. So, the illumination of a 2D normal is fundamental. We discuss how to position light sources around a set of 2D normals so that we can illuminate them in an efficient manner. Then, we discuss how to determine the orientation error of a single 2D normal, given a light source configuration and a specific amount of sensor noise.

We are able to visualize the solution space for the 2D lambertian illumination problem. This allows us to gain insight into the illumination planning problem. The solution space of the 3D lambertian illumination problem, which we discuss next, is much more complex. It is hard to visualize because of its high dimensionality.

We concentrate on visibility, exact coverage, and the accuracy of surface normal recovery. Our discrete normals exhibit lambertian reflectance characteristics. Our sensor noise model is a constant amount of sensor noise. (In 3D we will use a geometric modeler and a planning system to reason about surfaces. We will also use an accurate, statistical, sensor noise model.)

Our approach is to identify the visibility range for each normal. The visibility range tells us from which parts of the viewing circle we can see each normal, and where we can place a light source to illuminate each normal. After we have the visibility range for each normal, we break the viewing circle into visibility regions. Within each visibility region, certain normals are viewable. Then, we try to find combinations of visibility regions that provide an exact cover of the normals we are trying to view. Since this is a 2D lambertian problem, we need two light sources to determine surface orientation within each visibility region. Finally, we determine the most reliable lighting positions for recovering the orientation of the surface normals within each visibility region.

### 2.2.1 2D Visibility Regions

Given a set of discrete 2D normals ( $n_1, n_2, n_3, \dots$ ), we first find the visibility range for each normal. Since these are discrete normals, we do not need to consider occlusion. The visibility range of each normal is simply  $\pm 90^\circ$  with respect to the normal's orientation. Once we have calculated the visibility range for each normal, we divide the 2D viewing circle into visibility regions. These regions are formed by sorting the visibility ranges of all the normals into a continuous list. The list is then converted into intervals. Within each interval, certain normals will be visible.

For example, if we have normals at  $45^\circ, 90^\circ, 135^\circ$ , and  $180^\circ$  we have the following visibility

ranges:

normal designation	normal	visibility range designation	Visibility Range	
A	45°	VA	315.0°	135.0°
B	90.0°	VB	0.0°	180.0°
C	135°	VC	45.0°	225.0°
D	180°	VD	90.0°	270.0°

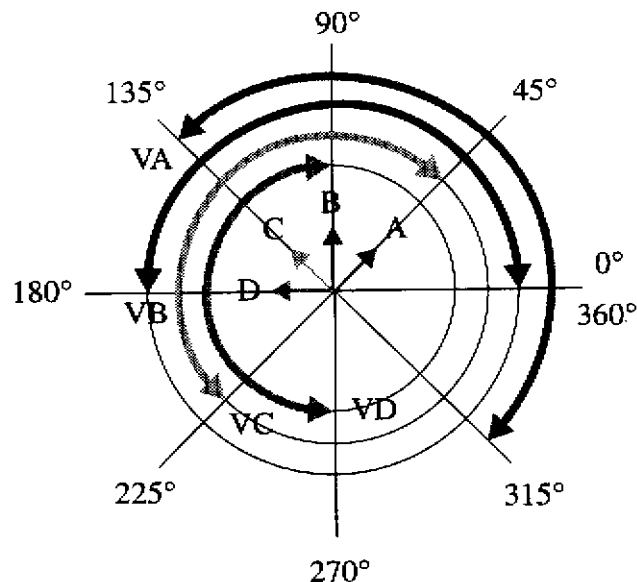


Fig. 2-2. Visibility ranges

2D Visibility range/region diagram:

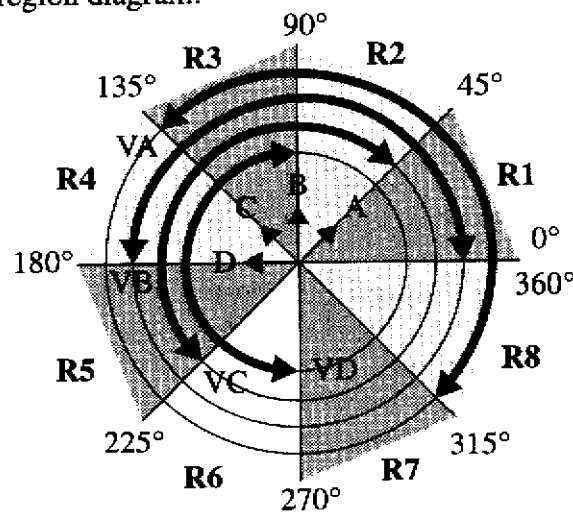


Fig. 2-3. Visibility range/region diagram

The associated visibility regions are:

visibility region		region designation	normals visible
0.0°	45.0°	R1	45.0° 90.0°
45.0°	90.0°	R2	45.0° 90.0° 135.0°
90.0°	135.0°	R3	45.0° 90.0° 135.0° 180.0°
135.0°	180.0°	R4	90.0° 135.0° 180.0°
180.0°	225.0°	R5	135.0° 180.0°
225.0°	270.0°	R6	180.0°
270.0°	315.0°	R7	none
315.0°	360.0°	R8	45.0°

### 2.2.2 2D Exact Covers

After we have the visibility regions, we find combinations of visibility regions that form exact covers of our set of normals (An exact cover contains all of the normals, non-redundantly.) Since the number of regions is small, we use exhaustive search to find the exact covers. If “n” is the number of visibility regions, the complexity of this search is  $O(2^n)$ . (In section 2.3, we develop a heuristic for finding 3D exact covers.) For the previous example, the exact covers are:

Cover number	visibility regions included
1	R3
2	R1, R5
3	R2, R6
4	R4, R8

### 2.2.3 2D Orientation Error

An error in measured intensity will cause an error in surface normal recovery. This can be seen from the lambertian equation:

$$\begin{bmatrix} S1x & S1y \\ S2x & S2y \end{bmatrix}^{-1} \begin{bmatrix} I1 \\ I2 \end{bmatrix} = \begin{bmatrix} Nx \\ Ny \end{bmatrix}$$

(S1x and S1y are the x and y components of the unit vector to light source number one. Nx and Ny are the x and y components of the unit surface normal. I1 is the measured intensity of N due to light source number one.)

An error in either I1 or I2 will cause an error in Nx and Ny:

$$\begin{bmatrix} S1x & S1y \\ S2x & S2y \end{bmatrix}^{-1} \begin{bmatrix} I1 + \delta I1 \\ I2 + \delta I2 \end{bmatrix} = \begin{bmatrix} Nx + \delta Nx \\ Ny + \delta Ny \end{bmatrix}$$

In matrix notation, we can write:

$$S^{-1} (I + \delta I) = N + \delta N$$

We call “ $N + \delta N$ ” a “noisy normal”.

The amount of disturbance caused by  $\delta I$  depends on the condition number of  $S$  [Strang 88]. If  $c$  is the condition number of  $S$  then:

$$\frac{|\delta N|}{|N|} \leq c \cdot \frac{|\delta I|}{|I|}$$

For example, if we have a normal at  $90^\circ$  (The nominal value of  $N_x = 0.0$ , and the nominal value of  $N_y = 1.0$ ),  $S_1$  at  $100^\circ$ ,  $S_2$  at  $80^\circ$ , and  $\delta I_1$  and  $\delta I_2$  are uniform distributions that range from  $-0.1$  to  $0.1$ , we will get the following noisy normal distribution in  $N_x$ - $N_y$  vector space:

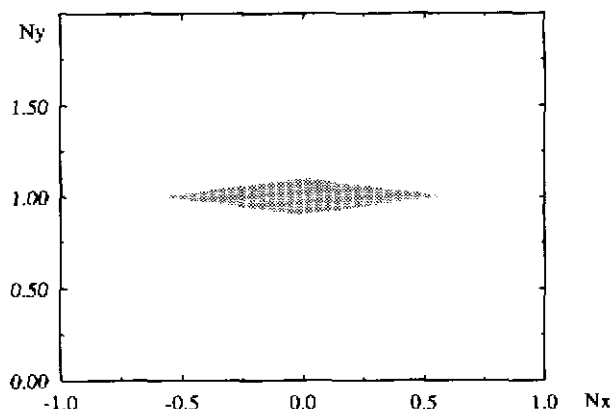


Fig. 2-4. Noisy normal distribution:  $N$  at  $90^\circ$ ,  $S_1$  at  $100^\circ$ ,  $S_2$  at  $80^\circ$ .

The condition number of  $S$  is 5.7. The magnitude of  $I$  and  $N$  are both 1.0, and  $\delta I = 0.1$ . Therefore

$$\frac{|\delta N|}{|N|} \leq 5.7 \cdot \frac{|0.1|}{|1|} \leq 0.57$$

which is the magnitude of the disturbance seen along  $N_x$  in the noisy normal distribution. So, the condition number gives us a way of predicting the magnitude of an expected error in  $N_x$ ,  $N_y$  vector space.

The noisy normal distributions provide insight into the effect of different source matrices. However the noisy normal distributions are only one component of the problem. Surface orientation is represented by a unit normal. The normals in the noisy normal distribution are not guaranteed to be unit normals. Therefore, we normalize the resulting values of  $N_x$  and  $N_y$ . The noisy, normalized, normal is:

$$N_{noise} = \frac{N_x + \delta N_x}{|N + \delta N|}, \frac{N_y + \delta N_y}{|N + \delta N|}$$

$$N_{noise} = N_{x_{noise}}, N_{y_{noise}}$$

When we do this, we perform a nonlinear transformation from  $N_x$ - $N_y$  vector space to the unit normal circle. The angle between a noisy normal and the nominal normal is the angular orientation error. For our 2D case, the angular orientation error is worst at the two extremes of the noisy normal distribution. This is shown below:

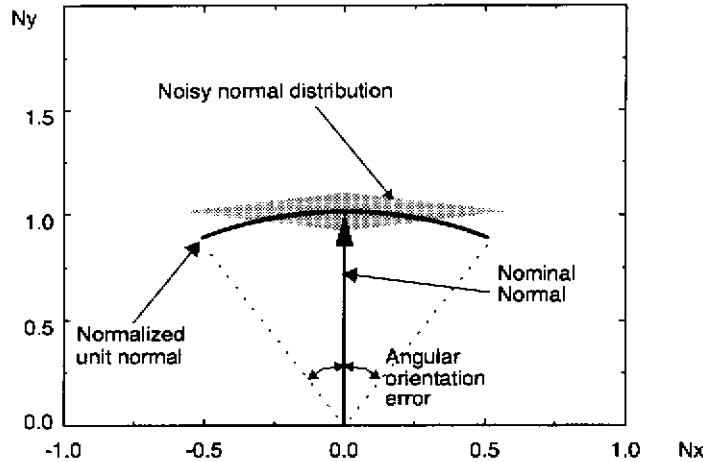


Fig. 2-5. Normalized noisy normal distribution:  $N$  at  $90^\circ$ ,  $S_1$  at  $100^\circ$ ,  $S_2$  at  $80^\circ$

There may be little correlation between the magnitude of the normal vector's error in  $N_x$ - $N_y$  vector space and the resulting angular orientation error. This point can be emphasized by looking at a second example. If we have a normal at  $90^\circ$ ,  $S_1$  at  $10^\circ$ ,  $S_2$  at  $170^\circ$ ,  $\delta I_1$  and  $\delta I_2$  are uniform distributions that range from -0.1 to 0.1, we will get the following normal distribution in  $N_x$ - $N_y$  vector space (The nominal normal is the point  $N_x = 0.0$ ,  $N_y = 1.0$ ):

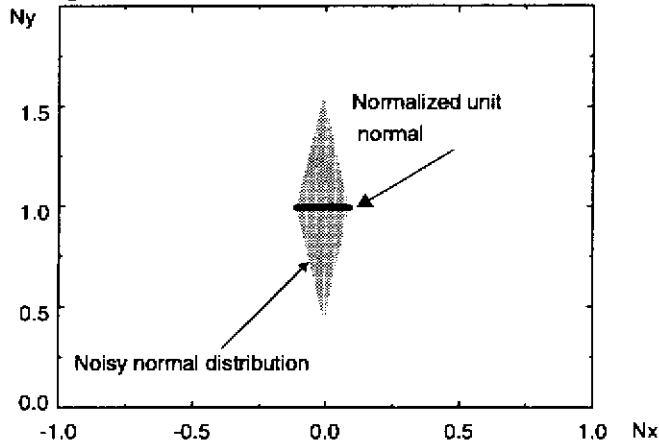


Fig. 2-6. Normalized noisy normal distribution:  $N$  at  $90^\circ$ ,  $S_1$  at  $10^\circ$ ,  $S_2$  at  $170^\circ$

In the two figures, the worst case error in  $N_x$ - $N_y$  vector space is the same. The noisy normal distribution in the two figures is the same except for a  $90^\circ$  rotation. The condition numbers of the two source matrices is also the same. However, normalization causes the angular orientation errors to be very different.

In order to calculate the amount of angular orientation error that we can expect, for a given  $S$ ,  $N$ , and  $\delta I$ , we calculate  $N + \delta N$ . We normalize the resulting  $N + \delta N$  vector. We call the normalized  $N + \delta N$  vector  $N_{\text{noisy}}$ . Then, we find the angular orientation error between  $N$  and

$N_{noise}$

$$\theta_{err} = \text{acos}(N \cdot N_{noise})$$

For the 2D case, we use the average of the two maximal angular orientation errors.

### 2.2.3.1 Angular Orientation Error Surface for One Normal

Next, we look at the error surface for a single normal at 90°. We use the following 2D global coordinate system for specifying the positions of the normal and light sources. (In places, we use the notation S1=10°, N=90°. This is a shorthand for  $\theta_S=10^\circ$ ,  $\theta_N=90^\circ$ .)

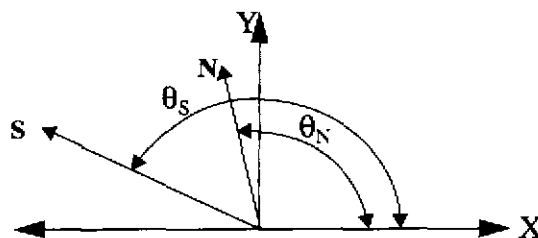


Fig. 2-7. Source/viewer frame of reference coordinate system

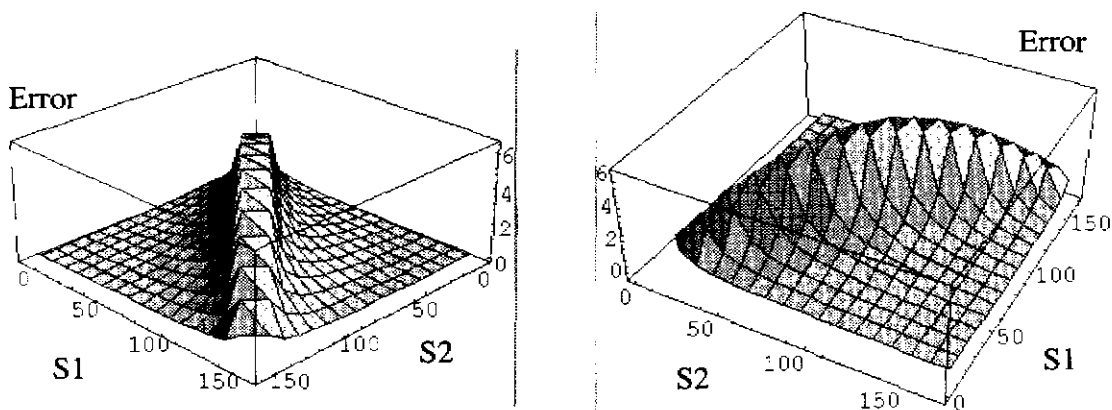


Fig. 2-8. Error surface:  $N=90^\circ$ ,  $\delta I=0.01$

The error is greatest when the light sources are close together and, the incident angle between each light source and the surface normal is small. Below are slices of the error sur-

face for  $S1=10^\circ$ ,  $S1=90^\circ$ , and  $S1=170^\circ$ .

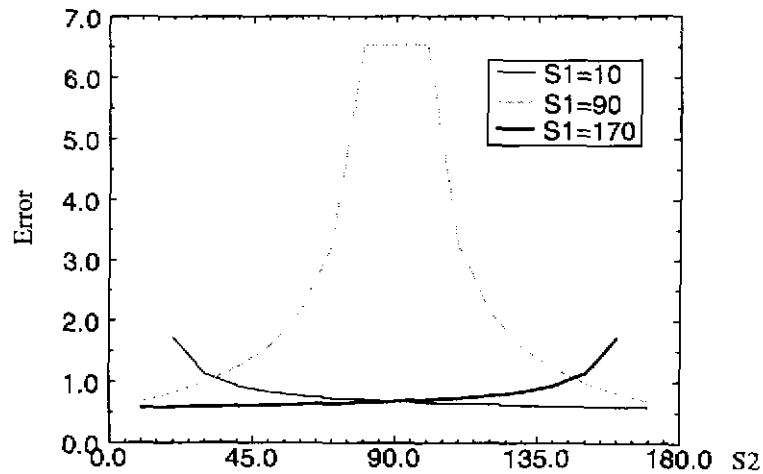


Fig. 2-9. 2D Lambertian error surface cross sections,  $N=90$ ,  $\delta I=0.01$

There are three factors that we identify as contributing to the shape of the error surface: the shape of the photometric function, the stability of the system of photometric equations, and the signal to noise ratio of our measurement.

We are using intensity to determine surface orientation. A change in intensity due to noise will cause a change in surface orientation. If we look at the cosine function, we can see that at small incident angles, the sensitivity of surface orientation to intensity noise will be high, and at large incident angles, the sensitivity will be much less.

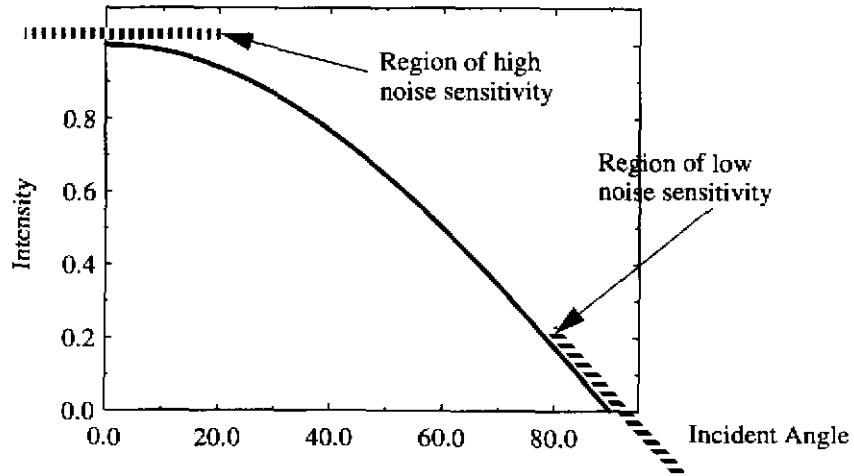


Fig. 2-10. Lambertian intensity function

This sensitivity is explicitly shown by calculating the derivative of incident angle with respect to intensity. This plot shows, for a single light source, how intensity noise will affect orientation. We are using two light sources to determine surface orientation, so this factor

cannot be considered alone.

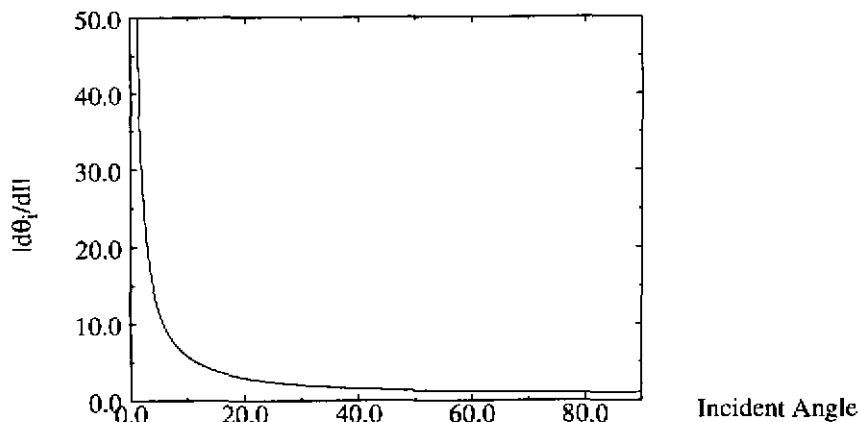


Fig. 2-11. |Derivativel of lambertian intensity function.

The second factor contributing to the shape of the error surface is the stability of the system of equations we are solving using S1 and S2. As the light sources become close together, the system approaches singularity, and becomes more sensitive to perturbations. The condition number of the source matrix, Fig. 2-12. , indicates how sensitive the system is to perturbations.

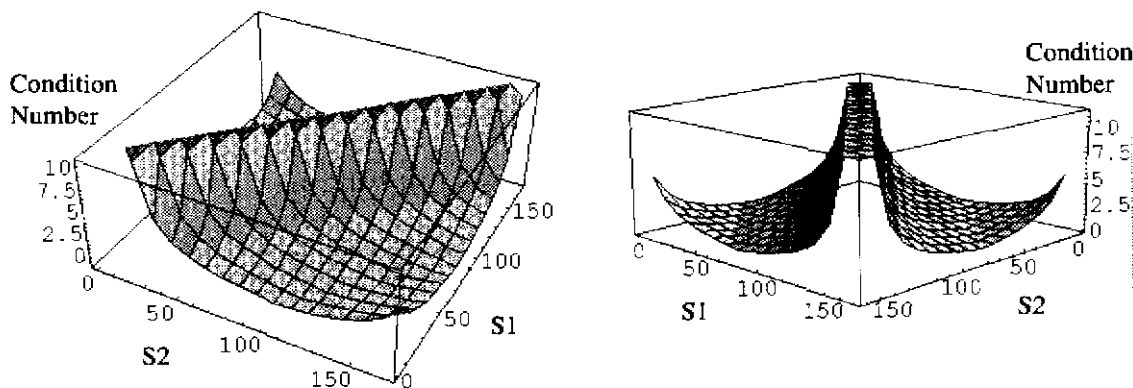


Fig. 2-12. Source matrix condition number.

The ridge along the line S1=S2 of the error surface, Fig. 2-8. , is due to the singularity of the system. The reason that the singularity ridge has its curved shape is the derivative function. Based on the condition number plot, the system is equally singular along the singularity ridge. However, when the incident angle is small, the system is more sensitive to intensity noise. As the incident angle becomes larger, the system's sensitivity becomes less, even though the system is singular. So for the singularity ridge, there are two factors that help to explain the shape: singularity and noise sensitivity. As we move away from the singularity ridge, noise sensitivity (the derivative function) explains the shape of the error surface.

A third factor to consider is the signal to noise ratio of our measurement. We can isolate this factor by changing the light source intensity. Below we plot angular error, versus source intensity, for different source configurations. As source intensity increases, the angular error decreases. This is because the signal to noise ratio is larger. The noise produces less relative disturbance to surface orientation. The plots approximately follow a  $K/(\text{Source Intensity})$

function, which is what we would expect. (The value of  $K$  depends on the source configuration.)

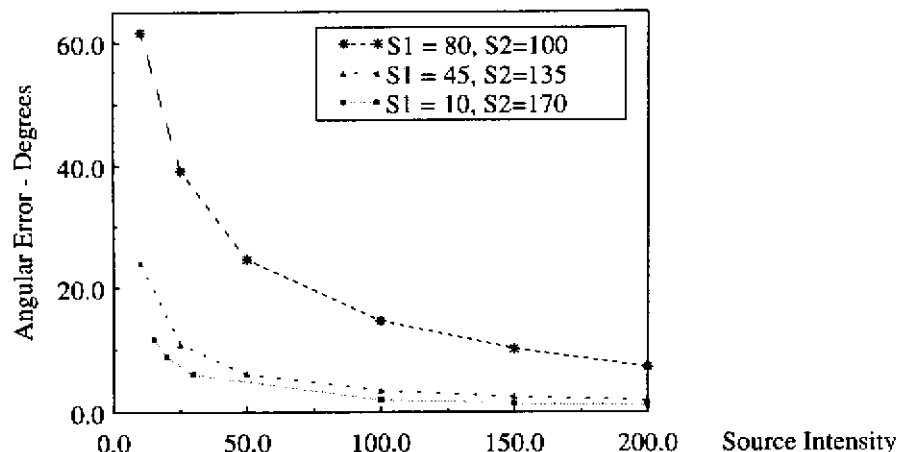


Fig. 2-13. Angular error versus source intensity.  $N = 90^\circ$ . ( $\pm 3\sigma$  noise model from section 2.5.1)

While these three factors give some insight into the error surface, it is important to remember that the error surface is a function of the system of photometric equations. The derivative of the intensity function, the stability of the system of equations, and the signal to noise ratio all contribute to the error surface. By considering each of these factors separately, we can gain some insight into the error surface. However, these factors act together, and cannot be uncoupled without altering the very system we are studying. So, in a real sense, the error surface is the only truthful representation of the system's behavior.

### 2.2.3.2 Angular Orientation Error Surface for Multiple Normals

Next, we go back to our "exact cover" example, where we had discrete 2D normals at  $45^\circ$ ,  $90^\circ$ ,  $135^\circ$ , and  $180^\circ$ . We let  $\delta I = 0.01$ , and assess our ability to accurately determine surface orientation within each visibility range, of each exact cover. Each visibility range contains certain normals. We move two light sources, in one degree increments, between the maximum and minimum visibility values of each visibility range. At each position, we find the total angular error, in degrees, for the normals within the visibility range. After searching through the entire visibility range, we find the light source placement with the minimum error.

We get the following results ("Total error" is the sum of the angular errors, in degrees, for the normals within the visibility range. The columns  $45^\circ$ ,  $90^\circ$ ,  $135^\circ$ , and  $180^\circ$  list the angular error, in degrees, for each of these normals. "Min S1" and "Min S2" are the light source

positions that produced the minimum error.):

Cover	Visibility Range		Total error	45°	90°	135°	180°	Min S1	Min S2
1	90.0	135.0	4.10	0.60	1.45	1.45	0.60	91.0	134.0
2	0.0	45.0	2.05	1.45	0.60			1.0	44.0
2	180.0	225.0	2.05			0.60	1.45	181.0	224.0
3	45.0	90.0	3.50	1.45	1.45	0.60		46.0	89.0
3	225.0	270.0	0.6				0.6	226.0	269.0
4	135.0	180.0	3.50		0.60	1.45	1.45	136.0	179.0
4	315.0	360.0	0.60	0.60				316.0	359.0

A tessellated error surface for cover 1 is show below. The error is greatest when the light sources are close together and is least when the light sources are far apart.

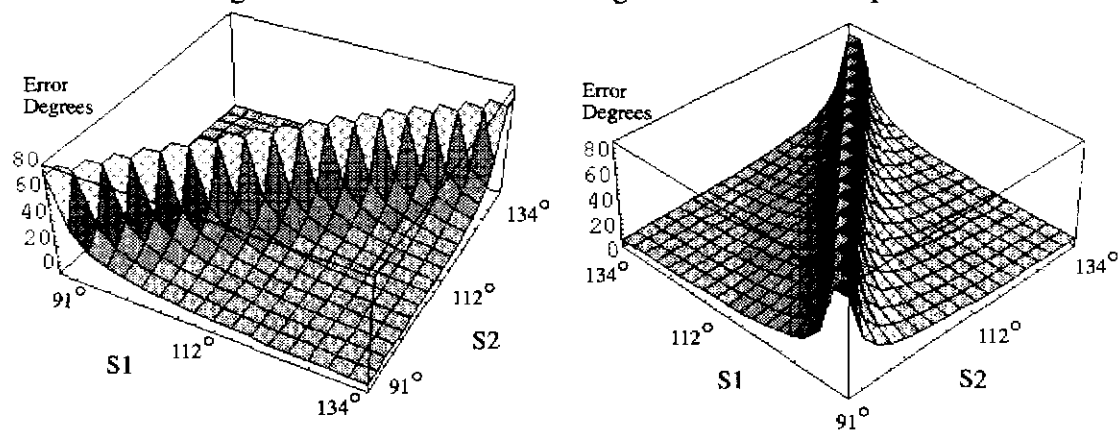


Fig. 2-14. 2D angular orientation error surface

## 2.3 3D Convex Illumination Covers

Finding illumination covers in 3D is similar to finding illumination covers in 2D. We are given a 3D convex polyhedral object, and a set of faces on the object that we want to illuminate. We want to place light sources around the object in a way that illuminates the specified set of object faces, while minimizing the total number of measurements we need to make.

### 2.3.1 3D Aspect Generation

In order to illuminate an object, we need to be able to divide the viewing sphere into aspects. Each aspect describes topologically connected viewing directions that see the same set of object faces. Eventually, aspects need to be combined in some manner that provides coverage of all the object faces that need to be illuminated. (We define our task to be illumination of a specified set of object faces. This set may include all object faces, or it may be a proper subset of all object faces.)

A combination of aspects that views all specified faces of an object in a non-redundant manner is called an exact cover. Given the list of faces visible from each aspect and a list of all

the faces on the object that we are illuminating, we can determine combinations of aspects that form exact covers.

### **2.3.1.1 Aspect Generation Background**

Koenderink and van Doorn [Koenderink 79] described aspects and their associated data structure the visual potential (aspect graph). Since then, many researchers [Bowyer 90] have explored aspect graphs, and their application to computer vision tasks. The primary application of aspect graphs to computer vision has been object recognition [Ikeuchi 88] [Hebert 85]. Aspect graphs are used to predict potential object appearances. Then, sensor measurements, which can recognize an object based upon the set of possible object appearances and sensor measurements, can be planned. There are two types of aspect prediction possible: exact aspect graphs and approximate aspect graphs. Exact aspect graphs [Gigus 91] [Kriegman 90] [Stewman 87] [Plantinga 90] use a 3D model of an object to predict where in viewpoint space visual events occur. Once the location of a visual event is known, viewpoint space can be partitioned into regions. Each region will correspond to an aspect. Exact aspect graphs are mathematically complete. They describe every aspect that an object produces, no matter how small. However, producing an exact aspect graph for general objects is a non-trivial problem which is still an area of active research.

The approximate aspect graph approach [Ikeuchi 88] [Hebert 85] uses a tessellated viewing sphere that surrounds the object. Views from each viewpoint on the viewing sphere are generated. Views that are topologically equivalent are merged into aspects. The approximate aspect graph method, unlike the exact aspect graph method, will work on all classes of objects. By using this approach, we will be able to illuminate a large class of objects.

The approximate aspect graph approach misses aspects that are close to the object being viewed (usually the viewing sphere is much larger than the object). The method may miss small aspects if the tessellation is not fine enough and is computationally intensive.

### **2.3.1.2 Aspect Generation Implementation**

For our application, aspects that are close to the object are not important. We are trying to generate a macroscopic level illumination plan for an entire object, not a microscopic illumination plan for a partial face. Small aspects are undesirable because they are unstable, and computational load is not issue because the illumination plan can be generated off-line. So, the approximate aspect graph approach, which works on a wide class of objects, meets our requirements.

We generate CAD models of objects that we want to illuminate by using the "Vantage" geometric modeling system [Kumar 91] [Ikeuchi 91]. Using these models and the 3D-to-2D scene generation capabilities of Vantage, we generate orthographic projections, from various viewpoints, of a tessellated icosahedron. By comparing the area of each visible object face with its foreshortened projected area, we can determine which object faces are completely visible from each viewpoint. If the face is more than 99% visible, we consider the face to be completely visible.

Once we know which object faces are visible from each icosahedron viewpoint, we merge adjacent icosahedron viewpoints that view the same set of object faces. The resulting merged set of icosahedron viewpoints forms an aspect. Each aspect is a continuous viewing region. A camera or light source placed anywhere within the region will view the same set of object faces.

### 2.3.2 3D Exact Coverage

The problem of finding all exact covers of a set of faces is equivalent to the set/subset exact cover problem. This problem is known to be NP-complete [Cormen 90]. In order to decrease the complexity of finding exact covers, we developed a heuristic search approach to the problem. Our heuristic measure is the number of object faces covered by the aspect. Our algorithm is as follows:

1. Select an object face.
2. Find the largest aspect,  $A_{max_1}$ , (aspect that sees the most object faces) that contains this object face.
3. Delete any aspects that overlap  $A_{max_1}$ , including  $A_{max_1}$ , from the aspect-list.
4.  $n = 1$ .
5. Find the largest remaining aspect in the aspect-list,  $A_{max_n}$ .
6. See if the combination of  $A_{max_1}, A_{max_2}, \dots, A_{max_n}$  covers all object faces. If so, return the exact cover:  $A_{max_1}, A_{max_2}, \dots, A_{max_n}$ .
7. If not, delete any aspects that overlap  $A_{max_n}$ , including  $A_{max_n}$ , from the aspect-list.
8. If the aspect-list is empty, signal failure and return.
9.  $n = n + 1$ .
10. Go to step 5.

In steps 2 and 5, if there are two or more aspects that are the largest aspects, we trace out all of the largest aspects in parallel. We can expand our criteria for finding the next aspect to expand in steps 2 and 5 to include the largest aspects, the 2nd largest aspects, ..., the  $q$ th largest aspects. As  $q$  increases, the algorithm will approach exponential complexity.

The maximal aspect heuristic was chosen because we are trying to minimize the number of sensor measurements needed to cover an object. By choosing aspects that cover as many object faces as possible, we maximize the coverage of each sensor measurement. This should tend to minimize the number of sensor measurements needed.

We do not offer a formal proof that our algorithm will succeed for all objects. (The success of the algorithm is dependent on the tessellation of the viewing sphere since some aspects might be missed if the tessellation is not fine enough.) However, we can say that as our search expands to include the  $q$ th largest aspect, the aspect size will in the worst case approach the size of a single face. This is possible in the case of cube, where it is possible to have singular aspects that contain each cube face. Then, an exact cover can be formed by combining these single face aspects. As object complexity increases, the object will eventu-

ally approach a tessellated sphere. In this case, two views, 180° apart, provide an exact cover.

In order to test our algorithm against the set of exact covers, we compared our level one search (only the largest aspects), with deeper level searches (largest aspects, the 2nd largest aspects, ..., the qth largest aspects) for the following objects:

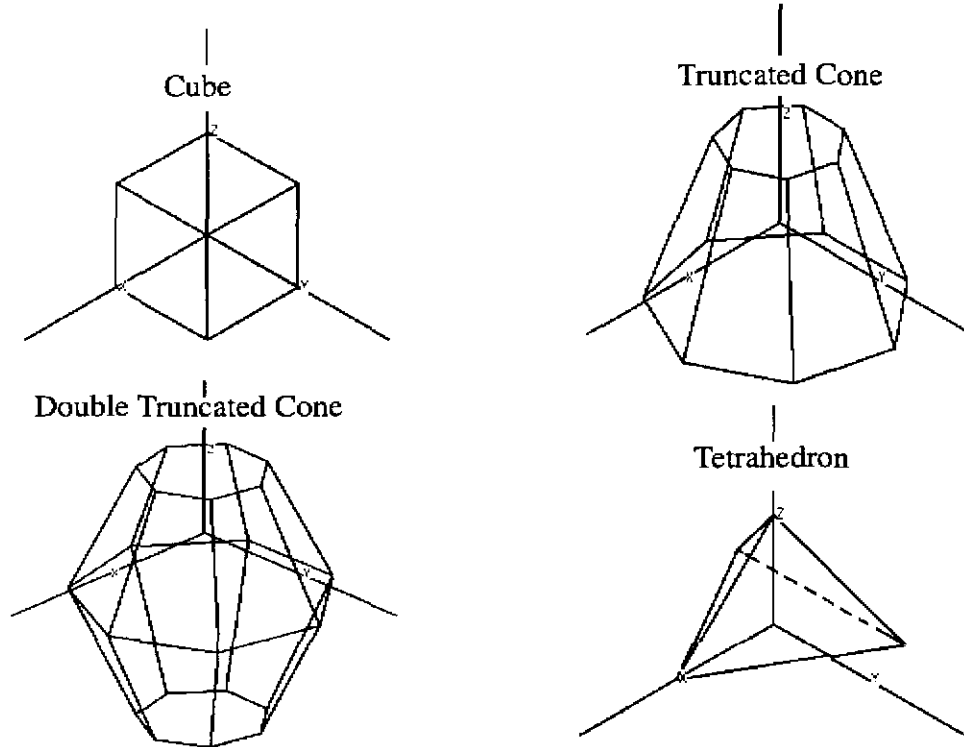


Fig. 2-15. Convex polyhedra used for exact cover tests.

Aspects are formed by using an 3-frequency (320 face) icosahedron. The icosahedron has a radius equal to 1000 times the largest diameter of the object being illuminated. Views are generated using orthographic projection. Viewpoints are located at the center of each icosahedron face.

The table below shows the number of exact covers versus search depth. The covers include aspects made up of one or more viewpoints.

Search Depth	Number of Exact Covers			
	cube	tetrahedron	truncated cone	double truncated cone
1	4	12	41	79
2	68	21	45	79
3	68	23	45	79
4		23		

Ideally, for the cube, the largest aspect at search depth level 1 would view 3 cube faces. At

search depth level 2, the largest aspect and 2nd largest aspect would view 2 or 3 cube faces. At search depth level 3, the largest aspect, 2nd largest aspect, and 3rd largest aspect would view 1, 2, or 3 cube faces. The reason that we do not see a jump in the number of aspects for the cube when we increase the search depth from 2 to 3 is that the icosahedron's viewpoints do not line up with the cube's faces. So, we do not have any aspects that see only one cube face. We only have aspects that see two or three cube faces. The single cube face aspects are actually accidental aspects. They are not really useful because they occur at one exact viewing direction. They are very unstable. In the case of the tetrahedron, we have a couple of aspects that see only one tetrahedron face. These aspects are large, containing many icosahedron viewpoints. We also have aspects that see two tetrahedron faces and three tetrahedron faces. Therefore, we have more jumps in the number of aspects for the tetrahedron than for the cube.

For photometric stereo, an illumination aspect needs to contain at least three viewpoints since we need to place three light sources in an aspect. If we only include aspects that contain three or more viewpoints, the number of exact covers will decrease. The table below shows the number of exact covers versus search depth, when only aspects which contain at least three viewpoints are allowed to be part of an exact cover.

Search Depth	Number of Exact Covers			
	cube	tetrahedron	truncated cone	double truncated cone
1	4	7	13	21
2	4	13	13	21
3	4	14	13	21

## 2.4 3D Convex Lambertian Illumination

Light source positioning in 3D is similar to light source positioning in 2D. The goal is to find the positions for three light sources that illuminate a given set of object faces while minimizing the "total orientation error" for the object faces. An exact illumination cover for a given set of object faces and a candidate set of light source positions is found using the heuristic developed in the previous section. Then, for each illumination aspect, three light sources are placed in all of the combinations of light source positions that comprise the illumination aspect. The number of combinations is  $\binom{N}{3}$ , since we are placing three light sources in the  $N$  light source positions that comprise the aspect. The "total orientation error" is evaluated for each combination. The light source positions that produce the minimum total orientation error are returned by the planner.

### 2.4.1 3D Orientation Error

As we developed in the two dimensional case, an error in measured intensity will cause an

error in surface normal recovery. This can be seen from the lambertian equation:

$$\begin{bmatrix} S1x & S1y & S1z \\ S2x & S2y & S2z \\ S3x & S3y & S3z \end{bmatrix}^{-1} \begin{bmatrix} I1 \\ I2 \\ I3 \end{bmatrix} = \begin{bmatrix} Nx \\ Ny \\ Nz \end{bmatrix}$$

I1, I2, and I3 are the mean, measured, intensities for **S1**, **S2**, and **S3** respectively. Noise in either I1, I2, or I3 will cause an error in Nx, Ny, and Nz, producing a noisy normal:

$$\begin{bmatrix} S1x & S1y & S1z \\ S2x & S2y & S2z \\ S3x & S3y & S3z \end{bmatrix}^{-1} \begin{bmatrix} I1 + \delta I1 \\ I2 + \delta I2 \\ I3 + \delta I3 \end{bmatrix} = \begin{bmatrix} Nx + \delta Nx \\ Ny + \delta Ny \\ Nz + \delta Nz \end{bmatrix}$$

In matrix notation, we can write:

$$S^{-1} (I + \delta I) = N + \delta N$$

The noisy, normalized, normal is:

$$N_{noise} = \frac{Nx + \delta Nx}{|N + \delta N|}, \frac{Ny + \delta Ny}{|N + \delta N|}, \frac{Nz + \delta Nz}{|N + \delta N|}$$

$$N_{noise} = Nx_{noise}, Ny_{noise}, Nz_{noise}$$

In the two dimensional case, the Nx-Ny error area is a quadrilateral. In three dimensions, the Nx-Ny-Nz error volume is an octahedron. In two dimensions, after normalization, the normal is projected onto the unit normal circle. In three dimensions, after normalization, the normal is projected onto the unit normal sphere. Fig. 2-16. shows an example of a distribution of normalized normals, using the intensity noise function from section 2.5.1.

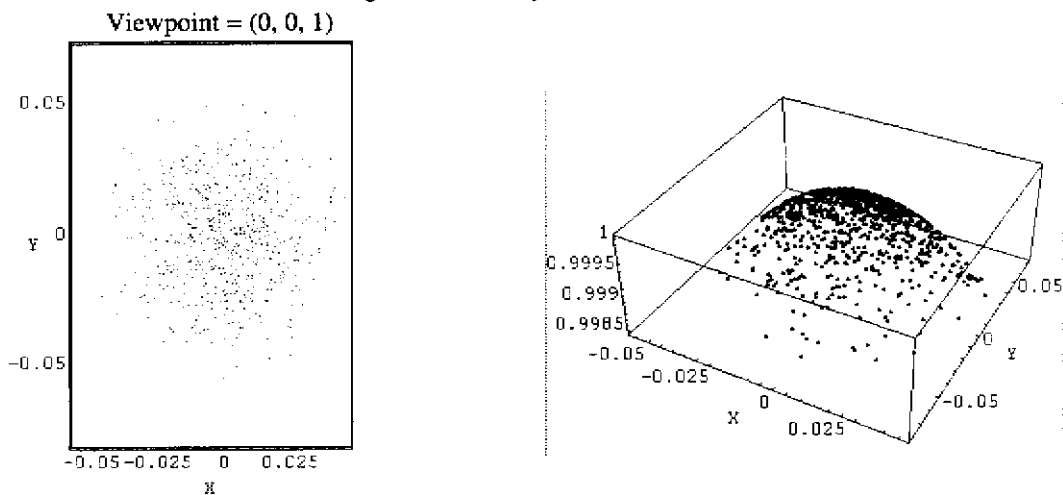


Fig. 2-16. 3D Normalized noisy normals:  $N = (0, 0, 1)$ ,  $S1 = (-.526, 0.0, .851)$ ,  $S2 = (-.809, -.309, .5)$ ,  $S3 = (-.809, .309, .5)$ ,  $I1 = I2 = I3 = 150$

We define the orientation error to be the angle between the nominal unit normal and the

noisy unit normal. The orientation error depends on how we define the  $\delta I$  terms. Initially we defined the worst case error to be:

$$\delta I = \pm 3\sigma_i$$

By letting I1, I2, and I3 independently take on a worst case  $+3\sigma_i$  or  $-3\sigma_i$  error, we generated 8 potential worst case errors. However, the probability of having I1, I2, and I3 simultaneously have  $3\sigma$  values is very small.

A more realistic method of determining the error is to have the planner conduct a simulation using the intensity noise function. If we know the mean intensity of each light source, (This can be determined if the object's pose, the light source directions, and the light source radiances are known.) and the corresponding value of  $\sigma_i$ , we can calculate a noisy surface orientation using the known light source positions. At each iteration, a random intensity for each light source is generated from the mean light source intensity and  $\sigma_i$  for that light source intensity. These three noisy intensity values are used to determine a noisy surface orientation. We repeat this 1000 times. We calculate the mean, noisy, surface orientation to be the center of mass of the 1000 noisy surface orientations:

$$\bar{N}_{noise} = \left( \frac{\sum_{i=1}^{1000} [N_{x_{noise}}]_i}{1000}, \frac{\sum_{i=1}^{1000} [N_{y_{noise}}]_i}{1000}, \frac{\sum_{i=1}^{1000} [N_{z_{noise}}]_i}{1000} \right)$$

For simulations, the mean noisy normal is always equal to the nominal normal. However, when we are making measurements, the actual orientation of the object is not precisely known. The mean measured noisy normal may be different from the simulator's nominal normal.

Using each noisy surface orientation and the mean, noisy, surface orientation, we calculate the orientation error.

$$\theta_{err} = \arccos(\bar{N}_{noise} \cdot N_{noise})$$

Using the 1000 values of orientation error that our simulation produced, we calculate the standard deviation of the orientation error,  $\sigma(\theta_{err})$ . (Orientation error is a positive valued function. We make it a two sided function when calculating the standard deviation.)

In order to compare illumination covers, we need a metric. We define the "total orientation error" for each illumination cover to be the sum of the errors for each face illuminated by the cover. Where the error for each face is 3 standard deviations. For n faces:

$$\theta_{totalerr} = \sum_{i=1}^n 3[\sigma(\theta_{err})]_i$$

#### 2.4.1.1 Source Normalization

In any real system, the light sources will have different radiances. This will affect the value

of  $\sigma(\theta_{err})$ . If the three light sources used to determine  $\mathbf{N}$  do not have the same radiances, the three raw intensity values ( $I_1$ ,  $I_2$ , and  $I_3$ ) need to be normalized. We normalize to the minimum light source radiance. If we define “minimax” to be the minimum light source radiance of the three light sources that we are using, then for three measured intensities, our normalization is:

$$i1_{norm_{meas}} = \left( \frac{minimax}{i1_{max}} \right) i1_{meas}$$

$$i2_{norm_{meas}} = \left( \frac{minimax}{i2_{max}} \right) i2_{meas}$$

$$i3_{norm_{meas}} = \left( \frac{minimax}{i3_{max}} \right) i3_{meas}$$

where  $i1_{max}$  is the radiance of light source one.

The normalization process affects the variance of the measured intensities and therefore affects  $\sigma(\theta_{err})$ . If the planner has knowledge about light source radiances, then it can take this information into account when it predicts  $\sigma(\theta_{err})$ .

The planner will predict the mean light source intensities for a face based upon the face’s assumed pose, and the known light source radiances:

$$\overline{i1_{plan}} = i1_{max} (\mathbf{S1} \cdot \mathbf{N})$$

$$\overline{i3_{plan}} = i3_{max} (\mathbf{S3} \cdot \mathbf{N})$$

$$\overline{i2_{plan}} = i2_{max} (\mathbf{S2} \cdot \mathbf{N})$$

where  $\mathbf{S1}$  is the direction of light source one,  $i1_{max}$  is the radiance of light source one, and  $\mathbf{N}$  is the normal of the face.

These mean intensities should be the intensities that irradiate the CCD of our camera. These mean intensities determine the variance of our measurement. So, for each mean intensity, our planner determines the standard deviation that we expect to measure. We will call these three values  $\sigma_{i1}$ ,  $\sigma_{i2}$ ,  $\sigma_{i3}$ .

However, the normalization of the intensity values affects these variances. So that:

$$\sigma_{i1_{plan}} = \left( \frac{minimax}{i1_{max}} \right) \sigma_{i1}$$

$$\sigma_{i2_{plan}} = \left( \frac{minimax}{i2_{max}} \right) \sigma_{i2}$$

$$\sigma_{i3_{plan}} = \left( \frac{minimax}{i3_{max}} \right) \sigma_{i3}$$

The planner's normalized predicted intensities are:

$$i1_{normplan} = \left( \frac{minimax}{i1_{max}} \right) \overline{i1_{plan}}$$

$$i2_{normplan} = \left( \frac{minimax}{i2_{max}} \right) \overline{i2_{plan}}$$

$$i3_{normplan} = \left( \frac{minimax}{i3_{max}} \right) \overline{i3_{plan}}$$

So, the intensity distributions used by the planner are:

$$N\left(i1_{normplan}, \sigma_{i1_{plan}}\right)$$

$$N\left(i2_{normplan}, \sigma_{i2_{plan}}\right)$$

$$N\left(i3_{normplan}, \sigma_{i3_{plan}}\right)$$

The planner can then use this distribution in its simulation. The planner uses these distributions to produce 1000 noisy sets of intensity values. Then, it uses these 1000 noisy sets of intensity values to calculate 1000 values of  $N_{noise}$ . Using the 1000 values of  $N_{noise}$ , the planner can calculate the standard deviation of surface orientation error,  $\sigma(\theta_{err})$ .

Generally, as the planner incorporates more of the factors that influence the measurements, the planner's predictions will become more accurate. It is an open question how accurate a planner should be. This will depend upon the application and the significance of the factors affecting the measurements. The amount of error caused by violating assumptions depends on how severely they are violated, and on how sensitive the measurements are to these violated assumptions.

## 2.4.2 Light Intensity Variance

The variance of the camera and digitizer,  $\sigma_i^2$ , is a function of light intensity as shown by Healey [Healey 94] [Healey 92] [Healey 91]. We have taken an empirical approach to determining the value of the function. In general, our measurements are in good agreement with Healey's. Since we are making measurements at one pixel, we ignore fixed pattern noise, which is a collection site to collection site nonuniformity in charge collection. The noise we are measuring is composed of shot noise, dark current noise, amplifier noise and quantization noise (amplifier and quantization noise are independent of intensity). At high levels of intensity, the poisson distribution of shot noise approaches a normal distribution [Oliver 65]. We estimate dark current noise with a constant.

## 2.4.3 Camera Viewpoint Selection

We need to position a camera so that the camera views all of the faces illuminated by each illumination aspect. Camera visibility is determined in an identical manner to determining light source visibility. The only difference is that the set of potential camera viewpoints may be different from the set of light source directions. Given a set of potential camera viewpoints, virtual cameras are positioned at each viewpoint. Object face visibility is determined

by using the Vantage geometric modelling system. If the set of illuminated faces is a subset of the set of visible faces, then the viewpoint is added to a list of candidate viewpoints. We select, from the list of candidate viewpoints, the camera viewpoint that views the set of faces with the least foreshortening. The idea of this metric is to maximize the area of each face in our image. Formally, over the set of possible viewpoints, we try to minimize:

$$\max\left(\frac{1}{\cos\theta_1}, \frac{1}{\cos\theta_2}, \dots, \frac{1}{\cos\theta_n}\right)$$

where  $\theta_i$  measures the angle between the viewpoint and faces 1 ... n.

#### 2.4.4 Object Pose Errors

There are two basic types of errors in photometric measurements of lambertian objects: random errors and fixed errors. Random errors are due to  $\sigma_i$ . These are the errors that we try to predict with our planner. Fixed errors include: errors in light source direction, errors in light source radiance, errors in the photometric function (deviation from pure lambertian). Fixed errors can be accounted for by a careful calibration procedure.

A third potential error is object pose error. Our planner assumes that the object being viewed is in a certain orientation. If the object is in a different orientation, the planner's predicted surface orientation error will be erroneous. A change in orientation will cause a change in the incident angles between the light sources and object faces. This will cause a change in expected mean light source intensities,  $\sigma_i$ , and thus the standard deviation of surface orientation error,  $\sigma(\theta_{err})$ .

The amount of change in mean light source intensities depends on the lambertian photometric function (the cosine function). If the incident angle is small, a small change in rotation will not cause a large change in the expected mean light source intensity. If the incident angle is large, a small change in rotation could cause a large change in the expected mean light source intensity.

## 2.5 3D Convex Lambertian Implementation

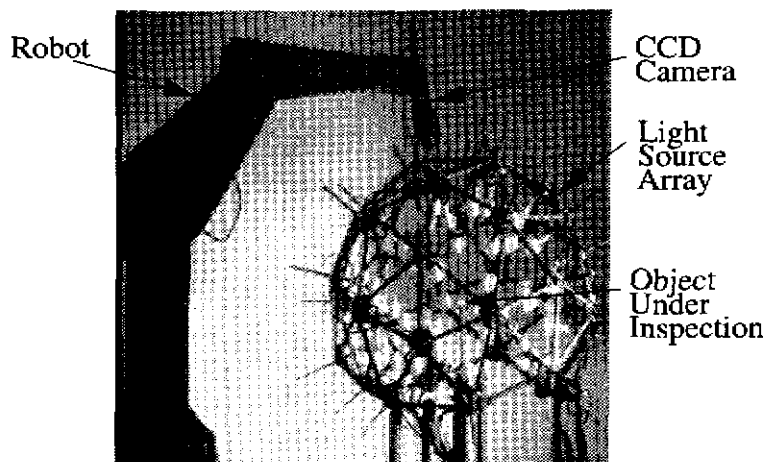


Fig. 2-17. Experimental setup

The 3D Lambertian planner was implemented in Lucid™ Common Lisp. Experiments were carried out using a Puma 560 robot and an array of light sources placed at the vertices of a 1-frequency icosahedron. (For structural reasons, 61 faces actually exist and 36 of the vertices have light sources). A Sony XC-57 camera, with a Nikon AF Nikkor Micro 105mm F2.8 lens, was mounted on the Puma's end effector. Camera viewpoints were located at the faces of the 1-frequency icosahedron. Because of robot workspace constraints, the Puma robot, with the camera mounted on it, could only reach 22 of the 61 icosahedron faces. Images were digitized using an Androx ICS-400 digitizer.

Hand/eye calibration was performed by using Tsai's camera calibration procedure [Tsai 87] and Lenz's hand/eye calibration procedure [Lenz 89]. Due to the large focal length of our lens, and the workspace limitations of the Puma robot, our target had to be very small. It was composed of an 8X8 grid of dots, with 2 dots missing for disambiguating orientation. The target was 6.7mm square with an inter-dot spacing of 0.95mm. In order to constrain the calibration, a non-coplanar method was employed. We used a Melles Griot laboratory jack to provide Z translation. Five images of the target, at different Z translations, were taken from each camera position. Five camera positions were used. After performing the hand/eye calibration we were able aim the camera with an accuracy of approximately  $1^\circ - 1.5^\circ$ .

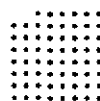


Fig. 2-18. Camera calibration target. Scale is approximately 2X.

### 2.5.1 Measurement of Light Intensity Variance

In order to measure  $\sigma_i$ , illumination, viewing geometry, camera temperature, and CCD voltages must be controlled. Any variance in any of these parameters will cause added variation in  $\sigma_i$ . Both our light source and Sony XC-57 camera were powered by linear DC supplies. (We found that controlling the camera with a standard switching camera power supply increased  $\sigma_i$ .) Camera temperature was held constant by allowing the camera to reach a

steady state temperature with respect to its environment. Viewing geometry was maintained by rigidly supporting the camera and target. Our target was of uniform matte reflectance.

We selected four pixels on the CCD, and took 1000 images of our fixed scene. Illumination was changed by varying the incident angle between the light source and target. We took measurements between mean intensities of 8 (dark current value) and 227. Normality was checked by plotting a histogram of intensity for each pixel, and by using the Kolmogorov-Smirnov test [Press 90]. The average significance level of the Kolmogorov-Smirnov test was 0.342. A representative histogram is shown below:

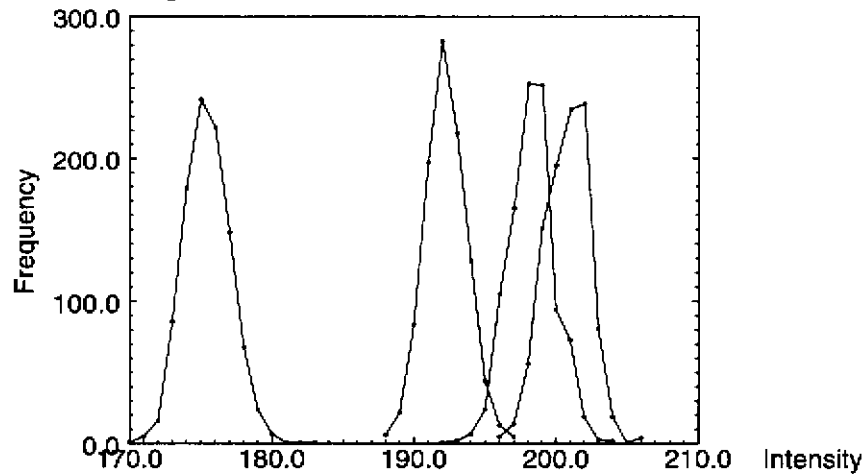


Fig. 2-19. Intensity histogram

For each pixel we calculated the mean, variance, and standard deviation of the intensity measurements. We fitted a second degree polynomial to the raw data, and used this polynomial in our planner. The plot of the standard deviation of intensity is shown below. The fitted polynomial is shown as the solid line.

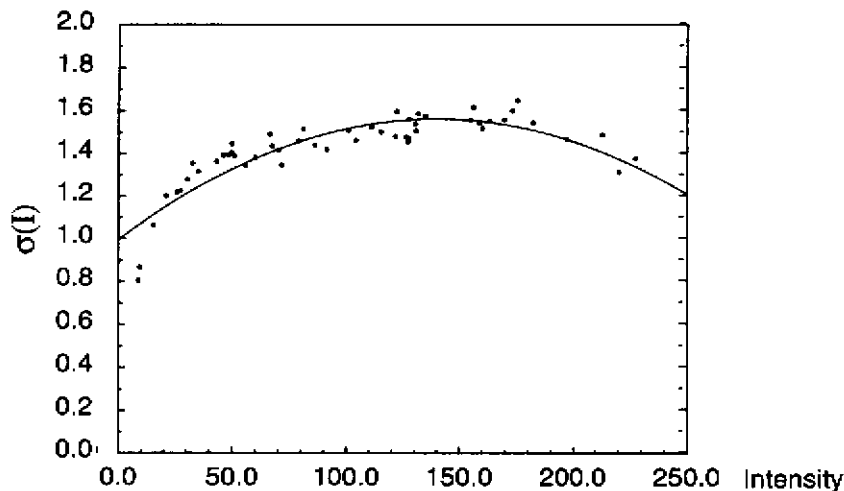


Fig. 2-20. Plot of  $\sigma_i$

## 2.6 3D Convex Lambertian Experiments

Experiments were conducted to validate the 3D lambertian illumination planner. We wanted

to verify that the illumination plans generated by the planner were valid and accurate. In order to do this, we tested the results of the planner for two illumination plans. One plan tested was one of the most accurate illumination plan generated by our illumination planner. The other plan tested was one of the least accurate illumination plan generated by our illumination planner. The results of the two plans were compared with each other and with the planner's predictions. We also verified that the light source viewpoint visibility and camera viewpoint visibility predicted by the planner were correct.

### 2.6.1 Chalk Cube

We milled a 0.59" cube out of 'railroad chalk'. The cube was mounted under our array of light sources. The cube was oriented so that the X, Y, and Z axes intersect at the center of the cube. The X axis intersects one edge of the cube. The Y axis intersects another edge of the cube. The Z axis intersects the center of the top face of the cube:

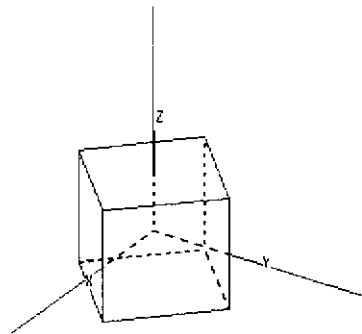


Fig. 2-21. Geometric model of chalk cube

The nominal orientation of the cube's faces is shown in the table below. The cube was supported by Face 6. So, this face was occluded.

Face	Nx	Ny	Nz
1	-0.707	0.707	0.0
2	-0.707	-0.707	0.0
3	0.707	-0.707	0.0
4	0.707	0.707	0.0
5	0.0	0.0	1.0
6	0.0	0.0	-1.0

The possible light source directions:

Light Source	Nx	Ny	Nz
1	-0.3090	-0.5000	0.8090
2	0.3090	-0.5000	0.8090
3	0.0000	0.0000	1.0000
4	0.0000	-0.8507	0.5257
5	0.5257	0.0000	0.8507
6	-0.5257	0.0000	0.8507
7	-0.8090	-0.3090	0.5000
8	-0.5000	-0.8090	0.3090
9	0.5000	-0.8090	0.3090
10	0.8090	-0.3090	0.5000
11	0.3090	0.5000	0.8090
12	-0.3090	0.5000	0.8090
13	0.0000	-1.0000	0.0000
14	0.8090	0.3090	0.5000
15	-0.8090	0.3090	0.5000
16	-0.8507	-0.5257	0.0000
17	0.8507	-0.5257	0.0000
18	0.0000	0.8507	0.5257
19	-1.0000	0.0000	0.0000
20	-0.5000	-0.8090	-0.3090
21	0.5000	-0.8090	-0.3090
22	1.0000	0.0000	0.0000
23	0.5000	0.8090	0.3090
24	-0.5000	0.8090	0.3090
25	0.0000	-0.8507	-0.5257
26	0.8507	0.5257	0.0000
27	-0.8507	0.5257	0.0000
28	-0.8090	-0.3090	-0.5000
29	0.8090	-0.3090	-0.5000
30	0.0000	1.0000	0.0000
31	-0.3090	-0.5000	-0.8090
32	0.3090	-0.5000	-0.8090
33	0.8090	0.3090	-0.5000
34	0.5000	0.8090	-0.3090
35	-0.5000	0.8090	-0.3090
36	-0.8090	0.3090	-0.5000

The possible viewing directions:

View	Nx	Ny	Nz
5	-0.3090	-0.1667	0.9363
15	-0.1667	0.9363	0.3090
16	0.1667	0.9363	0.3090
17	0.0000	0.3568	0.9342
18	0.0000	0.6667	0.7454
19	-0.3090	0.1667	0.9363
21	-0.5774	0.5774	0.5774
22	-0.2697	0.7697	0.5787
23	-0.5787	0.2697	0.7697
24	-0.7697	0.5787	0.2697
25	0.5774	0.5774	0.5774
26	0.2697	0.7697	0.5787
27	0.5787	0.2697	0.7697
28	0.7697	0.5787	0.2697
30	-0.7454	0.0000	0.6667
34	0.7454	0.0000	0.6667
37	-0.3568	0.9341	0.0000
41	0.3568	0.9341	0.0000

The best case illumination plans, assuming ideal, equal radiance, light sources, found by our planner are below. Cover 1 and cover 2 are not implementable because the indicated aspects are not viewable.

Cover	Aspect	Faces Covered	View	Light Sources
1	1	2, 3	none	13, 31, 32
1	2	1, 4, 5	18	11, 23, 24
2	1	1, 4	17	30, 34, 35
2	2	2, 3, 5	none	2, 8, 9
3	1	1, 2	19	16, 27, 36
3	2	3, 4, 5	30	5, 10, 14
4	1	3, 4	34	17, 26, 29
4	2	1, 2, 5	30	6, 7, 15

Inspectable faces are defined as the object faces that can be viewed from the set of possible viewpoints (face 6 is not inspectable). For each light source, we determine which of the inspectable faces are illuminated. (If a non-inspectable face is illuminated, we treat it as a

“don’t care”.) The different combinations of illuminated faces form illumination aspects. These aspects are formed into exact illumination covers. We used our “largest aspect” heuristic, with a search depth of one, to form the exact covers. It is possible that an illumination aspect contains a combination of object faces that is not viewable. This leads to the cases like covers 1 and 2, which both contain illumination aspects that are not viewable. (If a potential viewpoint views a non-inspectable face, we treat it as a “don’t care”.)

We implemented a near best case illumination plan for faces 3 and 4 using light sources 22, 29, 33 and viewpoint 34. The near worst case plan for faces 3 and 4 was light sources 22, 26, 29 and viewpoint 34. The planner determined that faces 1, 2, and 5 could only be illuminated by light sources 6, 7, 15. The camera viewpoint for faces 1, 2, and 5 was viewpoint 30.

We implemented these illumination plans on our experimental setup. The results, using measured radiance light sources:

			Planner Predictions	Measurements
Face	Light Sources	Pixel Number	$\sigma(\theta_{\text{err}})$ - Degrees	$\sigma(\theta_{\text{err}})$ - Degrees
3	22,29,33	1	1.92	1.81
3	22,29,33	2	1.92	1.81
3	22,26,29	1	2.55	2.90
3	22,26,29	2	2.55	3.00
4	22,29,33	3	1.95	1.98
4	22,29,33	4	1.95	2.10
4	22,26,29	3	2.78	3.01
4	22,26,29	4	2.78	3.06
1	6,7,15	5	1.82	1.91
1	6,7,15	6	1.82	1.85
2	6,7,15	7	1.75	2.14
2	6,7,15	8	1.75	2.08
5	6,7,15	9	1.80	1.70
5	6,7,15	10	1.80	1.98
5	6,7,15	11	1.80	1.72
5	6,7,15	12	1.80	1.68

Measurements were made by taking 1000 images with each light source. A small number of pixels (4) were recorded from each image. This produced a data stream for that pixel. By combining the data streams for the 3 light sources, we calculated the mean surface orientation and the standard deviation of surface orientation error.

In general, the measured standard deviation of orientation error are within 20% of the planner. Many are within 10%.

The difference between the near best case and near worst case plans should be noted. For Face 3, the near best case illumination plan results in a  $5.76^\circ$  predicted error,  $3\sigma(\theta_{err})$ . In contrast, the near worst case illumination plan results in  $7.65^\circ$  predicted error. For Face 4, the near best case illumination plan results in a  $5.85^\circ$  predicted error. In contrast, the near worst case illumination plan results in  $8.34^\circ$  predicted error.

Images of Faces 3 and 4 using light sources 22, 29, and 33. (Face 5 is not illuminated.)

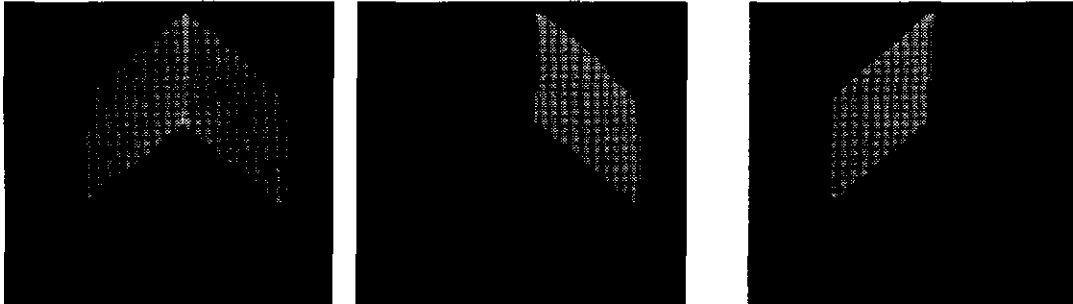


Fig. 2-22. Intensity images: faces 3 and 4 of cube

Needle map produced by the intensity images from light sources 22, 29, and 33.

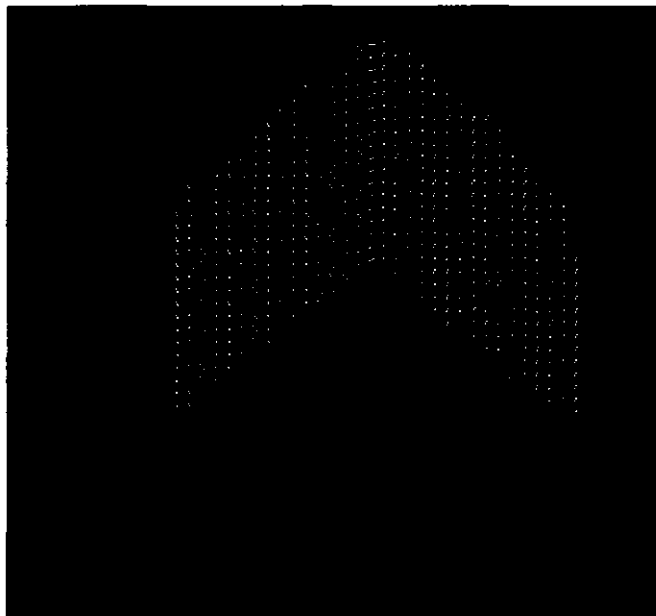


Fig. 2-23. Needle map: faces 3 and 4 of cube

Images of Faces 1, 2, and 5 using light sources 6, 7 and 15.

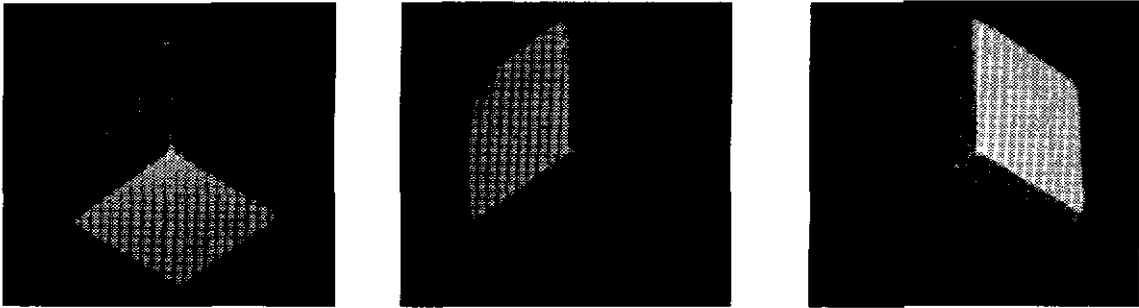


Fig. 2-24. Intensity images: faces 6, 7, and 15 of cube

Needle map produced by the intensity images from light sources 6, 7, and 15.

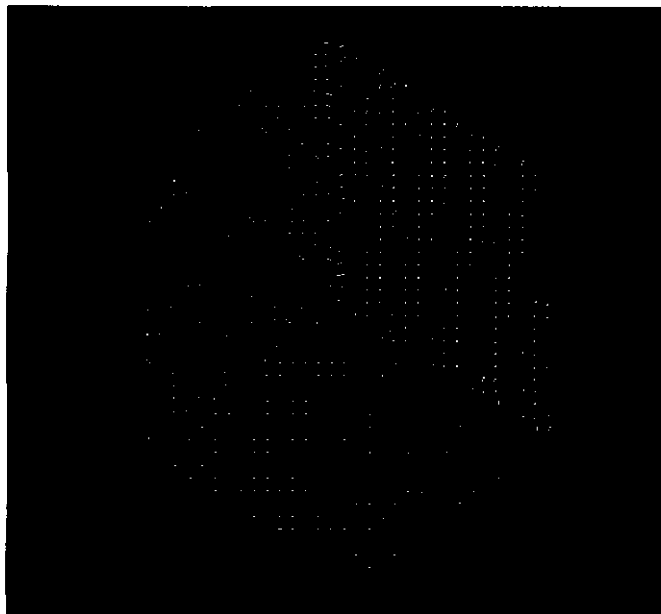


Fig. 2-25. Needle map faces: 6, 7, and 15 of cube

Illumination aspects from the 1, 1, 1 viewing direction (Numbers are light source numbers.)

Light sources that are shaded the same belong to the same illumination aspect.):

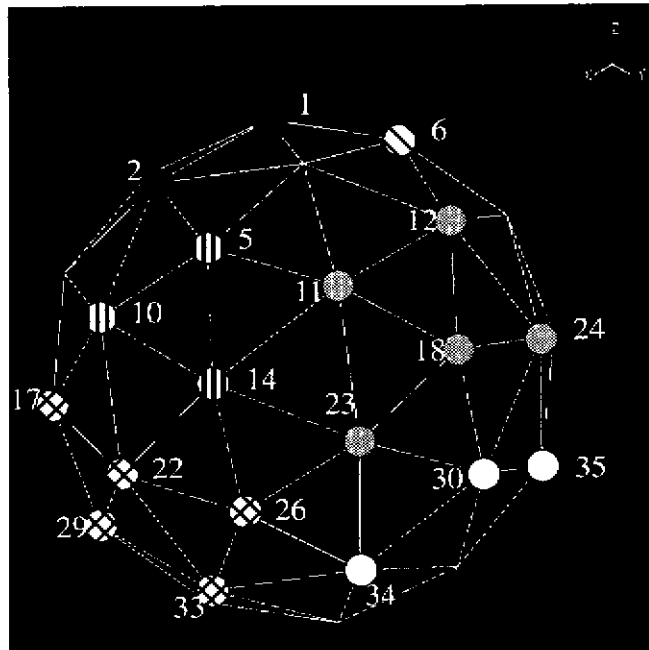


Fig. 2-26. Illumination aspects from the 1, 1, 1 viewing direction

Illumination aspects from the -1, 1, 1 viewing direction:

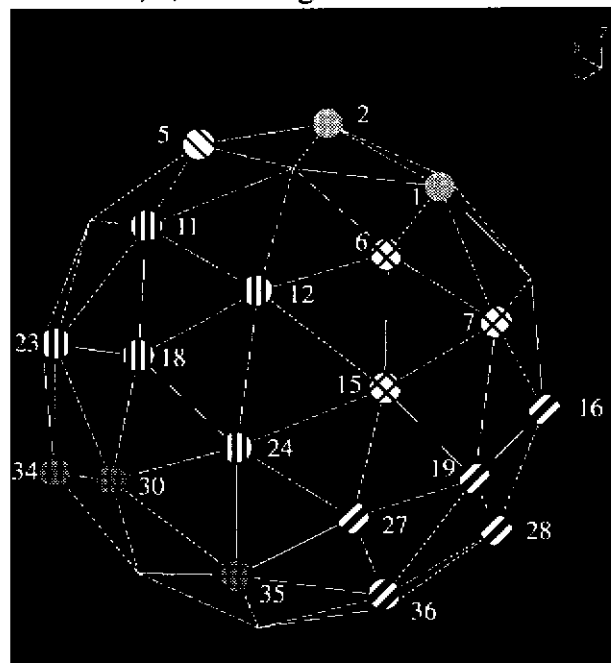


Fig. 2-27. Illumination aspects from the -1, 1, 1 viewing direction

Illumination aspects from the 0, 0, 1 viewing direction :

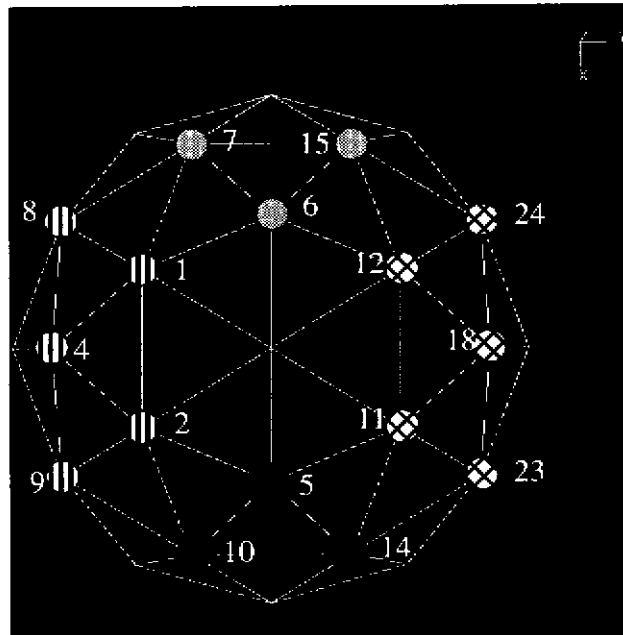


Fig. 2-28. Illumination aspects from the 0, 0, 1 viewing direction

## 2.7 2D Concave Lambertian Illumination

Now we consider the illumination of simple 2D concavities, concavities composed of two surface edges that are fully visible to each other. The illumination of a concavity requires the determination of visibility regions for the potential light sources. For the simple concavities that we are considering in our work, we define the visibility region as the extension of the surface edges that form the concavity. For example, if the concavity has sides at  $45^\circ$  and  $135^\circ$ , the region that can see the concavity is the visibility region extending from  $45^\circ$  to  $135^\circ$ . Any viewpoint in the visibility region can see both faces of the concavity, so the exact cover problem is trivial. (We do not consider partial visibility of a concave edge.)

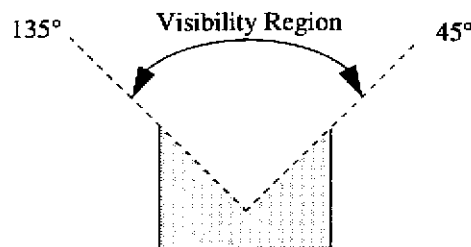


Fig. 2-29. Concave visibility region

Once we have determined the light source visibility region, we need to determine the optimal location for light source placement within that region.

Nayar [Nayar 90c] showed that a shape from intensity method, such as photometric stereo, applied to a concavity would produce a “pseudo shape”. The pseudo shape is shallower than the real concavity and the pseudo shape is invariant to light source placement. Therefore, no

matter where we place our light sources within the visibility region, the pseudo shape recovered using a method such as photometric stereo will produce the same shape.

If the pseudo shape is invariant to light source placement, what constitutes the light source placement problem? We define two possible concave light source placement problems. The first problem is measuring the pseudo shape with the highest reliability. We want to find the light source placement that yields the highest reliability. The second concave light source placement problem involves using the pseudo shape to recover the real shape using Nayar's interactive shape recovery algorithm. Depending on the initial reliability of the pseudo shape, the final shape of the iterative algorithm may be closer to the actual shape. One would want to find the light source placement that produced the most accurate final shape. We investigate the first light source placement problem. The second problem is for future research.

The goal of inspecting the pseudo shape is to find the light source positions that produce the minimum amount of uncertainty in the pseudo shape. The way to think about this problem is that interreflection causes a distorted shape, the pseudo shape. The pseudo shape stays the same no matter where we place our light sources. So, the apparent object we are inspecting stays the same no matter where we place our light sources. This is equivalent to inspecting a non-interreflecting lambertian object whose shape is equivalent to the pseudo shape. The process of interreflection that creates the pseudo shape is global, encompassing all of the surfaces that form the concavity. However, the problem of inspecting the pseudo shape is local. The reliability at each point of the pseudo shape only depends on the intensity at that point, not on any other points of the pseudo shape.

We can use the forward graphics solution [Goral 84] to predict the brightness of the concavity. The basic interreflection equation for diffuse surfaces is:

$$\text{Radiosity} = \text{Emission} + \text{Interreflection}$$

$$B(u) = E(u) + p(u) \int_D F(u, v) B(v) dv$$

F called the form factor. It is the fraction of the energy leaving surface u that arrives at surface v. E is the surface radiance due to a light source. p is the albedo of the surface. B is the aggregate surface radiance. D is all of the surfaces in the environment.

In discrete form,

$$B_j = E_j + p_j \sum_{i=1}^n F(i, j) B_i \quad j = 1, n$$

where n is the number of elements in the environment.

In the two-dimensional case, we can denote a pair of elements with i and j. r is the distance between the centers of the elements.  $N_i$  is the normal of element i.  $N_j$  is the normal of ele-

ment j.

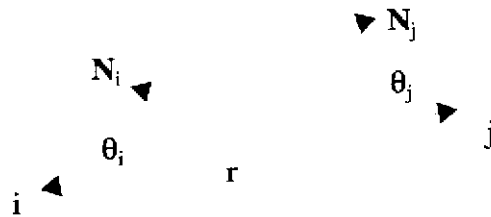


Fig. 2-30. Interreflection geometry

The form factor [Heckbert 91] between elements  $i$  and  $j$  is:

$$F(i, j) = V(i, j) \frac{\cos \theta_i \cos \theta_j}{2r} ds$$

$V$  is the visibility between face  $i$  and face  $j$ .  $V = 1$  if face  $i$  can see face  $j$ .  $V = 0$  otherwise. We use point to point form factors calculated between the center of each element, with a uniform mesh and constant elements.

We can express the discrete form of the radiosity equation in matrix form

$$(I - PF)B = E$$

$E$  and  $B$  are vectors of length  $n$ .  $E$  is the radiance of each element due to the light source.  $B$  is the aggregate radiance of an element due to interreflection and the light source.

$F$  is the square matrix of form factors.

$$F = \begin{bmatrix} F_{11} & F_{12} & \dots & F_{1n} \\ F_{21} & F_{22} & \dots & \dots \\ \dots & \dots & F_{33} & \dots \\ F_{n1} & \dots & \dots & F_{nn} \end{bmatrix}$$

$P$  is the diagonal albedo matrix.

$$P = \begin{bmatrix} P_1 & 0 & 0 & 0 \\ 0 & P_2 & 0 & 0 \\ 0 & 0 & P_3 & 0 \\ 0 & 0 & 0 & P_n \end{bmatrix}$$

In the forward solution, we know  $P$ ,  $F$ , and  $E$ . We want to solve for  $B$ , the brightness of the concavity with interreflection. The matrix equation is solved using the successive over relaxation method [Golub 89], with  $w = 1.4$ . Convergence usually occurs in approximately 15 iterations.

We solve the forward problem for two light sources,  $S1$  and  $S2$ .  $S1$  produces the brightness distribution  $B1$ .  $S2$  produces the brightness distribution  $B2$ . Once we have  $B1$  and  $B2$ , we

can solve for the pseudo shape using B1, S1, B2, and S2.

$$\begin{bmatrix} S1_x & S1_y \\ S2_x & S2_y \end{bmatrix}^{-1} \begin{bmatrix} B1 [i] \\ B2 [i] \end{bmatrix} = \begin{bmatrix} Nx [i] \\ Ny [i] \end{bmatrix} \quad i = 1, \dots, n$$

Where  $N_x$  and  $N_y$  are the normals of the pseudo shape, and  $n$  is the number of face elements.

If our goal is to inspect the pseudo shape with the highest reliability possible, the analysis is very similar to the 2D and 3D lambertian convex cases. The difference between the convex case and the pseudo shape case is that the pseudo shape is non-planar. The uncertainty for a planar convex face is constant since the variance of the face depends on the face's normal direction and the light source direction. A pseudo shape face is curved. Therefore, the uncertainty along the pseudo shape face varies. We could minimize the average angular orientation error of a pseudo shape face, or, if we were interested in a particular point, we could minimize the angular orientation error of that point. For the experiments that follow, we seek to minimize the error at the center of each face.

If B1 and B2 are the nominal light source intensities, noise in either B1 or B2 will cause an error in  $N_x$  and  $N_y$ , producing a noisy normal:

$$\begin{bmatrix} S1_x & S1_y \\ S2_x & S2_y \end{bmatrix}^{-1} \begin{bmatrix} B1 [i] + \delta B1 [i] \\ B2 [i] + \delta B2 [i] \end{bmatrix} = \begin{bmatrix} Nx [i] + \delta Nx [i] \\ Ny [i] + \delta Ny [i] \end{bmatrix} \quad i = 1, \dots, n$$

If we were to measure B1 and B2, both of which might be corrupted by errors, and we were to solve for  $N_x$  and  $N_y$ , we would normalize the resulting values of  $N_x$  and  $N_y$  because the surface normal is by definition a unit vector. The noisy, normalized, normal is:

$$N [i]_{noise} = \frac{Nx [i] + \delta Nx [i]}{|N [i] + \delta N [i]|}, \frac{Ny [i] + \delta Ny [i]}{|N [i] + \delta N [i]|} \quad i = 1, \dots, n$$

$$N [i]_{noise} = Nx [i]_{noise}, Ny [i]_{noise}$$

We define the orientation error to be the angle between the nominal unit normal and the noisy unit normal. We have the planner conduct a simulation using the intensity noise function. If we know the nominal intensity of each light source. (This can be determined if the object's pose, the light source directions, and the light source's radiance is known.) and the corresponding value of  $\sigma_i$ , we can calculate a noisy surface orientation using the known light source positions. At each iteration, a random intensity for each light source is generated from the mean light source intensity and  $\sigma_i$  for that light source intensity. These two noisy intensity values are used to determine a noisy surface orientation. We repeat this 1000 times. We calculate the mean, noisy, surface orientation to be the center of mass of the 1000 noisy surface orientations:

$$N [i]_{noise} = \frac{\sum_{j=1}^{1000} [Nx [i]_{noise}]_j}{1000}, \frac{\sum_{j=1}^{1000} [Ny [i]_{noise}]_j}{1000} \quad i = 1, \dots, n$$

Using each noisy surface orientation and the mean, noisy, surface orientation, we calculate the orientation error.

$$\theta [i]_{err} = \text{acos} \left[ N [i]_{noise} \bullet N [i]_{noise} \right] \quad i = 1, \dots, n$$

Using the 1000 values of orientation error that our simulation produced, we then determine the standard deviation of surface orientation error,  $\sigma(\theta_{err})$ .

We have performed simulations on a range of simple 2D concavities to explore the relationship between  $\sigma(\theta_{err})$  and concavity shape.

The first concavity is  $140^\circ$ .  $\rho = 0.8$ .  $n = 500$ . The intensity of both light sources was 200. Both sides of the concavity are the same length.

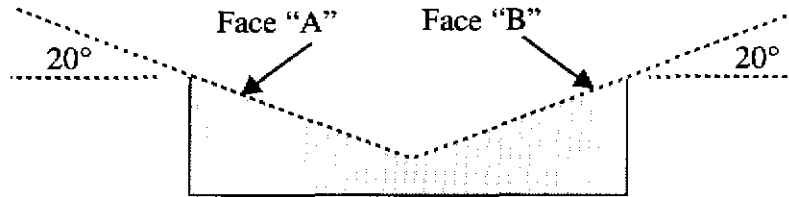


Fig. 2-31.  $140^\circ$  2D concavity

The shape and pseudo shape are shown here (The pseudo shape is the more concave shape.):



Fig. 2-32.  $140^\circ$  2D concavity shape and pseudo shape

The error surface for Face "A" is (S1, S2, and error are all in degrees):

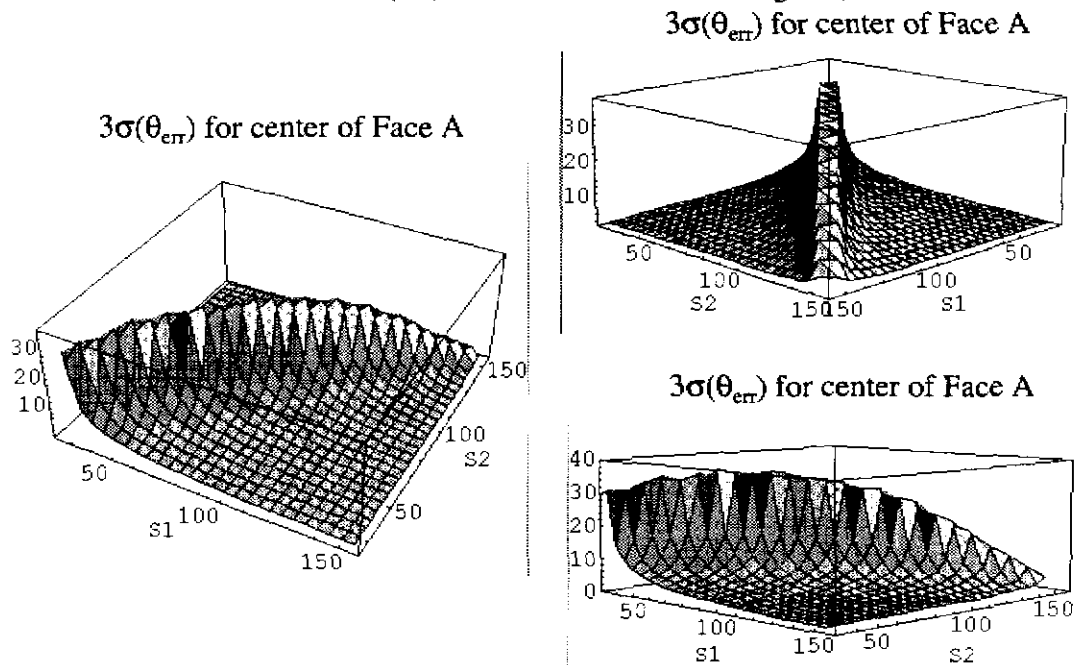


Fig. 2-33.  $140^\circ$  2D concavity error surface for center of face A

The maximum error is  $37.5^\circ$ . The minimum error is  $1.5^\circ$ . The search was conducted in  $5^\circ$  increments.

The second concavity is  $90^\circ$ .  $\rho = 0.8$ .  $n = 500$ . The intensity of both light sources was 200. Both sides of the concavity are the same length.

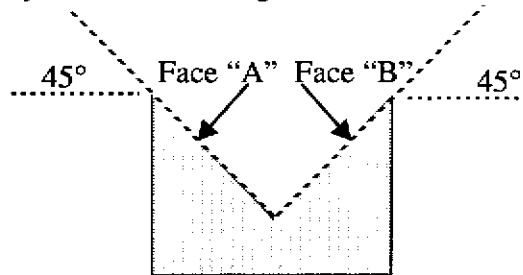


Fig. 2-34.  $90^\circ$  2D concavity

The shape and pseudo shape are shown here:

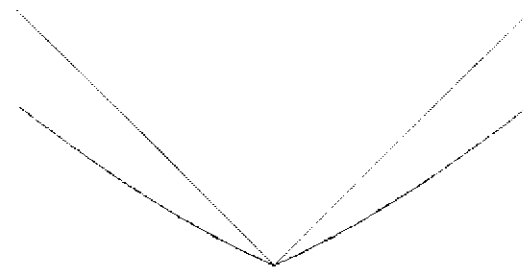


Fig. 2-35.  $90^\circ$  2D Concavity shape and pseudo shape

The error surface for Face A is (S1, S2, and error are all in degrees):

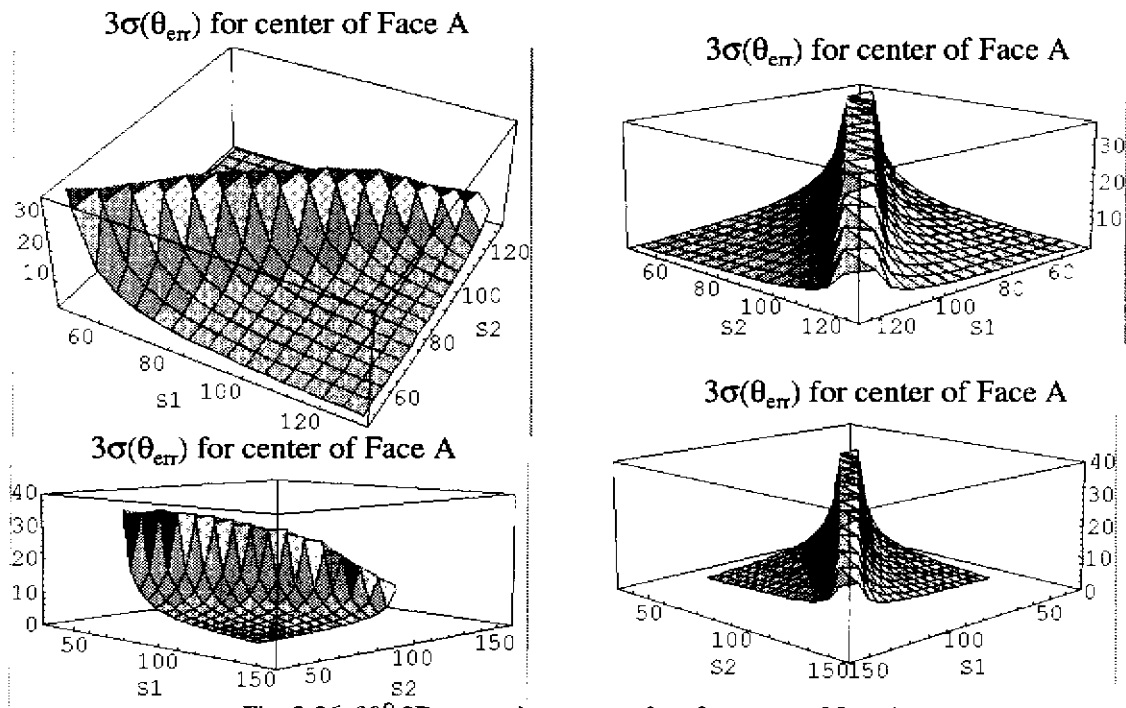


Fig. 2-36.  $90^\circ$  2D concavity error surface for center of face A

The maximum error is  $35.6^\circ$ . The minimum error is  $2.0^\circ$ . The search was conducted in  $5^\circ$  increments.

The third concavity is  $45^\circ$ .  $\rho = 0.8$ .  $n = 500$ . The intensity of both light sources was 200. Both sides of the concavity are the same length.

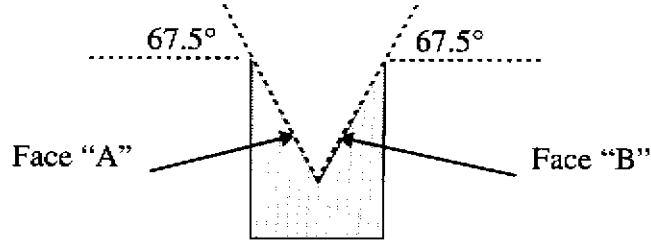


Fig. 2-37.  $45^\circ$  2D concavity

The shape and pseudo shape are shown here:

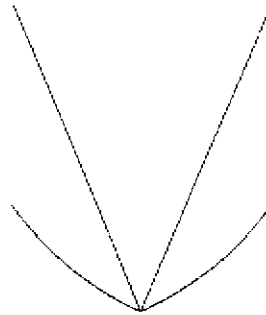


Fig. 2-38.  $45^\circ$  2D concavity shape and pseudo shape

The error surface for Face A is ( $S_1$ ,  $S_2$ , and error are all in degrees):

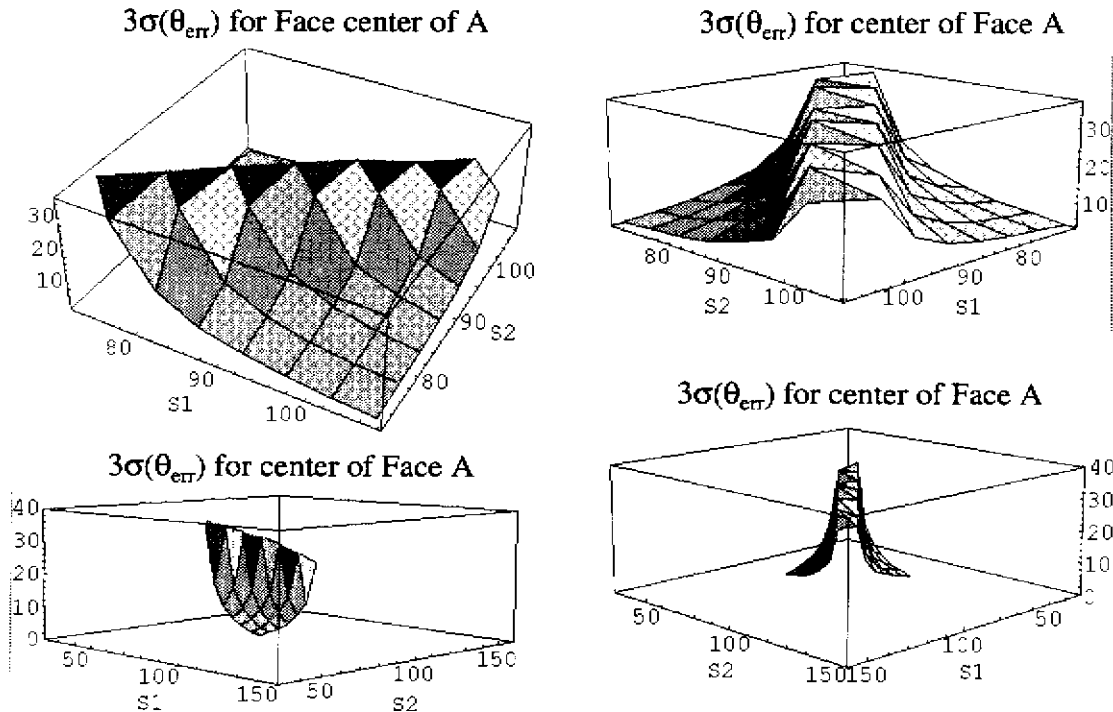


Fig. 2-39.  $45^\circ$  2D concavity error surface for center of face A

The maximum error is  $36.8^\circ$ . The minimum error is  $6.7^\circ$ . The search was conducted in  $5^\circ$  increments.

As the concavity becomes more acute, the pseudo shape becomes deeper and more concave. In addition, as the concavity becomes more acute, the visibility region becomes more acute. These two factors combine to increase the minimum error for a face. (The maximum error is largely a function of the separation between the light sources.)

As shown in section 2.2.3.1, a lambertian shape will produce high reliability when the angle between the light sources and normal are large. As a concavity becomes more acute, and the pseudo shape becomes deeper and more concave, the maximum angle between viewpoints in the visibility region and points along the pseudo shape will be smaller. This will cause the error to be larger, and more of the visibility region will produce large errors. For a shallow concavity, the pseudo shape will be less concave. Less of the visibility region will be at an acute angle to the pseudo shape. The maximum angle between viewpoints in the visibility region and points along the pseudo shape will be larger. This will cause the error to be smaller, and less of the visibility region will produce large errors.

We also looked at the variation in error along each face of the pseudo shape. (Points 0 to 249 belong to pseudo shape face A. Points 250 to 499 belong to pseudo shape face B.  $S1 = 72.5^\circ$ ,  $S2 = 107.5^\circ$ ,  $\rho = 0.8$ )

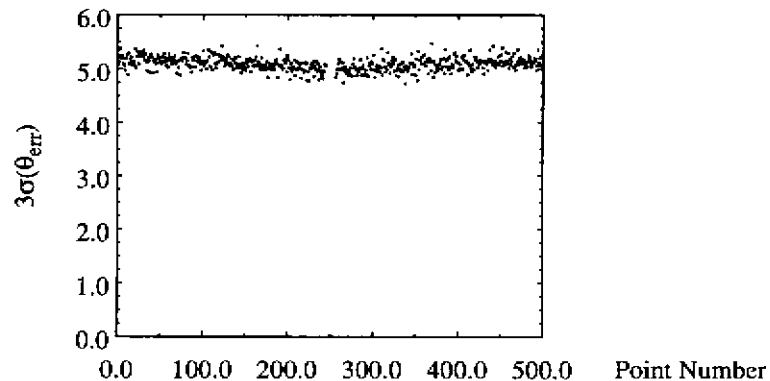


Fig. 2-40. Error across face A and Face B for  $140^\circ$  concavity

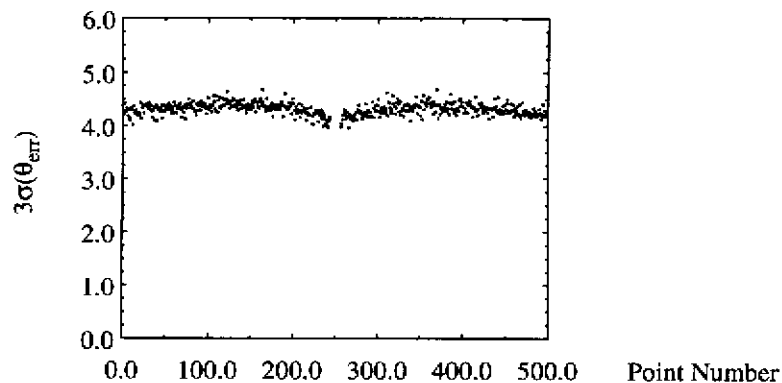


Fig. 2-41. Error across face A and Face B for  $90^\circ$  concavity

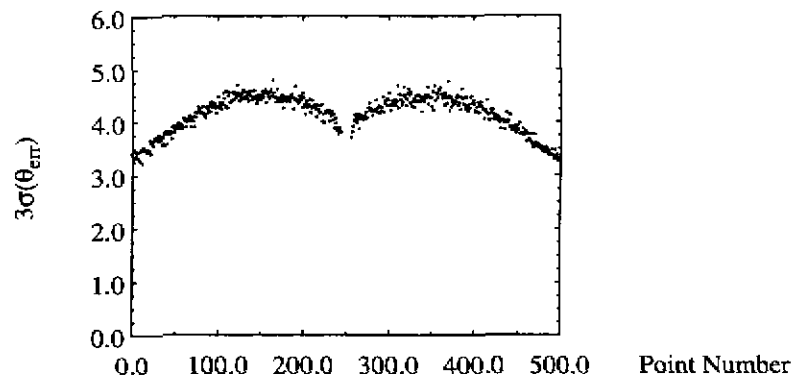


Fig. 2-42. Error across face A and Face B for 45° concavity

The variation in error along a face is a function of the curvature of the pseudo shape face. If the pseudo shape face is approximately flat, the angle between the light sources and face are approximately constant. Therefore, the error along the face is approximately constant. If the pseudo shape face has a high curvature, the angle between the light sources and face will vary. This will cause the error along the face to vary. The 45° concavity's pseudo shape has the highest curvature. Therefore, the error along its face varies the most.

## 2.8 3D Concave Lambertian Illumination

Now we consider the illumination of simple 3D concavities, concavities composed of two rectangular faces that are fully visible to each other. The solution of the 3D concave illumination problem is very similar to the solution of the 2D concave illumination problem.

In the three-dimensional case, we have elements  $i$  and  $j$ .  $r$  is the distance between the centers of the elements.  $N_i$  is the normal of element  $i$ .  $N_j$  is the normal of element  $j$ .

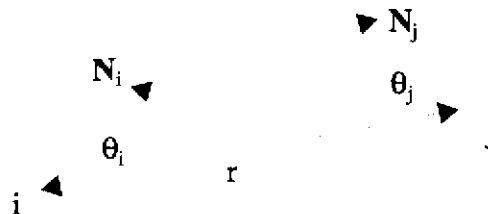


Fig. 2-43. Interreflection geometry

The form factor [Sparrow 78] between elements  $i$  and  $j$  is:

$$F(i, j) = V(i, j) \frac{\cos \theta_i \cos \theta_j}{\pi r^2} dA_j$$

$V$  is the visibility between face  $i$  and face  $j$ .  $V = 1$  if face  $i$  can see face  $j$ .  $V = 0$  otherwise.  $dA_j$  is the differential area of facet  $j$ .

We solve the forward problem for three light sources,  $S_1$ ,  $S_2$ , and  $S_3$ .  $S_1$  produces the

brightness distribution B1. S2 produces the brightness distribution B2. S3 produces the brightness distribution B3. Once we have B1, B2, and B3, we can solve for the pseudo shape using B1, S1, B2, S2, B3, and S3.

$$\begin{bmatrix} S1x & S1y & S1z \\ S2x & S2y & S2z \\ S3x & S3y & S3z \end{bmatrix}^{-1} \begin{bmatrix} B1 \\ B2 \\ B3 \end{bmatrix} = \begin{bmatrix} Nx \\ Ny \\ Nz \end{bmatrix}$$

Our goal is to inspect the pseudo shape with the highest reliability possible. The analysis is identical to the 3D convex case, Section 2.4.1. We use B1, B2, B3, Nx, Ny, and Nz to calculate the angular orientation error at each point on the pseudo shape. The difference between the convex case and the pseudo shape case is that the pseudo shape is non-planar. The uncertainty for a planar convex face is constant since the variance of the face depends on the face's normal direction and the light source direction. A pseudo shape face is curved. Therefore, the uncertainty along the pseudo shape face varies. We could minimize the average angular orientation error of a pseudo shape face, or if we were interested in a particular point, we could minimize the angular orientation error of that point. For the experiments that follow, we seek to minimize the error at the center of each face.

### 2.8.1 Implementation

We implemented our 3D concave planner in C instead of in LISP because of the large computational expense involved in the forward prediction problem. Our 3D planner accepts the vertex coordinates of two rectangular faces. Each face is tessellated into an NxN grid of elements. (For these experiments N = 15.) All combinations of light sources that are visible to both faces are included in a potential source list. The forward prediction is performed for each combination of light sources in the source list. Then, the angular orientation error is calculated at the center of both faces. A viewpoint that satisfies the minimum foreshortening criteria is used.

## 2.9 3D Concave Lambertian Illumination Experiments

Experiments were conducted to validate the concave lambertian illumination planner. We wanted to verify that the illumination plans generated by the planner were valid and accurate. In order to do this, we tested the results of the planner for two illumination plans. One plan tested was one of the most accurate illumination plan generated by our illumination planner. The other plan tested was one of the least accurate illumination plan generated by our illumination planner. The results of the two plans were compared with each other and with the planner's predictions. We also verified that the light source viewpoint visibility and camera viewpoint visibility predicted by the planner were correct.

### 2.9.1 Chalk Concavity

We constructed a simple concavity. Two rectangular faces were milled out of railroad chalk. The two faces were held in a holder that formed a 90° concavity.

The concavity was oriented so that the X, Y, and Z axes intersect at the center of the concavity. The X axis coincides with the cusp of the concavity. The Z axis bisects the concavity (it points up). By using a Macbeth ColorChecker color rendition chart, we determined that the albedo of the railroad chalk was 0.936.

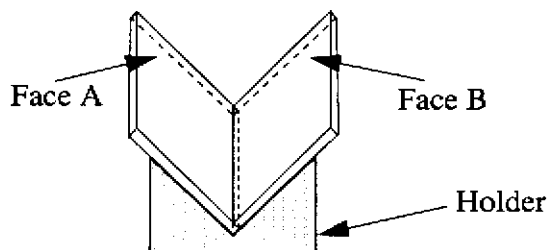


Fig. 2-44. 90° Chalk concavity

The nominal orientation of the concavity's faces is shown in the table below.

Face	Nx	Ny	Nz
A	0.0	0.707	0.707
B	0.0	-0.707	0.707

Our light sources are 2" in diameter and they are 9" from our object. They subtend an angle of 12.5°. In order to ensure that all of the light source is visible to each illuminated face, we impose a limit on the light source incident angle: the angle between a light source and Face A or Face B cannot be more than 77.5°. Seven light sources satisfy this condition: S1, S2, S3, S5, S6, S11, and S12. We measured the intensities of these light sources using the same material that the chalk faces were made of.

The possible light source directions:

Light Source	Nx	Ny	Nz	Source Intensity
1	-0.3090	-0.5000	0.8090	176.2
2	0.3090	-0.5000	0.8090	207.0
3	0.0000	0.0000	1.0000	207.4
5	0.5257	0.0000	0.8507	185.7
6	-0.5257	0.0000	0.8507	205.2
11	0.3090	0.5000	0.8090	192.3
12	-0.3090	0.5000	0.8090	208.2

The possible viewing directions:

View	Nx	Ny	Nz
5	-0.3090	-0.1667	0.9363
15	-0.1667	0.9363	0.3090
16	0.1667	0.9363	0.3090
17	0.0000	0.3568	0.9342
18	0.0000	0.6667	0.7454
19	-0.3090	0.1667	0.9363
21	-0.5774	0.5774	0.5774
22	-0.2697	0.7697	0.5787
23	-0.5787	0.2697	0.7697
24	-0.7697	0.5787	0.2697
25	0.5774	0.5774	0.5774
26	0.2697	0.7697	0.5787
27	0.5787	0.2697	0.7697
28	0.7697	0.5787	0.2697
30	-0.7454	0.0000	0.6667
34	0.7454	0.0000	0.6667
37	-0.3568	0.9341	0.0000
41	0.3568	0.9341	0.0000

The planner selected viewpoint 5 as the least foreshortening viewpoint.

We implemented two of the best illumination plans and two of the worst illumination plans. The planner predictions and measurements are for a point near the center of each face.

In general, the predictions for the best case illumination plans are within 15% of the predictions. The predictions for the worst case illumination plans are not as accurate, with errors running up to 30%. The reason for the difference in accuracy is the very nature of the best case versus worst case plans. The best case illumination plans produce a small amount of error when there is a disturbance in intensity. We have considered this disturbance to be from the light intensity variance of the CCD and digitizer. The best case plan has a low sensitivity to this noise, while the worst case plan has a high sensitivity. An intensity disturbance can also be caused by a deviation between the planner's photometric model and the actual photometric model. Our chalk surface is not perfectly lambertian (Fig. 2-45. ). So, there are discrepancies between the intensities that our planner predicts and our measurements. Since our worst case plan has a higher sensitivity to these intensity deviations, the accuracy of these plans is worse. This observation makes us conclude that less sensitive plans will also produce more accurate results when there are deviations in the expected pho-

tometric model.

		Planner Predictions	Measurements
Face (center of face)	Light Sources	$\sigma(\theta_{err})$ - Degrees	$\sigma(\theta_{err})$ - Degrees
A	1,12,6	4.05	4.71
B	1,12,6	4.11	4.97
A	1,12,5	1.23	1.42
B	1,12,5	1.22	1.35
A	2,11,6	1.14	1.25
B	2,11,6	1.15	1.26
A	2,11,5	4.22	3.05
B	2,11,5	4.23	3.51

The deviation that we measured between the chalk and the ideal lambertian model is shown below.

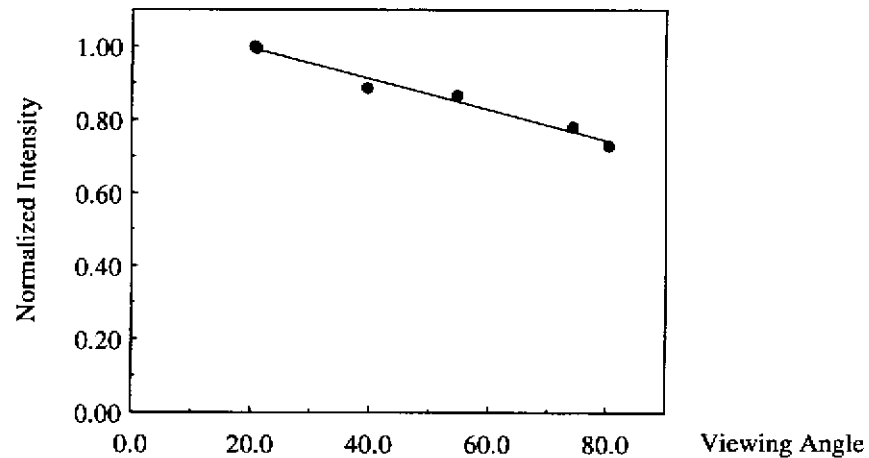


Fig. 2-45. Chalk: Intensity versus viewing angle. (incident angle = 0° )

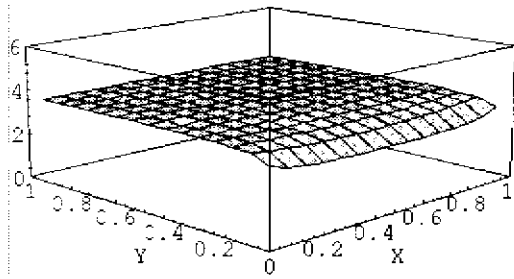
A lambertian surface's intensity should be viewer independent. The chalk exhibits some reduction in intensity with increased viewing angle. This caused the brightness predicted by the planner to be greater than measurements. The next table lists predicted brightness versus measured brightness near the center of each face.

			Planner Prediction	Measurement	Percent Error
Face (center of face)	Sources in Group	Light Source	I	I	
A	1, 12, 6	1	61.0	57.4	-5.9
A	1, 12, 6	12	165.3	150.0	-9.3
A	1, 12, 6	6	119.0	113.1	-5.0
B	1, 12, 6	1	165.3	147.3	-10.9
B	1, 12, 6	12	61.0	52.7	-13.6
B	1, 12, 6	6	119.0	109.8	-7.7
A	1, 12, 5	1	61.0	57.4	-5.9
A	1, 12, 5	12	165.3	150.0	-9.3
A	1, 12, 5	5	119.0	99.2	-16.6
B	1, 12, 5	1	165.3	147.3	-10.9
B	1, 12, 5	12	61.0	52.7	-13.6
B	1, 12, 5	5	119.0	97.0	-18.5
A	2, 11, 6	2	66.8	64.4	-3.6
A	2, 11, 6	11	181.1	171.0	-5.6
A	2, 11, 6	6	130.3	124.0	-4.8
B	2, 11, 6	2	181.1	164.4	-9.4
B	2, 11, 6	11	66.8	55.3	-17.2
B	2, 11, 6	6	130.3	120.2	-7.8
A	2, 11, 5	2	64.4	62.1	-3.6
A	2, 11, 5	11	174.6	164.8	-5.6
A	2, 11, 5	5	125.7	104.8	-16.6
B	2, 11, 5	2	174.6	158.5	-9.2
B	2, 11, 5	11	64.4	53.3	-17.2
B	2, 11, 5	5	125.7	102.4	-18.5

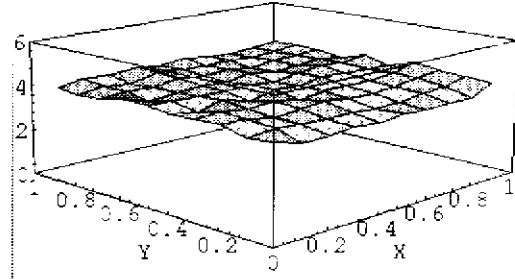
We measured a 10X10 array of points on each face of the concavity. This allows us to compare the predicted and measured error surfaces,  $3\sigma(\theta_{err})$ , Fig. 2-46. and Fig. 2-48. .

We are also able to compare the predicted and measured intensity profiles for each face. The shape of the two surfaces is very close. As expected, the measured intensity surface is attenuated, Fig. 2-47. and Fig. 2-49. .

An intensity image of the concavity and a needle map of the concavity is shown in Fig. 2-

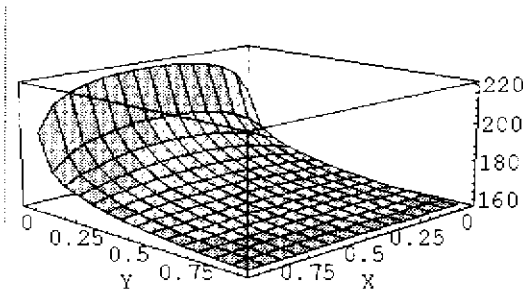


Planner

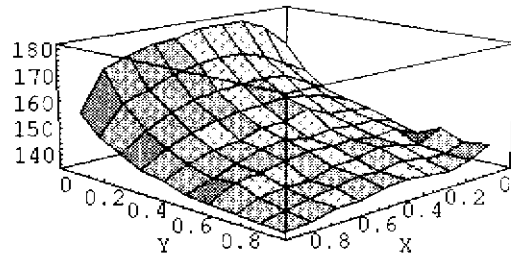


Measurement

Fig. 2-46. Best plan error surface, face B, 90° chalk concavity, sources: 1, 12, 5

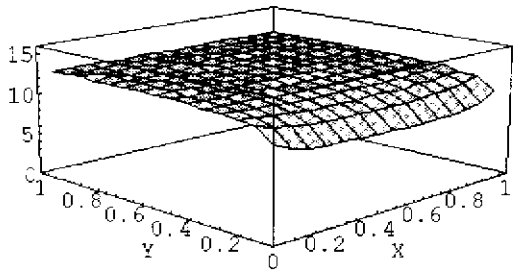


Planner

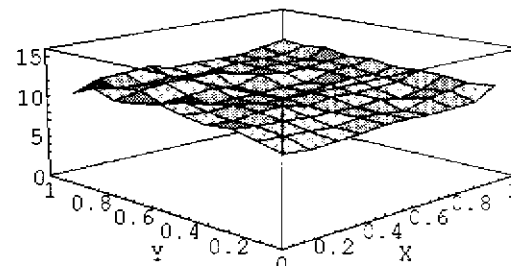


Measurement

Fig. 2-47. Best plan intensity, face B, 90° chalk concavity, sources: 1, 12, 5

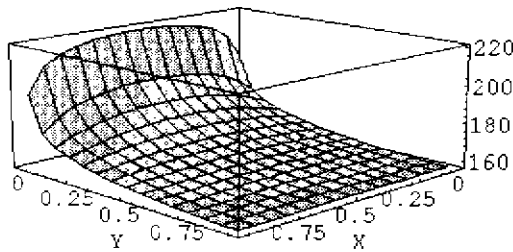


Planner

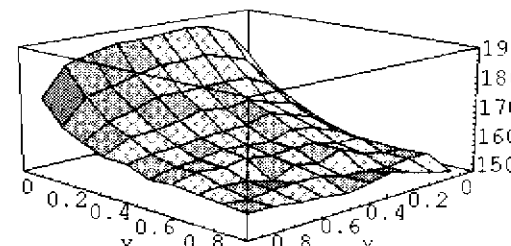


Measurement

Fig. 2-48. Worst plan error surface, face B, 90° chalk concavity, sources: 2, 11, 5



Planner



Measurement

Fig. 2-49. Worst plan intensity, face B, 90° chalk concavity, sources: 2, 11, 5

50. .

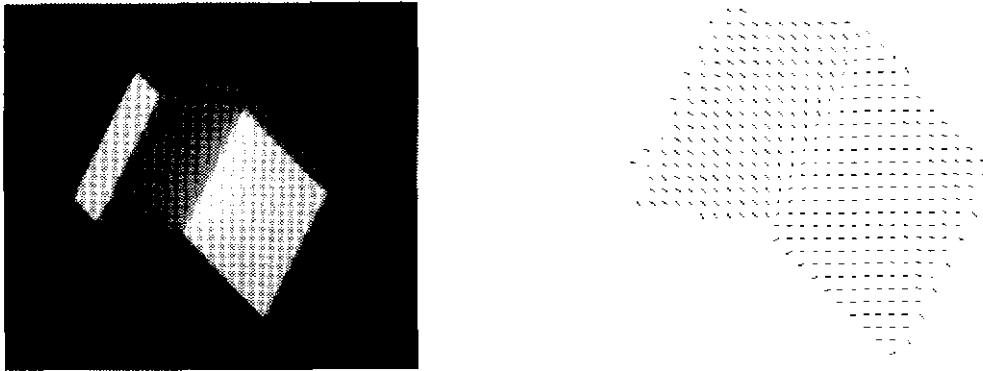


Fig. 2-50. Intensity image from source 1, and needle map from sources: 1, 12, 5

## 2.10 2D Lambertian Source Error

Even though we have primarily been concerned with finding the sensitivity of surface orientation to random errors, primarily intensity noise, fixed errors are also an issue. Fixed errors include: errors in source location, errors in source intensity, and errors in the photometric model. Errors in source intensity and errors in the photometric model can be viewed as intensity disturbances. Therefore, the analysis of orientation error due to intensity noise applies to these fixed errors. Places in the intensity noise error surface that produced a small error due to intensity noise, will also produce a small error due to source intensity error or photometric error. Places in the intensity noise error surface that produced a large error due to intensity noise, will also produce a large error due to source intensity error or photometric error.

Source location errors are fundamentally different. In this section, we investigate errors in surface normal orientation due to source location errors in a 2D lambertian system.

### 2.10.1 2D Lambertian Source Error

In the nominal 2D lambertian system:

$$I1 = (\cos\theta_{i1}) = \cos(\theta_{S1} - \theta_N)$$

$$I2 = (\cos\theta_{i2}) = \cos(\theta_{S2} - \theta_N)$$

If  $\theta_{S1}$  or  $\theta_{S2}$  is incorrect

$$\theta'_{S1} = \theta_{S1} + \delta\theta_{S1}$$

$$\theta'_{S2} = \theta_{S2} + \delta\theta_{S2}$$

we will produce a corrupted intensity:

$$I1' = \cos(\theta'_{S1} - \theta_N)$$

$$I2' = \cos(\theta'_{S2} - \theta_N)$$

Then the corrupted intensity will be converted into a surface orientation using the incorrect

pair (the nominal pair) of source directions:

$$\begin{bmatrix} S1x & S1y \\ S2x & S2y \end{bmatrix}^{-1} \begin{bmatrix} I1' \\ I2' \end{bmatrix} = \begin{bmatrix} Nx \\ Ny \end{bmatrix}$$

The important thing to realize is that both the intensities and source directions are incorrect.

Ray, Birk, and Kelly [Ray 83] finds the sensitivity of p and q with respect to changes in the azimuth and zenith angles of each light source. Their formulation involves finding partial derivatives of a closed form expression for p and q:

$$q_n = f(I_1, I_2, I_3, \theta_p, \phi_{1p}, \phi_{2p}, \phi_{3p})$$

$$p_n = F(q_n, I_1, I_2, I_3, \theta_p, \phi_{1p}, \phi_{2p}, \phi_{3p})$$

Their formulation for finding the sensitivities of light source position errors amounts to creating an erroneous light source position, leaving the intensities the same, and finding the change in surface orientation. While this is mathematically the expression for the sensitivity of surface orientation to errors in source position, their formulation does not reflect what happens when one makes a photometric measurement with erroneous light source positions. It does not include the perturbed intensities caused by the incorrect source locations, and the incorrect use of the nominal source locations in interpreting these perturbed intensities.

In order to visualize the orientation error surface due to source position error, we generated an error surface for a normal at 90°. We moved two light sources between 0° and 180°. At each source position we used four combinations of source position error (+δS1, +δS2), (+δS1, -δS2), (-δS1, +δS2), and (-δS1, -δS2). δS was set equal to 2°. Our error was set equal to the average of the two worst errors.

The error surface has four quadrants: in quadrant one, S1 and S2 are less than 90°; in quadrant two, S1 and S2 are greater than 90°; in quadrant three, S1 is less than 90° and S2 is greater than 90°; and in quadrant four, S1 is greater than 90° and S2 is less than 90°. When both S1 and S2 are on opposite sides of the normal, the error is bounded by the source error. This is seen in quadrants one and two. The error surface is flat in these two quadrants, and the error is equal to 2°. This even holds when the two light sources are very close to the normal. When the light sources are on the same sides of the normal, the error can become very big. This is seen in quadrants three and four.

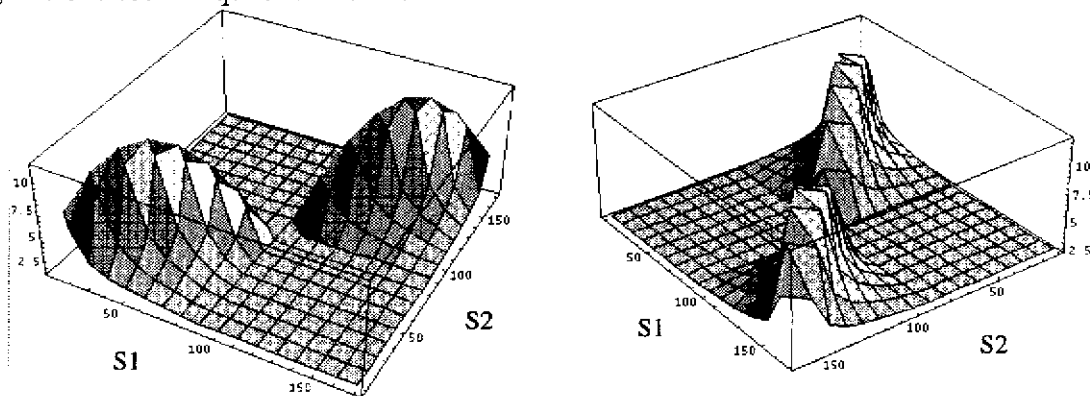


Fig. 2-51. Orientation error surface: δS=2°, N=90°.

In order to gain some insight into the source error surface, we use a ratio function diagram. The ratio function diagram shows normalized light source intensity versus surface orientation for two light sources, and the ratio of  $I_1/I_2$ . Photometric stereo can be thought of as measuring the intensity of a surface for different light source directions, and then calculating surface orientation by calculating the ratios of these intensities.

First, we look at the case, where the light sources are on opposite sides of the normal. We construct a ratio function diagram for the nominal source positions of  $S_1=45^\circ$ ,  $S_2=135^\circ$ . Our normal is at  $90^\circ$ . The diagram below show that at  $90^\circ$ , the ratio of  $I_1/I_2$  equals 1.0.

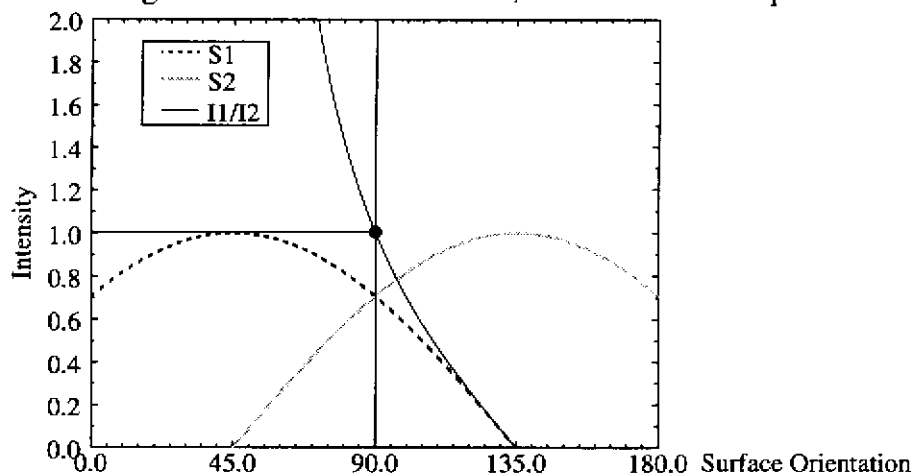


Fig. 2-52. Ratio function diagram:  $S_1=45^\circ$ ,  $S_2=135^\circ$

Now, we construct ratio function diagrams for a normal at  $90^\circ$ , and source positions that are perturbed by  $\pm 5^\circ$ . First, we move  $S_1 +5^\circ$  and  $S_2 -5^\circ$ , so that  $S_1=50^\circ$  and  $S_2=130^\circ$ . We find that at  $90^\circ$ , the ratio is equal to 1.0.

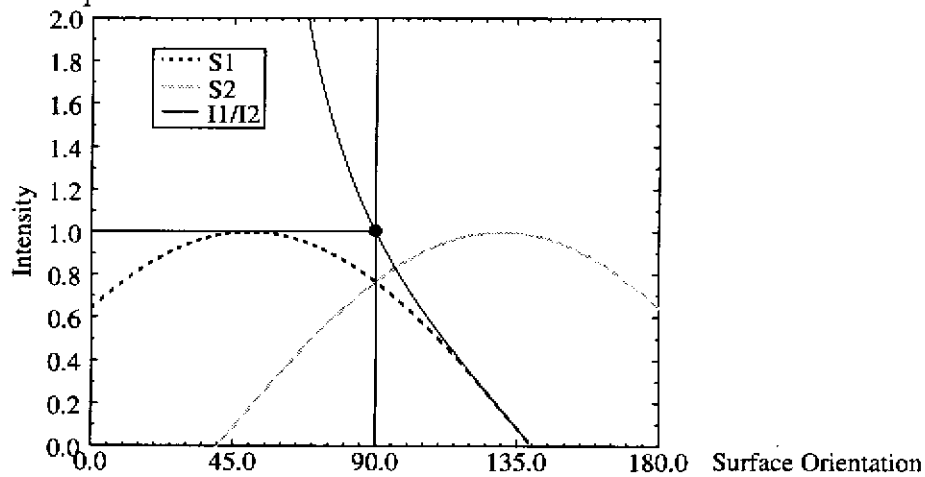
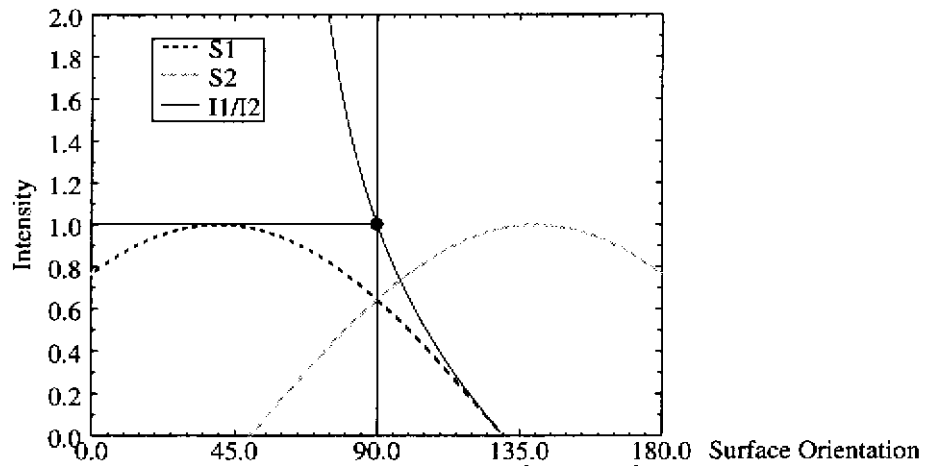


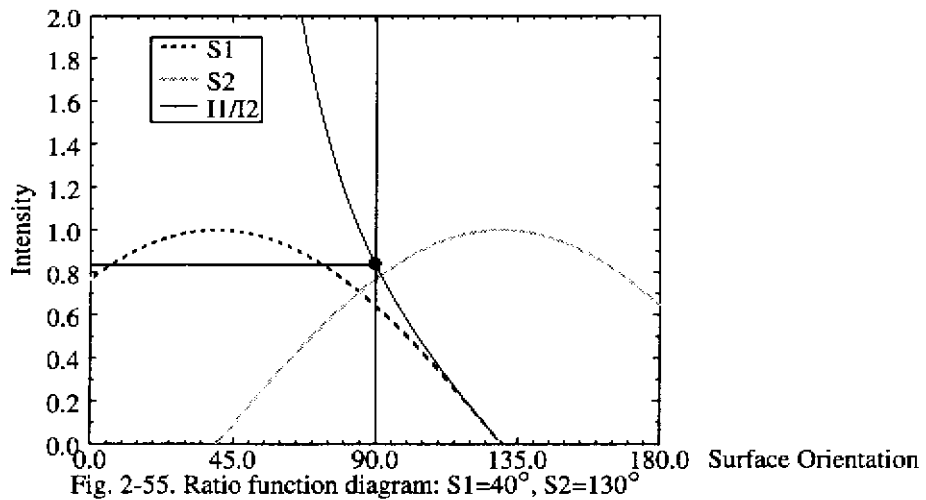
Fig. 2-53. Ratio function diagram:  $S_1=50^\circ$ ,  $S_2=130^\circ$

If we move  $S_1 -5^\circ$  and  $S_2 +5^\circ$ , so that  $S_1=40^\circ$  and  $S_2=140^\circ$ , we find that at  $90^\circ$ , the ratio is

equal to 1.0.



If we move  $S1 -5^\circ$ , and  $S2 -5^\circ$ , so that  $S1= 40^\circ$  and  $S2=130^\circ$ , we find that at  $90^\circ$ , the ratio changes to approximately 0.82. Both light sources are moving in the same direction, and by the same amount. Both intensity curves are being shifted by the same amount. The ratio curve is the same as the  $S1=45^\circ$  and  $S2=135^\circ$  case, but it is shifted  $5^\circ$  in the negative direction.



If we move  $S1 +5^\circ$ , and  $S2 +5^\circ$ , so that  $S1= 50^\circ$  and  $S2=140^\circ$ , we find that at  $90^\circ$ , the ratio changes to approximately 1.2. The ratio curve is the same as the  $S1=45^\circ$  and  $S2=135^\circ$  case,

but it is shifted  $5^\circ$  in the positive direction.

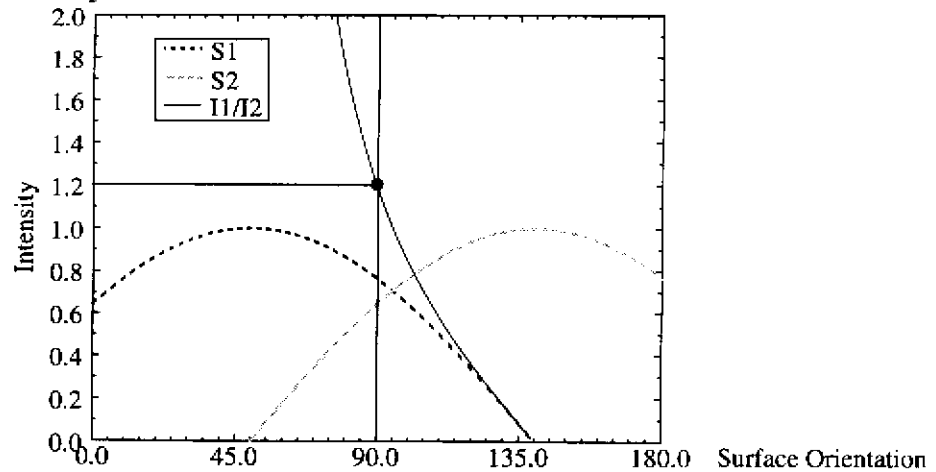


Fig. 2-56. Ratio function diagram:  $S1=50^\circ$ ,  $S2=140^\circ$

Next, we plot the nominal and perturbed ratios on the nominal ( $S1=45^\circ$  and  $S2=135^\circ$ ) ratio function diagram. This diagram shows us how we would interpret the intensity ratios produced by the erroneous source positions given the nominal light source positions. We see that the ratio produced by the case when  $S1=50^\circ$  and  $S2=130^\circ$  would be interpreted as a surface orientation of  $90^\circ$ . The case when  $S1=40^\circ$  and  $S2=140^\circ$  will also be interpreted as a surface orientation of  $90^\circ$ . The case when  $S1=50^\circ$  and  $S2=130^\circ$  will produce a surface orientation of  $85^\circ$ . This is a  $5^\circ$  surface orientation error, and is equal to the shift in both light sources. The case when  $S1=40^\circ$  and  $S2=130^\circ$  will produce a surface orientation of  $95^\circ$  which is also a  $5^\circ$  surface orientation error.

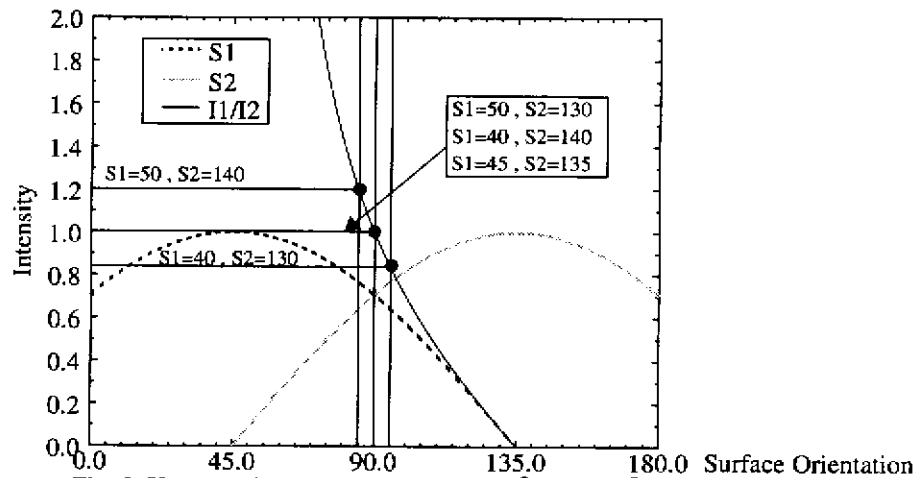
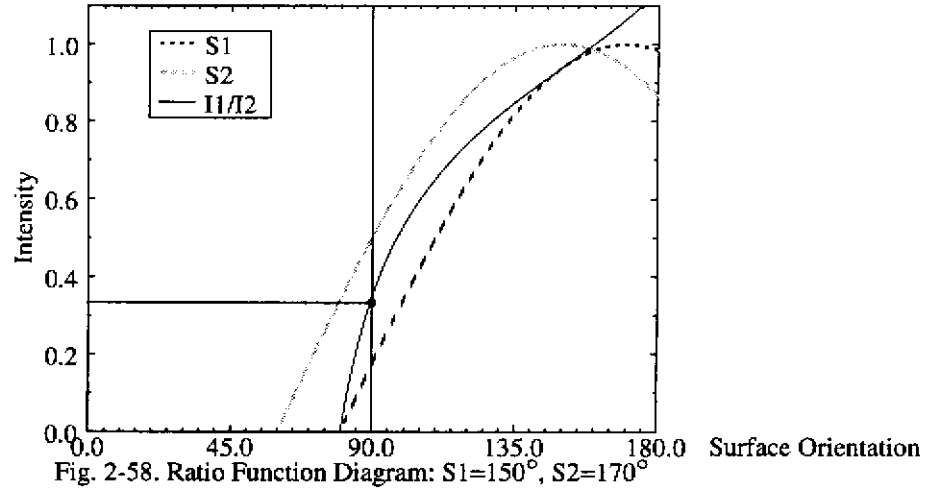


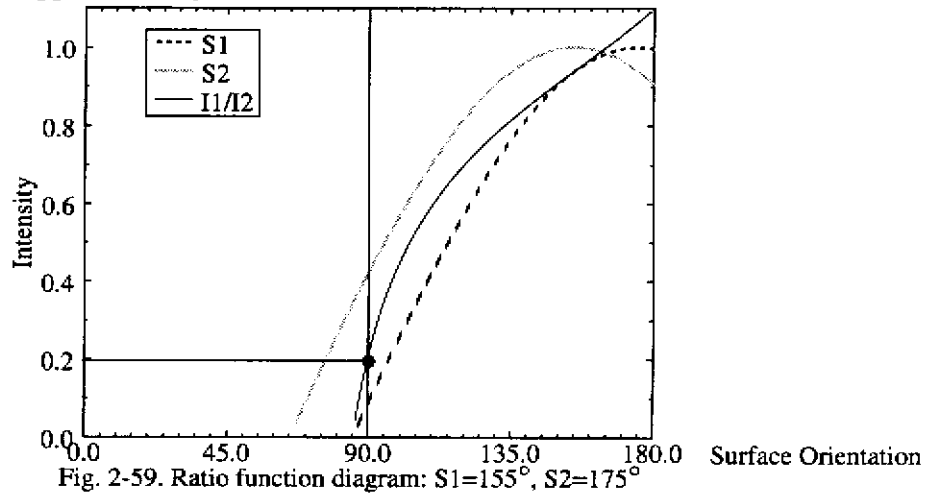
Fig. 2-57. Ratio function diagram:  $S1=45^\circ$ ,  $S2=135^\circ$

We can make some general conclusions for the case when both light sources are on opposite sides of the normal. For the same amount of source position error, the orientation error when both light sources move in the same direction is going to be greater than when both light sources move in opposite directions. The worst case orientation error is going to be produced when both light sources move in the same direction. The worst case orientation error will be equal to the source position error of both light sources. Other normals that are illuminated by both  $S1$  and  $S2$ , will also fall within this error bound.

Next, we look at the case where both light sources are on the same side of the normal. This will produce a different error bound than the case where both light sources are on opposite sides of the normal. We construct a ratio function diagram for nominal source positions of  $S_1=150^\circ$ ,  $S_2=170^\circ$ . Our normal is at  $90^\circ$ . The diagram below show that at  $90^\circ$ , the ratio of  $I_1/I_2$  equals approximately 0.32.

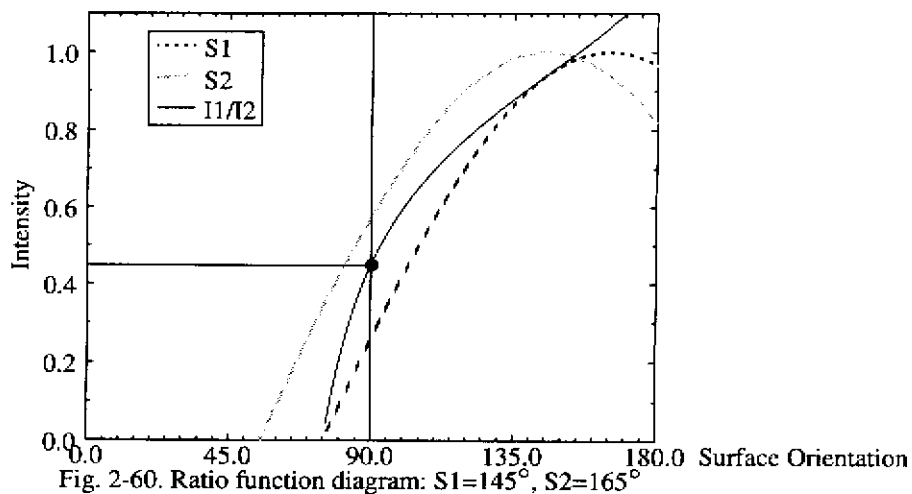


Now, we construct ratio function diagrams for a normal at  $90^\circ$ , and source positions that are perturbed by  $\pm 5^\circ$ . If we move  $S_1 +5^\circ$  and  $S_2 +5^\circ$ , so that  $S_1= 155^\circ$  and  $S_2=175^\circ$ , we find that the ratio equals approximately 0.2.

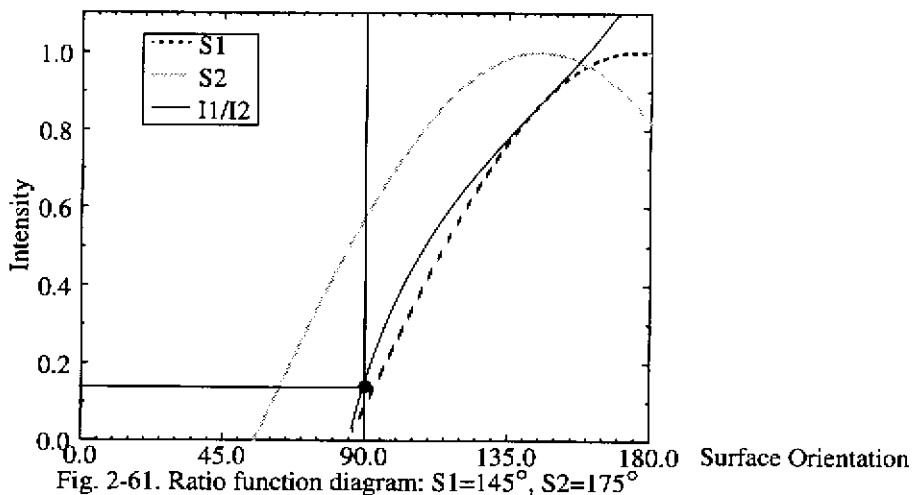


If we move  $S_1 -5^\circ$  and  $S_2 -5^\circ$ , so that  $S_1= 145^\circ$  and  $S_2=165^\circ$ , we find that the ratio equals

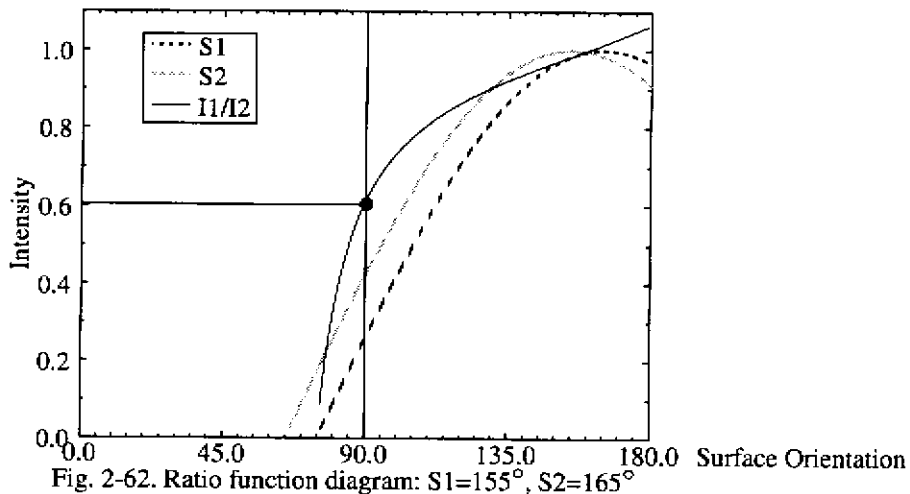
approximately 0.43.



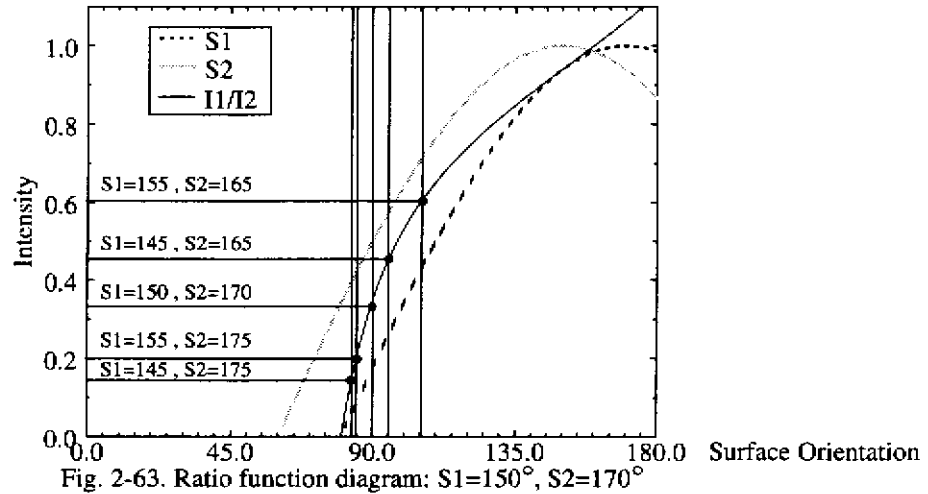
If we move  $S1 -5^\circ$  and  $S2 +5^\circ$ , so that  $S1=145^\circ$  and  $S2=175^\circ$ , we find that the ratio equals approximately 1.3.



If we move  $S1 +5^\circ$  and  $S2 -5^\circ$ , so that  $S1=155^\circ$  and  $S2=165^\circ$ , we find that the ratio equals approximately 0.6.



We plot the nominal and perturbed ratios on the nominal ( $S1= 150^\circ$  and  $S2=170^\circ$ ) ratio function diagram. This diagram shows us how we would interpret the intensity ratios produced by the erroneous source positions given the nominal light source positions. We see that the ratio produced by the case when  $S1= 155^\circ$  and  $S2=175^\circ$  would be interpreted as a surface orientation to  $85^\circ$ . This is a  $5^\circ$  surface orientation error, and is equal to the shift in both light sources. The case when  $S1=145^\circ$  and  $S2=165^\circ$  will be interpreted as a surface orientation of  $95^\circ$  which is also a  $5^\circ$  surface orientation error. The case when  $S1=145^\circ$  and  $S2=175^\circ$  will produce a surface orientation of  $84^\circ$ . The case when  $S1=155^\circ$  and  $S2=165^\circ$  will produce a surface orientation of  $106^\circ$ .



We can make some general conclusions for the case when both light source are on the same side of the normal. When the light sources move in the same direction, the error is equal to the light source shift. This is the same as when the light sources were on opposite sides of the normal. However, when the light sources move in opposite directions, the error can become very large. In general, for the case when the light sources are on the same side of the normal, we cannot say what the bounds of the orientation error is.

### 2.10.2 3D Lambertian Source Error

Next we constructed a 3D simulator, and sampled 3D space to see if the same trends applied. Our normal is along the Z axis. We produced noisy source positions for each mean source position. For a source specified by:  $S(\theta, \phi)$  we generate random positions of  $S(N(\theta, \sigma_s), N(\phi, \sigma_s))$ , where  $\sigma_s$  is the standard deviation of our source uncertainty. For our experiments we set  $\sigma_s$  equal to  $2^\circ$ . We produced 1000 noisy source positions, and calculated

the mean orientation error.

Case	S1		S2		S3		Average Error
	theta	phi	theta	phi	theta	phi	
1	60	0	60	120	60	240	2.0
2	10	0	10	120	10	240	2.0
3	80	0	80	120	80	240	2.0
4	60	0	80	120	80	240	2.2
5	30	0	60	120	10	240	2.3
6	30	0	60	60	30	120	2.5
7	30	0	80	60	80	300	3.3
8	30	30	60	0	60	60	3.5
9	0	0	10	60	10	80	6.4
10	60	0	80	60	80	300	7.3
11	30	0	60	60	60	300	7.6

For cases 1, 2, and 3,  $\phi_{S1} = 0^\circ$ ,  $\phi_{S2} = 120^\circ$ ,  $\phi_{S3} = 240^\circ$ , and  $\theta_{S1} = \theta_{S2} = \theta_{S3}$ . This places the three light sources on “opposite sides of the normal” in a “3D sense”. The error is a minimum, and is independent of  $\theta_S$ . Cases 4 and 5 are somewhat less well separated, and the error increases. In cases 6 through 11, the light sources become less well separated in  $\phi$ , and the error increases further. However, the 3D cases are not as easy to categorize as the 2D cases are. For example, case 8 seems less well separated than case 10, but the error for case 8 is significantly less.

We have not been able to construct a closed form 3D metric which expresses how insensitive a particular light source configuration will be with respect to source error. The best that can be done is to conduct a simulation to see how each potential source configuration will perform. However, it is clear that sources that are distributed around a normal are better than sources which are crowded on one side of the normal.

## 2.11 Summary

This chapter has discussed the illumination of lambertian surfaces. We have discussed the illumination of 2D and 3D convex surfaces, and we have discussed the illumination of 2D and 3D simple concavities. Our illumination planner uses a noise model of the CCD, the lambertian reflectance model, and a candidate light source configuration to perform a statistical simulation which determines how much uncertainty we can expect in our shape measurement. This technique is used throughout the remainder of the thesis. We have conducted experiments that have validated our methodology for 3D convex and 3D concave lambertian surfaces. We have also discussed how the planner can use a CAD model to illuminate a specified set of object faces in an efficient manner, and we have briefly discussed how light source positional uncertainty affects the accuracy of our shape measurement. The next chapter discusses the illumination of rough diffuse surfaces



## Chapter 3

# Illumination of Rough Diffuse Surfaces

This chapter discusses the 2D illumination of rough diffuse surfaces, surfaces that follow the Oren-Nayar reflection model. The Oren-Nayar reflection model is a generalization of the Lambertian model, that allows a much larger class of surfaces to be considered. We discuss the determination of surface orientation in the presence of intensity noise.

### 3.1 Oren-Nayar Rough Diffuse Model

The Lambertian model was proposed by Lambert to describe surfaces that appear equally bright from all directions. Oren and Nayar [Oren 95] developed the rough diffuse model to describe the reflectance properties of diffuse surfaces whose brightness is also a function of viewing direction. Their model applies to rough, diffuse, surfaces when many surface facets are viewed by each camera pixel, and the facet area is much greater than the wavelength of incident light. Facets are modeled by V-cavities.

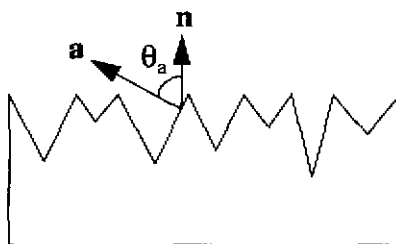


Fig. 3-1. V cavity facet geometry

$n$  is the normal of the surface,  $a$  is the normal of a facet,  $\theta_a$  is the angle between the facet normal and the surface normal.

The Oren-Nayar model accounts for masking, shadowing, and interreflection between facets. Masking occurs when one facet in a V-cavity occludes the viewer's visibility of the second facet in the V-cavity. Shadowing occurs when one facet in a V-cavity occludes the light source's visibility of the second facet in the V-cavity. Masking and shadowing affect the projected radiance of the facet. Interreflection occurs between the facets of the V-cavity and increases the radiance of the surface, especially when the surface is illuminated and viewed

from opposite directions.

The geometry for the Oren-Nayar model for a surface patch with normal,  $N$ , illuminated by a light source at  $(\theta_i, \phi_i)$ , and viewed from  $(\theta_r, \phi_r)$  is:

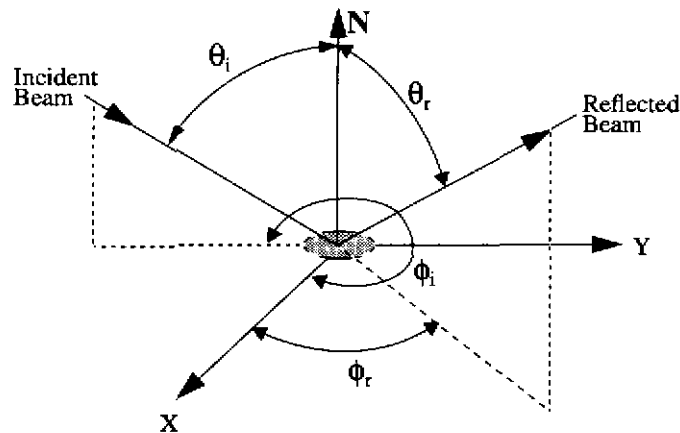


Fig. 3-2. Surface patch geometry

In integral form the Oren-Nayar model is:

$$L_r = \int_0^{\frac{\pi}{2}} P(\theta_a) L_{rp}(\theta_a) \sin \theta_a d\theta_a$$

$L_r$  is the radiance of the surface.  $P(\theta_a)$  is called the slope area distribution. It is the fraction of surface area that is occupied by facets with a surface normal equal to  $\theta_a$ . For a gaussian, isotropic, surface,  $P(\theta_a)$  is a gaussian distribution. The distribution has zero mean, and  $\sigma$  is the standard deviation of the distribution.  $L_{rp}(\theta_a)$  is the radiance of a facet that has a normal equal to  $\theta_a$ .

Due to the complexity of the integral form of  $L_r$ , the integral cannot be easily evaluated. Oren and Nayar created a functional approximation of the integral model by finding basis functions for  $L_r$ . A separate functional approximation was made for the component due to direct illumination and for the component due to interreflection.

The functional model approximation is:

$$L_r = L_r^1 + L_r^2$$

$$L_r^1 = \frac{\rho}{\pi} E_o \cos \theta_i \left[ C_1 + \cos(\phi_r - \phi_i) C_2 \tan \beta + (1 - |\cos(\phi_r - \phi_i)|) C_3 \tan\left(\frac{\alpha + \beta}{2}\right) \right]$$

$$L_r^2 = 0.17 \frac{\rho^2}{\pi} E_o \cos \theta_i \frac{\sigma^2}{\sigma^2 + 0.13} \left[ 1 - \cos(\phi_r - \phi_i) \left(\frac{2\beta}{\pi}\right)^2 \right]$$

$$\alpha = \text{Max}[\theta_r, \theta_i]$$

$$\beta = \text{Min}[\theta_r, \theta_i]$$

$L_r$  is the radiance of the surface.  $L_r^1$  is the radiance of the surface due to direct illumination.

$L_r^2$  is the radiance of the surface due to interreflection.  $\rho$  is the albedo of the surface.  $E_o$  is the irradiance of a fully illuminated facet, when  $\theta_i = 0$ .

$C_1, C_2, C_3$ , are coefficients.

$$C_1 = 1 - 0.5 \frac{\sigma^2}{\sigma^2 + 0.33}$$

$$C_2 = \begin{cases} \left( \frac{0.45 \frac{\sigma^2}{\sigma^2 + 0.09} \sin \alpha}{\sigma^2 + 0.09} \right) & \text{if } \cos(\phi_r - \phi_i) \geq 0 \\ \left( \frac{0.45 \frac{\sigma^2}{\sigma^2 + 0.09} \left( \sin \alpha - \left( \frac{2\beta}{\pi} \right)^3 \right)}{\sigma^2 + 0.09} \right) & \text{otherwise} \end{cases}$$

$$C_3 = 0.125 \left( \frac{\sigma^2}{\sigma^2 + 0.09} \right) \left( \frac{4\alpha\beta}{\pi^2} \right)^2$$

### 3.2 Surface Orientation Calculation

In order to determine surface orientation, we need to solve a system of rough diffuse equations. (Oren and Nayar determined surface orientation for their 2D photometric stereo measurements by using a lookup table.) We can solve a system of rough diffuse equations by forming a set of equations that express ratios of intensities.

For example in a 2D lambertian system,

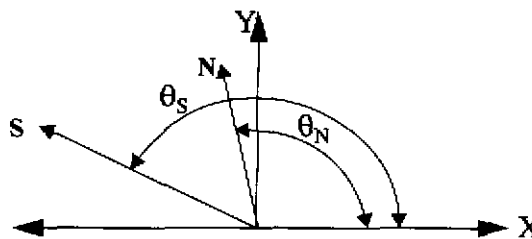


Fig. 3-3. 2D Lambertian geometry

we could solve the 2D system of lambertian equations like this:

$$I_1 = \rho \cos(\theta_{S1} - \theta_N) \quad I_2 = \rho \cos(\theta_{S2} - \theta_N)$$

Then, we form the ratio's of intensities.

$$\frac{I_1}{I_2} = \frac{\cos(\theta_{S1} - \theta_N)}{\cos(\theta_{S2} - \theta_N)}$$

$$I_1 \cos(\theta_{S2} - \theta_N) = I_2 \cos(\theta_{S1} - \theta_N)$$

We bring everything over to one side, and define F as:

$$F = I_1 \cos(\theta_{S2} - \theta_N) - I_2 \cos(\theta_{S1} - \theta_N) = 0$$

This equation can be solved, iteratively, using the Newton-Raphson method

$$\theta_{N+1} = \theta_N - \frac{F}{F'}$$

In a similar manner, we can solve a system of three equations for the Oren-Nayar diffuse model. We will denote the Oren-Nayar model with  $f$ . The source and view directions, in the global coordinate system, are fixed, and we know  $\sigma$ .

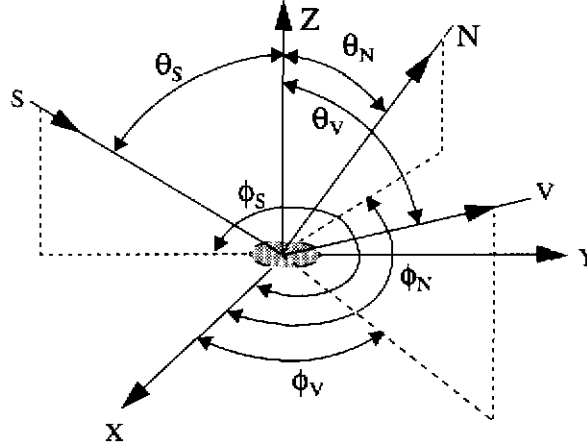


Fig. 3-4. Global coordinate system

We want to solve for the normal's orientation in the global coordinate system. The functional model is expressed in local coordinates. We convert from the global coordinate frame to the local coordinate frame in order to evaluate  $f$ . For our initial guess, we use the lambertian model to solve for normal's orientation, N, using (I1,I2,I3).

$$I_1 = f(\theta_{S1}, \phi_{S1}, \theta_N, \phi_N, \theta_V, \phi_V) \quad I_2 = f(\theta_{S2}, \phi_{S2}, \theta_N, \phi_N, \theta_V, \phi_V) \quad I_3 = f(\theta_{S3}, \phi_{S3}, \theta_N, \phi_N, \theta_V, \phi_V)$$

$$F_1 = I_1 f(\theta_{S2}, \phi_{S2}, \theta_N, \phi_N, \theta_V, \phi_V) - I_2 f(\theta_{S1}, \phi_{S1}, \theta_N, \phi_N, \theta_V, \phi_V) = 0$$

$$F_2 = I_1 f(\theta_{S3}, \phi_{S3}, \theta_N, \phi_N, \theta_V, \phi_V) - I_3 f(\theta_{S1}, \phi_{S1}, \theta_N, \phi_N, \theta_V, \phi_V) = 0$$

The system is solved, iteratively, using the Newton-Raphson method.

$$\begin{bmatrix} -F_1 \\ -F_2 \end{bmatrix} = \begin{bmatrix} \frac{\partial F_1}{\partial \theta_N} & \frac{\partial F_1}{\partial \phi_N} \\ \frac{\partial F_2}{\partial \theta_N} & \frac{\partial F_2}{\partial \phi_N} \end{bmatrix} \begin{bmatrix} \delta\theta_N \\ \delta\phi_N \end{bmatrix}$$

$$\theta_{N+1} = \theta_N + \delta\theta_N \quad \phi_{N+1} = \phi_N + \delta\phi_N$$

$\theta_N$  is positive. If  $\theta_N$  becomes negative, we add  $\pi$  to  $\phi_N$  and make  $\theta_N$  positive. We keep  $\phi_N$  between  $-2*\pi$  and  $2*\pi$ .

The conversion from the global coordinate frame to the local coordinate frame is accomplished as follows. In 3D, we know  $\theta_S, \phi_S, \theta_V, \phi_V, \theta_N, \phi_N$ . We want to solve for  $\theta_l, \theta_r,$

and  $(\phi_r - \phi_i)$ . These can be solved for by using spherical triangles [Rosenbach 61].

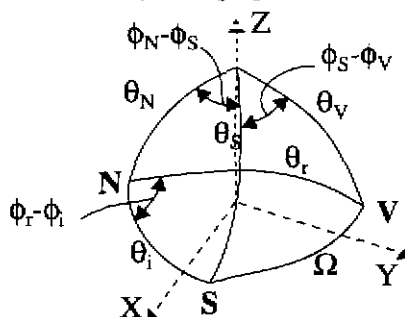


Fig. 3-5. Global and local coordinate system spherical triangles

$$\cos \theta_i = \cos \theta_N \cos \theta_S + \sin \theta_N \sin \theta_S \cos (\phi_N - \phi_S)$$

$$\cos \theta_r = \cos \theta_N \cos \theta_V + \sin \theta_N \sin \theta_V \cos (\phi_N - \phi_V)$$

$$\cos \Omega = \cos \theta_S \cos \theta_V + \sin \theta_S \sin \theta_V \cos (\phi_S - \phi_V)$$

$$\cos (\phi_r - \phi_i) = \frac{(\cos \Omega - \cos \theta_i \cos \theta_r)}{(\sin \theta_i \sin \theta_r)}$$

### 3.3 2D Rough Diffuse Error Surfaces

We performed 2D simulations to determine the sensitivity of rough diffuse surface orientation with respect to intensity noise. For the simulations that follow our 2D normal is  $N=90^\circ$ . We move two light sources between  $0^\circ$  and  $180^\circ$ . At each light source combination, we calculate the nominal intensity of the normal for both light sources. Then we create a noisy intensity using our intensity noise function for both light sources. We calculate N using the two noisy intensity values. We repeat this 1000 times and calculate the standard deviation of the angular orientation error. Our total error is equal to three sigma.

The 2D error surfaces for the Oren-Nayar rough diffuse model are similar to the lambertian error surfaces. There are 2nd order differences between the two sets of error surfaces. We can gain some insight into these differences by examining the intensity surfaces for the rough diffuse model. (In the 2D case, the viewer and light source are in the same plane of incidence. A 3D case, in which the light source and viewer are not in the same plane, will produce different intensity surfaces, and different error surfaces.) We use the following 2D global coordinate system for specifying the positions of the viewer, normal, and light sources.

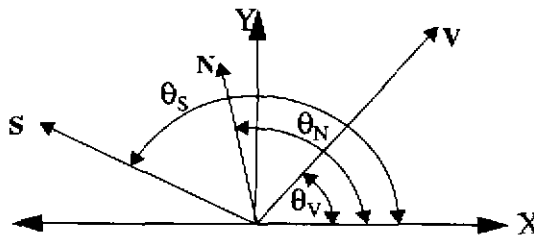


Fig. 3-6. Source/viewer frame of reference coordinate system

Below is the intensity surface for  $\sigma = 10^\circ$ . The intensity surface shows intensity versus incident angle and viewing angle for a normal at  $\theta_N = 90^\circ$ . When  $\sigma$  is small, the intensity surface is close to lambertian.

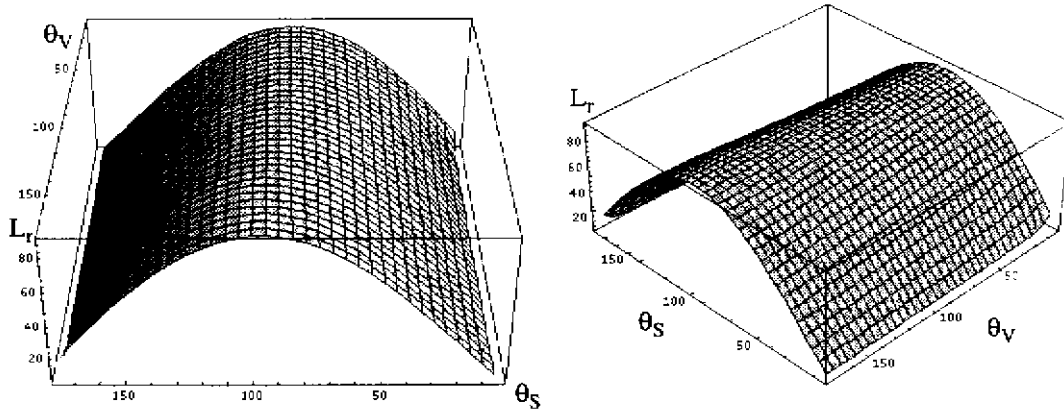


Fig. 3-7. Rough diffuse intensity surface,  $\sigma = 10^\circ$ ,  $\theta_N = 90^\circ$ ,  $\rho = 0.9$ ,  $E_0 = 314$ .

Intensity does vary with viewing direction. When  $\theta_s = 90^\circ$  ( $\theta_i = 0^\circ$ ), the functional approximation becomes near lambertian. Intensity versus view angle becomes constant.

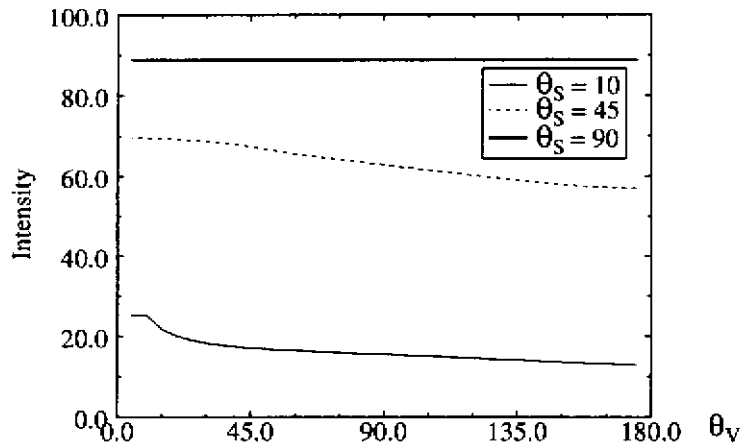


Fig. 3-8. Rough diffuse intensity versus viewing angle,  $\sigma = 10^\circ$ ,  $\theta_N = 90^\circ$ ,  $\rho = 0.9$ ,  $E_0 = 314$ .

For a fixed viewing direction, intensity does deviate from the lambertian cosine function. When  $\theta_v = 90^\circ$  ( $\theta_r = 0^\circ$ ), the functional approximation becomes near lambertian. Intensity

versus incident angle is a cosine function.

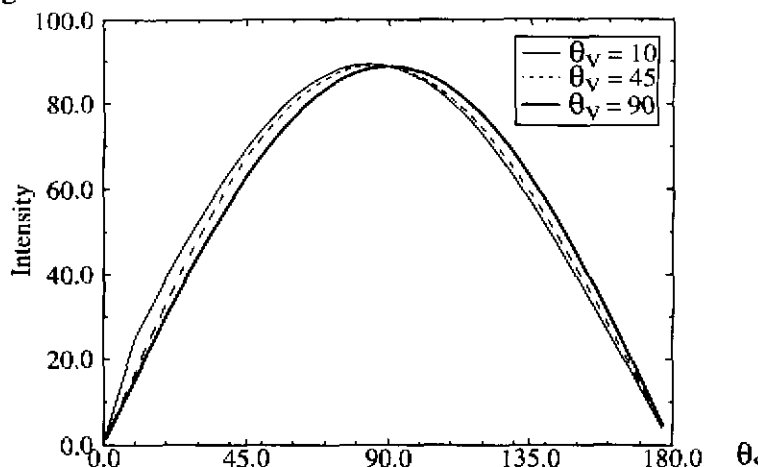


Fig. 3-9. Rough diffuse intensity versus source direction,  $\sigma = 10^\circ$ ,  $\theta_N = 90^\circ$ ,  $\rho = 0.9$ ,  $E_o = 314$

As the deviations between the lambertian and the rough diffuse intensity surfaces become greater, the deviations between the two classes of error surfaces will also become greater. There are two types of differences between the intensity surfaces of the rough diffuse case and the lambertian case that contribute to the differences in the error surfaces. The first factor is the steepness of the intensity surface. As can be seen in Fig. 3-9. , there are places where the rough diffuse intensity curves are steeper than the cosine function, and there are places where the rough diffuse intensity curves are less steep than the cosine function. A steeper intensity surface will cause a decrease in noise sensitivity, while a flatter intensity surface will cause an increase in noise sensitivity. The second factor is the magnitude of the intensity surface. As can be seen in Fig. 3-8. , intensity does vary with viewing direction. As the intensity increases, the signal to noise ratio becomes greater, decreasing the noise sensitivity. As the intensity decreases, the signal to noise ratio decreases, increasing the noise sensitivity.

Below are rough diffuse error surfaces for  $\sigma = 10^\circ$  and  $\theta_N = 90^\circ$ . They are very similar to the lambertian error surface for  $\theta_N = 90^\circ$ . This is because the rough diffuse intensity surface for  $\sigma = 10^\circ$  is close to lambertian.

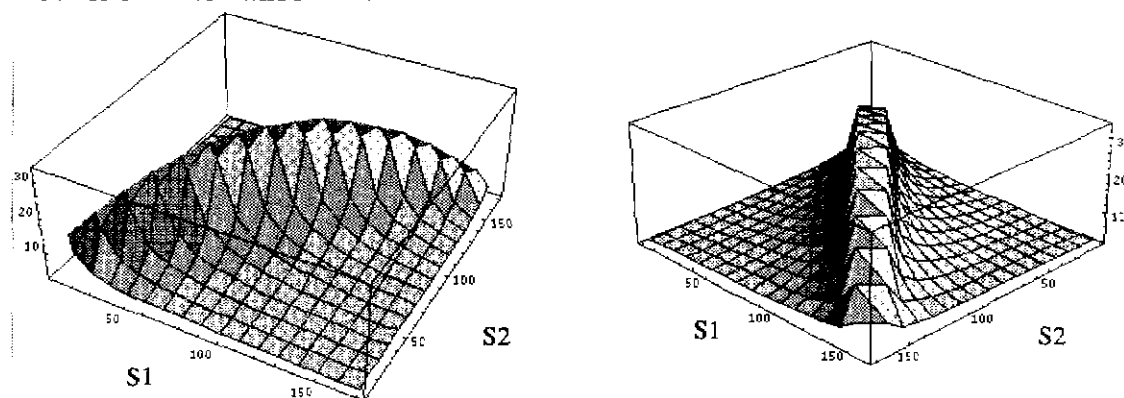


Fig. 3-10. Rough diffuse error surface,  $\sigma = 10^\circ$ ,  $\theta_V = 10^\circ$ ,  $\theta_N = 90^\circ$ ,  $\rho = 0.9$ ,  $E_o = 314$ .

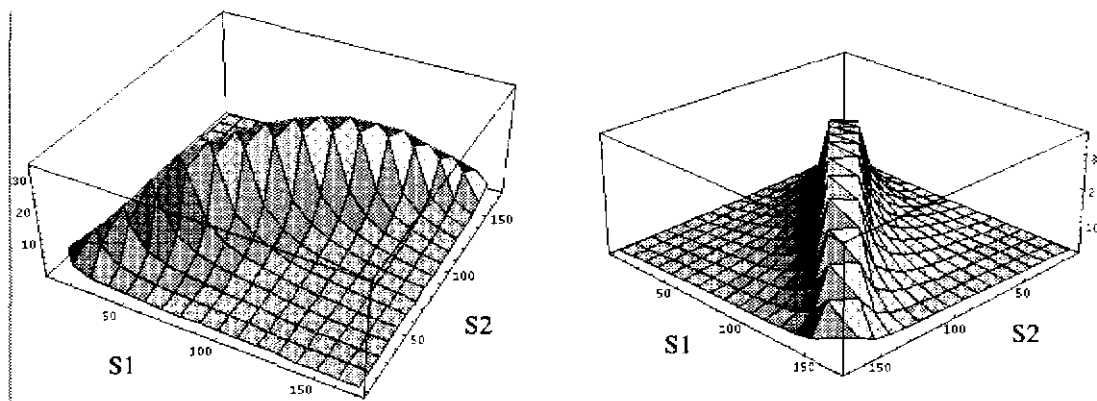


Fig. 3-11. Rough diffuse error surface,  $\sigma = 10^\circ$ ,  $\theta_V = 45^\circ$ ,  $\theta_N = 90^\circ$ ,  $\rho = 0.9$ ,  $E_o = 314$ .

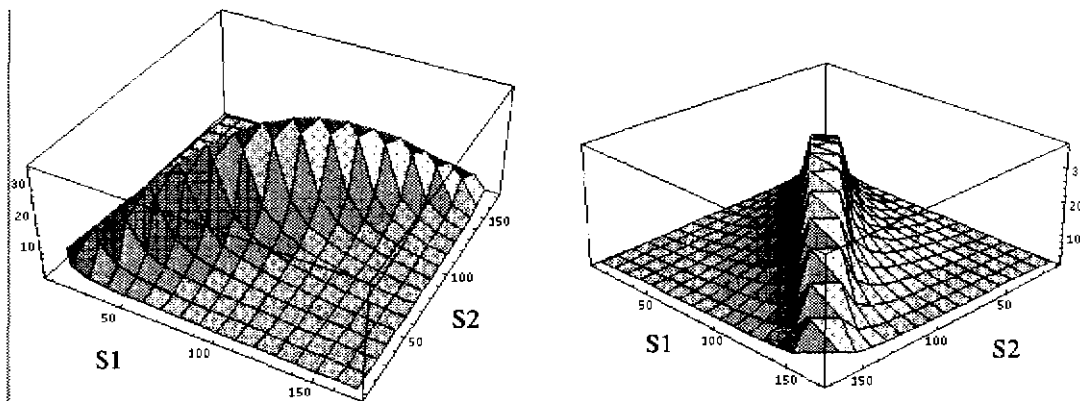


Fig. 3-12. Rough diffuse error surface,  $\sigma = 10^\circ$ ,  $\theta_V = 90^\circ$ ,  $\theta_N = 90^\circ$ ,  $\rho = 0.9$ ,  $E_o = 314$ .

If we look at cross sections of these error surfaces, we can see some second order differences between these error surfaces and a lambertian error surface. (These second order effects are much more apparent for the  $\sigma = 30^\circ$  error surfaces.) The error surface cross section curves for  $\theta_{S1} = 10^\circ$  and  $\theta_{S1} = 170^\circ$  would be symmetric for a lambertian error surface. For the rough diffuse error surface, they are not. For example, when  $\theta_V = 45^\circ$ , the curve for  $\theta_{S1} = 170^\circ$  has a larger average error than the  $\theta_{S1} = 10^\circ$  curve. There are two identifiable factors that contribute to this. The  $\theta_V = 45^\circ$  intensity curve is flatter when  $\theta_S > 90^\circ$  than when  $\theta_S < 40^\circ$ . This increases the noise sensitivity. Also, the intensity is less for a rough diffuse surface when the viewer is not near the light source. The decrease in intensity causes the signal to noise ratio to become worse, increasing the angular error. When  $\theta_V = 90^\circ$ , the inten-

sity surface is near lambertian, causing the cross section to be symmetric.

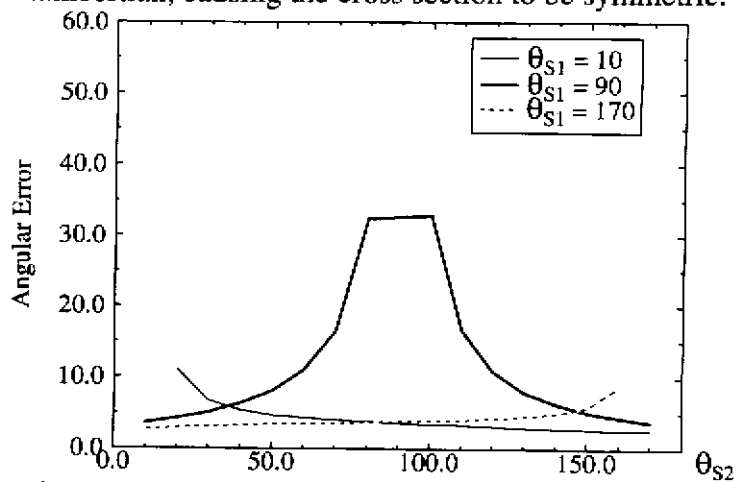


Fig. 3-13. Rough diffuse error surface cross section,  $\sigma = 10^\circ$ ,  $\theta_V = 10^\circ$ ,  $\theta_N = 90^\circ$ ,  $\rho = 0.9$ ,  $E_o = 314$ .

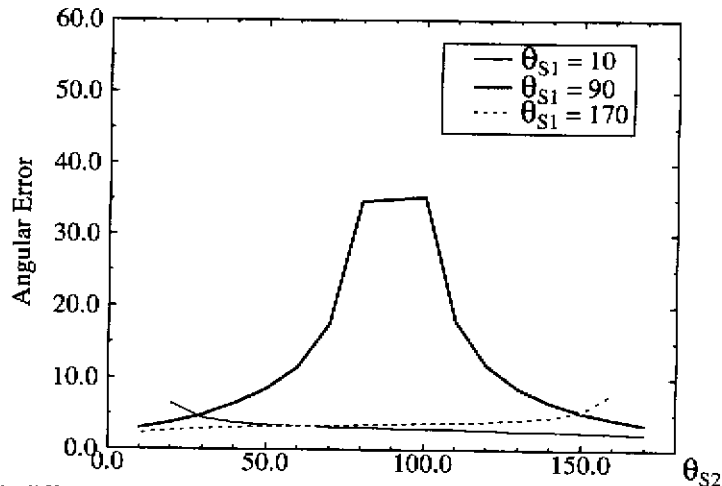


Fig. 3-14. Rough diffuse error surface cross section,  $\sigma = 10^\circ$ ,  $\theta_V = 45^\circ$ ,  $\theta_N = 90^\circ$ ,  $\rho = 0.9$ ,  $E_o = 314$ .

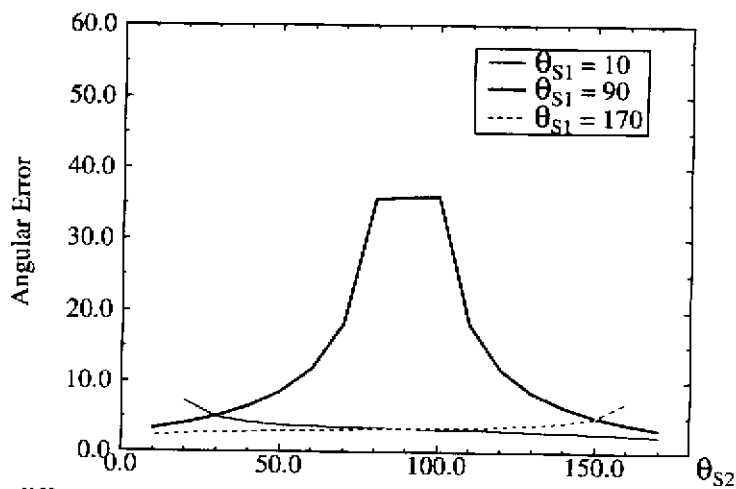


Fig. 3-15. Rough diffuse error surface cross section,  $\sigma = 10^\circ$ ,  $\theta_V = 90^\circ$ ,  $\theta_N = 90^\circ$ ,  $\rho = 0.9$ ,  $E_o = 314$ .

When  $\sigma$  is larger, the intensity surface deviates substantially from lambertian. Below is the intensity surface for  $\sigma = 30^\circ$ . The intensity surface shows intensity versus incident angle and viewing angle for a normal at  $\theta_N = 90^\circ$ .

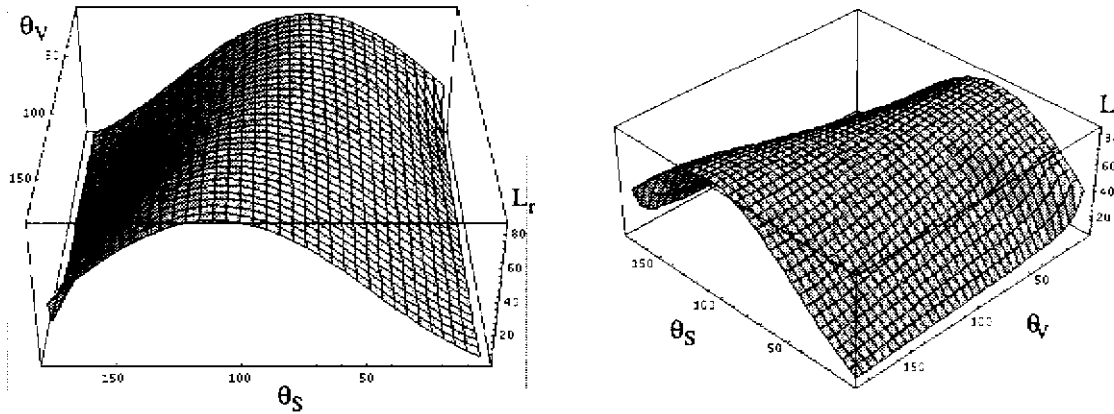


Fig. 3-16. Rough diffuse intensity surface,  $\sigma = 30^\circ$ ,  $\theta_N = 90^\circ$ ,  $\rho = 0.9$ ,  $E_0 = 314$ .

For large  $\sigma$ , intensity varies strongly with viewing direction, except when,  $\theta_S = 90^\circ$  ( $\theta_i = 0^\circ$ ). When  $\theta_S = 90^\circ$  ( $\theta_i = 0^\circ$ ), the functional approximation becomes near lambertian. Intensity versus view angle becomes constant.

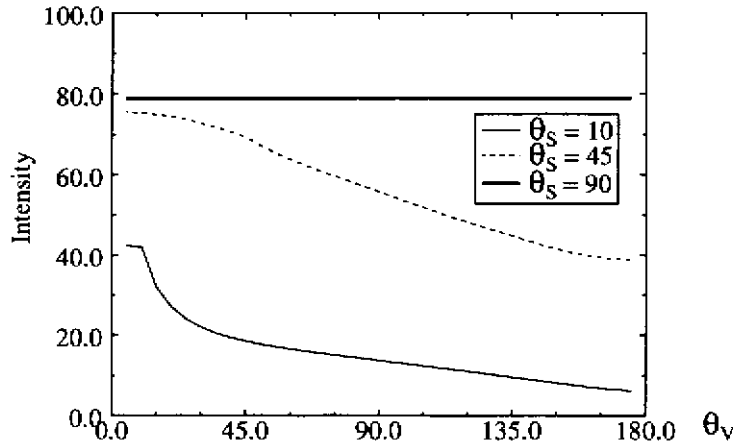


Fig. 3-17. Rough diffuse intensity versus viewing angle,  $\sigma = 30^\circ$ ,  $\theta_N = 90^\circ$ ,  $\rho = 0.9$ ,  $E_0 = 314$ .

For a large  $\sigma$  and a fixed viewing direction, the intensity versus incident angle curves vary substantially from a cosine curve. When  $\theta_V = 90^\circ$  ( $\theta_r = 0^\circ$ ), the functional approximation

becomes near lambertian. Intensity versus incident angle is a cosine function.

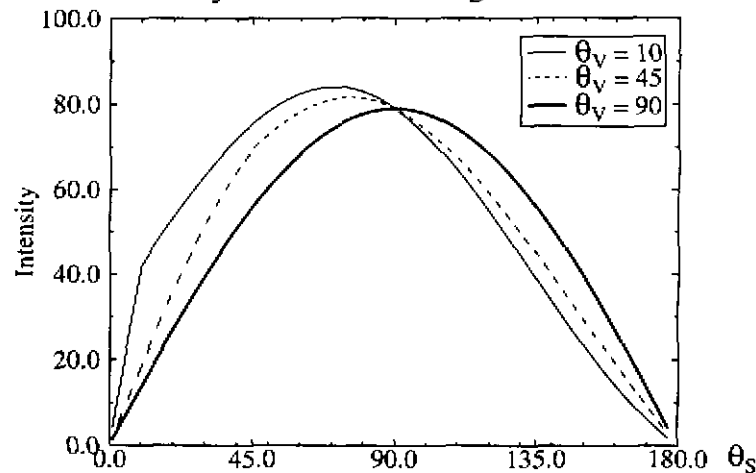


Fig. 3-18. Rough diffuse intensity versus source direction,  $\sigma = 30^\circ$ ,  $\theta_N = 90^\circ$ ,  $\rho = 0.9$ ,  $E_0 = 314$

The shape of the angular orientation error surface is related to the magnitude of the derivative of the rough diffuse intensity function. We calculated the derivative by calculating the change in intensity for a small change in surface orientation ( $d\theta_N = 0.0001$  radians).

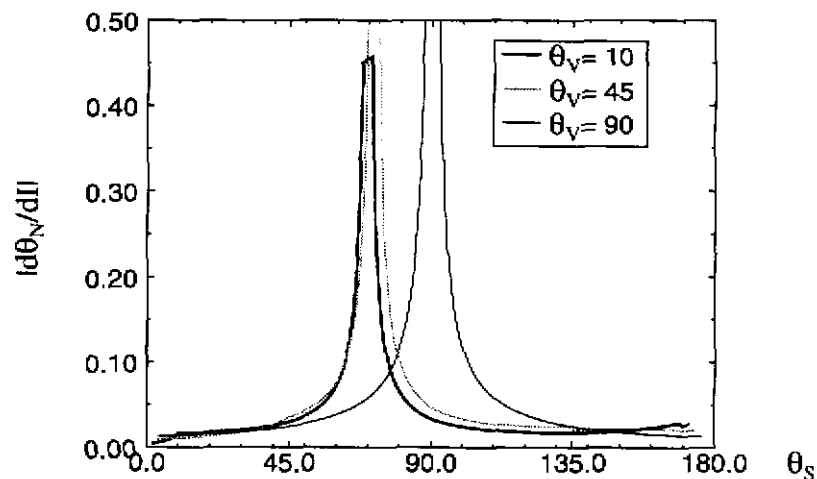


Fig. 3-19. |Derivative of Rough diffuse intensity,  $\sigma = 30^\circ$ ,  $\theta_N = 90^\circ$ ,  $\rho = 0.9$ ,  $E_0 = 314$

The  $|d\theta_N/dI|$  function shows that the derivative will be great when we are at the center of the intensity peak. The magnitude of the central derivative peak is not significant since the derivative becomes unbounded at this point. The  $\theta_V = 90^\circ$  derivative curve is the same shape as a lambertian intensity functions' derivative. The  $\theta_V = 45^\circ$  derivative curve has a larger derivative on the  $\theta_S > 90^\circ$  half of the curve. This is because the intensity curve is flatter when  $\theta_S > 90^\circ$ , and is steeper when  $\theta_S < 90^\circ$ . The  $\theta_V = 10^\circ$  derivative curve is reasonably symmetric except that it increases when  $\theta_S > 130^\circ$ .

The deviations between the lambertian error surface and the  $\sigma = 30^\circ$  error surfaces are greater than the deviations between the lambertian error surface and the  $\sigma = 10^\circ$  error surfaces. However, the deviations are still 2nd order. The  $\theta_V = 10^\circ$  error surface is very similar to a lambertian error surface. The major difference is that the  $\theta_V = 10^\circ$  singularity spine is

not as curved as a lambertian error surface. A factor that may contribute to this is the shape of the derivative function. As we move away from the singularity peak, the  $\theta_V = 10^\circ$  derivative function is flatter than the  $\theta_V = 90^\circ$  derivative function (which is a cosine function). In fact, for  $\theta_S > 130^\circ$ , the derivative increases. The  $\theta_V = 90^\circ$  derivative function monotonically decreases, as we move away from the singularity peak.

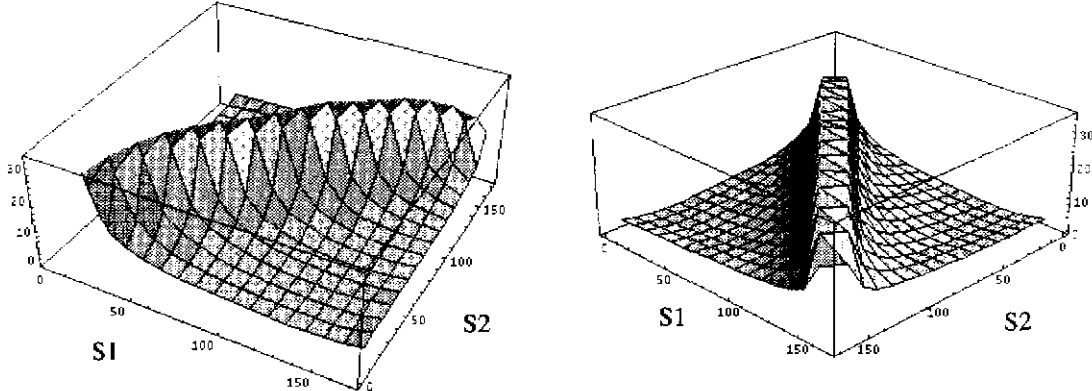


Fig. 3-20. Rough diffuse error surface,  $\sigma = 30^\circ$ ,  $\theta_V = 10^\circ$ ,  $\theta_N = 90^\circ$ ,  $\rho = 0.9$ ,  $E_0 = 314$ .

The  $\theta_V = 45^\circ$  surface's singularity spine has a sharp decrease near  $\theta_S = 45^\circ$ . If we look at the derivative function for  $\theta_V = 45^\circ$ , in Fig. 3-19. , we see that the derivative decreases abruptly when  $\theta_V < 45^\circ$ . This will decrease the noise sensitivity.

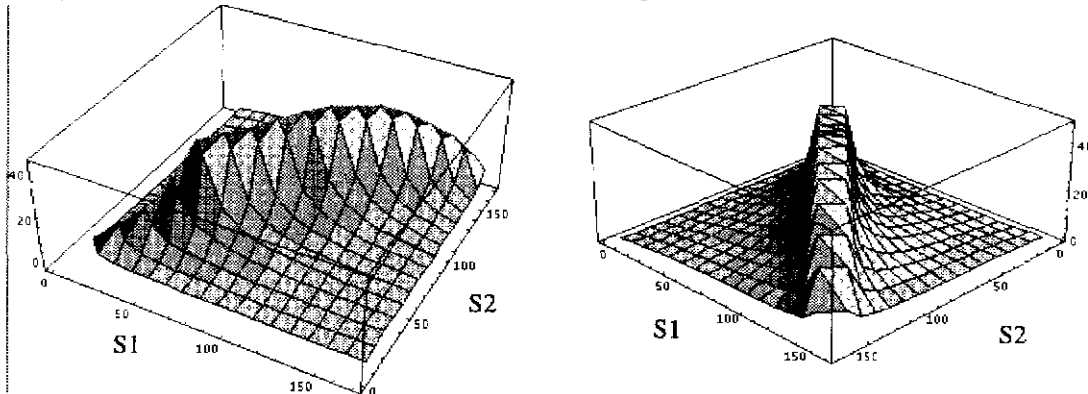


Fig. 3-21. Rough diffuse error surface,  $\sigma = 30^\circ$ ,  $\theta_V = 45^\circ$ ,  $\theta_N = 90^\circ$ ,  $\rho = 0.9$ ,  $E_0 = 314$ .

The  $\theta_V = 90^\circ$  surface's singularity is close to lambertian. If we look at the intensity curve for  $\theta_V = 90^\circ$ , in Fig. 3-18. , we see that it is a cosine function.

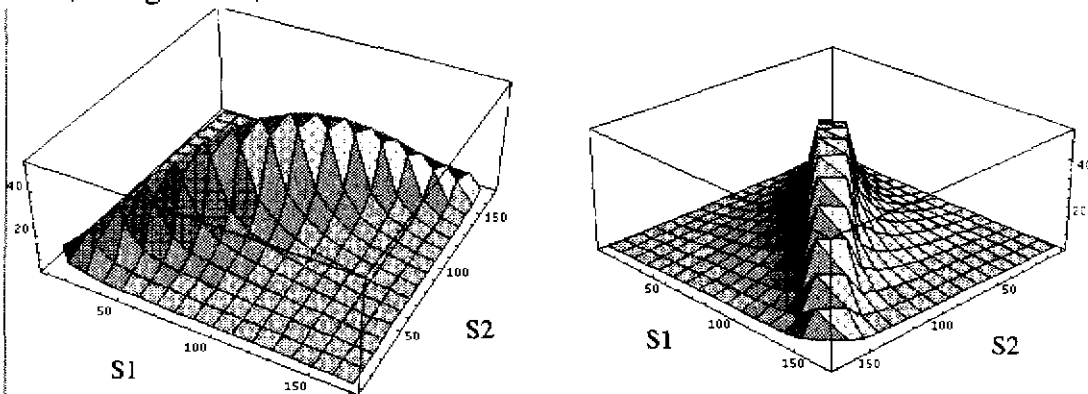


Fig. 3-22. Rough diffuse error surface,  $\sigma = 30^\circ$ ,  $\theta_V = 90^\circ$ ,  $\theta_N = 90^\circ$ ,  $\rho = 0.9$ ,  $E_0 = 314$ .

If we look at cross sections of these error surfaces, we can see some second order differences between these error surfaces and a lambertian error surface. The error surface cross section curves for  $\theta_{S1}=10^\circ$  and  $\theta_{S1}=170^\circ$  would be symmetric for a lambertian error surface. For the rough diffuse error surface, they are not. For example, when  $\theta_V = 45^\circ$ , the curve for  $\theta_{S1}=170^\circ$  has a larger average error than the  $\theta_{S1}=10^\circ$  curve. There are two identifiable factors that contribute to this. The  $\theta_V = 45^\circ$  derivative curve has a larger derivative on the  $\theta_S > 90^\circ$  half of the curve. This is because the intensity curve is flatter when  $\theta_S > 90^\circ$ , and is steeper when  $\theta_S < 40^\circ$ . This increases the noise sensitivity. Also, the intensity is less for a rough diffuse surface when the viewer is not near the light source. The decrease in intensity causes the signal to noise ratio to become worse, increasing the angular error. When  $\theta_V = 90^\circ$ , the intensity surface is near lambertian, causing the cross section to be symmetric. In the region of  $\theta_{S2}=150^\circ$  to  $170^\circ$ ,  $\theta_V = 10^\circ$  has the greatest error,  $\theta_V = 45^\circ$  has less error and  $\theta_V = 90^\circ$  has the least error. In the region of  $\theta_{S2}=20^\circ$  to  $30^\circ$ ,  $\theta_V = 10^\circ$  has the greatest error,  $\theta_V = 90^\circ$  has less error and  $\theta_V = 45^\circ$  has the least error. These errors correlate with the derivative magnitudes in these regions.

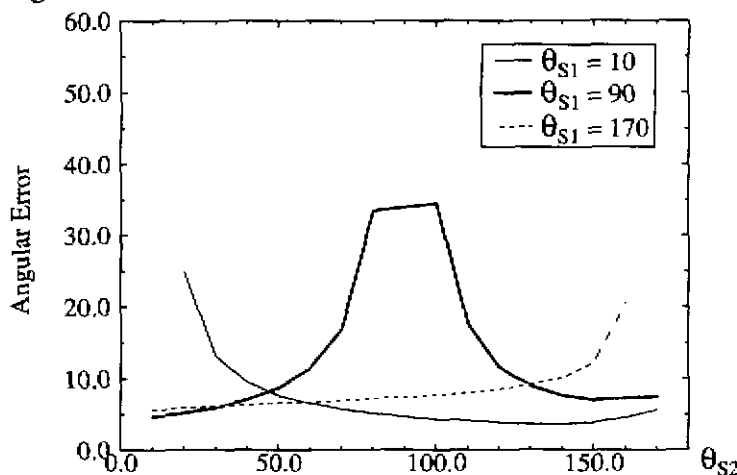


Fig. 3-23. Rough diffuse error surface cross section,  $\sigma = 30^\circ$ ,  $\theta_V = 10^\circ$ ,  $\theta_N = 90^\circ$ ,  $\rho = 0.9$ ,  $E_0 = 314$ .

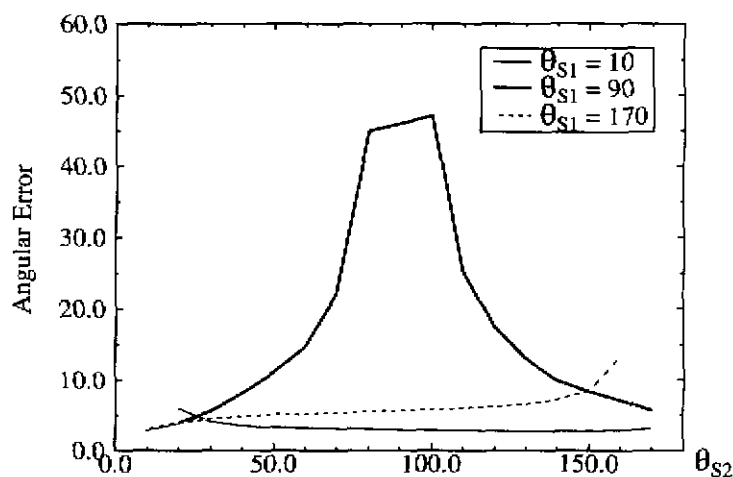


Fig. 3-24. Rough diffuse error surface cross section,  $\sigma = 30^\circ$ ,  $\theta_V = 45^\circ$ ,  $\theta_N = 90^\circ$ ,  $\rho = 0.9$ ,  $E_0 = 314$ .

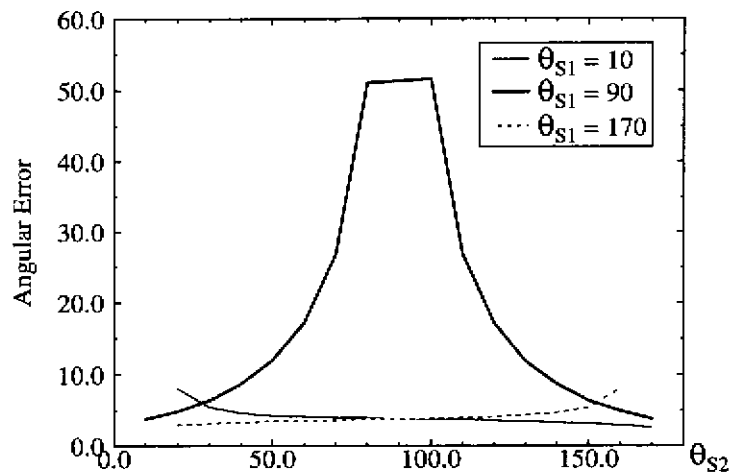


Fig. 3-25. Rough diffuse error surface cross section,  $\sigma = 30^\circ$ ,  $\theta_V = 90^\circ$ ,  $\theta_N = 90^\circ$ ,  $\rho = 0.9$ ,  $E_0 = 314$ .

## 3.4 Experiments

### 3.4.1 Experimental Setup

We mounted a Sony XC-57 camera with a Fujinon 9mm, F1.4 CCTV lens at the far end of an aluminum beam. The near end of the beam was attached to a worm gear driven rotary table which allowed the beam to be rotated in a circular arc, parallel to the floor. An optical encoder attached to the axis of rotation allowed the angular position of the camera to be measured. The distance from the front of the lens to the center of rotation was 61 cm.

Three 12 VDC xenon light bulbs were mounted on light stands, so that the filament was at approximately the same height as the camera's optical axis, and so that the filament was perpendicular to the axis of rotation. The light sources were positioned 99 cm from the center of rotation. The worm gear's encoder was used to measure the angular position of the light sources.



Fig. 3-26. 2D rough diffuse experimental setup.

### 3.4.2 Rough Painted Sandpaper

A 2.5" X 3.5" piece of rough sandpaper (Adalox coarse-60) was painted with flat white paint and was mounted on a black aluminum block. The sandpaper was positioned so that its center was coincident with the axis of rotation.

Images of the sandpaper were taken for  $\theta_i = 30^\circ, 50^\circ, \text{ and } 70^\circ$ , and  $\theta_r$  varying between  $-60^\circ$  ( $\theta_r = 60^\circ, \phi_r = 180^\circ$ ) and  $70^\circ$  ( $\theta_r = 70^\circ, \phi_r = 0^\circ$ ). By using a Macbeth ColorChecker color rendition chart, we determined that the albedo of the paint was 0.813. We then used the Levenberg-Marquardt method to fit the Oren-Nayar functional model approximation to the measurements. The central 50% of each image was averaged to obtain each data point. The best fit value for  $\sigma$  was 23.2, and the best fit value for  $E_o$  was 335.3. The solid lines are the functional model approximation using the best fit values for  $\sigma$ , and  $E_o$ . The dotted lines are the measured values of intensity for the rectangular area of the sample. (Along the X axis of the plot, when  $\theta_r$  is less than zero, this should be interpreted as  $\phi_r = -180^\circ$  and  $\theta_r$  is positive. When  $\theta_r$  is positive,  $\phi_r = 0^\circ$ )

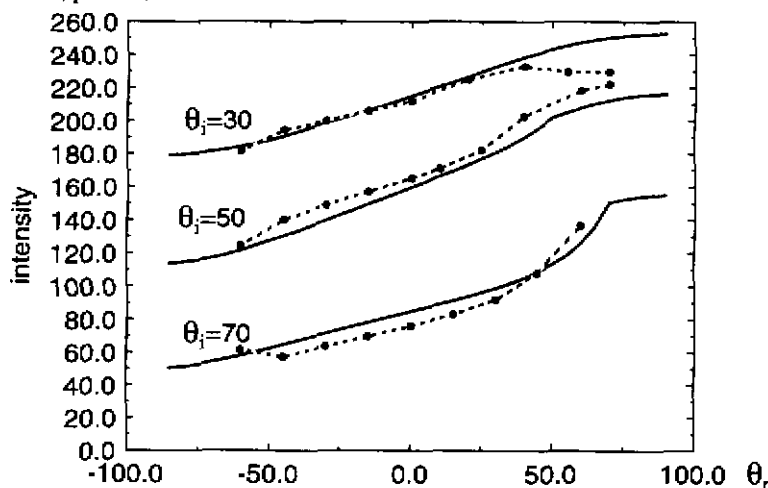


Fig. 3-27. Measurements versus fitted Oren-Nayar model for rough painted sandpaper. Best fit parameters are:  $\sigma=23.2$ ,  $E_o=335.3$ ,  $\rho=.813$

The camera was positioned so that we averaged a large number of sandpaper facets in each pixel of the camera. We implemented two high error plans and two low error plans. For the two viewpoints that we used, the sandpaper sample occupied an area of approximately 70 pixels square in the resulting image. We sampled this 70X70 pixel area using a 10X10 point grid, discarding an approximate 3 pixel border on the perimeter of the sample.

The images of the sandpaper, for the two viewpoints, and three light sources are below:

$V(\theta, \phi)$	$S(\theta, \phi)$		
	30, 0	50, 0	50, $\pi$
60, $\pi$			
20, $\pi$			

The planner's predictions versus the average measurements for the 10X10 grid are below. In general, the measurements are within 15% of the planner's predictions.

			Planner Predictions			Measurements		
S1 ( $\theta, \phi$ )	S2 ( $\theta, \phi$ )	V ( $\theta, \phi$ )	$\sigma(\theta_{err})$ - Degrees	I1	I2	$\bar{\sigma}(\theta_{err})$ - Degrees	$\bar{I}1$	$\bar{I}2$
30, 0	50, $\pi$	20, $\pi$	.55	112.4	173.2	.63	110.1	167.0
30, 0	50, 0	20, $\pi$	1.72	177.1	112.4	2.0	176.1	110.1
30, 0	50, 0	60, 0	1.2	142.8	211.0	1.1	132.5	208.5
30, 0	50, $\pi$	60, 0	0.52	139.7	142.8	0.59	132.9	132.5

The intensity surfaces for the six combinations of view direction and light direction are shown in Fig. 3-28. through Fig. 3-33. . The surfaces are in general smooth. The small irregularities, bumps and valleys, are due to irregularities in the sample. Some of the surfaces which have a large incident angle ( $\theta_i = 50$ ), show a small amount of radiometric fall off across the intensity surface.

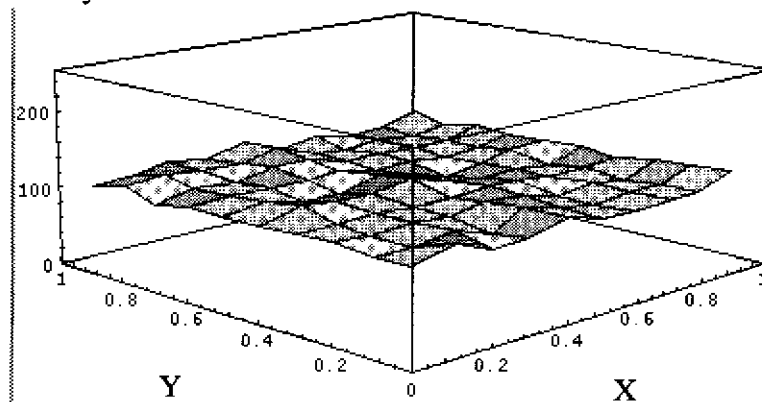


Fig. 3-28. Intensity surface. S1=(30, 0), V=(20,  $\pi$ )

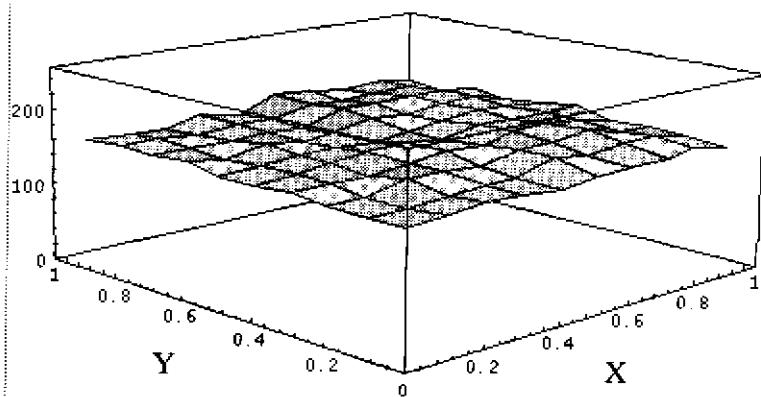


Fig. 3-29. Intensity surface.  $S_2=(50, \pi)$ ,  $V=(20, \pi)$

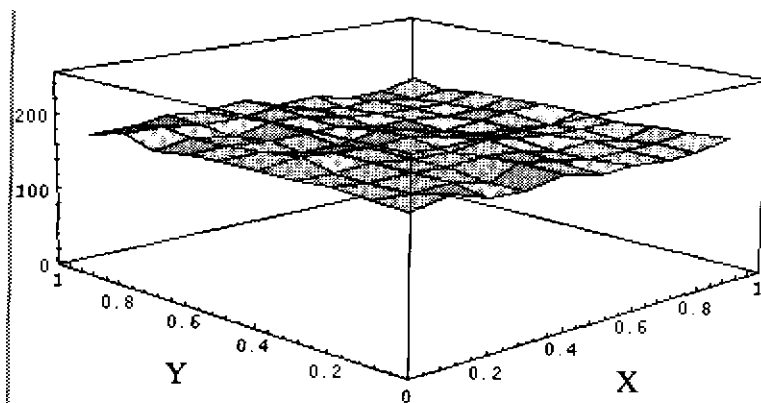


Fig. 3-30. Intensity surface.  $S_2=(50, 0)$ ,  $V=(20, \pi)$

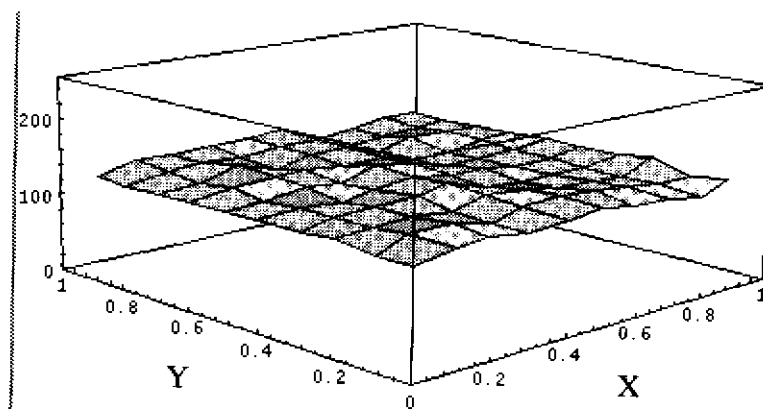


Fig. 3-31. Intensity surface.  $S_1=(30, 0)$ ,  $V=(60, 0)$

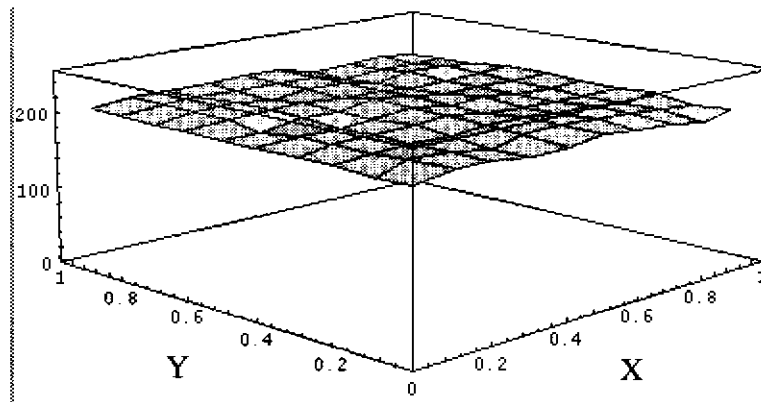


Fig. 3-32. Intensity surface.  $S_2=(50, 0)$ ,  $V=(60, 0)$

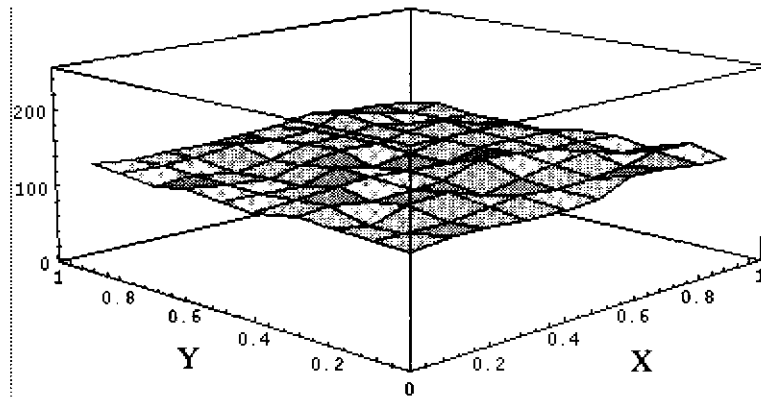


Fig. 3-33. Intensity surface.  $S_2=(50, \pi)$ ,  $V=(60, 0)$

The error surfaces for the four plans are shown in Fig. 3-34. through Fig. 3-37. . The bumps and valleys in the error surfaces are due to the small bumps in the intensity surfaces. The error surface in Fig. 3-37. shows some tilt which is caused by the radiometric fall off in the associated intensity surfaces.

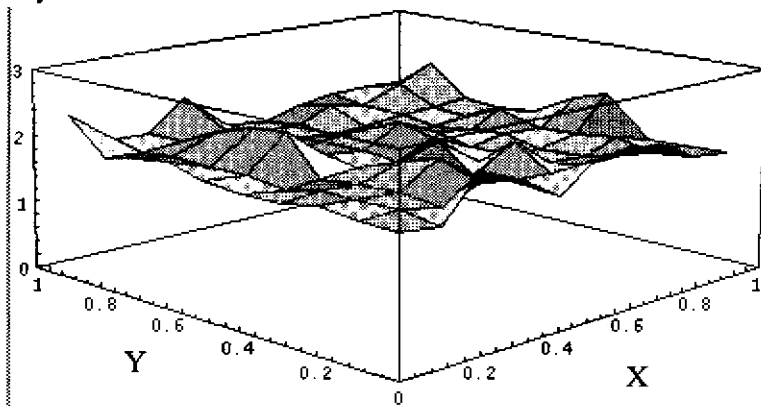
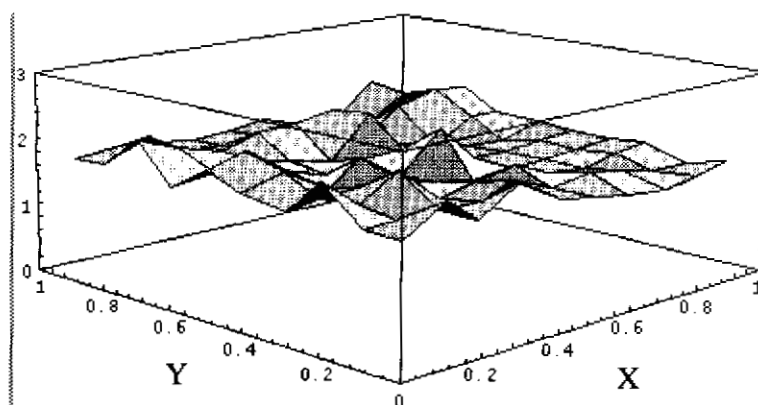
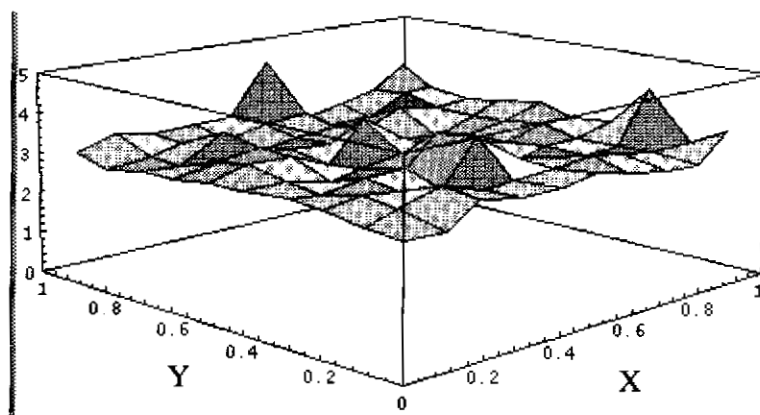
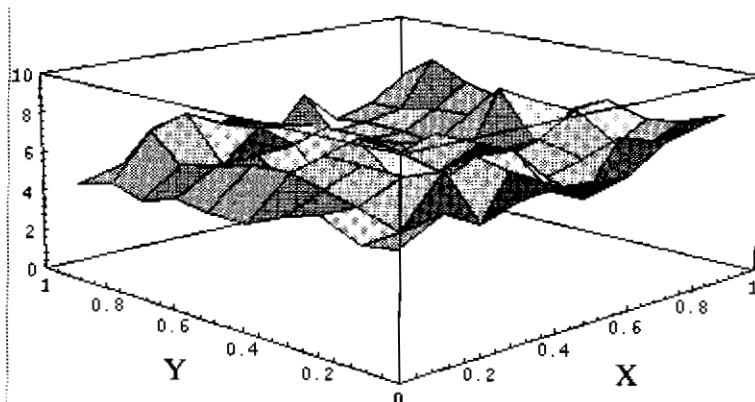


Fig. 3-34.  $3\sigma$  Error surface.  $S_1=(30, 0)$ ,  $S_2=(50, \pi)$ ,  $V=(20, \pi)$

Fig. 3-35.  $3\sigma$  Error surface.  $S1=(30, 0)$ ,  $S2=(50, \pi)$ ,  $V=(60, 0)$ Fig. 3-36.  $3\sigma$  Error surface.  $S1=(30, 0)$ ,  $S2=(50, 0)$ ,  $V=(60, 0)$ Fig. 3-37.  $3\sigma$  Error surface.  $S1=(30, 0)$ ,  $S2=(50, 0)$ ,  $V=(20, \pi)$ 

### 3.5 Summary

This chapter discussed the 2D illumination of rough diffuse surfaces. We found that for small  $\sigma$ , the orientation error surfaces were very similar to the lambertian orientation error surfaces. As  $\sigma$  increases, the intensity surfaces and orientation error surfaces have greater

deviations from lambertian. We conducted experiments which validated the illumination planner's predictions. The next chapter discusses the illumination of specular spike surfaces.

# Chapter 4

## Illumination of Specular Spike Surfaces

This chapter discusses the 2D illumination of specular spike surfaces. We discuss the determination of surface orientation in the presence of intensity noise. The specular spike model describes reflection from smooth surfaces, such as polished metals. Unlike the lambertian and rough diffuse cases, we use extended light sources in this chapter.

### 4.1 Specular Spike Model

According to Nayar [Nayar 91a], the specular spike component is dominant when  $\sigma_h/\lambda < 0.025$ .  $\sigma_h$  is the standard deviation of the normally distributed height distribution that describes the roughness of the surface.  $\lambda$  is the wavelength of the incident light. Specular spike reflection occurs when  $\theta_i = \theta_r$ , and all of the light from a point light source at  $\theta_i$  is reflected into a viewer at  $\theta_r$ .

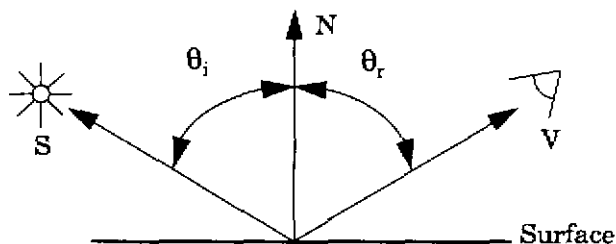


Fig. 4-1. Specular geometry

### 4.2 Extended Light Sources

If we are trying to illuminate a distribution of normals with a point light source, we will only be able to illuminate one of the normals at a time. Therefore, extended light sources are often used to illuminate specular spike surfaces. Extended light sources are composed of a point light source and a light diffusive material. The point light source is mounted at some height above the diffusive material. The radiance distribution of an extended light source depends on the shape of the diffuser and the position of the light source with respect to the diffuser. We examine the sensitivity of orientation error to intensity noise for a 2D circular diffuser. A circular diffuser allows many surface orientations of an object to be illuminated by using multiple, point, light sources spaced evenly outside of the diffuser. Nayar [Nayar

90b] developed this device and called it a photosampler.

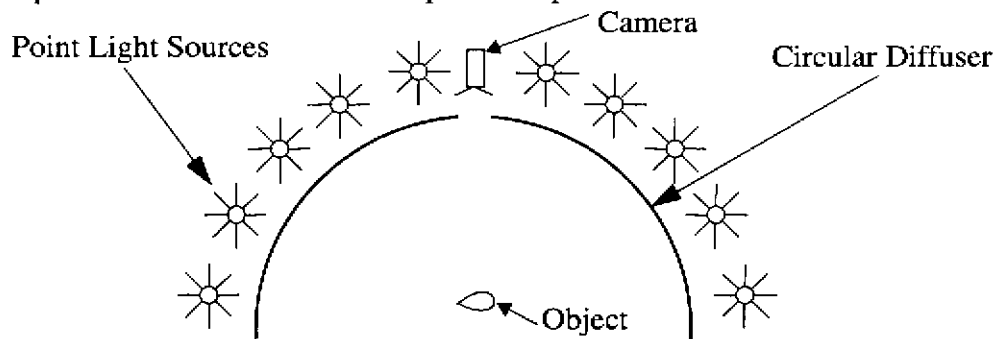


Fig. 4-2. 2D photosampler

If we have a point light source at a distance “H” above a circular diffuser of radius R:

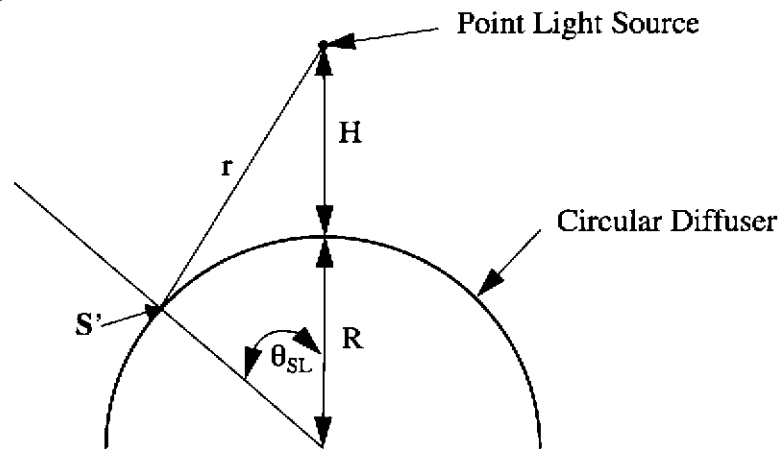


Fig. 4-3. Extended source geometry

The intensity at the specular point, S', is [Nayar 90b]:

$$E = \frac{L(R + H) \cos \theta_{SL} - R}{[(H + R - R \cos \theta_{SL})^2 + (R \sin \theta_{SL})^2]^{1.5}}$$

$\theta_{SL}$  is the local extended source specular angle. It is the angle between the center of the extended source and the specular point, S'. If  $\theta_{SL}$  is outside the range of illumination, the above expression will give a negative intensity. This allows us to determine whether a point is within the illuminating range of an extended light source.  $\theta_{SG}$  is the global specular angle. It indicates the position of the specularity in the global coordinate system. The global coordinate system is used to locate the viewer,  $\theta_v$ , surface normal,  $\theta_N$ , and the center of the

extended light source,  $\theta_{SGC}$ .

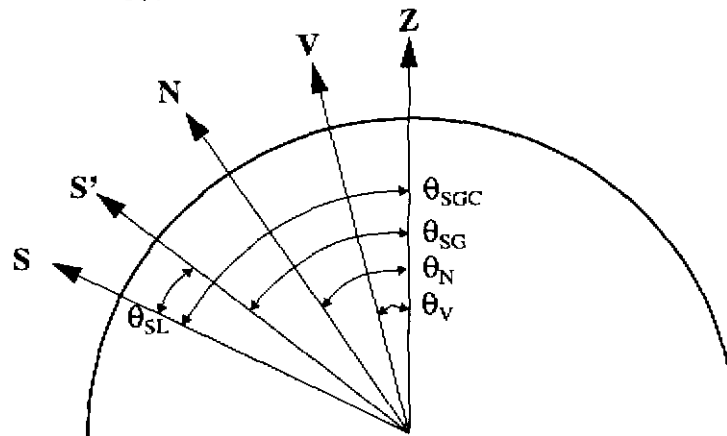


Fig. 4-4. Global/local specular notation

A typical plot of an extended source's radiance, for  $R = 30$ , and  $H = 10$ :

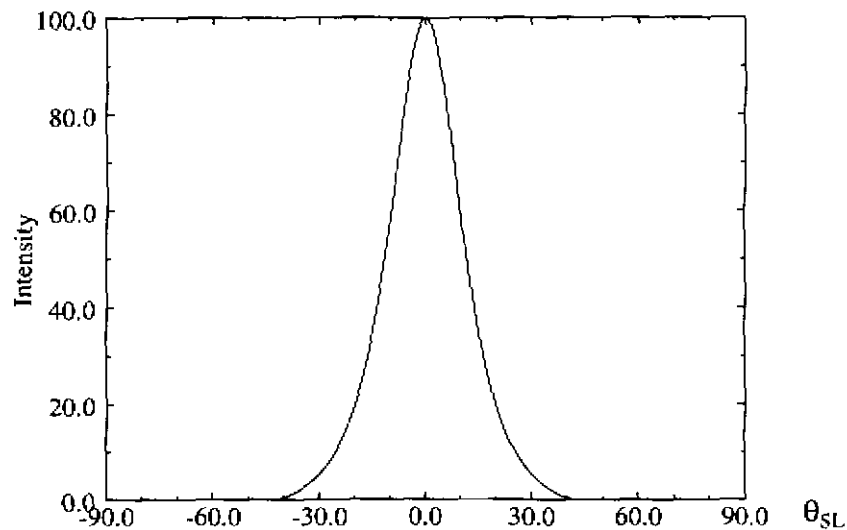


Fig. 4-5. Extended light source intensity  $R=30$ ,  $H=10$

The intensity is greatest where the diffuser is closest to the point source,  $\theta_{SL} = 0$ , and it decreases in an approximately exponential manner as  $\theta_{SL}$  increases.

We need to determine where an extended light source can be placed so that it illuminates an object. This depends on the surface orientation,  $\mathbf{N}$ , that we are trying to illuminate and the viewer's position,  $\mathbf{V}$ . Once  $\mathbf{N}$  and  $\mathbf{V}$  are known we can find the specular point,  $\mathbf{S}'$ . This is the point in space that will reflect into the viewer. If we know the position of an extended light source,  $\theta_{SGC}$ , we can find the angle between the specular point and the extended light source's center,  $\theta_{SL}$ . This will tell us the radiance of the extended light source at the specu-





Convergence is not guaranteed. As the derivative of the ratio function approaches zero, it is possible for next guess normal to exist outside of the illuminated part of the extended light source. If this happens, convergence will not occur. The derivative of the ratio function will be close to zero when the light sources are close together, and the specular point is near the peripheral of the extended light sources.

## 4.4 2D Specular Spike Error Surfaces

We performed 2D simulations to determine the sensitivity of specular spike surface orientation with respect to intensity noise. For the simulations that follow our 2D normal is located at  $\theta_N=90^\circ$ . We move two light sources between  $\theta_{SGC}=0^\circ$  and  $\theta_{SGC}=180^\circ$ . At each light source combination, we calculate the nominal intensity of the normal for both light sources. Then we create a noisy intensity using our intensity noise function for both light sources. We calculate  $N$  using the two noisy intensity values. We repeat this 1000 times and calculate the standard deviation of the angular orientation error. Our total error is equal to three sigma.

The shape of the angular orientation error surface will be related to the derivative of the extended source intensity function. If we look at  $|d\theta_{SL}/dI|$  we will gain some intuition into the shape of the orientation error surfaces.

We examine error surfaces for extended sources with a width of  $106.3^\circ$  ( $R=30, H=20$ ),  $82.8^\circ$  ( $R=30, H=10$ ),  $62.0^\circ$  ( $R=30, H=5$ ), and  $45.2^\circ$  ( $R=30, H=2.5$ ). For all of these surfaces  $N=90^\circ$  and  $V=80^\circ$ , so the specular point occurs at  $100^\circ$ . The radiance of the point light source,  $L$ , is adjusted so that the extended light source will have a radiance of 255, when  $\theta_{SL}$  equals 0. We include source positions that produce an intensity greater than 5. For source positions that have an intensity less than 5, we set the error to zero, for plotting purposes.

The first error surface we examine is for an extended source with  $R=30$  and  $H=20$ . The width of the illuminating region of the extended source is  $106.3^\circ$ .

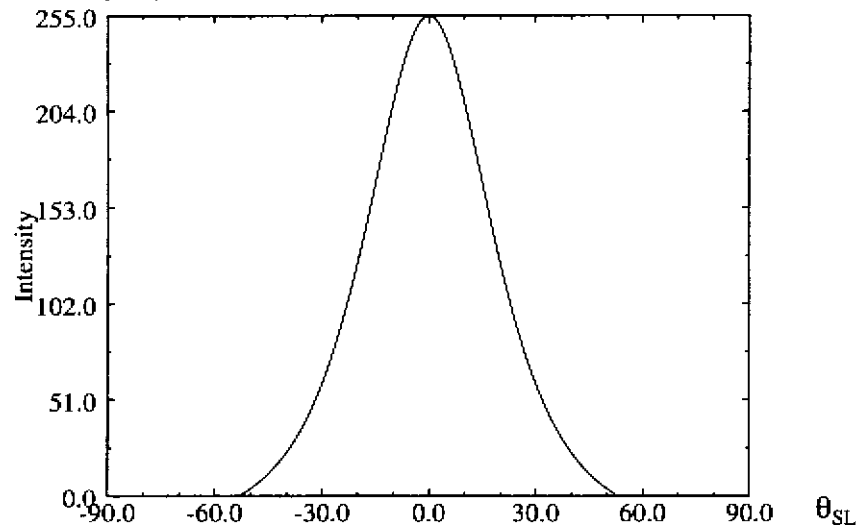


Fig. 4-8. Extended light source intensity  $R=30, H=20$

The  $|d\theta_{SL}/dI|$  function shows that the derivative will be great when we are at the center of the

extended source. The derivative quickly decreases to a minimum, and then steadily increases as  $\theta_{SL}$  increases. The magnitude of the central derivative peak is not significant since the derivative becomes infinite when  $\theta_{SL}$  equals 0. For this extended light source, the derivative has a minimum at  $\theta_{SL} = 14.4^\circ$ , and is equal to 0.002. The value of the derivative when  $\theta_{SL}$  becomes maximal is dependent on the curvature of the intensity function as the intensity approaches zero. The maximum value for this extended light source is 0.015. (The maximum values are at the end of the tails of the  $|d\theta_{SL}/dI|$  function. We exclude the central derivative peak.)

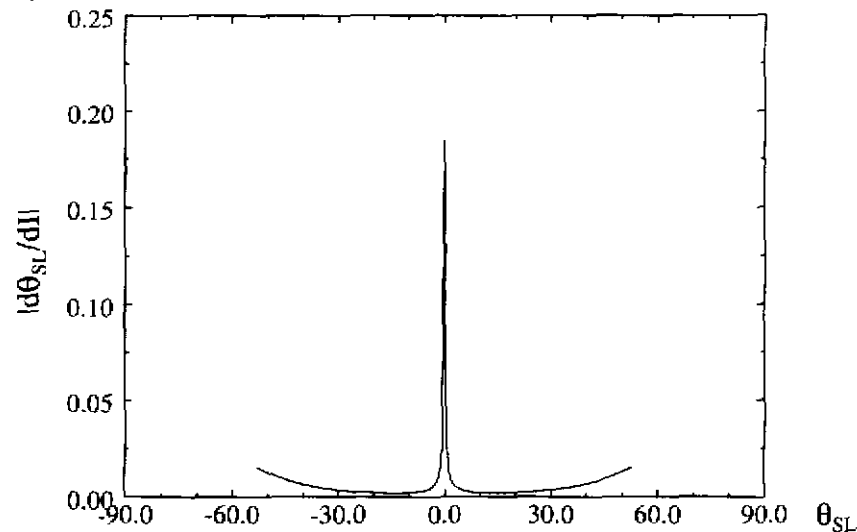


Fig. 4-9. Derivative of extended light source intensity  $R=30$ ,  $H=20$

The error surface shows that the error is smallest when we are close, but somewhat offset from the center of the extended light source. The error increases steadily as  $\theta_{SL}$  increases. The minimum error occurs when  $S1 = 88.55^\circ$  ( $\theta_{SL1} = 11.45^\circ$ ) and  $S2 = 110.7^\circ$  ( $\theta_{SL2} = 10.70^\circ$ ), and is equal to 0.256. The location of the minimum corresponds well with the location of the minimum in the intensity derivative function.

We do not see a peak in the error surface corresponding to the central derivative peak of the  $|d\theta_{SL}/dI|$  function. The central derivative peak occurs at the singularity of the intensity profile,  $\theta_{SL} = 0^\circ$ . The derivative quickly decreases as  $\theta_{SL}$  increases. If we look at the intensity function around  $\theta_{SL} = 0^\circ$ , we can see that for finite amounts of the intensity noise, the angular change in  $\theta_{SL}$  will not be as large as the  $|d\theta_{SL}/dI|$  function indicates. In addition, the intensity is greatest near  $\theta_{SL} = 0^\circ$ . This makes the signal to noise ratio the greatest, decreasing the effect of the derivative. With these factors in mind, we see that the singularity ridge, in the

error surface, is approximately flat near  $\theta_{SL}=0^\circ$ .

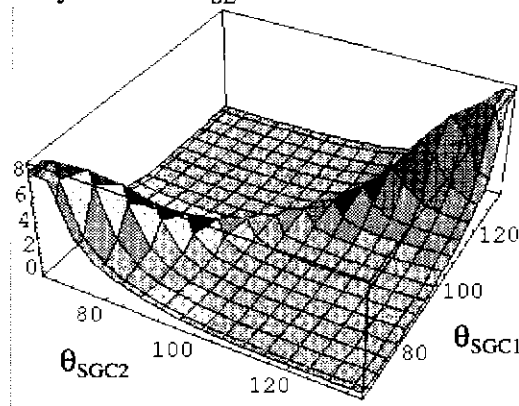


Fig. 4-10. 2D Specular error surface. R=30, H=20, V=80, N=90, L=102000

We examine a cross section of the surface near  $S1=100$ . (This is the specular angle for  $V=80$ .) We can see more clearly that the error does in fact increase as  $\theta_{SL}$  increases. The minimum error occurs at  $\theta_{SGC2}=88.55$  ( $\theta_{SL2}=11.45^\circ$ ), which is close to where the minimum was in the  $|\frac{d\theta_{SL}}{dI}|$  function. The maximum value of the cross section is approximately 1.3.

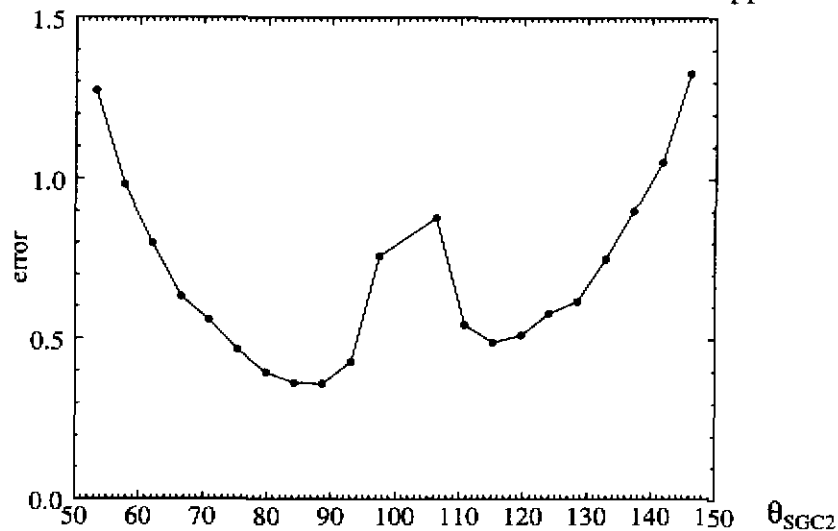


Fig. 4-11. 2D Specular error surface cross section,  $S1=101.83$ . R=30, H=20, V=80, N=90, L=102000

Next we examine an extended source with  $R=30$  and  $H=10$ . The width of the illuminating

region of the extended source is  $82.8^\circ$ .

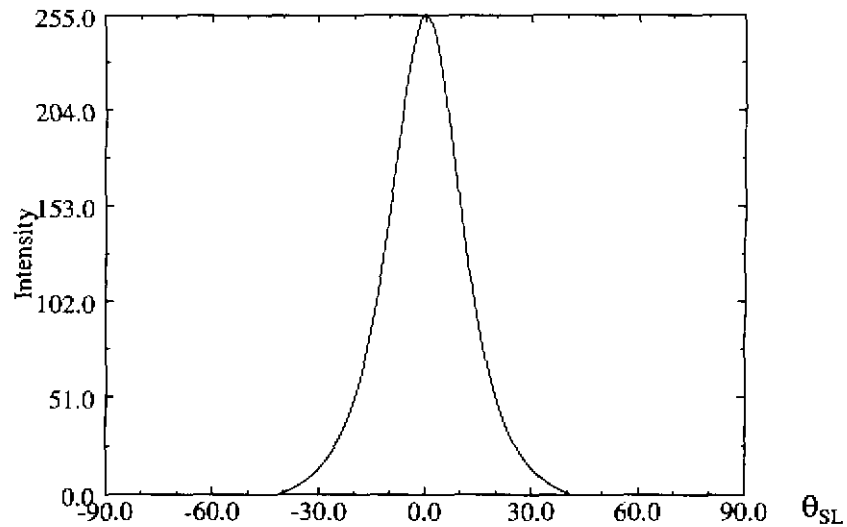


Fig. 4-12. Extended light source intensity  $R=30$ ,  $H=10$

The  $|d\theta_{SL}/dI|$  function for this extended light source has a minimum at  $\theta_{SL} = 8.1^\circ$ , and the minimum is equal to 0.0012. This is 40% less than the  $H=20$  case. The maximum value for this extended light source is 0.027.

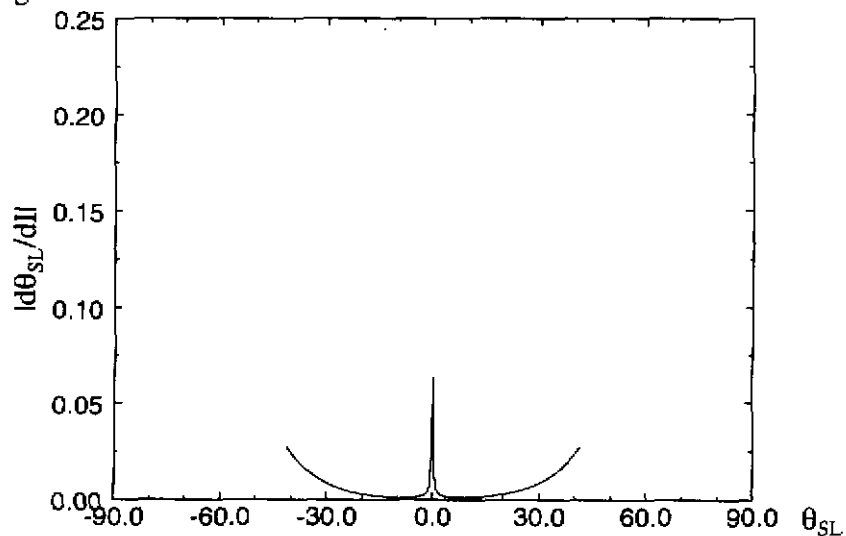


Fig. 4-13. Derivative of extended light source intensity  $R=30$ ,  $H=10$

The error surface shows that the error is smallest when we are close, but somewhat offset from the center of the extended light source. The error increases steadily as  $\theta_{SL}$  increases. The minimum error occurs when  $S1 = 93.2^\circ$  ( $\theta_{SL1} = 6.8^\circ$ ) and  $S2 = 107.0^\circ$  ( $\theta_{SL2} = 7.0^\circ$ ), and is equal to 0.153. The location of the minimum corresponds well with the location of the minimum in the intensity derivative function. This error is approximately 40% less than the

H=20 case, which is the same percentage that the minimum derivative values differ by.

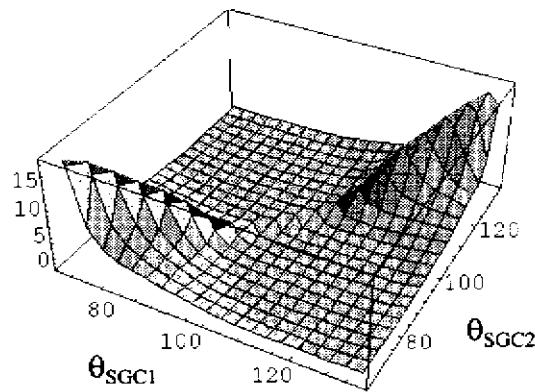


Fig. 4-14. 2D Specular error surface R=30, H=10, V=80, N=90, L=25500

We examine a cross section of the surface near  $S1=100$ . (This is the specular angle for  $V=80$ .) The minimum error occurs at  $\theta_{SGC2}=93.17$  ( $\theta_{SL2}=6.83^\circ$ ), which is close to where the minimum was in the  $|d\theta_{SL}/dI|$  function. The maximum value of the cross section is approximately 1.8, which is 34% greater than the H=20 case.

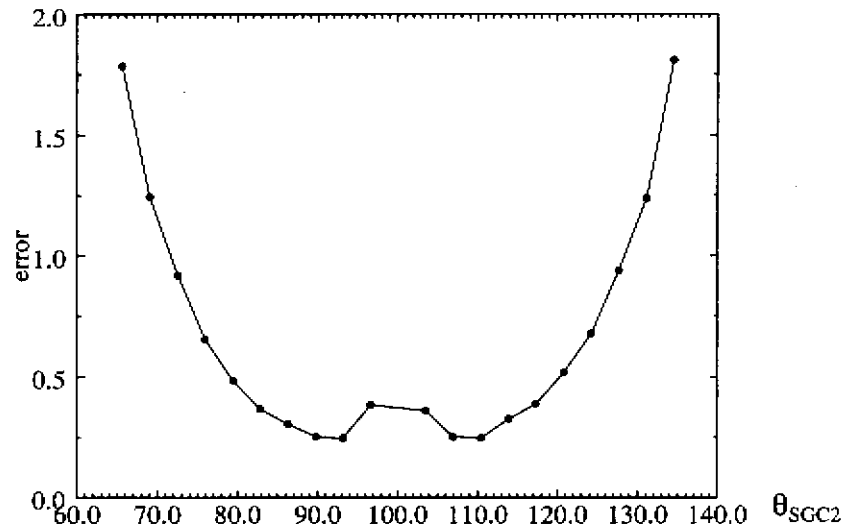


Fig. 4-15. 2D specular error surface cross section  $S1=100.07$ , R=30, H=10, V=80, N=90, L=25500

Next we examine an extended source with R=30 and H=5. The width of the illuminating

region of the extended source is  $62.0^\circ$

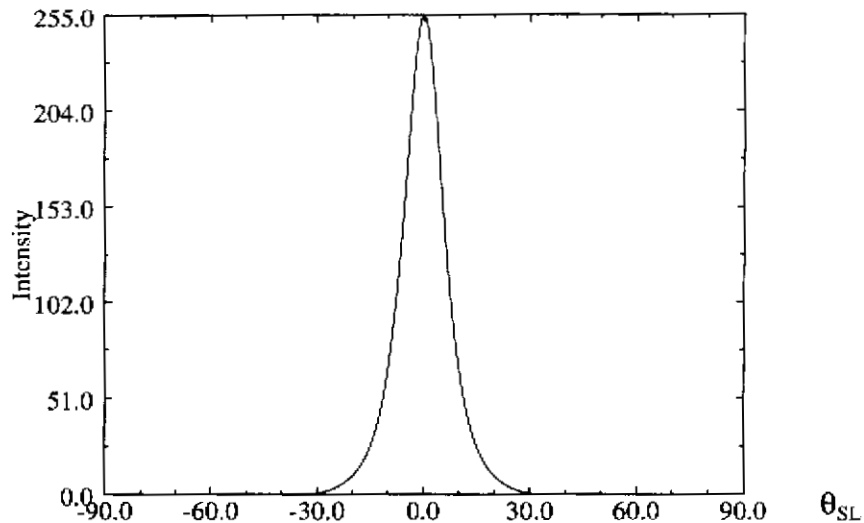


Fig. 4-16. Extended light source intensity R=30, H=5

The  $|d\theta_{SL}/dI|$  function for this extended light source has a minimum at  $\theta_{SL} = 4.5^\circ$ , and is equal to 0.00067. This is 66% less than the H=20 case. The maximum value for this extended light source is 0.047.

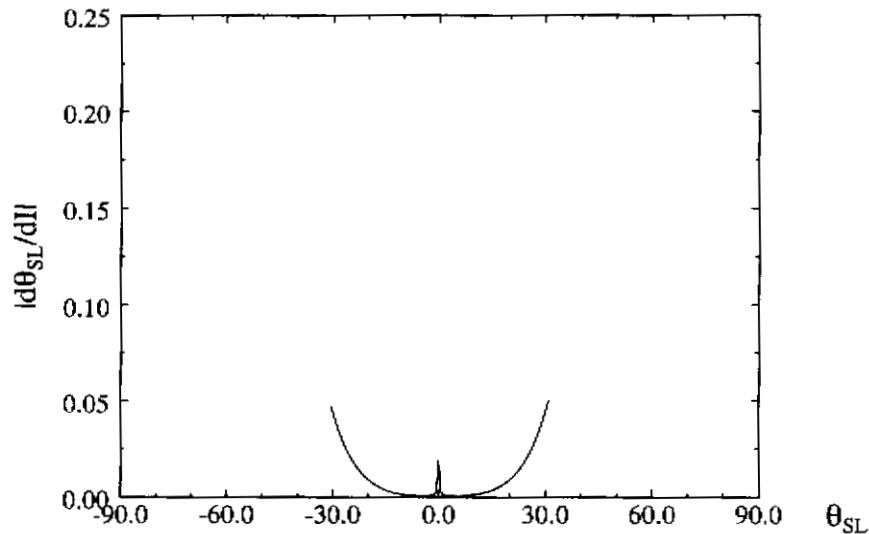


Fig. 4-17. Derivative of extended light source intensity R=30, H=5

The error surface shows that the error is smallest when we are close, but somewhat offset from the center of the extended light source. The error increases steadily as  $\theta_{SL}$  increases. The minimum error occurs when  $S1 = 95.6^\circ$  ( $\theta_{SL1} = 4.4^\circ$ ) and  $S2 = 103.3^\circ$  ( $\theta_{SL2} = 3.3^\circ$ ), and is equal to 0.086. The location of the minimum corresponds well with the location of the minimum in the intensity derivative function. This error is approximately 66% less than the

H=20 case, which is the same percentage that the minimum derivative values differ by.

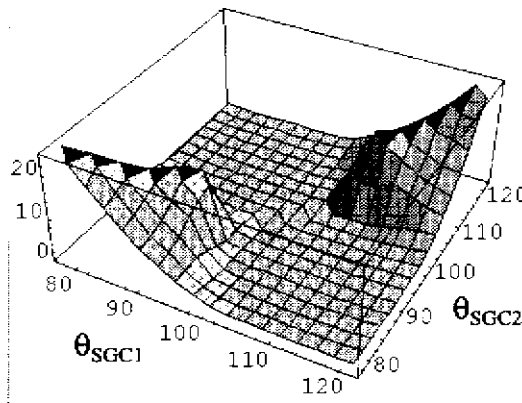


Fig. 4-18. 2D specular error surface R=30, H=5, V=80, N=90, L=6375

We examine a cross section of the surface near  $S1=100$ . (This is the specular angle for  $V=80$ .) The minimum error occurs at  $\theta_{SGC2}=95.59$  ( $\theta_{SL2}=4.41^\circ$ ), which is close to where the minimum was in the  $|\partial\theta_{SL}/\partial I|$  function. The maximum value of the cross section is approximately 1.7, which is 30% greater than the H=20 case.

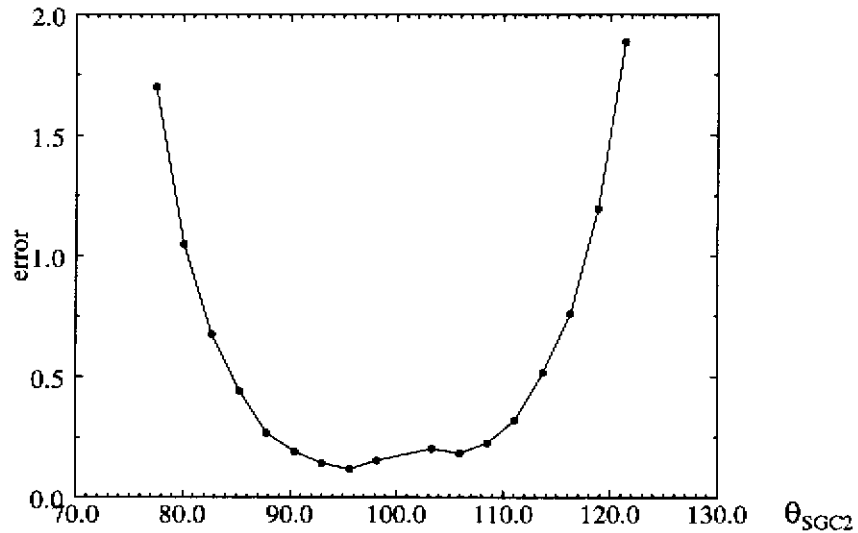


Fig. 4-19. 2D specular error surface cross section  $S1=100.76$ , R=30, H=5, V=80, N=90, L=6375

Next we examine an extended source with R=30 and H=2.5. The width of the illuminating

region of the extended source is  $45.2^\circ$

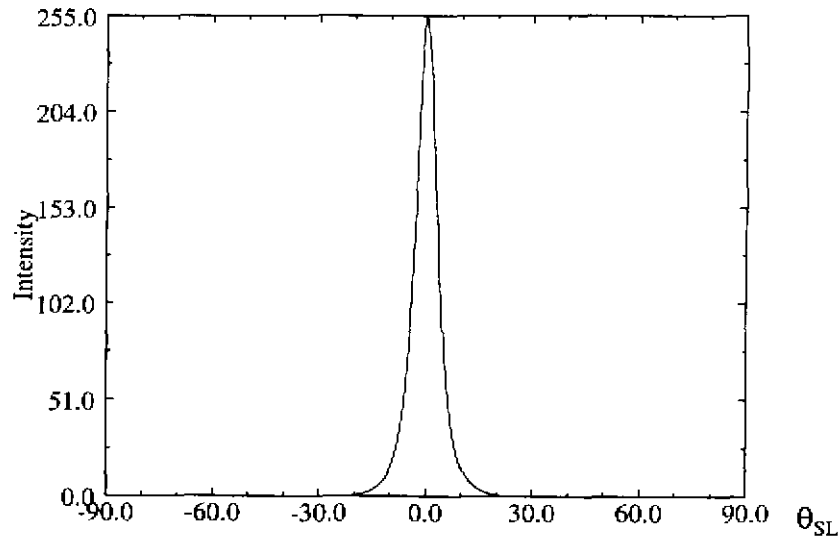


Fig. 4-20. Extended light source intensity  $R=30$ ,  $H=2.5$

The  $|d\theta_{SL}/dI|$  function for this extended light source has a minimum at  $\theta_{SL} = 2.2^\circ$ , and is equal to 0.00036. This is 82% less than the  $H=20$  case. The maximum value for this extended light source is 0.094.

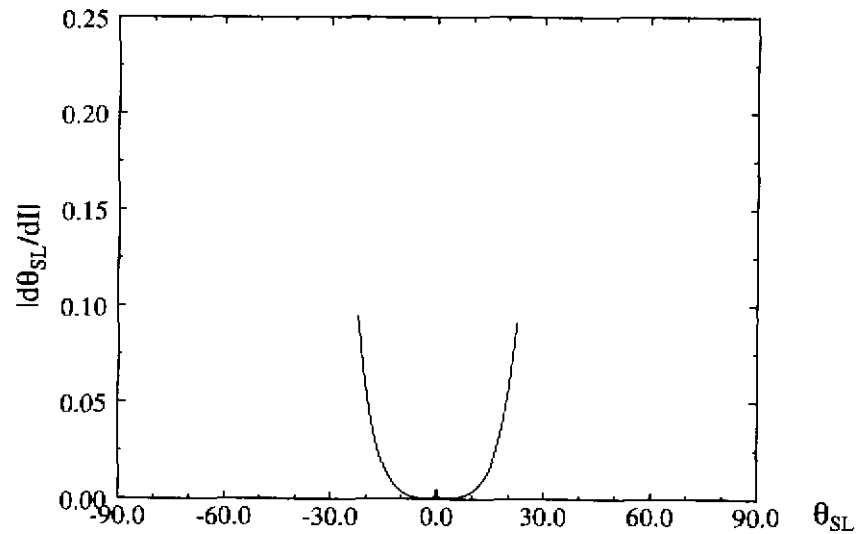


Fig. 4-21. Derivative of extended light source intensity  $R=30$ ,  $H=2.5$

The error surface shows that the error is smallest when we are close, but somewhat offset from the center of the extended light source. The error increases steadily as  $\theta_{SL}$  increases. The minimum error occurs when  $S1 = 98.0^\circ$  ( $\theta_{SL2} = 2.0^\circ$ ) and  $S2 = 101.8^\circ$  ( $\theta_{SL2} = 1.8^\circ$ ), and is equal to 0.046. The location of the minimum corresponds well with the location of the minimum in the intensity derivative function. This error is approximately 82% less than the

H=20 case, which is the same percentage that the minimum derivative values differ by.

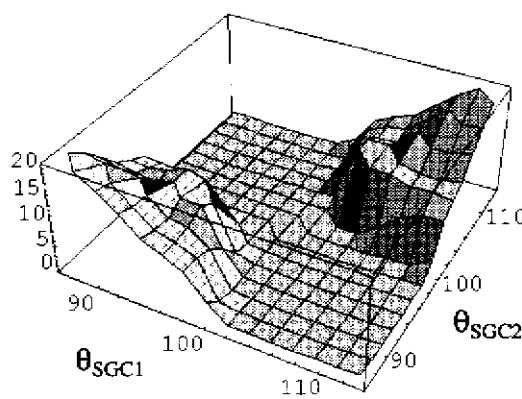


Fig. 4-22. 2D Specular Error Surface R=30, H=2.5, V=80, N=90, L=1593.75

We examine a cross section of the surface near  $S1=100$ . The minimum error occurs at  $\theta_{SGC2}=101.79$  ( $\theta_{SL2}=1.79^\circ$ ), which is close to where the minimum was in the  $|d\theta_{SL}/dI|$  function. The maximum value of the cross section is approximately 2.5 on one side and approximately 4.1 on the other side.

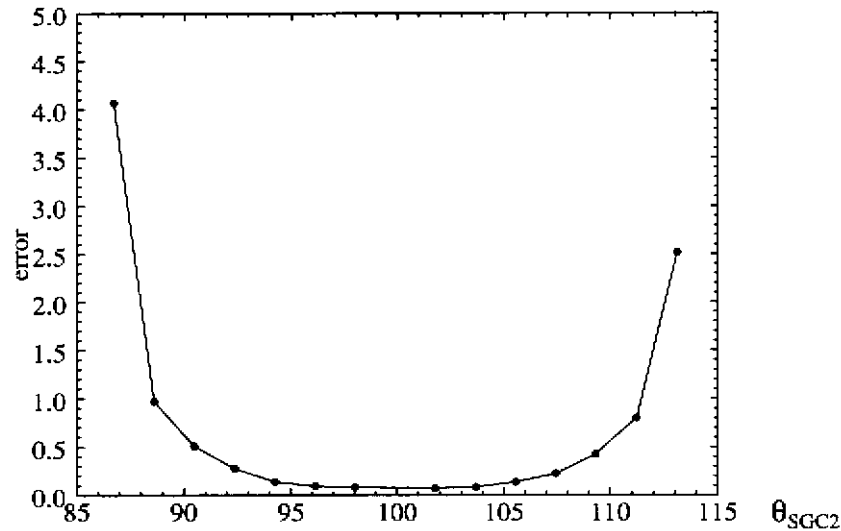


Fig. 4-23. 2D Specular error surface cross section S1=99.9, R=30, H=2.5, V=80, N=90, L=1593.75

The simulations show that as the extended light source intensity function becomes narrower, the minimum error decreases. This is because the sides of the intensity function become steeper. In addition, the percentage of the error surface that has a large error increases. This is because the tails of the intensity function become flat at a less gradual rate, and because the percentage of the intensity function within the tail region increases.

## 4.5 Experiments

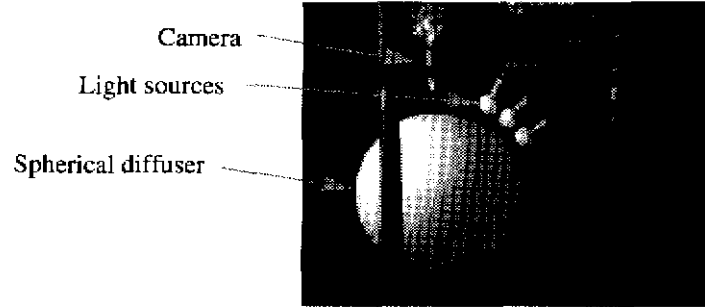


Fig. 4-24. Experimental setup

We conducted a series of experiments using a 16" diameter spherical diffuser. We positioned three 40watt, 16.5G, light bulbs around the photosampler. We performed two sets of experiments. The first experiment was the illumination of a polished aluminum plate. The plate measured 0.5" X 0.5". The second set of experiments was the illumination of a polished 0.5" diameter stainless steel cylinder. Our camera was mounted so that  $\theta_v=0^\circ$ .

### 4.5.1 Extended Light Source Model

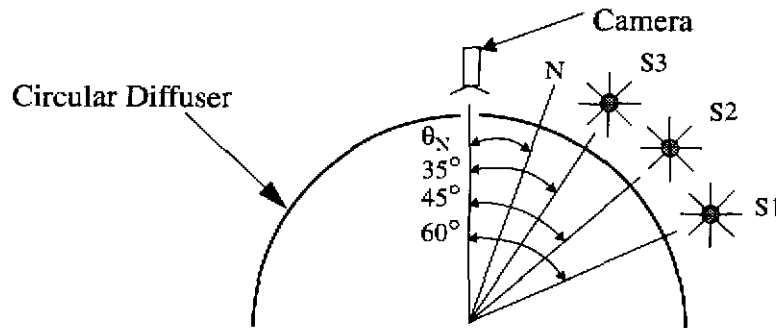


Fig. 4-25. Nominal experimental setup

We made refined models of the light source positions by illuminating a polished ball bearing with each light source. We then fitted our extended light source model to the image by using the Levenberg-Marquardt method [Press 90].

$$E = \frac{L(R+H)\cos\theta_{SL} - R}{[(H+R-R\cos\theta_{SL})^2 + (R\sin\theta_{SL})^2]^{1.5}}$$

$$\theta_{SL} = \theta_{SGC} - 2\theta_N$$

We fitted the  $\theta_{SGC}$ ,  $H$ , and  $L$  parameters.  $\theta_N$  is known from the dimensions of the ball bearing in the image. The following three figures show the measured intensities and the fitted

model. The model fit is generally very good. The error is greatest near the peak intensity.

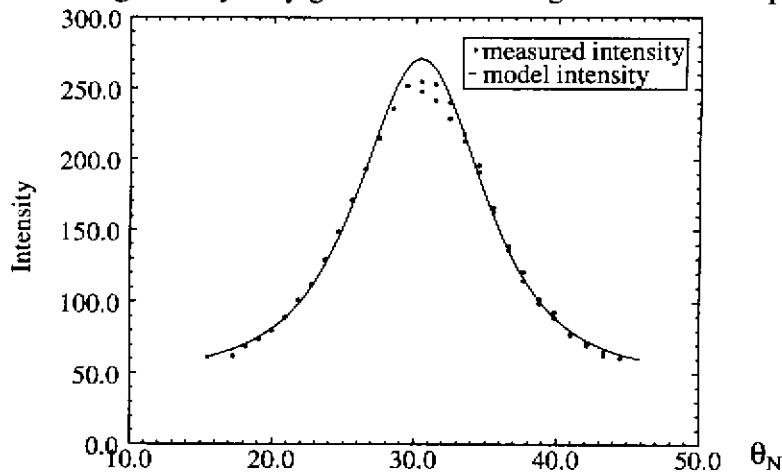


Fig. 4-26. Measured and model intensity for S1.  $R=8$ ,  $\theta_{SGC}=60.8$ ,  $\phi_{SGC}=0$ ,  $H=2.2$ ,  $L=1047.1$

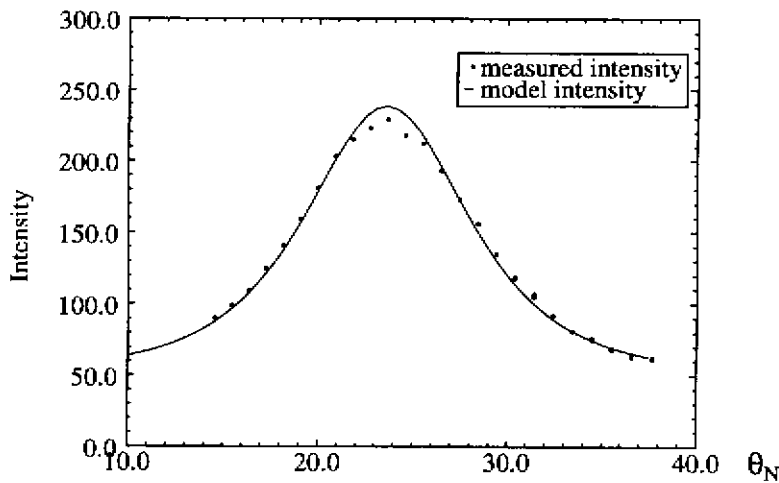


Fig. 4-27. Measured and model intensity for S2.  $R=8$ ,  $\theta_{SGC}=47.2$ ,  $\phi_{SGC}=0$ ,  $H=2.2$ ,  $L=888.5$

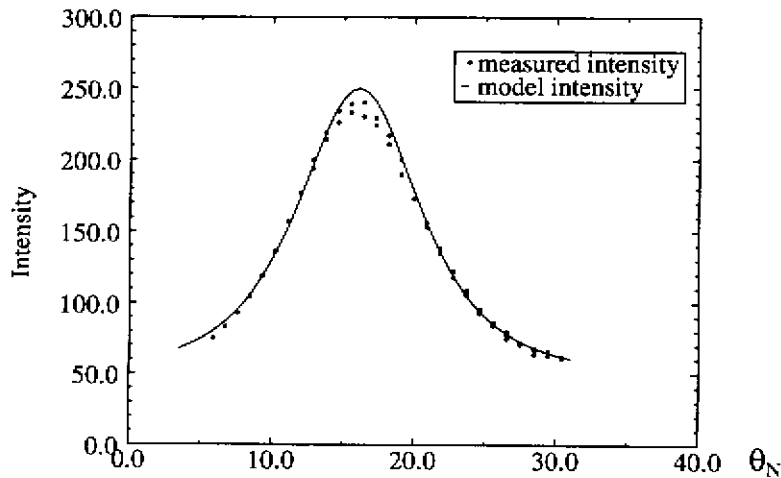


Fig. 4-28. Measured and model intensity for S3.  $R=8$ ,  $\theta_{SGC}=32.1$ ,  $\phi_{SGC}=0$ ,  $H=2.2$ ,  $L=943.7$

### 4.5.2 Polished Aluminum Plate

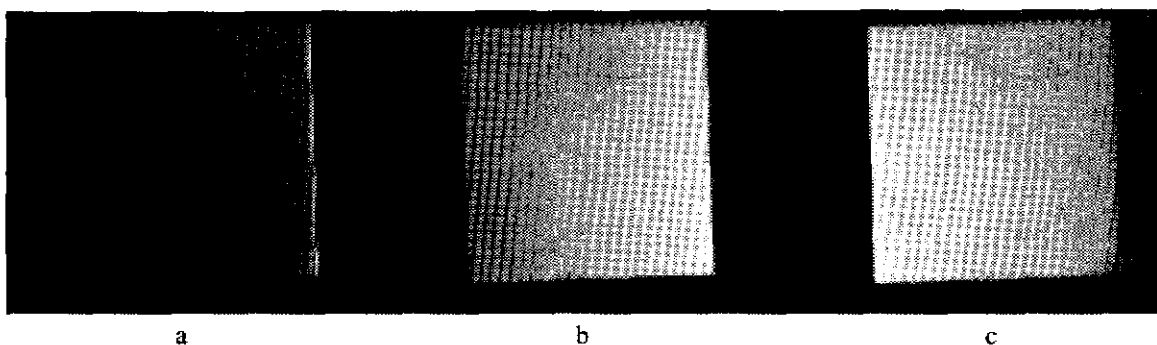


Fig. 4-29. Images of plate. a) S1. b) S2. c) S3

The first experiment was the illumination of a polished aluminum plate. Our sample measured 0.5" X 0.5", and we mounted it so that  $\theta_N=19.6^\circ$ . The area of the plate subtends an angle of approximately  $3.6^\circ$  with respect to the camera lens, which is approximately 8" away. This causes the specular point on the extended light source to vary over the surface of the plate, producing an intensity gradient across the plate. In addition, due to polishing, the regions near the corners were not flat. In order to reduce these effects, we used only the central 50% of each image. So, the actual portion of the plate that we used was approximately 0.25" X 0.25". This area of the plate subtends an angle of approximately  $1.8^\circ$  with respect to the camera lens. So, we still have an intensity gradient across the plate.

Even though there was intensity gradient across the plate, the intensities at the center of the plate were close to the planner's prediction's, for all three light sources. The least sensitive plans produced results that were very close to the planner's predictions. The most sensitive plans were more sensitive to the intensity gradient across the plate. These results varied across the plate. At the center of the plate, where the intensities were close to the planner's predictions, the orientation errors were close to the planner's predictions.

We averaged a 10X10 pixel region at the center of each image. The averages were within 3.5% of the planner predictions.

	Planner	Measurement - Averaged Region
Light Source	I	$\bar{I}$
S1	23.6	22.8
S2	114.5	118.1
S3	133.2	131.4

The gradient across each surface depends on the slope of the intensity function near the nominal specular point. It also depends on the precise orientation of the plate. Nominally the plate, which is 3 dimensional, is aligned with the X/Y axes of the light source/camera sys-

tem. However, the intensity profiles indicate that the plate was in fact slightly misaligned.

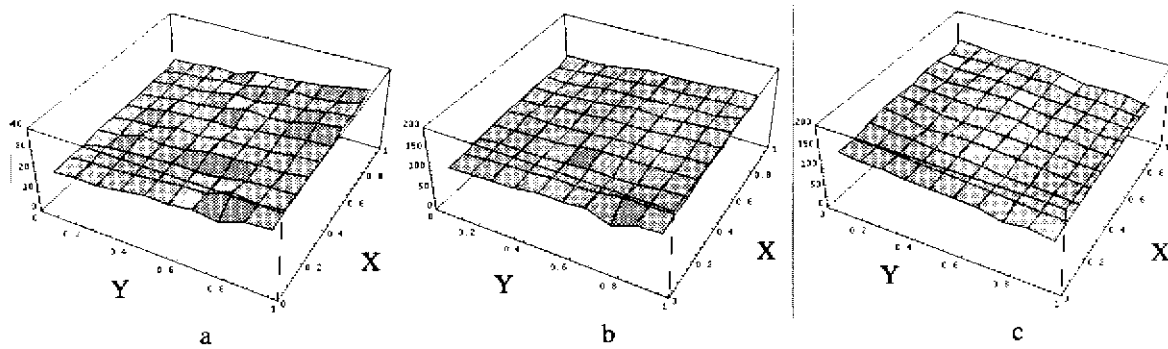


Fig. 4-30. Intensity surfaces. a) S1. b) S2. c) S3

The deviation between the planner's prediction of error and the measured error is due to the difference between the planner's intensity prediction and the measured intensity. Also, as the plan sensitivity increases, this deviation in intensity prediction will cause the discrepancy between the planner's error prediction and the measurement to increase. As expected, the predictions of the least sensitive plan are closest to the measurements. The predictions of the most sensitive plan are farthest from the planner measurements.

Light Sources	Planner $\sigma(\theta_{err})$ - Degrees	Measurement $\sigma(\theta_{err})$ - Degrees
S1, S2	0.19	0.19
S1, S3	0.46	0.56
S2, S3	3.19	4.18

The least sensitive plan used S2 and S3. This surface is flat. As the planner's sensitivity increases, the tilt of the error surface increases.

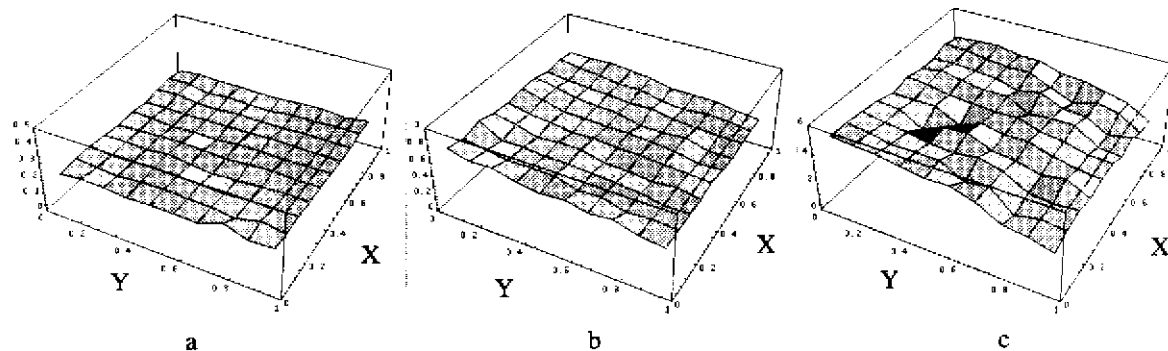


Fig. 4-31. Error surfaces. a) S1, S2. b) S1, S3. c) S2, S3

### 4.5.3 Polished Aluminum Cylinder

Our second set of experiments was performed on a polished, 0.5" diameter, stainless steel cylinder. We illuminated the cylinder with the same sets of light sources that we used for the aluminum plate. The region of the cylinder that was illuminated by each light source varied.

For each combination of light sources, we used the region of the cylinder that was illuminated by both light sources, with an intensity greater than 5.0.

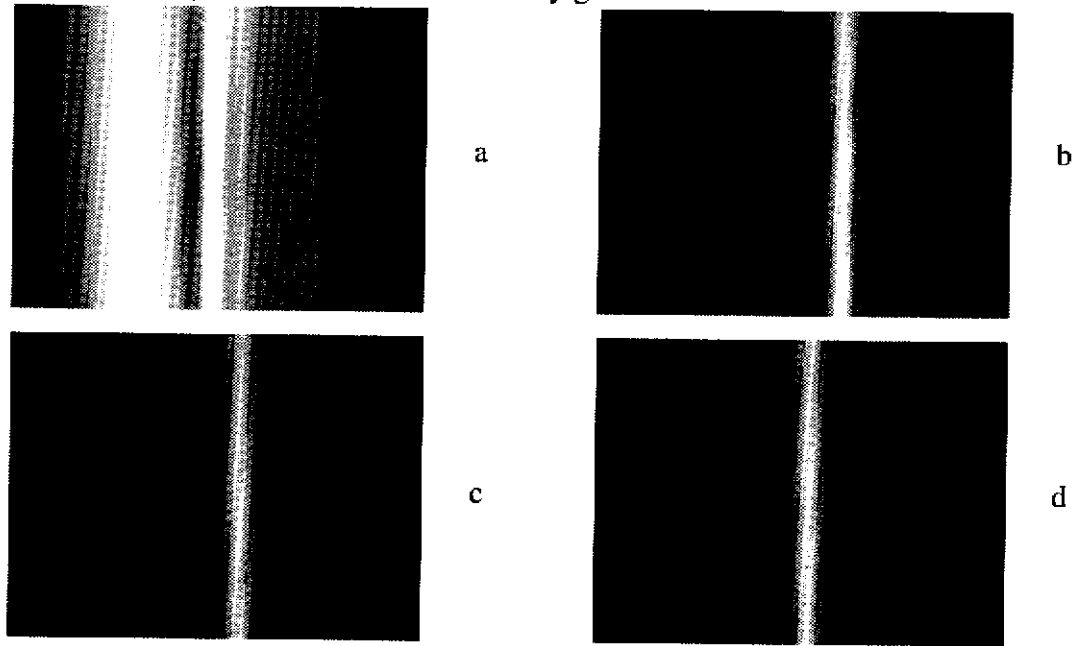


Fig. 4-32. Cylinder images. a) cylinder outline. b) S1. c) S2. d) S3

The following three figures show the planner and measured intensity surfaces for the three light sources. The intensity predictions are very close to the measurements.

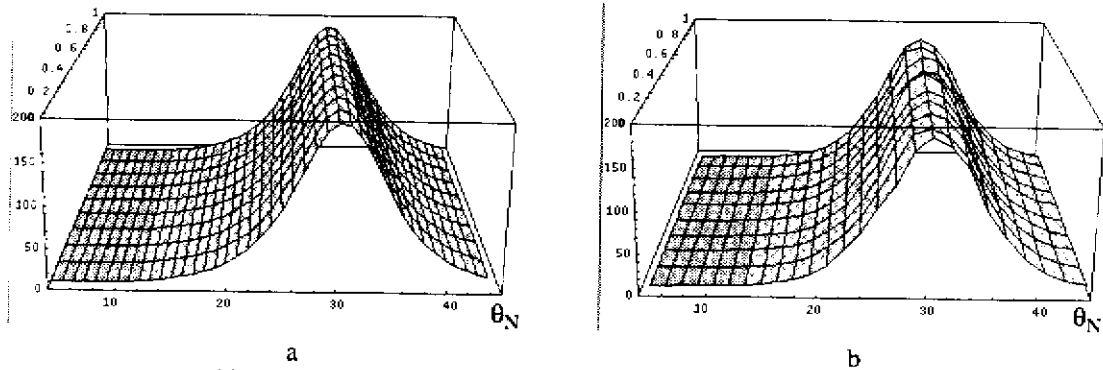


Fig. 4-33. Cylinder intensity surfaces for S1. a) plan b) measurement

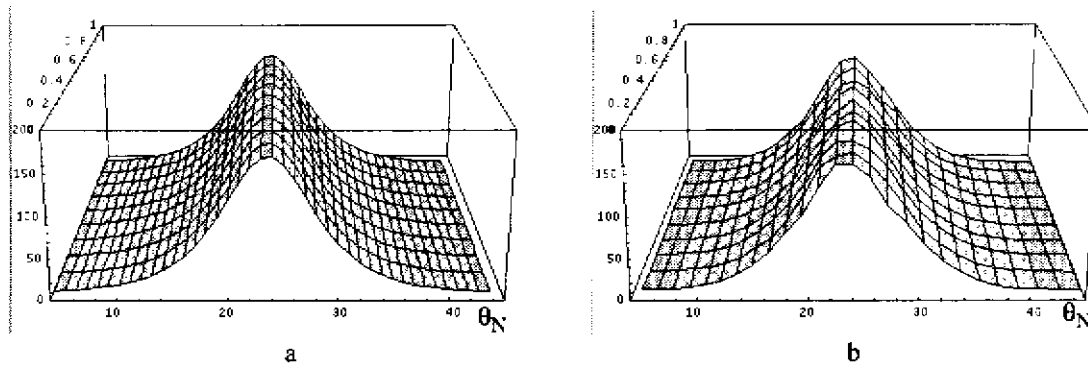


Fig. 4-34. Cylinder intensity surfaces for S2. a) plan b) measurement

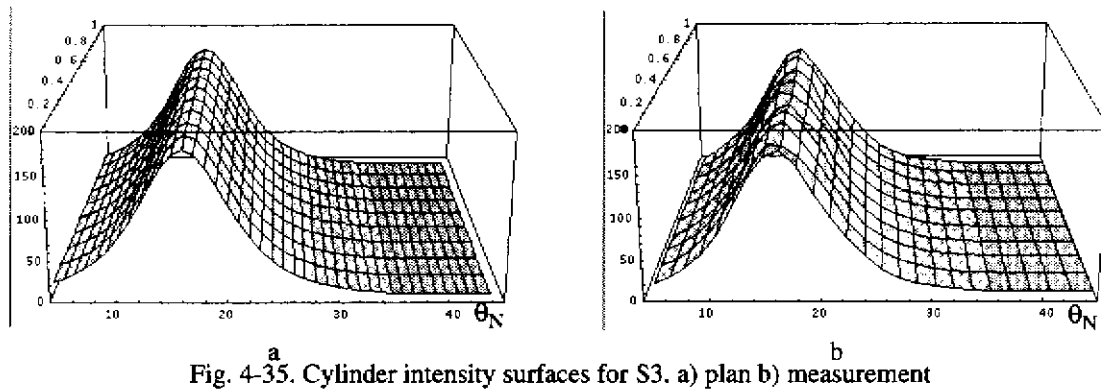


Fig. 4-35. Cylinder intensity surfaces for S3. a) plan b) measurement

The following three figures show the planner and measured error surfaces for the three combinations of light sources. The planner predictions are very close to the measurements. Around the peaks of the error surfaces, deviations between the planner and measurements are due to the sampling granularity of the measurements. In addition, this part of the error surface is produced by the minimum intensity of the extended light source's intensity distribution.

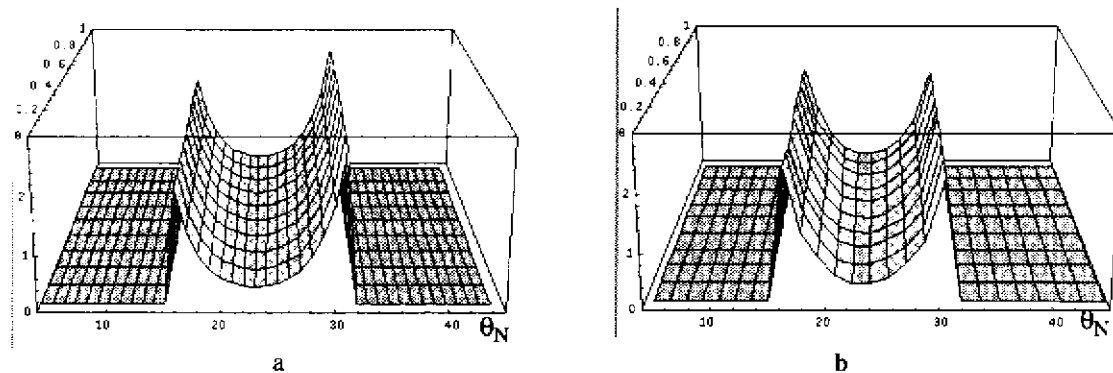


Fig. 4-36. Cylinder error surface for S1, S3. a) plan b) measurement

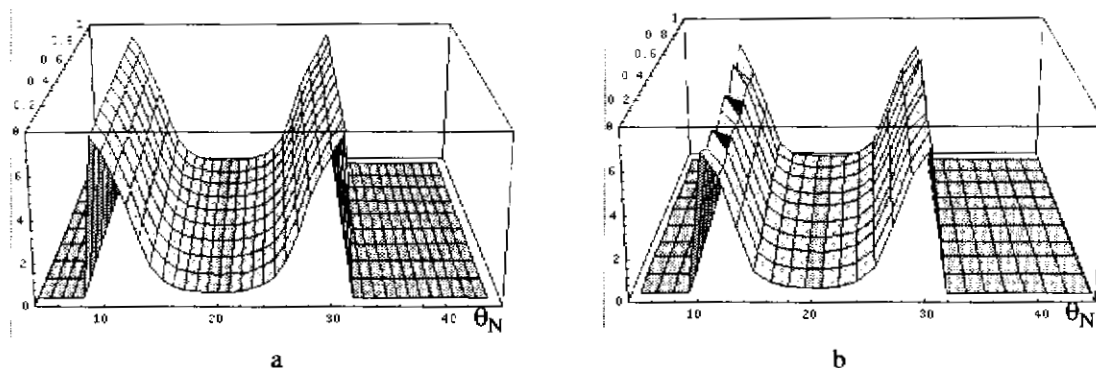


Fig. 4-37. Cylinder error surface for S2, S3. a) plan b) measurement

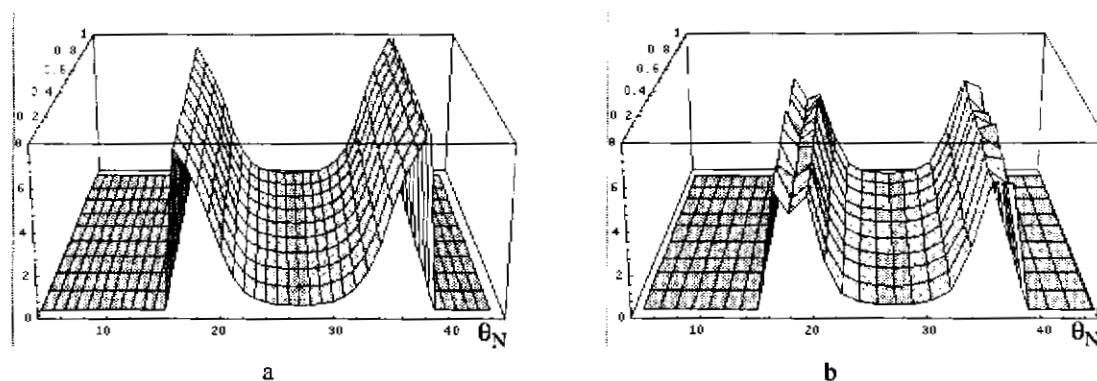


Fig. 4-38. Cylinder error surface for S1, S2. a) plan b) measurement

We plotted the mean surface orientation of the cylinder versus the nominal surface orientation. The nominal surface orientation was based upon the dimensions of the cylinder in the image. For each nominal surface orientation, there are multiple measured points. The deviation from nominal surface orientation is proportional to the error in the ratio of the measured intensities.

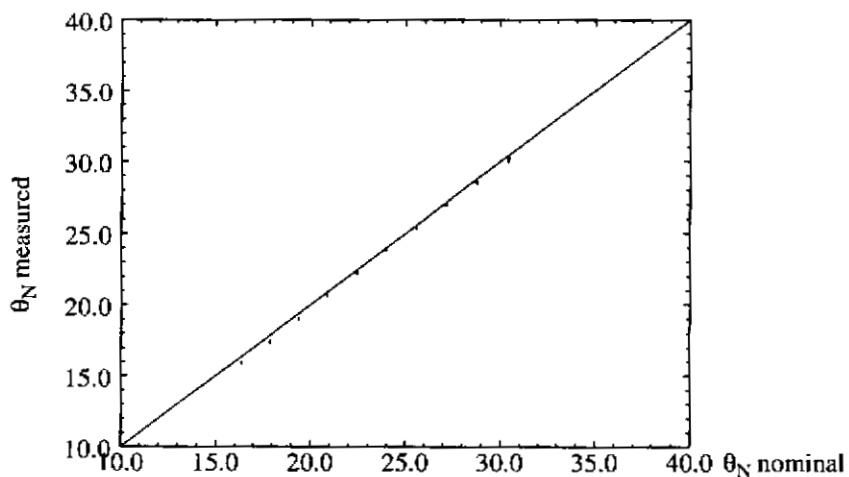


Fig. 4-39. Cylinder nominal versus measured mean surface orientation, S1, S3

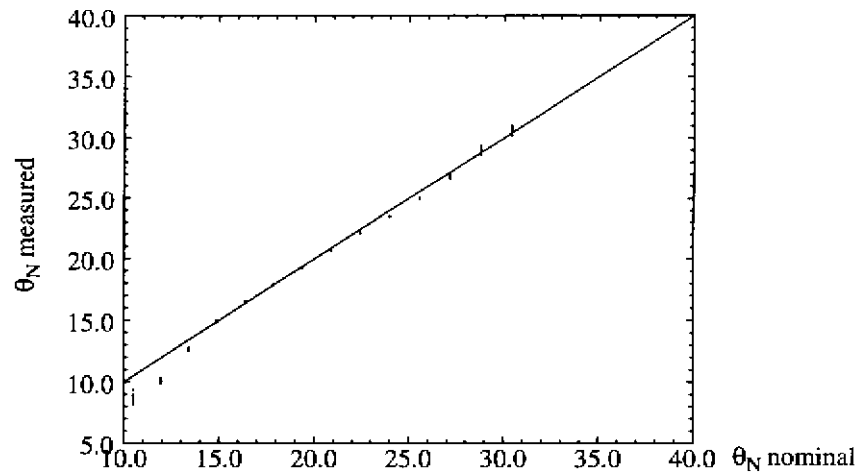


Fig. 4-40. Cylinder nominal versus measured mean surface orientation, S2, S3

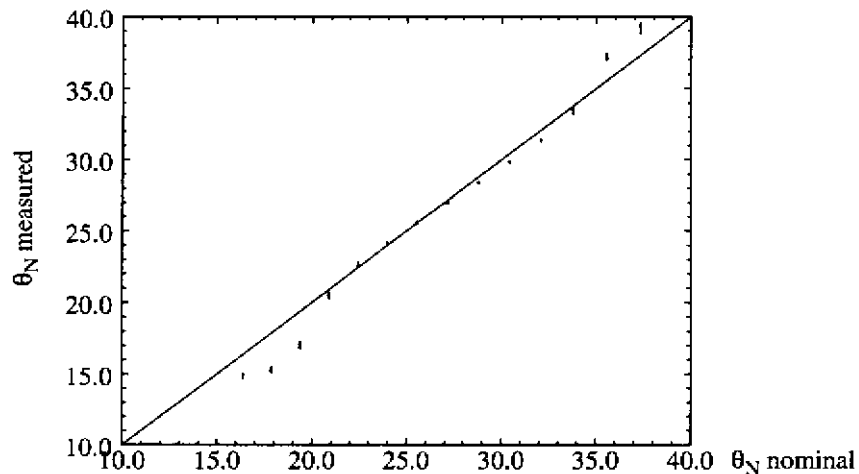


Fig. 4-41. Cylinder nominal versus measured mean surface orientation, S1, S2

## 4.6 Summary

This chapter discussed the illumination of 2D specular spike surfaces. The error surfaces for the specular spike case are very different from the lambertian and rough diffuse error surfaces. We showed that this is because of the shape of the extended light source intensity function. Our experiments validated the illumination planner. The next chapter discusses the illumination of specular lobe surfaces.

## Chapter 5

# Illumination of Specular Lobe Surfaces

### 5.1 Introduction

This chapter discusses the 2D illumination of specular lobe surfaces, surfaces that follow the lobe part of the Torrance-Spawrow model. We discuss two problems. The first problem is the determination of surface orientation, in the presence of intensity noise, when the specular parameters are known. The second problem is the determination of the specular parameters, in the presence of intensity noise, when surface orientation is known.

### 5.2 Specular Lobe Model

The Torrance-Spawrow model [Torrance 67] is a geometrical optics model of reflection for rough surfaces. The model describes reflection for surfaces that exhibit a specular lobe. (Torrance and Spawrow added a lambertian component to the specular lobe to make their model more general. We neglect the lambertian component in this chapter.)

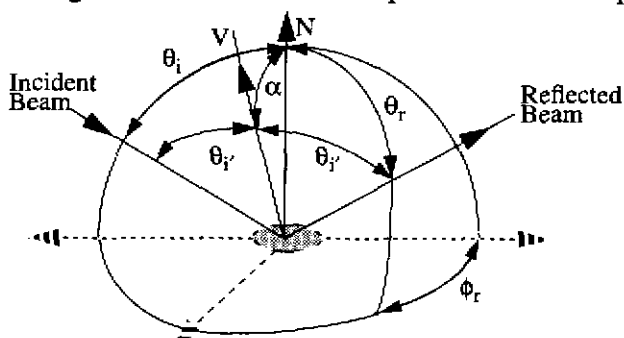


Fig. 5-1. Geometry for Torrance-Spawrow model

For a fixed incident light angle, and for a given material, the surface radiance is:

$$I = F(\theta_i', \eta') \left[ \frac{G(\theta_i', \theta_r', \phi_r)}{\cos \theta_r'} \right] \exp(-c^2 \alpha^2)$$

$F(\theta_i', \eta')$  is the Fresnel reflectance coefficient.  $(\theta_i')$  is the local angle of incidence.  $\eta'$  is the

complex index of refraction.) Since  $F$  is material dependent and can be approximated by a constant for certain ranges of illumination, we will be assuming that  $F$  is equal to unity.  $G(\theta_i, \theta_r, \phi_p)$  is the geometric attenuation factor. This accounts for masking and shadowing of one micro facet by adjacent micro facets. "c" is a constant which is proportional to surface roughness.

With some notational simplifications, our specular lobe model becomes:

$$I = B \frac{G}{\cos \theta_r} \exp(-K\alpha^2)$$

We call  $B$  the specular intensity, and  $K$  the specular sharpness.

We use the following 2D global coordinate system for specifying the position of the viewer, normal and light sources.

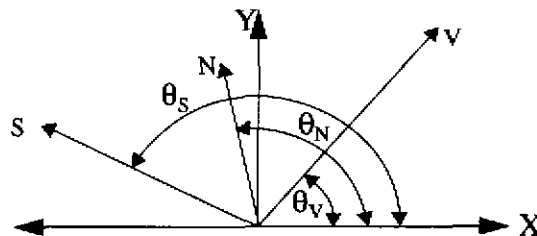


Fig. 5-2. Source/viewer frame of reference coordinate system

Below are intensity surfaces for  $B=100$ ,  $N=90$ ,  $K=10$  and  $B=100$ ,  $N=90$ ,  $K=20$ . The surfaces show intensity as a function of source direction and viewing direction. .

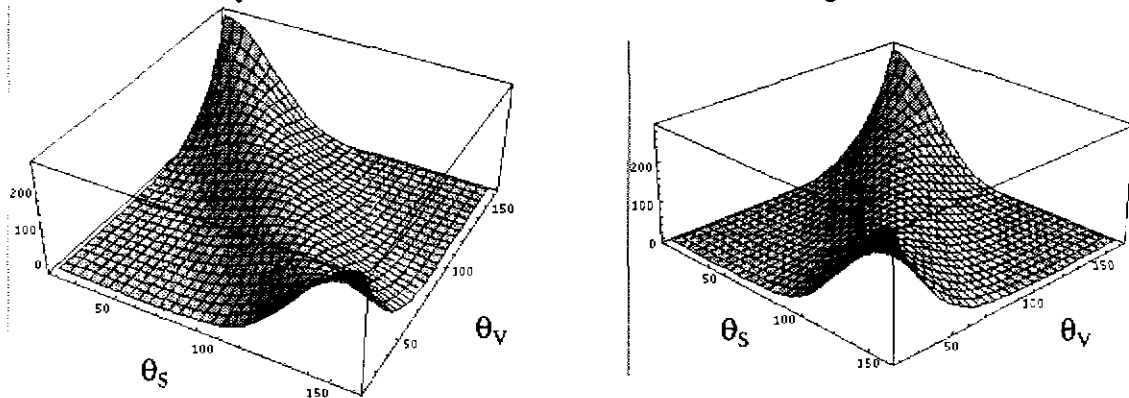


Fig. 5-3. Specular lobe intensity surface,  $K=10.0$ ,  $B=100$ ,  $N=90$ .

As  $K$  increases, the specular lobe becomes narrower.

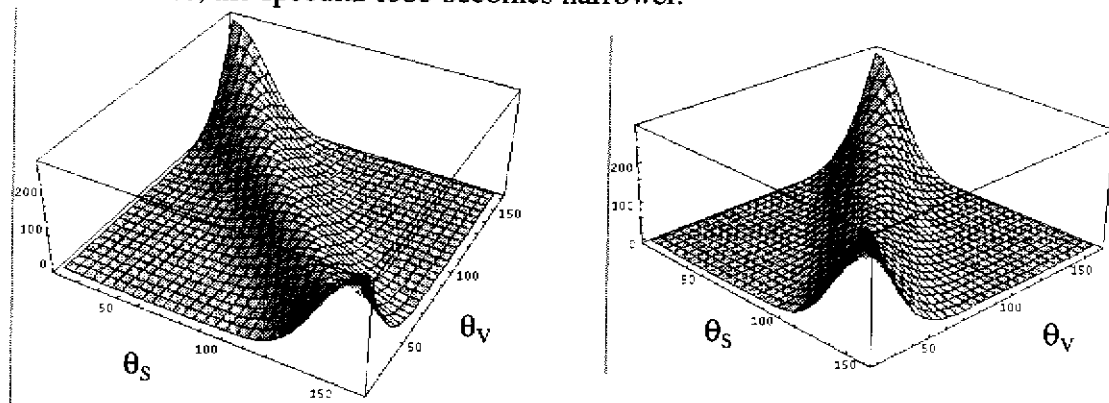


Fig. 5-4. Specular lobe intensity surface,  $K=20.0$ ,  $B=100$ ,  $N=90$ .

Below are 2D cross sections of these intensity surfaces for  $V=80^\circ$ ,  $V=50^\circ$ , and  $V=30^\circ$ .

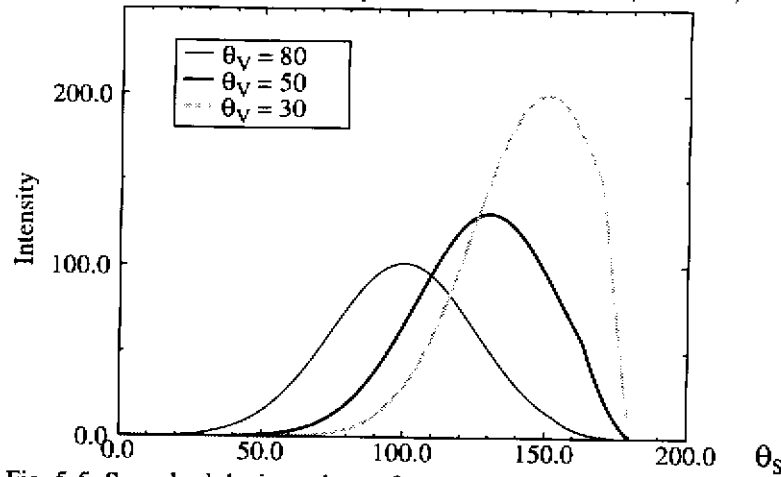


Fig. 5-5. Specular lobe intensity surface cross section,  $K=10.0$ ,  $B=100$ ,  $N=90$ .

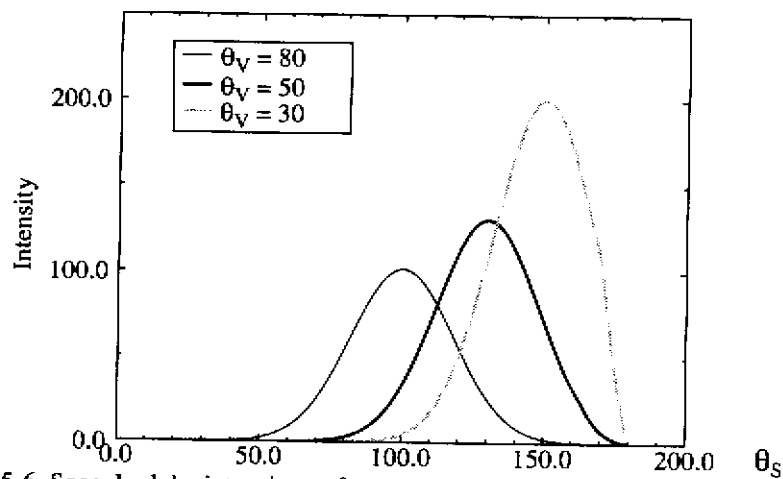


Fig. 5-6. Specular lobe intensity surface cross section,  $K=20.0$ ,  $B=100$ ,  $N=90$ .

## 5.3 Surface Orientation Calculation

In order to determine surface orientation, we need to solve a system of specular lobe equations. We can solve a system of specular lobe equations by forming a set of equations that express ratio's of intensities. The source and view directions in the world coordinate system are known. We want to solve for the normal's orientation. For our initial guess, we use the centroid of the source/view bisectors for the two light sources.

$$\begin{aligned}
 I_1 &= f(\theta_{S1}, \phi_{S1}, \theta_N, \phi_N, \theta_V, \phi_V) \\
 I_2 &= f(\theta_{S2}, \phi_{S2}, \theta_N, \phi_N, \theta_V, \phi_V) \\
 F_1 &= I_1 f(\theta_{S2}, \phi_{S2}, \theta_N, \phi_N, \theta_V, \phi_V) - I_2 f(\theta_{S1}, \phi_{S1}, \theta_N, \phi_N, \theta_V, \phi_V) = 0
 \end{aligned}$$

The system is solved, iteratively, using the Newton-Raphson method.

$$\begin{aligned}
 -F_1 &= \frac{\partial F_1}{\partial \theta_N} \delta \theta_N \\
 \theta_{N+1} &= \theta_N + \delta \theta_N
 \end{aligned}$$

$\theta_N$  is positive. If  $\theta_N$  becomes negative, we add  $\pi$  to  $\phi_N$  and make  $\theta_N$  positive. We keep  $\phi_N$  between  $-2*\pi$  and  $2*\pi$ .

## 5.4 2D Specular Lobe Error Surfaces

We performed 2D simulations to determine the sensitivity of specular lobe surface orientation to intensity noise. For the simulations that follow our 2D normal is located at  $N=90^\circ$ . We move two light sources between  $0^\circ$  and  $180^\circ$ . At each light source combination, we calculate the nominal intensity of the normal for both light sources. Then we create a noisy intensity using our intensity noise function for both light sources. We calculate  $N$  using the two noisy intensity values. We repeat this 1000 times and calculate the standard deviation of the angular orientation error. Our total error is equal to three sigma. We include source positions that produce an intensity greater than 5. For source positions with an intensity less than 5, we set the error to zero, for plotting purposes.

The shape of the angular orientation error surface is related to the magnitude of the derivative of the specular lobe intensity function. We calculated the derivative by calculating the change in intensity for a small change in surface orientation ( $d\theta_N = 0.0001$  radians).

First, we look at error surfaces for a specular lobe having  $K=10$  and  $B=100$ . We consider three viewing directions,  $30^\circ$ ,  $50^\circ$ , and  $80^\circ$ .  $N=90^\circ$  in all cases. The  $|\partial \theta_N / \partial I|$  function shows that the derivative will be great when we are at the center of the specular lobe. The derivative quickly decreases to a minimum, and then steadily increases as we move away from the specular lobe peak. The magnitude of the central derivative peak is not significant since the derivative becomes unbounded at this point. The derivative for  $V=30^\circ$  has a minimum at

$\theta_s=124.5^\circ$ , and it is equal to 0.0018. A near minimum occurs near  $\theta_s=170$ .

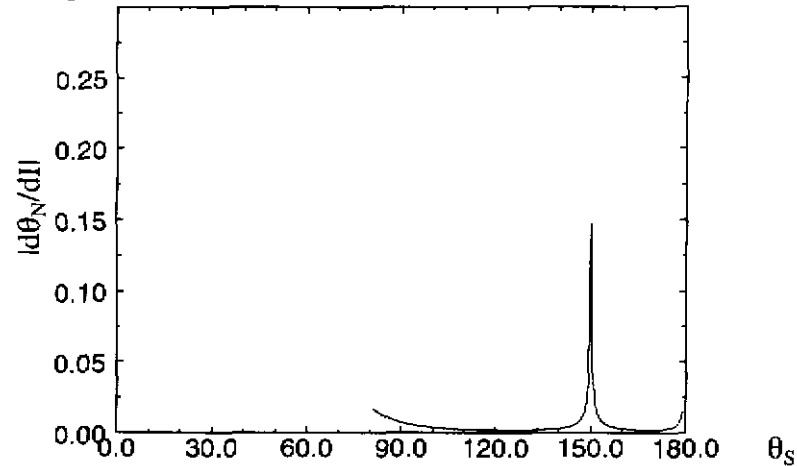


Fig. 5-7. |Derivative of specular lobe intensity,  $K=10$ ,  $B=100$ ,  $V=30$ ,  $N=90$ .

The error surface for  $K=10$ ,  $B=100$ , and  $V=30$  has a minimum at  $S1=170$  and  $S2=125$ , and is equal to 0.50. This location of the minimum corresponds well with the location of the minima in the intensity derivative function.

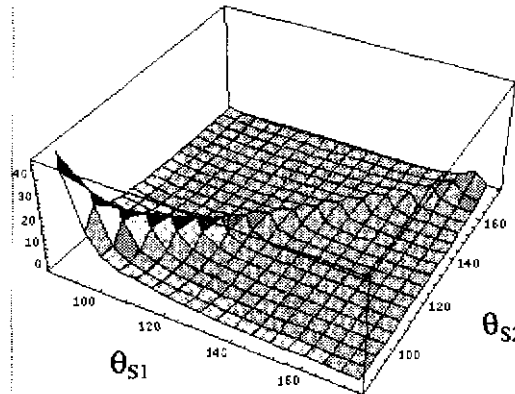


Fig. 5-8. Specular lobe error surface,  $K=10$ ,  $B=100$ ,  $V=30$ ,  $N=90$ .

We do not see a peak in the error surface corresponding to the central derivative peak of the  $|d\theta_N/dI|$  function. The central derivative peak occurs at the singularity of the intensity profile,  $\theta_s=150^\circ$ . The derivative quickly decreases as  $\theta_s$  increases. If we look at the intensity function around  $\theta_s=150^\circ$ , we can see that for finite amounts of the intensity noise, the angular change in  $\theta_N$  will not be anywhere near as large as the  $|d\theta_N/dI|$  function indicates. In addition, the intensity is greatest near  $\theta_s=150^\circ$ . This makes the signal to noise ratio the greatest, decreasing the effect of the derivative. With these factors in mind, we see that the singularity ridge is approximately flat near  $\theta_s=150^\circ$ .

We examine a cross section of the error surface for a light source at  $\theta_{S1}=150$ . (This is the specular angle for  $V=30$ .) We see more clearly that the error increases as the light source moves away from the specular angle. The cross section is in good agreement with the deriv-

ative curve. The cross section has a minimum at  $\theta_{S1}=120$  and is equal to 0.764.

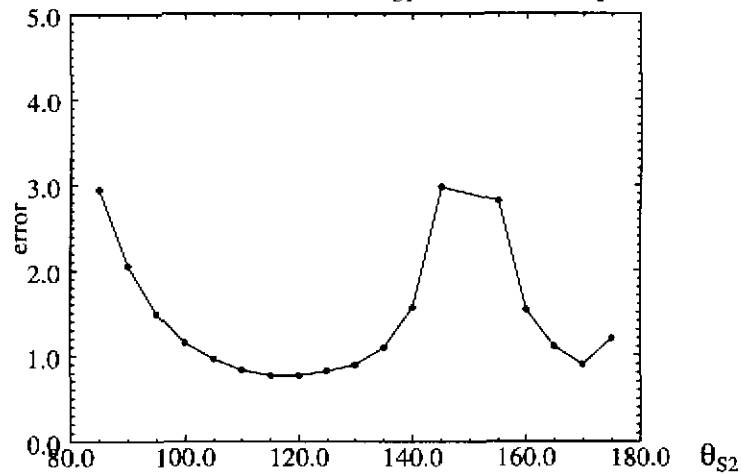


Fig. 5-9. Specular lobe error surface cross section,  $S1=150$ ,  $K=10$ ,  $B=100$ ,  $V=30$ ,  $N=90$ .

Next, we look at the error surface for  $K=10$ ,  $B=100$ , and  $V=50$ . The  $Id\theta_N/dII$  function has minima at  $\theta_S=104.5$  and  $\theta_S=155.5$ . At both minima, the derivative is equal to 0.0028. This is 53% greater than the  $V=30$  case.

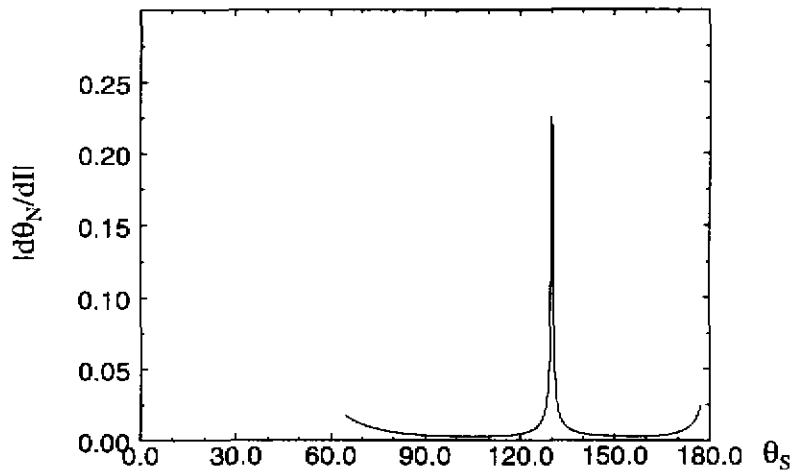


Fig. 5-10. Derivative of specular lobe intensity,  $K=10$ ,  $B=100$ ,  $V=50$ ,  $N=90$ .

The error surface for  $B=100$ ,  $K=10$ , and  $V=50$ , has a minimum at  $\theta_{S1}=160$  and  $\theta_{S2}=105$ , and is equal to 0.6912. This location of the minimum corresponds well with the location of the minima in the intensity derivative function. The error is approximately 38% greater than the

V=30 case.

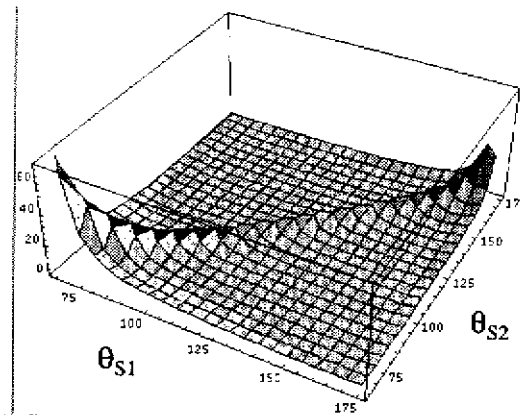


Fig. 5-11. Specular lobe error surface, K=10, B=100, V=50, N=90.

The error surface cross section is for a light source at  $\theta_{S1}=130$ . (This is the specular angle for V=50.) The minimum, which occur at  $\theta_{S2}=95.0$  and at  $\theta_{S2}=160.0$ , are equal to 1.14, which is 49% greater than the V=30 case.

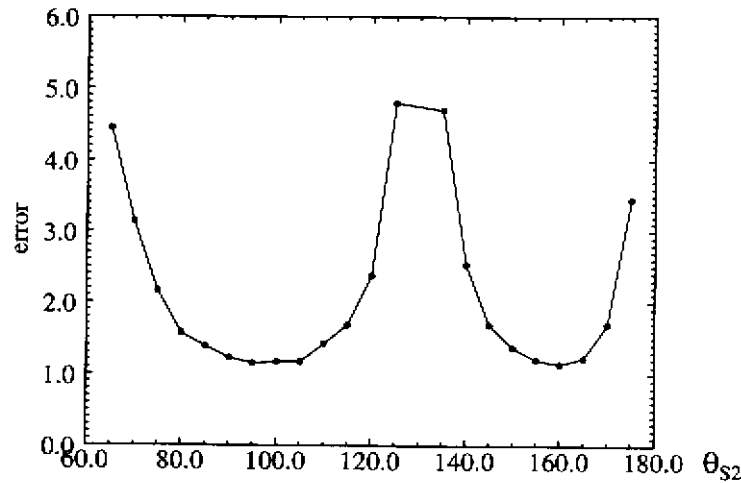


Fig. 5-12. Specular lobe error surface cross section, S1= 130, K=10, B=100, V=50, N=90

Next, we examine K=10, B=100, and V=80. The  $|d\theta_N/dI|$  function has minima at  $\theta_S=126.0$

and  $\theta_s=74.0$ . The minima are equal to 0.0036, which is 97% greater than the  $V=30$  case.

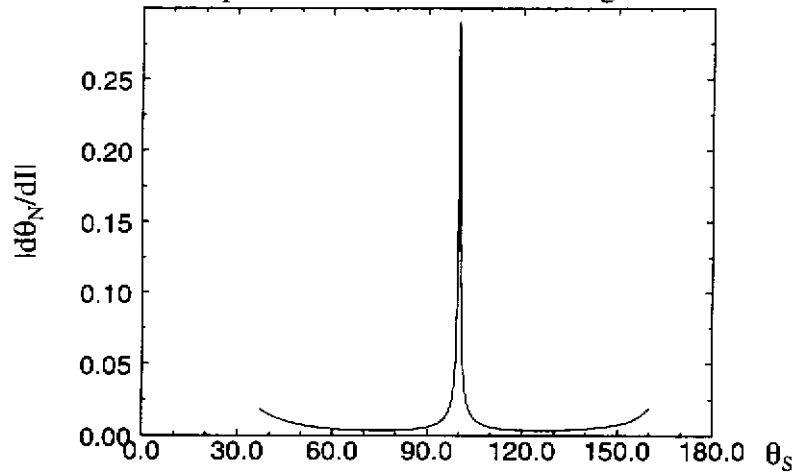


Fig. 5-13. |Derivative of specular lobe intensity,  $K=10$ ,  $B=100$ ,  $V=80$ ,  $N=90$ .

The error surface has a minimum at  $\theta_{s1}=130$  and  $\theta_{s2}=70$ . It is equal to 0.844, which is 69% greater than the  $V=30$  case. This location of the minimum corresponds well with the location of the minima in the intensity derivative function.

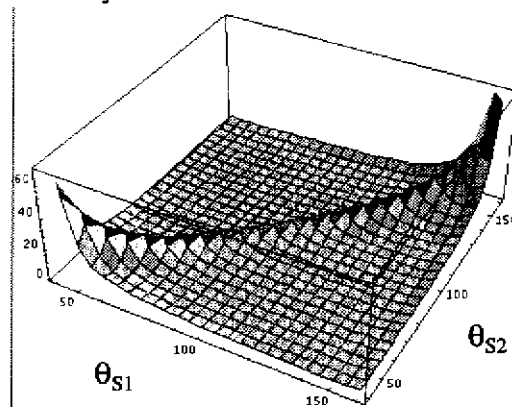


Fig. 5-14. Specular lobe error surface,  $K=10$ ,  $B=100$ ,  $V=80$ ,  $N=90$ .

The error surface cross section is for a light source at  $\theta_{s1}=100.0$ . (This is the specular angle for  $V=80$ .) It has a minimum at  $\theta_{s2}=70.0$  which is equal to 1.348. This is 76% greater than

the  $V=30$  case. A near minimum occurs at  $\theta_{S2}=135.0$ , and is equal to 1.401.

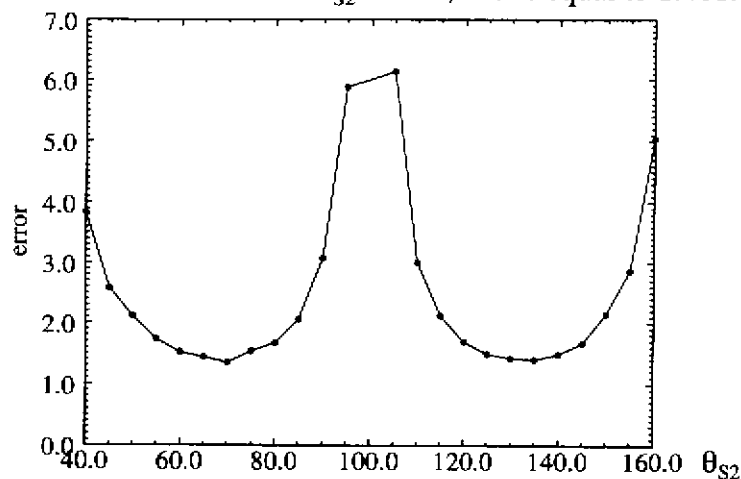


Fig. 5-15. Specular lobe error surface cross section,  $S1=100$ ,  $K=10$ ,  $B=100$ ,  $V=80$ ,  $N=90$

The error surfaces show that as the extant angle decreases, the minimum error increases. This is because the steepness of the sides of the intensity function, where the minimum error occurs, decreases. This increases the minimum of the  $|d\theta_N/dI|$  function.

Next, we look at the  $K=20.0$  case. The first case we look at is for  $K=20$ ,  $B=100$ , and  $V=30$ . The  $|d\theta_N/dI|$  function has minima at  $\theta_S=132.0$  and  $\theta_S=168.0$ . The minima are equal to 0.0013.

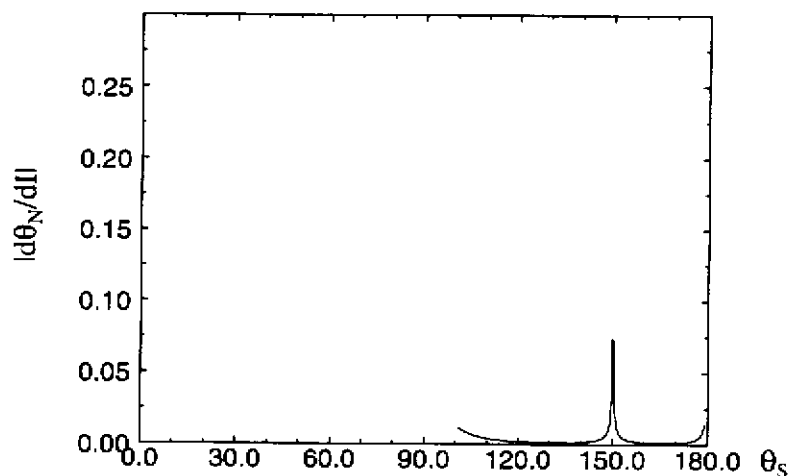


Fig. 5-16. Derivative of specular lobe intensity,  $K=20$ ,  $B=100$ ,  $V=30$ ,  $N=90$ .

The error surface has a minimum at  $\theta_{S1}=130$  and  $\theta_{S2}=170$ . The minimum is equal to 0.345. This location of the minimum corresponds well with the location of the minima in the inten-

sity derivative function

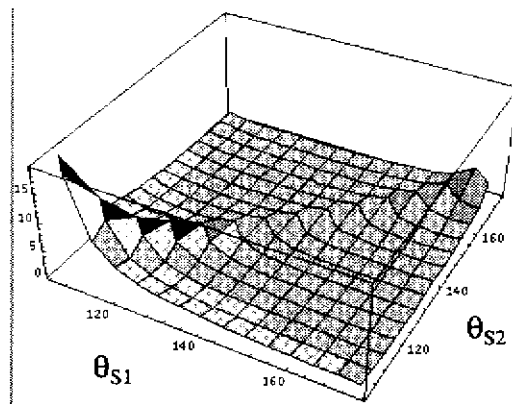


Fig. 5-17. Specular lobe error surface,  $K=20$ ,  $B=100$ ,  $V=30$ ,  $N=90$ .

The cross section is for a light source at  $\theta_{S1}=150$ . (This is the specular angle for  $V=30$ .) It has a minimum at  $\theta_{S2}=130$ , and is equal to 0.538. A near minimum occurs at  $\theta_{S2}=170.0$  and is equal to 0.549.

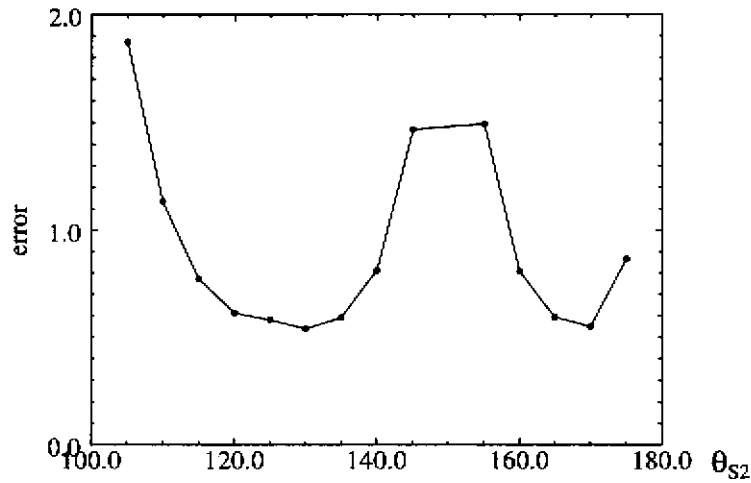


Fig. 5-18. Specular lobe error surface cross section,  $S1=150$ ,  $K=20$ ,  $B=100$ ,  $V=30$ ,  $N=90$

Next, we look at the case where  $K=20$ ,  $B=100$ , and  $V=50$ . The  $|\partial\theta_N/\partial I|$  function has minima at  $\theta_S=112.0$  and  $\theta_S=148.0$ . Both minima are equal to 0.002, which is 53% greater than the

V=30 case.

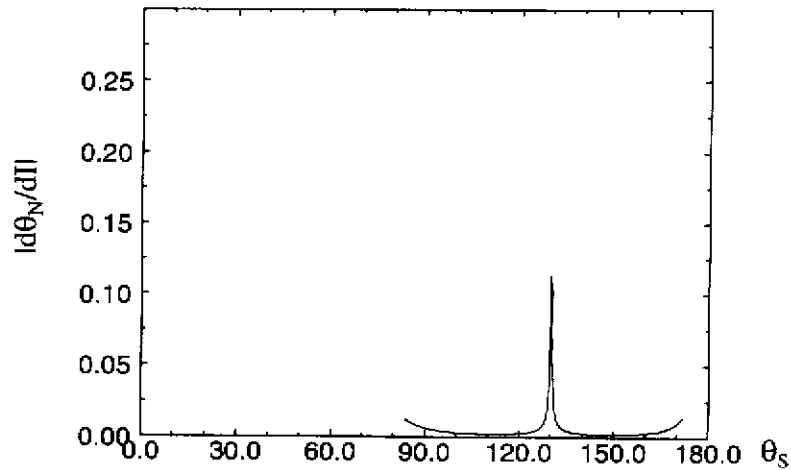


Fig. 5-19. |Derivative of specular lobe intensity,  $K=20$ ,  $B=100$ ,  $V=50$ ,  $N=90$ .

The error surface has a minimum at  $\theta_{S1}=110$  and  $\theta_{S2}=150$ . The minimum is equal to 0.48, which is 39% greater than the  $V=30$  case. This location of the minimum corresponds well with the location of the minima in the intensity derivative function.

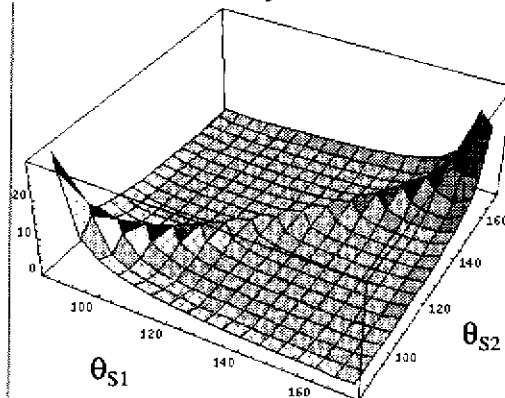


Fig. 5-20. Specular lobe error surface,  $K=20$ ,  $B=100$ ,  $V=50$ ,  $N=90$ .

The error surface cross section is for a light source at  $\theta_{S1}=130$ . (This is the specular angle for  $V=50$ .) The minimum occurs at  $\theta_{S2}=105.0$  and is equal to 0.777, which is 44% greater

than the  $V=30$  case. A near minimum occurs at  $\theta_{S2}=150.0$  and is equal to 0.812.

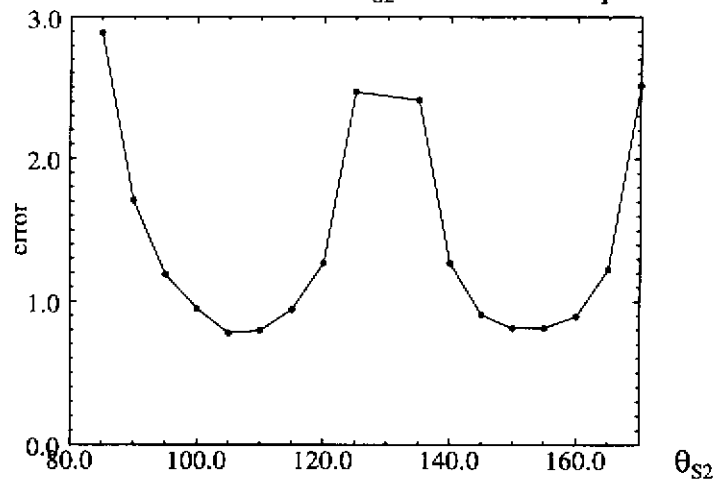


Fig. 5-21. Specular lobe error surface cross section,  $S1=130$ ,  $K=20$ ,  $B=100$ ,  $V=50$ ,  $N=90$

The last case we look at is for  $K=20$ ,  $B=100$ , and  $V=80$ . The  $Id\theta_N/dI$  function has minima at  $\theta_S=82.0$  and  $\theta_S=118.0$ . Both minima are equal to 0.0026, which is 97% greater than the  $V=30$  case.

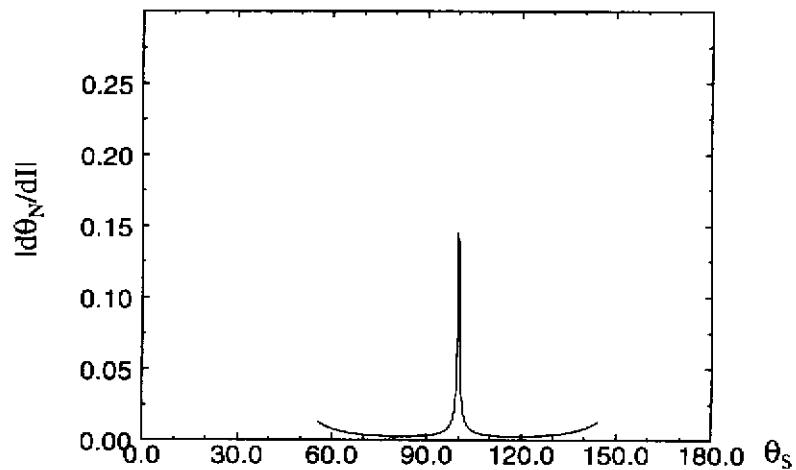


Fig. 5-22. Derivative of specular lobe intensity,  $K=20$ ,  $B=100$ ,  $V=80$ ,  $N=90$ .

The error surface has a minimum at  $\theta_{S1}=120$  and  $\theta_{S2}=80$ . The minimum is equal to 0.590, which is 71% greater than the  $V=30$  case. This location of the minimum corresponds well

with the location of the minima in the intensity derivative function

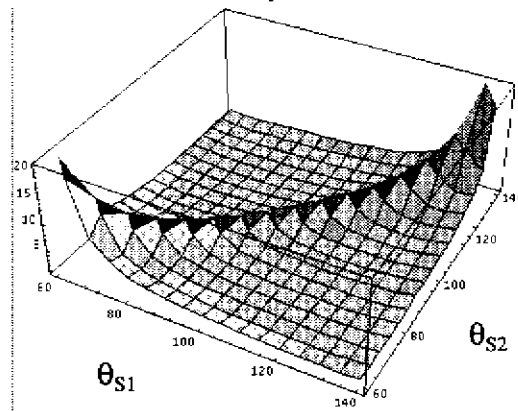


Fig. 5-23. Specular lobe error surface,  $K=20$ ,  $B=100$ ,  $V=80$ ,  $N=90$ .

The error surface cross section is for a light source at  $\theta_{S1}=100.0$ . (This is the specular angle for  $V=80$ .) The minimum occurs at  $\theta_{S2}=75.0$ . It is equal to 0.967, which is 80% greater than the  $V=30$  case. A near minimum occurs at  $\theta_{S2}=125.0$ , and is equal to 0.971.

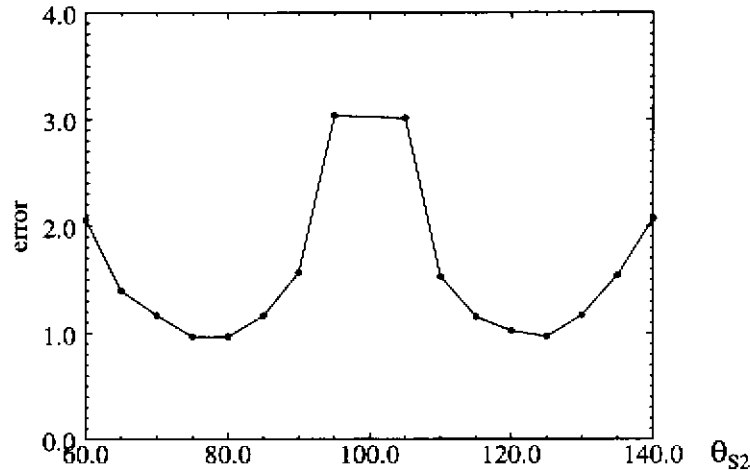


Fig. 5-24. Specular lobe error surface cross section,  $S1=100$ ,  $K=20$ ,  $B=100$ ,  $V=80$ ,  $N=90$

The error surfaces show that as  $K$  becomes greater, the minimum error decreases. This is because the steepness of the sides of the intensity function, where the minimum error occurs, increases with  $K$ . This decreases the minimum of the  $|\partial\theta_N/\partial I|$  function.

## 5.5 Estimation of $B$ and $K$

Next, we examine the problem where we know 2D surface orientation, we would like to recover the specular intensity,  $B$ , and the specular sharpness,  $K$ . We try to estimate  $B$  and  $K$  using only two intensity measurements. If we take more measurements, our estimation of  $B$  and  $K$  will become more robust. However, two measurements is the minimum number required, and this problem formulation allows us to visualize how our parameter estimation varies as a function of light source positions. We try to maximize parameter estimation with respect to intensity noise.

In order to develop an intuition for what the sensitivity of the specular lobe parameter estimation is with respect to intensity noise, we will make some further simplifications to our model for this introductory example. We will assume that  $G$  is equivalent to unity and that the viewing direction is fixed. With these simplifications our model becomes:

$$I = B' \exp(-K\alpha^2)$$

If we let  $B' = 100$  and  $K = .01$ , we get these plots for  $I$  and  $dK/dI$ .

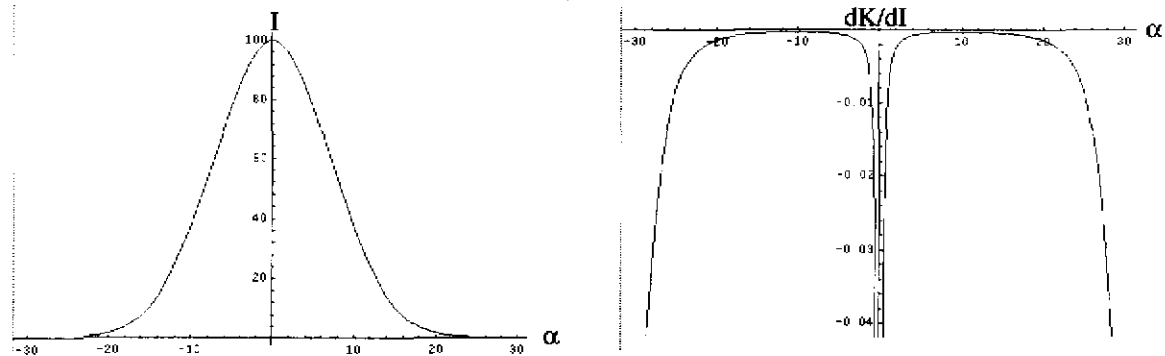


Fig. 5-25. Intensity Plot ( $B'=100$ ,  $K=0.01$ ) and  $dK/dI$  plot

We see that our estimate of  $K$  is very bad if we are very close to peak or near the tails. This makes intuitive sense. We can't estimate the width of the gaussian from just the peak value. There can be many gaussian distributions going through the same peak. The same can be said about the tails. In order to estimate the width of the function we need data along the sides. The minimum error would occur when  $1/K = \alpha^2$ .

We can analytically express  $dB/dI$

$$\frac{dB}{dI} = \frac{1}{\exp(-K\alpha^2)}$$

This has a minimum when  $\alpha = 0$ , when we are at the peak. This also makes intuitive sense. If we want to estimate the magnitude of the gaussian, we need to measure at the peak.

From this simple example, we can expect that our estimate of  $B$  will be best when at least one of our light sources is near the peak intensity. Our estimate of  $K$  will be best when at least one of our light sources is along the side of the intensity distribution. We will see that having both light sources on the sides does not constrain the solution as well as having one light source near the peak and one light source along the side. This is because the extracted value of  $K$  is dependent on both the height and width of the distribution.

## 5.6 2D B and K Error Surfaces

We performed a series of 2D simulations using our intensity noise function to see how the estimate of  $B$  and  $K$  varied as function of light source position. We solved for  $B$  and  $K$  using the Levenberg-Marquardt [Press 90] method.

For the simulations that follow our 2D normal is at  $90^\circ$ . We move two light sources between  $0^\circ$  and  $180^\circ$ . At each light source combination, we calculate the nominal intensity of the normal for both light sources. Then we create a noisy intensity using our intensity noise function for both light sources. We estimate  $B$  and  $K$  using the two noisy intensity values. We repeat this 200 times and calculate the mean error in the estimate of  $B$  and  $K$ . We include source positions that produce an intensity greater than 10. For source positions with an intensity less than 10, we set the error to zero, for plotting purposes.

We note that with two points, the fit is not very stable, especially in places where the light sources are close together, and the system is close to singularity. At these places the system is not well conditioned, and noise can cause large changes in our parameter estimates. So, the variance of the parameter estimates are large. This variance is less when the system is well conditioned, and is greater when the system is ill conditioned. Of course, the fit will become more stable as more light sources are used to make the estimation.

First we look at surfaces for  $K = 10$ ,  $B=100$ , and  $V=80$ . The  $B$  error surface has a minimum when at least one light source is close to the peak. When the light sources are close together ( $S1 = S2$ ), the error becomes large. This is one of the spines of the error surface. The second spine of the error surface occurs when  $\alpha$  is the same for both light sources. This produces a singular system because the intensity of the normal will be the same for both light sources, even though they are at different locations. The location of the viewer will determine the specular angle and will therefore determine when this condition will occur. Different viewing directions will cause a displacement of the second spine, while the  $S1 = S2$  spine will always be stationary. The minimum error occurs when  $S1 = 100^\circ$  and  $S2 = 110^\circ$ , and is equal to 1.06. (In the  $B$  and  $K$  error surfaces plots that follow, each figure contains two plots of the same surface using different scale factors for the Z axis.)

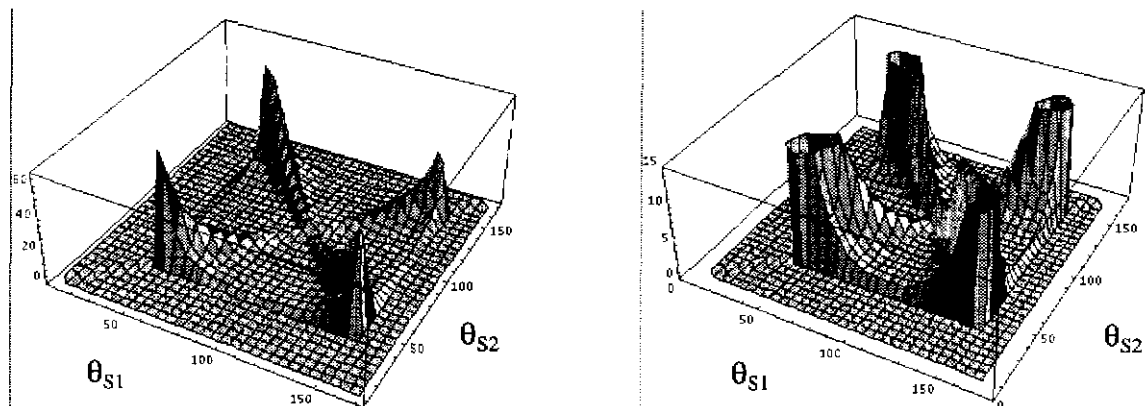


Fig. 5-26.  $B$  error surface.  $B=100$ ,  $K=10$ ,  $V=80^\circ$ ,  $N=90^\circ$ ,  $K_0=15$ ,  $B_0=110$ .

The  $K$  error surface has a minimum when the one light source is near the peak of the intensity function and one light source is along the side of the intensity function. This is because the extracted value of  $K$  is dependent on both the height and width of the distribution. Again we see the two spines for  $S1 = S2$  and when  $\alpha$  is the same for both light sources. The

minimum error occurs when  $S1 = 60^\circ$  and  $S2 = 100^\circ$ , and is equal to .26.

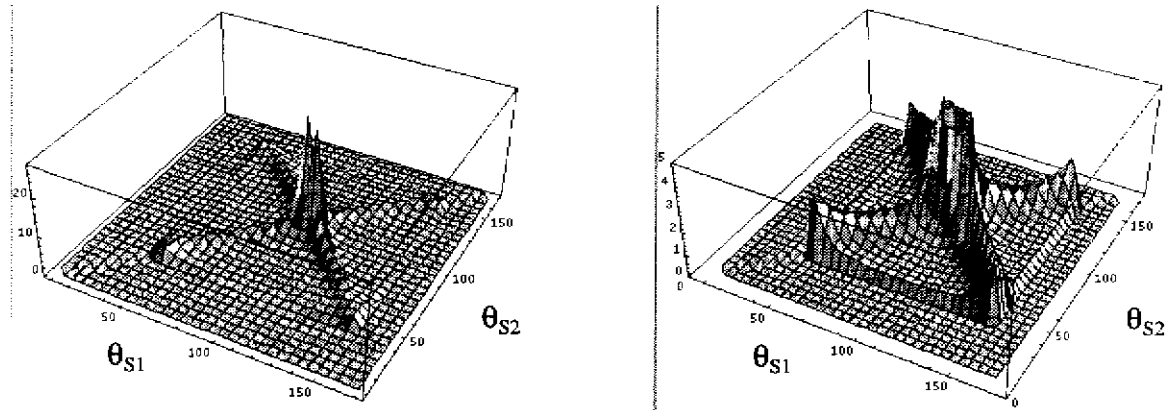


Fig. 5-27. K error surface.  $B=100, K=10, V=80^\circ, N=90^\circ, K_0=15, B_0=110$ .

Changing the starting point of the fitting process does not alter the surface appreciably. The first two error surfaces had starting points of  $K_0 = 15, B_0 = 110$ . We change the starting point to  $K_0 = 20, B_0 = 80$ . The minimum error of the B error surface occurs at  $S1 = 100^\circ$  and  $S2 = 110^\circ$ , and is equal to 1.06. This is the same as for the initial condition  $K_0 = 15, B_0 = 110$ .

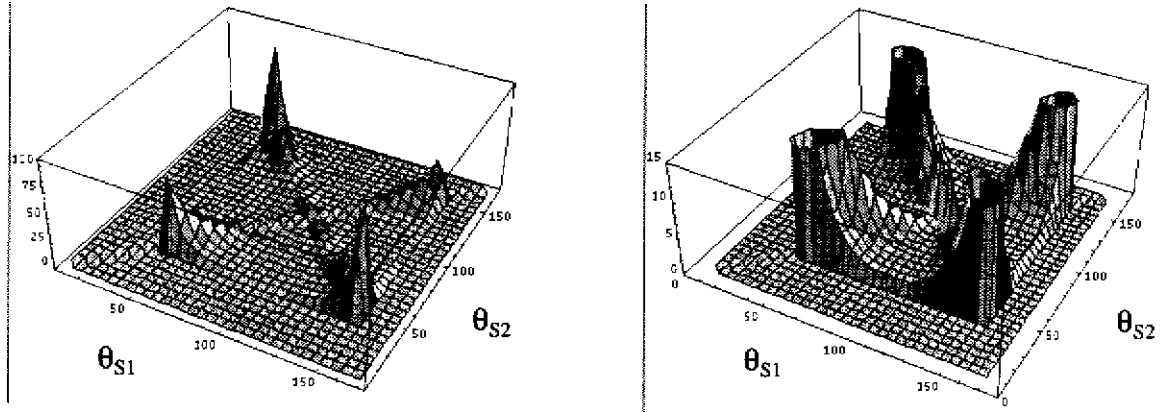


Fig. 5-28. B error surface.  $B=100, K=10, V=80^\circ, N=90^\circ, N=90^\circ, K_0=20, B_0=80$ .

The minimum error of the K error surface occurs when  $S1 = 60^\circ$  and  $S2 = 100^\circ$ , and is equal

to .26. This is the same as the initial condition  $B_0 = 110, K_0 = 15$ .

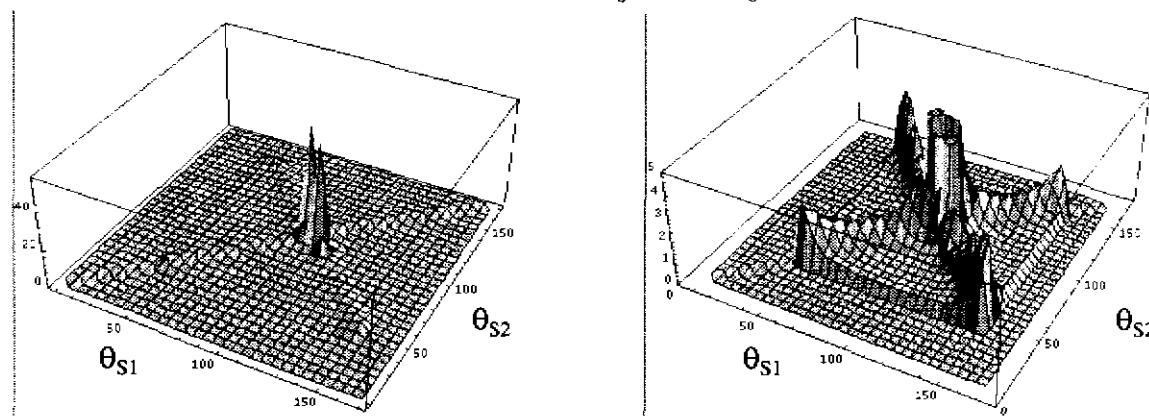


Fig. 5-29. K error surface.  $B=100, K=10, V=80^\circ, N=90^\circ, K_0=20, B_0=80$ .

Next we generated a new set of error surfaces for  $K = 20, B=100$ , and  $V=80$ . The B error surface has a minimum error when  $S1 = 70^\circ$  and  $S2 = 100^\circ$ , and is equal to 1.07. This minimum is approximately the same as the  $K = 10, V=80$ , case.

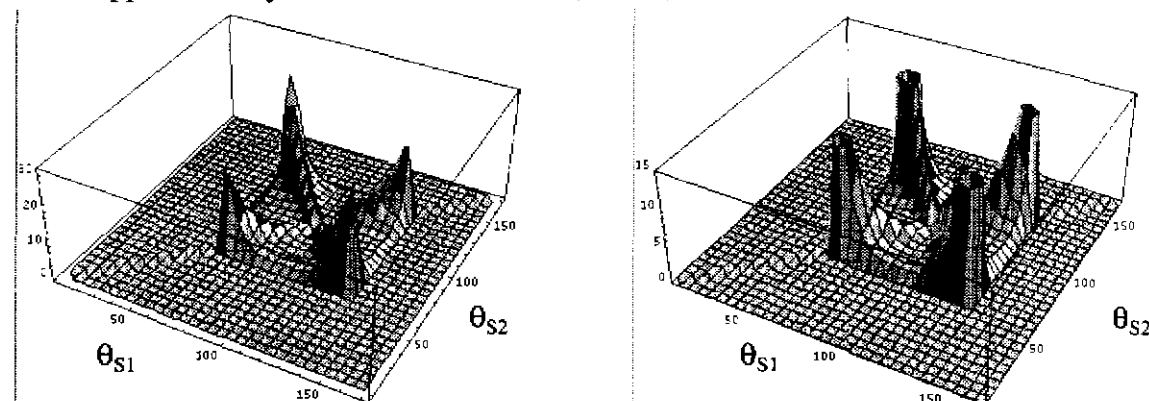


Fig. 5-30. B error surface.  $B=100, K=20, V=80^\circ, N=90^\circ, K_0=25, B_0=110$ .

The K error surface has a minimum error when  $S1 = 105^\circ$  and  $S2 = 70^\circ$ , and is equal to 0.53. This error is approximately double the K error for  $K = 10, V=80$ . When the gaussian is narrower, the same amount of intensity noise will cause a greater change in the width of the gaussian.

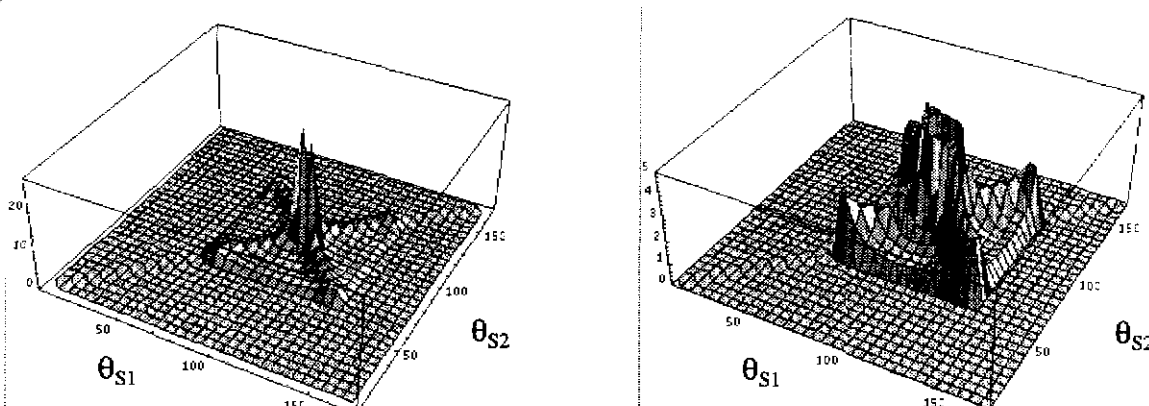


Fig. 5-31. K error surface.  $B=100, K=20, V=80^\circ, N=90^\circ, K_0=25, B_0=110$ .

The next set of simulations used a viewing angle of  $50^\circ$ . First we look at  $K = 10$ ,  $B=100$ , and  $V=50$ . The minimum for the B error surface occurs when  $S1 = 128^\circ$  and  $S2 = 98^\circ$ , and is equal to 0.859. The minimum error is about 19% less than the  $K=10$ ,  $V=80^\circ$  case. The peak intensity of the  $V=50^\circ$  case is about 30% more than the  $K=10$ ,  $V=80^\circ$  case. This will give a better signal to noise ratio and will decrease the amount of error.

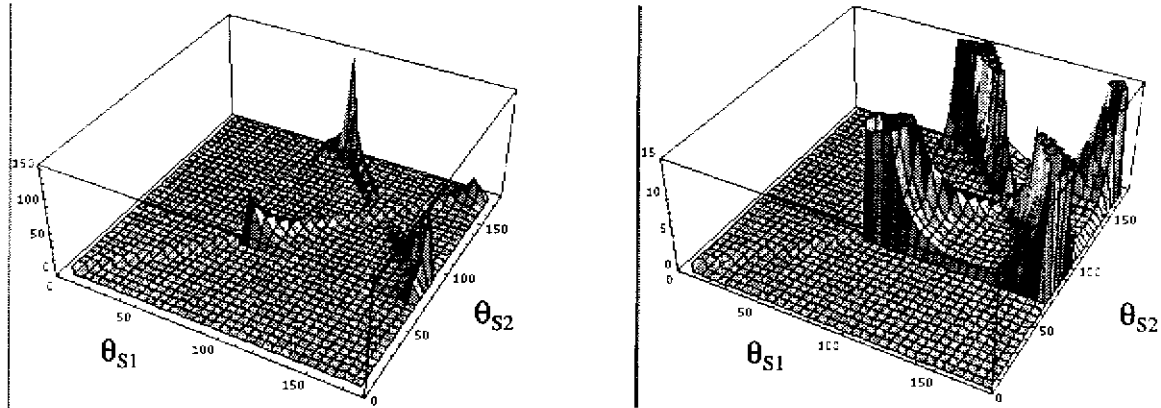


Fig. 5-32. B error surface.  $B=100$ ,  $K=10$ ,  $V=50^\circ$ ,  $N=90^\circ$ ,  $K_0=15$ ,  $B_0=110$ .

The minimum error of the K error surface occurs when  $S1 = 128^\circ$  and  $S2 = 88^\circ$ , and is equal to 0.201. The minimum error is about 23% less than the  $K=10$ ,  $V=80^\circ$  case. As the extant angle increases, the minimum error decreases. This is because the steepness of the sides of the intensity function, where the minimum error occurs, increases. This decreases the value of the minimum of the  $dK/dI$  function.

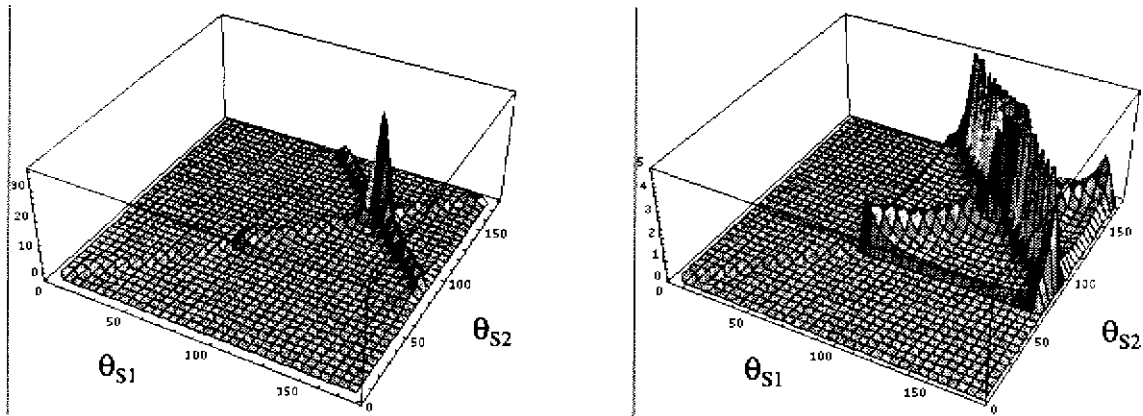


Fig. 5-33. K error surface.  $B=100$ ,  $K=10$ ,  $V=50^\circ$ ,  $N=90^\circ$ ,  $K_0=15$ ,  $B_0=110$ .

Next, we look at  $K = 20$ ,  $B=100$ , and  $V=50$ . The minimum error of the B error surface occurs when  $S1 = 130^\circ$  and  $S2 = 120^\circ$ , and is equal to 0.830. The minimum error is about

22% less than the  $K=20, V=80^\circ$  case.

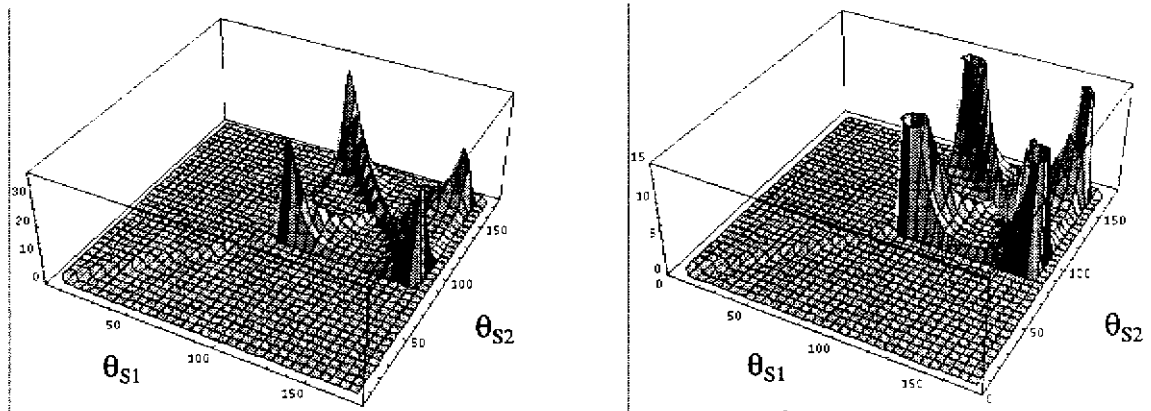


Fig. 5-34. B error surface.  $B=100, K=20, V=50^\circ, N=90^\circ, K_0=25, B_0=110$ .

The minimum error of the K error surface occurs when  $S1 = 130^\circ$  and  $S2 = 100^\circ$ , and is equal to 0.424. The minimum error is about 20% less than the  $K=20, V=80^\circ$  case, and is about double the  $K=10, V=50$  case.

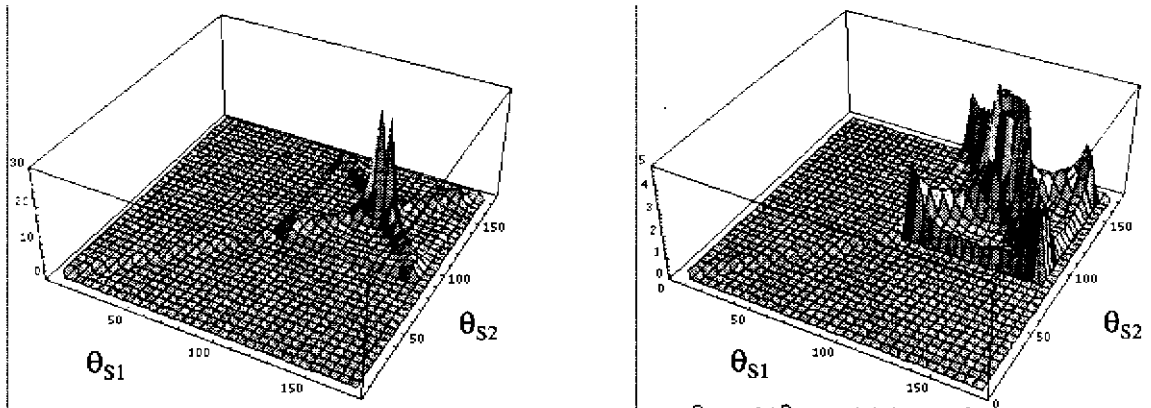


Fig. 5-35. K error surface.  $B=100, K=20, V=50^\circ, N=90^\circ, K_0=25, B_0=110$ .

The next set of simulations used a viewing angle of  $V=30^\circ$ . First we look at  $K = 10, B=100$ , and  $V=30$ . The minimum error of the B error surface occurs when  $S1 = 155^\circ$  and  $S2 = 95^\circ$ , and is equal to 0.55. The minimum error is about 48% less than the  $K=10, V=80^\circ$  case. The peak intensity of the  $V=30^\circ$  case is about 200% more than the  $K=10, V=80^\circ$  case. This will give a better signal to noise ratio and will decrease the amount of error.

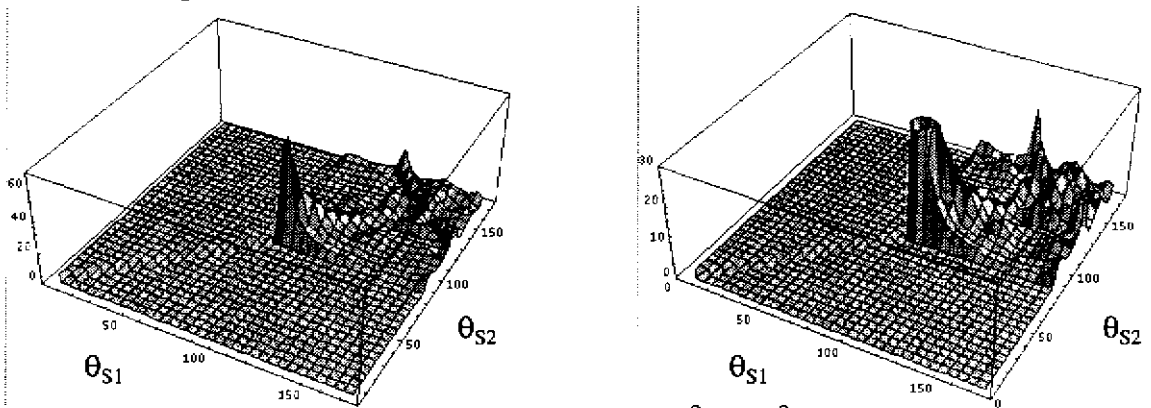


Fig. 5-36. B error surface.  $B=100, K=10, V=30^\circ, N=90^\circ, K_0=15, B_0=110$ .

The minimum error of the K error surface occurs when  $S1 = 145^\circ$  and  $S2 = 105^\circ$ , and is equal to 0.143. The minimum error is about 45% less than the  $K=10, V=80^\circ$  case.

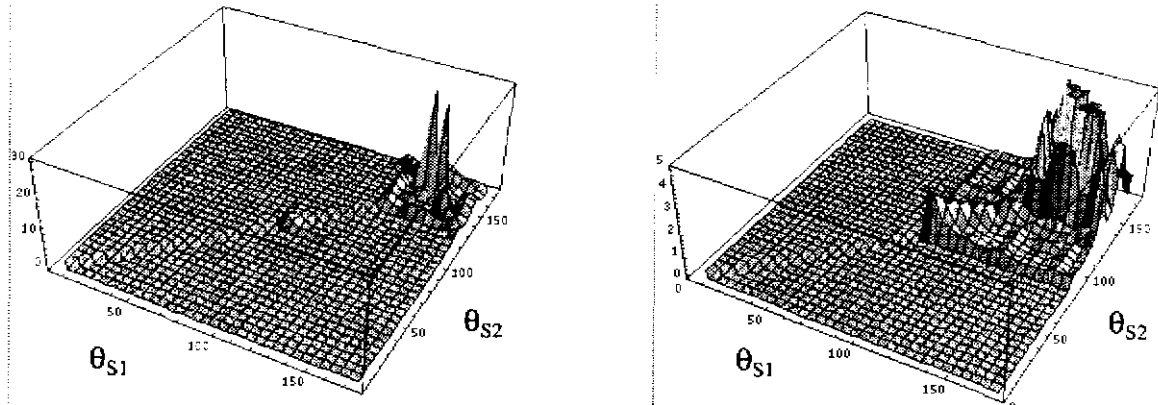


Fig. 5-37. K error surface.  $B=100, K=10, V=30^\circ, N=90^\circ, K_0=15, B_0=110$ .

The  $K=20, B=100, V=30^\circ$  simulation did not produce a smooth error surface. The intensity lobe is so narrow that we can never get very far from singularity. So, even though the lobe's intensity is greater than the  $K=20, V=80^\circ$  case, the errors are approximately the same magnitude. The minimum error for the B error surface occurs when  $S1 = 140^\circ$  and  $S2 = 145^\circ$ , and is equal to 1.16. The minimum error is about 9% more than the  $K=20, V=80^\circ$  case.

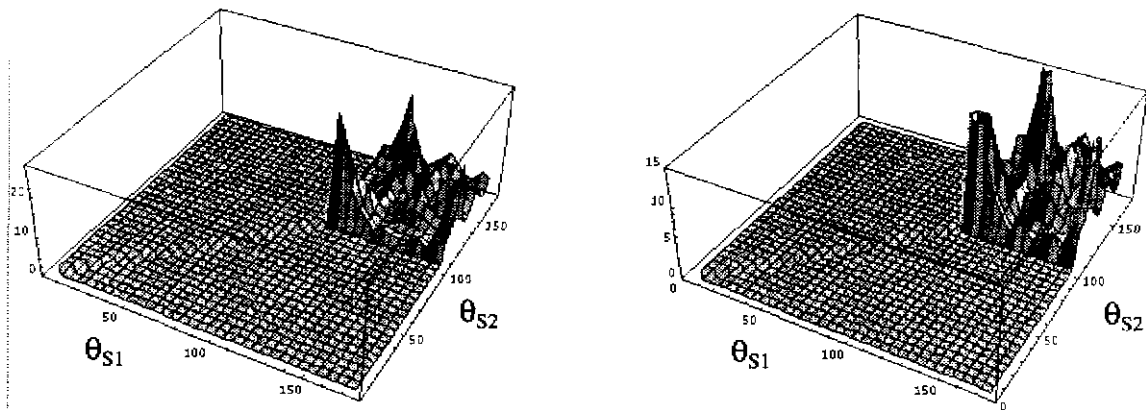


Fig. 5-38. B error surface.  $B=100, K=20, V=30^\circ, N=90^\circ, K_0=25, B_0=110$ .

The minimum error for the K error surface occurs when  $S1 = 140^\circ$  and  $S2 = 110^\circ$ , and is equal to 0.445. The minimum error is about 16% less than the  $K=20, V=80^\circ$  case.

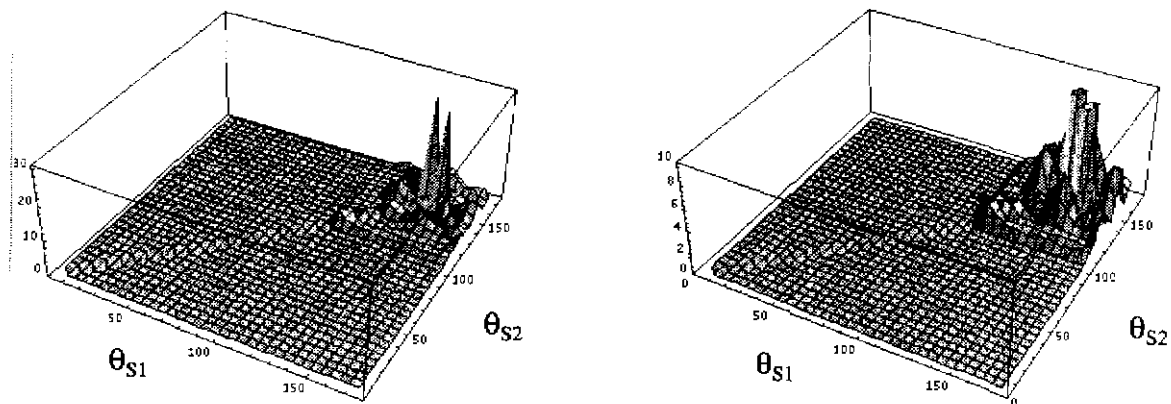


Fig. 5-39. K error surface.  $B=100, K=20, V=30^\circ, N=90^\circ, K_0=25, B_0=110$ .

In order to gain some insight into how the surface normal orientation uncertainty would effect the B and K estimation, we did an additional set of simulations. In this set of simulations the orientation of N has an uncertainty.

$$\theta_n = N(\bar{\theta}_n, \sigma(\theta_n))$$

We performed simulations for  $\sigma(\theta_n)$  equal to  $1^\circ$ ,  $2^\circ$ , and  $3^\circ$ , for the  $K=10$ ,  $B=100$ ,  $V=80^\circ$  case. The first set of simulations is for  $\sigma(\theta_n) = 1^\circ$ . The minimum error of the B error surface occurs when  $S1 = 150^\circ$  and  $S2 = 100^\circ$ , and is equal to 1.14. This error is approximately 8% greater than the no noise case.

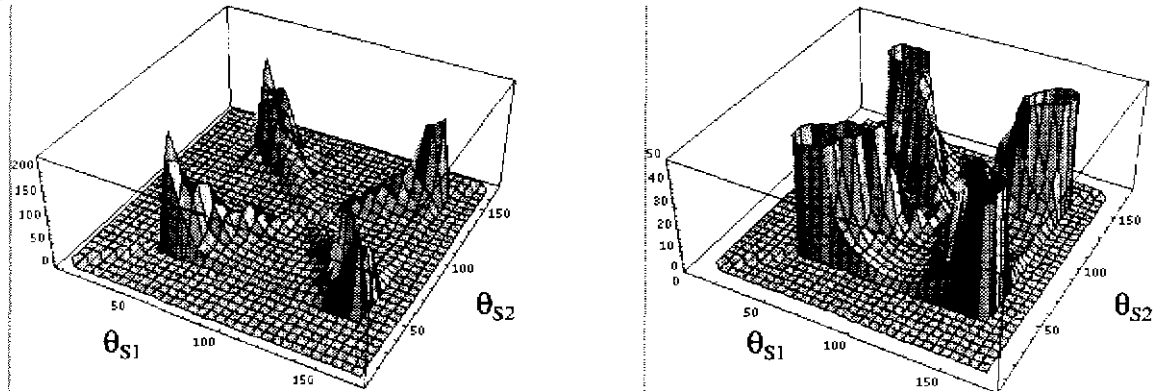


Fig. 5-40. B error surface.  $B=100$ ,  $K=10$ ,  $V=80^\circ$ ,  $N=90^\circ$ ,  $K_0=15$ ,  $B_0=110$ ,  $\sigma(\theta_n) = 1^\circ$ .

The minimum error of the K error surface occurs when  $S1 = 45^\circ$  and  $S2 = 95^\circ$ , and is equal to .63. This error is approximately 142% greater than the no noise case.

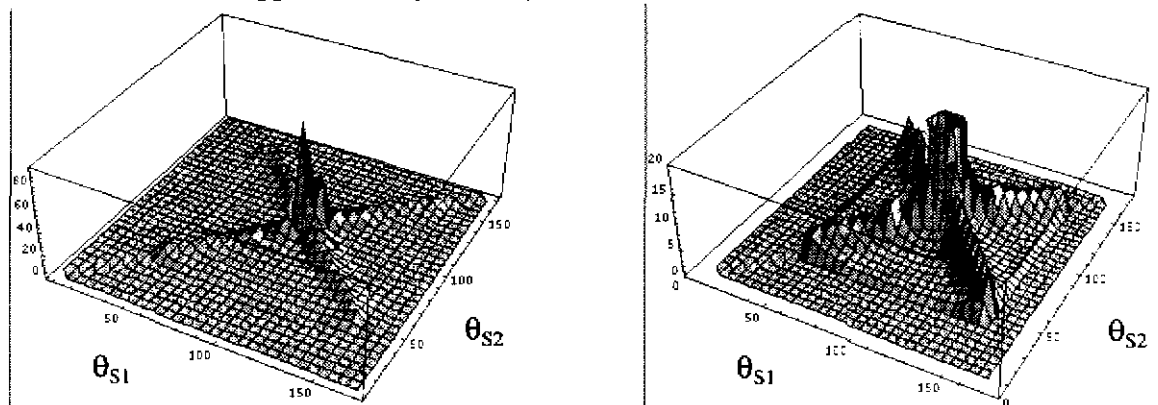


Fig. 5-41. K error surface.  $B=100$ ,  $K=10$ ,  $V=80^\circ$ ,  $N=90^\circ$ ,  $K_0=15$ ,  $B_0=110$ ,  $\sigma(\theta_n) = 1^\circ$ .

The second set of simulations is for  $\sigma(\theta_n) = 2^\circ$ . The minimum error of the B error surface occurs when  $S1 = 100^\circ$  and  $S2 = 60^\circ$ , and is equal to 1.74. This error is approximately 64%

greater than the no noise case.

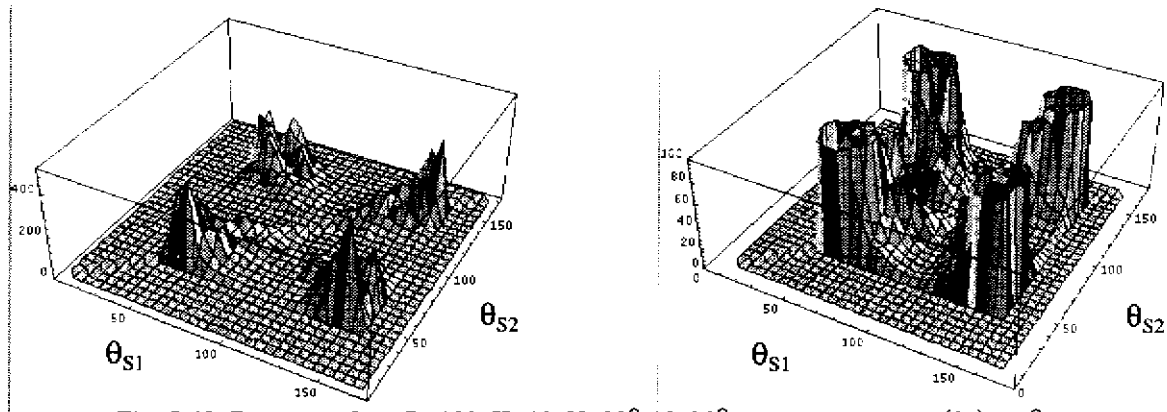


Fig. 5-42. B error surface.  $B=100, K=10, V=80^\circ, N=90^\circ, K_0=15, B_0=110, \sigma(\theta_n) = 2^\circ$ .

The minimum error of the K error surface occurs when  $S1 = 45^\circ$  and  $S2 = 95^\circ$ , and is equal to 1.13. This error is approximately 335% greater than the no noise case.

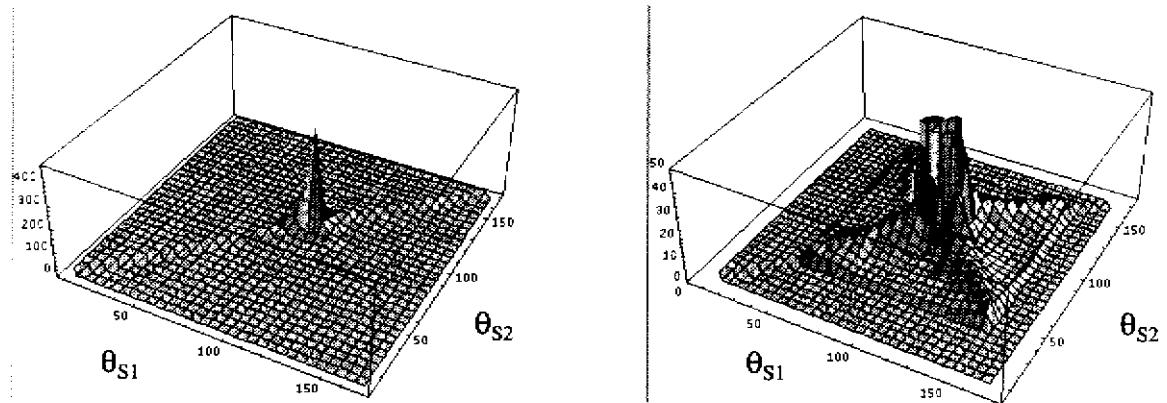


Fig. 5-43. K error surface.  $B=100, K=10, V=80^\circ, N=90^\circ, K_0=15, B_0=110, \sigma(\theta_n) = 2^\circ$ .

The third set of simulations is for  $\sigma(\theta_n) = 3^\circ$ . The minimum error of the B error surface occurs when  $S1 = 45^\circ$  and  $S2 = 100^\circ$ , and is equal to 2.98. This error is approximately 181% greater than the no noise case.

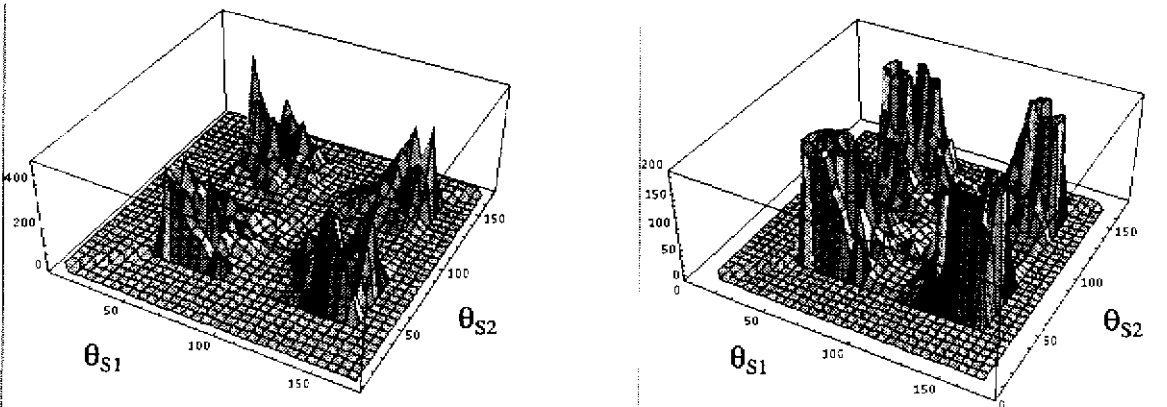


Fig. 5-44. B error surface.  $B=100, K=10, V=80^\circ, N=90^\circ, K_0=15, B_0=110, \sigma(\theta_n) = 3^\circ$ .

The minimum error of the K error surface occurs when  $S1 = 45^\circ$  and  $S2 = 95^\circ$ , and is equal

to 1.69. This error is approximately 550% greater than the no noise case.

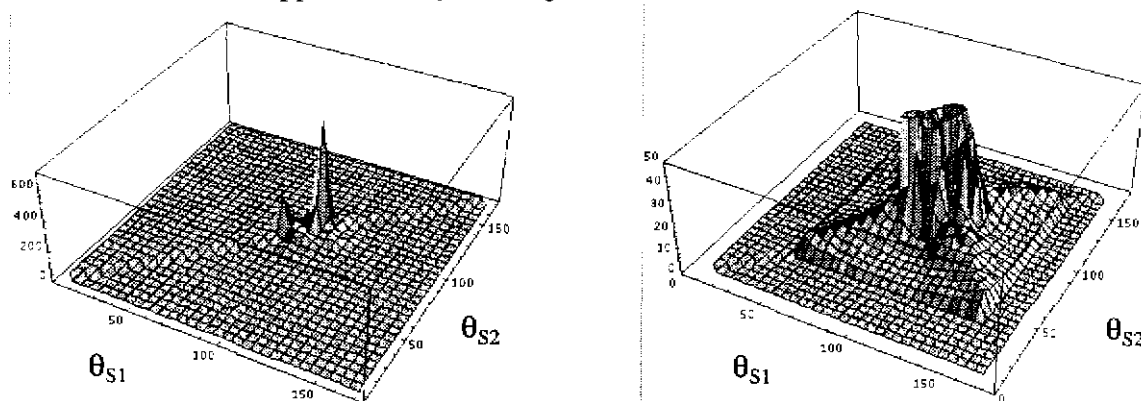


Fig. 5-45. K error surface.  $B=100$ ,  $K=10$ ,  $V=80^\circ$ ,  $N=90^\circ$ ,  $K_0=15$ ,  $B_0=110$ ,  $\sigma(\theta_n) = 3^\circ$ .

Both  $B$  and  $K$  are sensitive to perturbation in  $\theta_n$ . As  $\sigma(\theta_n)$  increases, the minimum error in both parameters increases. However,  $K$  is much more sensitive to these perturbations.

## 5.7 Summary

This chapter discussed the illumination of 2D specular lobe surfaces. We discussed the estimation of surface orientation, in the presence of intensity noise, when  $B$  and  $K$  were known. We also discussed the estimation of  $B$  and  $K$ , in the presence of intensity noise, when surface orientation was known. Finally, we discussed the effect of surface orientation uncertainty on the estimation of  $B$  and  $K$ . In the next chapter we discuss the illumination of hybrid surfaces. These surfaces contain a specular lobe in addition to a lambertian component.



# Chapter 6

## Illumination of Hybrid Surfaces

### 6.1 Introduction

This chapter discusses the illumination of hybrid surfaces, surfaces that include both the specular lobe and lambertian components of the Torrance-Sparrow model. We use a method called “four light photometric stereo”. The four light photometric stereo method describes constraints on light source placement that allow the shape, specular intensity, and specular sharpness of a hybrid object to be measured, and the method also describes how to use the intensity noise function of the camera/digitizer to segment pixels into specular and nonspecular pixels. Unlike previous chapters, we do not explore a systematic way of achieving appropriate light source positions. We concentrate on how appropriate light source positions can allow us to determine shape, specular intensity, and specular sharpness. By specifying the correct constraints on light source placement we can increase the amount of information that is available to us.

Conceptually, the problem we are solving has three parts: shape extraction, pixel segmentation, and specular intensity/specular sharpness extraction. The shape information is produced directly by three light and four light photometric stereo methods. After we have shape information, we can apply different techniques to determine which pixels are specular and which are nonspecular. Then, we can use the specular pixels and shape information, in conjunction with a simplified Torrance-Sparrow reflectance model, to determine the specular intensity and specular sharpness.

### 6.2 Shape and Segmentation using Four Light Photometric Stereo

The set of surface orientations that a light source can illuminate can be represented using the gaussian sphere, which we use to represent the set of all possible surface orientations. The set of surface orientations that are visible to a light source will be one half of the gaussian sphere. The set of surface orientations that are visible to a camera is another half of the gaussian sphere. (In our coordinate system, the viewing axis is always along the +Z axis.) The

set of surface orientations that are both illuminated and visible will be the intersection of the visible half of the gaussian sphere with the illuminated half of the gaussian sphere. We represent the “visible and illuminated” part of the gaussian sphere by showing the visible half of the gaussian sphere and a shadow line for each light source which indicates which part of the visible sphere is illuminated.

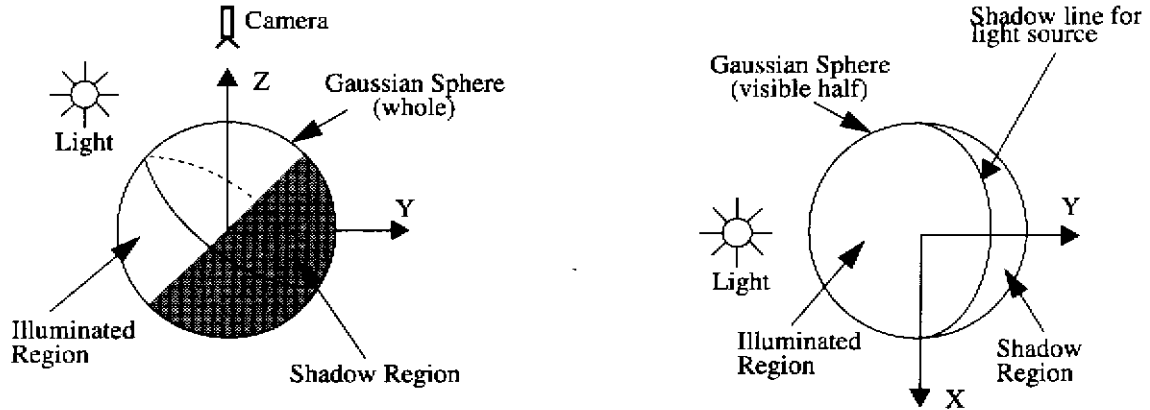


Fig. 6-1. a) Illuminated gaussian sphere. b) illuminated and visible gaussian sphere.

We can illuminate an object with four, appropriately spaced, light sources to produce three types of illumination regions: regions illuminated by all four light sources, regions illuminated by three light sources, and regions illuminated by only two light sources.

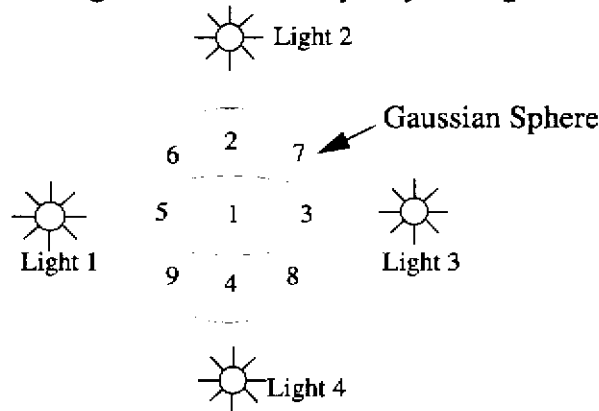


Fig. 6-2. Illumination regions

Region 1 is illuminated by all four light sources. Regions 2, 3, 4, and 5 are illuminated by three light sources. Regions 6, 7, 8, and 9 are illuminated by two light sources. The region boundaries are formed by the shadow lines of each light source. The size and shape of each region is dependent on the positions of the light sources. It is important to note that an object does not have to have all three types of regions in order to apply these methods.

Different information is available in each of the three categories of regions. Therefore, we use different techniques for determining surface shape and for performing pixel segmentation in each region.

### 6.2.1 Assumptions

We assume that the specular lobes produced by the light sources do not intersect. The amount of light source separation needed to achieve this depends on specular sharpness. We assume that the reflectance properties, diffuse albedo, and specular albedo are constant over the surface of the object. There is no interreflection. We restrict the illumination angle to be less than 40 degrees and the viewing angle to be less than 80 degrees. These angular restrictions allow us to use a simplified form of the Torrance-Sparrow model, and is explained later in the paper. Light source directions are known without any uncertainty, and we assume parallel incident light. The four light illuminated region has no other requirements. The three light illuminated region requires lambertian illumination from at least two light sources. The third light source can be either lambertian or specular. The region must be in the shadow of the fourth light source. The two light illuminated region must have lambertian illumination from two light sources, and the region must be in the shadow of the third and fourth light sources. In order to have information to fit to the specular lobe parameters, we require that there is a specularity, and that the specularity extends over a range of surface orientations.

### 6.2.2 Shape and Segmentation in the Four Light Region

Coleman and Jain [Coleman 82] proposed using four lights to determine the shape of surfaces that were nonlambertian. The method is only valid in regions illuminated by all four light sources, the region labeled 1. They proposed to calculate four albedo values based on the four possible combinations of three light sources. For a perfectly lambertian surface, the four albedos would be identical. But, for surfaces that exhibit some specularity, this is not the case. If we assume that the specular lobes of each light source do not intersect, then a specularity in one light source will cause the three albedos that use that light source to be high, while the albedo that does not use the light source will be low. Given four intensity values, ( $I_1, I_2, I_3, I_4$ ), and four light source directions, ( $S_1, S_2, S_3, S_4$ ), we can define four albedos, ( $R_a, R_b, R_c, R_d$ ), as follows:

$$\mathbf{S}_a = \begin{bmatrix} S_{1x} & S_{1y} & S_{1z} \\ S_{2x} & S_{2y} & S_{2z} \\ S_{3x} & S_{3y} & S_{3z} \end{bmatrix} \quad \mathbf{S}_b = \begin{bmatrix} S_{2x} & S_{2y} & S_{2z} \\ S_{3x} & S_{3y} & S_{3z} \\ S_{4x} & S_{4y} & S_{4z} \end{bmatrix} \quad \mathbf{S}_c = \begin{bmatrix} S_{3x} & S_{3y} & S_{3z} \\ S_{4x} & S_{4y} & S_{4z} \\ S_{1x} & S_{1y} & S_{1z} \end{bmatrix} \quad \mathbf{S}_d = \begin{bmatrix} S_{4x} & S_{4y} & S_{4z} \\ S_{1x} & S_{1y} & S_{1z} \\ S_{2x} & S_{2y} & S_{2z} \end{bmatrix}$$

$$\mathbf{I}_a = \begin{bmatrix} I_1 \\ I_2 \\ I_3 \end{bmatrix} \quad \mathbf{I}_b = \begin{bmatrix} I_2 \\ I_3 \\ I_4 \end{bmatrix} \quad \mathbf{I}_c = \begin{bmatrix} I_3 \\ I_4 \\ I_1 \end{bmatrix} \quad \mathbf{I}_d = \begin{bmatrix} I_4 \\ I_1 \\ I_2 \end{bmatrix}$$

$$R_a = |(\mathbf{S}_a)^{-1} \mathbf{I}_a|$$

$$R_b = |(\mathbf{S}_b)^{-1} \mathbf{I}_b|$$

$$R_c = |(\mathbf{S}_c)^{-1} \mathbf{I}_c|$$

$$R_d = |(\mathbf{S}_d)^{-1} \mathbf{I}_d|$$

(S1x, S1y, and S1z are the x, y, and z components of the unit vector to light source number one)

If I1 is specular, Ra, Rc, and Rd will be elevated above their lambertian levels. Rb will be equal to the lambertian albedo, since I2, I3, and I4 are not specular (Our assumption is that for each image point, at most one light source will be specular.).

Therefore, we can identify the nonspecular light sources, by using the four albedos, and we can use these nonspecular light sources to produce a valid surface normal. In the above example, we would determine that Rb is the minimum albedo, and then use I2, I3, and I4 to determine the surface normal. Since the surface is lambertian, the surface normal is equal to:

$$\begin{bmatrix} S2x & S2y & S2z \\ S3x & S3y & S3z \\ S4x & S4y & S4z \end{bmatrix}^{-1} \begin{bmatrix} I2 \\ I3 \\ I4 \end{bmatrix} = \begin{bmatrix} Nx \\ Ny \\ Nz \end{bmatrix}$$

However, due to image noise, the four albedos will never be exactly equal. We need to establish a threshold to determine when the differences in albedo indicate a specularity, and when they are just due to random events. Coleman and Jain define albedo deviation, Rdev:

$$Rdev = \left( \sum_{i=a,b,c,d} (Ri - Rmean) \right) / (4Rmin)$$

If  $Rdev > Rt$ , they classify the pixel as specular, otherwise it is lambertian.  $Rt$  is a manually selected threshold. The use of an arbitrarily selected threshold makes this classification scheme ad hoc.

We propose a better classification scheme which would use the variance of the camera's intensity response to determine a statistically meaningful threshold. If  $\sigma_i^2$  is the camera's intensity variance measured at a particular pixel, then we can establish a specular threshold based on a  $\pm 3\sigma$  distribution [Bevington 69]. We assume that the light source directions are known without any uncertainty. Then, in the case where R1 is the maximum albedo and R2 is the minimum albedo, we can define Rdev as:

$$Rdev = R1 - R2$$

If Rdev is greater than the specular threshold, one of the light sources is specular.

We can determine an accurate surface normal if a pixel is specular, by using the light sources from the minimum albedo to determine the surface normal. If a pixel is not specular, we can use any of the three light sources to determine the surface normal.

### 6.2.2.1 Specular Threshold in Four Light Illuminated Region

A pixel is specular if Rdev is greater than the specular threshold:

$$rdev > 6 \sqrt{\left(\frac{\partial}{\partial I1} R1 + \frac{\partial}{\partial I1} R2\right)^2 \sigma_i^2 + \left(\frac{\partial}{\partial I2} R1 + \frac{\partial}{\partial I2} R2\right)^2 \sigma_i^2 + \left(\frac{\partial}{\partial I3} R1 + \frac{\partial}{\partial I3} R2\right)^2 \sigma_i^2 + \left(\frac{\partial}{\partial I4} R1 + \frac{\partial}{\partial I4} R2\right)^2 \sigma_i^2}$$

If an albedo does not use a particular light source, the terms involving its partial derivatives simply go to zero. The partial derivatives are not complex, and exact expressions can easily be derived. This threshold defines a  $6\sigma$  separation between R1 and R2.

### 6.2.3 Shape and Segmentation in the Three Light Region

It is possible to determine shape and to perform segmentation in the three light illuminated region. In Fig. 6-3. , the region labeled 3 is illuminated by light sources 2, 3, and 4. Its borders are formed by the shadow lines of light sources 1, 4, and 2. We will assume that illumination by light sources 2 and 4 will be lambertian in region 3. Illumination by light source 3 may be specular or lambertian. Region 3 will be in the shadow of light source 1.

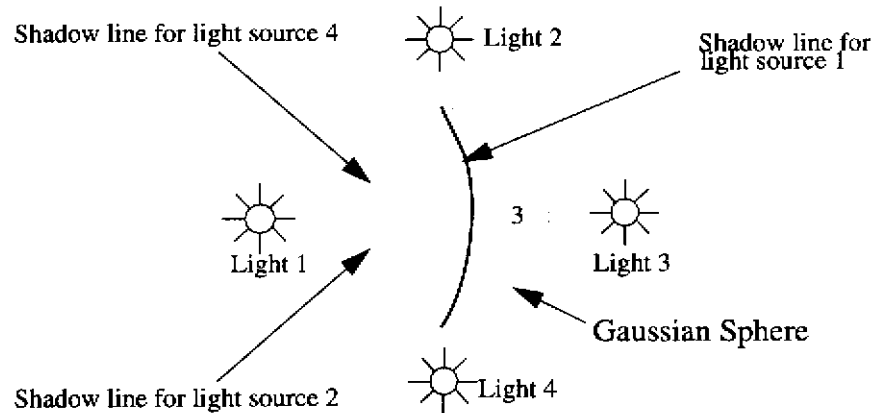


Fig. 6-3. Three light illuminated region

Under these assumptions, we can determine an accurate surface normal using light source 2, light source 4, and the shadow line of light source 1. We do not use light source 3 because it may be specular. We can write three equations, in three unknowns:

$$\frac{I_2}{\rho} = S2xNx + S2yNy + S2zNz$$

$$\frac{I_4}{\rho} = S4xNx + S4yNy + S4zNz$$

$$(Nx)^2 + (Ny)^2 + (Nz)^2 = 1$$

The albedo,  $\rho$ , the light source directions  $S2$  and  $S4$ , and the image intensities  $I2$  and  $I4$  are known. The albedo is calculated from the albedos of the lambertian pixels within a  $10 \times 10$  pixel area within the four light illuminated region. The surface normal is by definition a unit vector.

This set of three equations has two sets of solutions. If we define the following intermediate variables:

$$a = \frac{S2x}{S2z} \quad b = \frac{S2y}{S2z} \quad g = \frac{I2}{\rho S2z} \quad c = \frac{S4x}{S4z} \quad d = \frac{S4y}{S4z} \quad h = \frac{I4}{\rho S4z}$$

$$e = \frac{-g+h}{c-a} \quad f = \frac{d-b}{c-a}$$

$$A = f^2 a^2 + f^2 - 2abf + b^2 + 1$$

$$B = 2agf - 2efa^2 - 2ef + 2abe - 2bg$$

$$C = -2age + a^2 e^2 + e^2 + g^2 - 1$$

The two sets of surface normal solutions are:

$$\begin{aligned}
 Ny_1 &= \frac{-B + \sqrt{B^2 - 4AC}}{2A} & Ny_2 &= \frac{-B - \sqrt{B^2 - 4AC}}{2A} \\
 Nx_1 &= e - fNy_1 & Nx_2 &= e - fNy_2 \\
 Nz_1 &= g - aNx_1 - bNy_1 & Nz_2 &= g - aNx_2 - bNy_2
 \end{aligned}$$

The proper solution can be selected by using the boundary condition of light source one's shadow line. On the shadow line of light source 1, the following equation holds:

$$S1xNx + S1yNy + S1zNz = 0$$

In region number 3,

$$S1xNx + S1yNy + S1zNz < 0$$

So we can select the proper solution by seeing if this condition holds for each solution. (It is possible that due to degenerate positioning of light sources 1, 2, and 4, that both surface normals are on the same side of light source one's shadow line. We do not consider this case.)

### 6.2.3.1 Threshold for Selecting Proper Surface Normal Solution

Selecting the proper solution becomes more complex in the presence of intensity noise, which causes uncertainty in the normals, and uncertainty in the location of the shadow line. We assume that the light source directions are known without any uncertainty. The intensity values and the albedo have variances. Based on these variances, we can express the uncertainty of the surface normals. We will continue using the example above. The light source variances are  $\sigma^2_{I2}$  and  $\sigma^2_{I4}$ . The albedo variance is  $\sigma^2_p$ . The uncertainty of the surface normals is:

$$\begin{aligned}
 \sigma^2_{Nx_1} &= \left(\frac{\partial}{\partial I2}Nx_1\right)^2\sigma^2_{I2} + \left(\frac{\partial}{\partial I4}Nx_1\right)^2\sigma^2_{I4} + \left(\frac{\partial}{\partial p}Nx_1\right)^2\sigma^2_p \\
 \sigma^2_{Ny_1} &= \left(\frac{\partial}{\partial I2}Ny_1\right)^2\sigma^2_{I2} + \left(\frac{\partial}{\partial I4}Ny_1\right)^2\sigma^2_{I4} + \left(\frac{\partial}{\partial p}Ny_1\right)^2\sigma^2_p \\
 \sigma^2_{Nz_1} &= \left(\frac{\partial}{\partial I2}Nz_1\right)^2\sigma^2_{I2} + \left(\frac{\partial}{\partial I4}Nz_1\right)^2\sigma^2_{I4} + \left(\frac{\partial}{\partial p}Nz_1\right)^2\sigma^2_p
 \end{aligned}$$

A similar set of expressions can be derived for the variances of the second set of surface normals. (The partial derivatives of these expressions are very complex. Therefore, the partial derivatives are approximated with a discrete partial derivative.) Using this set of variances we can decide whether a pixel is on the correct side of the shadow line. For a pixel to confidently be in region number 3, the following relation must hold for its surface normal:

$$S1xNx_1 + S1yNy_1 + S1zNz_1 < 3\sqrt{\sigma^2_{Nx_1}(S1x)^2 + \sigma^2_{Ny_1}(S1y)^2 + \sigma^2_{Nz_1}(S1z)^2}$$

This expression expresses with a  $3\sigma$  confidence that the surface normal solution is in the three light illuminated region, region number 3. We will have a similar expression for  $Nx_2, Ny_2, Nz_2$ . It is possible that we cannot confidently say that either set of surface normals is in

region number 3. (This expression is false for both sets of surface normals.) These pixels are flagged with a special classification.

At this point, we have derived how to confidently determine surface normals for the three light illuminated region. We also need to classify pixels as specular or lambertian.

### 6.2.3.2 Specular classification of Pixels in the Three Light Illuminated Region

In order to classify a pixel as specular, we can determine whether its measured brightness, with respect to a given light source, is larger than its predicted lambertian brightness for the same light source. We can determine the predicted lambertian brightness of a pixel in the three light illuminated region by using the surface normal derived in the preceding section, the source directions (which are known), and the lambertian albedo. Using the example of the preceding section, we want to determine if the measured brightness due to light source three is greater than its lambertian brightness. If the derived normal vector for the pixel under consideration is  $(N_x, N_y, N_z)$ , and the measured brightness of the pixel due to light source three is  $I_3$ , then the pixel is specular if:

$$I_3 > \rho (S_3xN_x + S_3yN_y + S_3zN_z)$$

We need to consider the uncertainty of  $I_3$ ,  $\rho$ ,  $N_x$ ,  $N_y$ , and  $N_z$ . The uncertainty of the predicted lambertian brightness,  $I_{lam}$ , is  $\sigma_{I_{lam}}^2$ .

$$I_{lam} = \rho (S_3xN_x + S_3yN_y + S_3zN_z)$$

$$\sigma_{I_{lam}}^2 = \left( \frac{\partial I_{lam}}{\partial \rho} \right)^2 \sigma_{\rho}^2 + \left( \frac{\partial I_{lam}}{\partial N_x} \right)^2 \sigma_{N_x}^2 + \left( \frac{\partial I_{lam}}{\partial N_y} \right)^2 \sigma_{N_y}^2 + \left( \frac{\partial I_{lam}}{\partial N_z} \right)^2 \sigma_{N_z}^2$$

If  $\sigma_{I_3}^2$  is the uncertainty of the measured brightness, then we can say that the pixel is specular, assuming a  $3\sigma$  distribution, if:

$$I_3 - I_{lam} > 6 \sqrt{\sigma_{I_{lam}}^2 + \sigma_{I_3}^2}$$

### 6.2.3.3 Imaginary Surface Normal Solutions in Three Light Region

It is possible that the surface normal solutions in the three light illuminated region will be imaginary. This can happen when one pixel is brighter than a lambertian pixel could be. This could be caused by interreflection or an unexpected specularity. It can also occur if there is an error in the lambertian albedo,  $\rho$ . The existence of an imaginary solution can be understood with the following description. The solution to the set of surface normal equations corresponds to finding the points on a lambertian gaussian sphere that are the intersections of two isobright contours. One isobright contour is caused by  $S_2$ , and has intensity  $I_2$ . The other isobright contour is produced by  $S_4$ , and has intensity  $I_4$ . If we imagine that we are illuminating a gaussian sphere (which contains all surface normals), these two isobright contours will be two circles. The two circles will in general intersect in at most two places. These two intersection points correspond to the two real solutions to the surface normal equations. However, if one circle gets smaller (which corresponds to the pixel getting

brighter, as might be caused by interreflection), at some point the isobright contours will fail to intersect. When the contours fail to intersect, the solutions to the surface normal equations will become imaginary.

### 6.2.4 Shape and Segmentation in the Two Light Region

It is possible to determine the surface normal in the region illuminated by only two lights. We will assume that light sources 2 and 3 produce lambertian illumination in region 7. Region 7 is in the shadow of light sources 1 and 4.

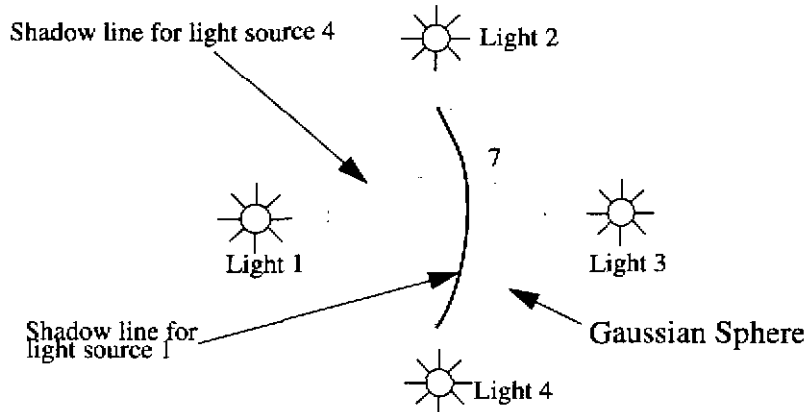


Fig. 6-4. Two light illuminated region.

We can write the following set of equations:

$$\frac{I_2}{\rho} = S2_x N_x + S2_y N_y + S2_z N_z$$

$$\frac{I_3}{\rho} = S3_x N_x + S3_y N_y + S3_z N_z$$

$$(N_x)^2 + (N_y)^2 + (N_z)^2 = 1$$

The equations will yield two sets of surface normal solutions, and can be solved using the methods of the three light illuminated region.

The proper solution can be selected by using the boundary condition for light source one's shadow line, and the boundary condition for light source four's shadow line. In region number 7,

$$S1_x N_x + S1_y N_y + S1_z N_z < 0 \wedge S4_x N_x + S4_y N_y + S4_z N_z < 0$$

#### 6.2.4.1 Threshold for Selecting Proper Surface Normal Solution

If we consider the uncertainty due to intensity noise, the following two relations must hold:

$$S1_x N_{x_1} + S1_y N_{y_1} + S1_z N_{z_1} < 3 \sqrt{\sigma_{N_{x_1}}^2 (S1_x)^2 + \sigma_{N_{y_1}}^2 (S1_y)^2 + \sigma_{N_{z_1}}^2 (S1_z)^2}$$

$$S4_x N_{x_1} + S4_y N_{y_1} + S4_z N_{z_1} < 3 \sqrt{\sigma_{N_{x_1}}^2 (S4_x)^2 + \sigma_{N_{y_1}}^2 (S4_y)^2 + \sigma_{N_{z_1}}^2 (S4_z)^2}$$

where  $(N_{x_1}, N_{y_1}, N_{z_1})$  is one of the surface normal solutions. A similar set of equations hold

for the second set of surface normal solutions. The surface normal variances are calculated using the expressions derived for the three light illuminated region.

#### 6.2.4.2 Specular Classification of Pixels in the Two Light Illuminated Region

There is not enough information available to confidently classify pixels as specular in the two light illuminated region. If our assumption, that light source one and light source four produce lambertian illumination, is broken, the surface normal solutions may become imaginary. If the lambertian albedo is correct, and there are no interreflections, then the existence of imaginary surface normal solutions indicates a specularity in one of the two light sources. Pixels may not be sufficiently specular to cause the surface normal solutions to become imaginary. In this case, the surface normal solutions will be erroneous, and it will be not be possible to detect the condition.

#### 6.2.5 Consistent Segmentation

There is no guarantee that the statistical segmentation of specular and lambertian pixels within the three light illuminated region and the four light illuminated region will produce consistent segmentations. The uncertainty of the segmentation in the three light illuminated region has a higher uncertainty than the segmentation in the four light illuminated region. The derivation of the surface normals in the three light illuminated region involves a lot of computation; this increases their variance, making  $\sigma_{\text{lam}}^2$  large.

In order to produce consistent segmentations, we increase the uncertainty threshold of the four light illuminated region by 2X, to match three light illuminated region. The amount of increase was found by observing the segmentation of synthesized images.

Therefore, a pixel in the four light illuminated region is specular if:

$$r_{dev} > 1.2 \sqrt{\left(\frac{\partial}{\partial I1} R1 + \frac{\partial}{\partial I1} R2\right)^2 \sigma_i^2 + \left(\frac{\partial}{\partial I2} R1 + \frac{\partial}{\partial I2} R2\right)^2 \sigma_i^2 + \left(\frac{\partial}{\partial I3} R1 + \frac{\partial}{\partial I3} R2\right)^2 \sigma_i^2 + \left(\frac{\partial}{\partial I4} R1 + \frac{\partial}{\partial I4} R2\right)^2 \sigma_i^2}$$

### 6.3 Extracting Specular Intensity and Specular Sharpness

The Torrance-Sparrow reflectance model allows us to determine the specular intensity and specular sharpness of an object. In this section, we develop a simplified version of the Torrance-Sparrow model. Then, we develop the specular intensity and specular sharpness extraction algorithms.

#### 6.3.1 Simplified Torrance-Sparrow Model

The Torrance-Sparrow model is a geometrical optics model of reflection for rough surfaces.



rough a surface is. We then have:

$$E = B \left( \frac{\exp(-K\alpha^2)}{N_z} \right)$$

The total surface radiance will be the sum of the underlying lambertian radiance, A, and the radiance of the specular lobe.

$$E = A + B \left( \frac{\exp(-K\alpha^2)}{N_z} \right)$$

### 6.3.2 Determination of Specular Intensity and Specular Sharpness

Once the surface shape is determined and the specular pixels are extracted, the specular intensity and specular sharpness can be determined. In the simplified Torrance-Sparrow model, we need to determine B, the specular intensity, and K, the specular sharpness.

Using the extracted surface normals and lambertian albedo, we can determine the lambertian intensity at each image point.

$$A = \rho (S_x N_x + S_y N_y + S_z N_z)$$

We can define D, the difference between the measured image brightness at each specular pixel and the lambertian intensity.

$$D = I - A$$

Our model is:

$$D = B \left( \frac{\exp(-K\alpha^2)}{N_z} \right)$$

Some surfaces that we have measured have an offset between the lobe and the underlying lambertian component. We add an offset term to compensate for this. Our model becomes:

$$D = B \left( \frac{\exp(-K\alpha^2)}{N_z} \right) + Offset$$

$\alpha$  can be determined from the light source direction, which is known, and from the surface normal, which is also known. The remaining unknowns, B, K, and Offset, can be solved for by searching in three dimensional (B,K, Offset) space.

We can define the CHISQR error as the difference between the actual value of D and the value of D based on the current value of (B,K, Offset).

$$CHISQR = \sum_{i,j} [ (I(i,j) - A(i,j)) - D(B, K, Offset) ]^2$$

CHISQR is a measure of how good the current estimate of (B,K, Offset) fits the actual image data. When CHISQR equals zero the model fits the data exactly. We can search in three dimensional CHISQR space for the minimum value of CHISQR. This point will give us the best estimate of (B, K, Offset).

The search direction can be determined using a variety of methods such as line search, gradient descent search, and conjugate gradient descent search. We chose gradient descent. It

offers a reasonable trade-off between algorithmic complexity and search efficiency. We can define the gradient of CHISQR in each of the three dimensions, (B, K, Offset).

$$\nabla_B CHISQR = \frac{CHISQR((B, K, OFFSET) + \delta B) - CHISQR(B, K, OFFSET)}{\delta B}$$

$$\nabla_K CHISQR = \frac{CHISQR((B, K, OFFSET) + \delta K) - CHISQR(B, K, OFFSET)}{\delta K}$$

$$\nabla_{Offset} CHISQR = \frac{CHISQR((B, K, OFFSET) + \delta Offset) - CHISQR(B, K, OFFSET)}{\delta Offset}$$

The gradients are normalized with respect to the unit vector formed by the three components, (B, K, Offset). Then, the negative of the gradient is multiplied by the step size ( $\delta B$ ,  $\delta K$ ,  $\delta Offset$ ) and is added to the previous value of (B, K, Offset) to produce the new search point. The search continues until the value of CHISQR reaches a minimum.

## 6.4 Results

### 6.4.1 Simulations:

Synthesized images of a sphere, including gaussian intensity noise, were created to test the validity of our algorithms.

#### 6.4.1.1 Synthesized Images

Four images of a synthetic sphere were generated with the following light source directions:

	Sx	Sy	Sz
Light source one	-.541	.681	.494
Light source two	.661	.588	.466
Light source three	.592	-.632	.499
Light source four	-.631	-.555	.541

Image characteristics are:  $\rho = 147$ ,  $B = 50$ ,  $K = 16$ ,  $\sigma_i^2 = 0.8$ .

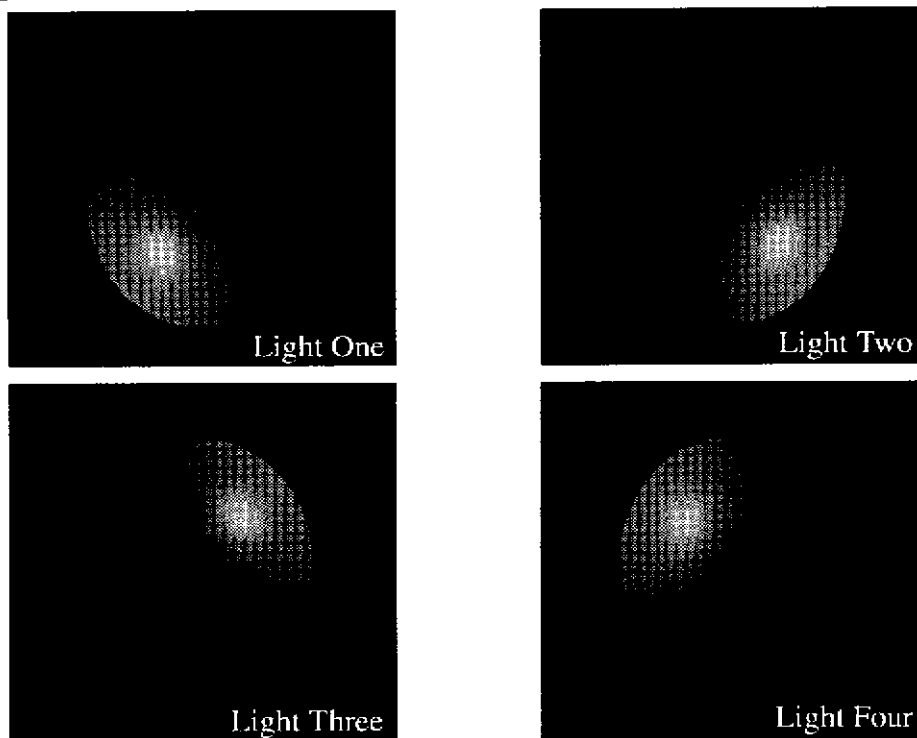


Fig. 6-7. Synthetic sphere images.

The pixel segmentation for the above images is:

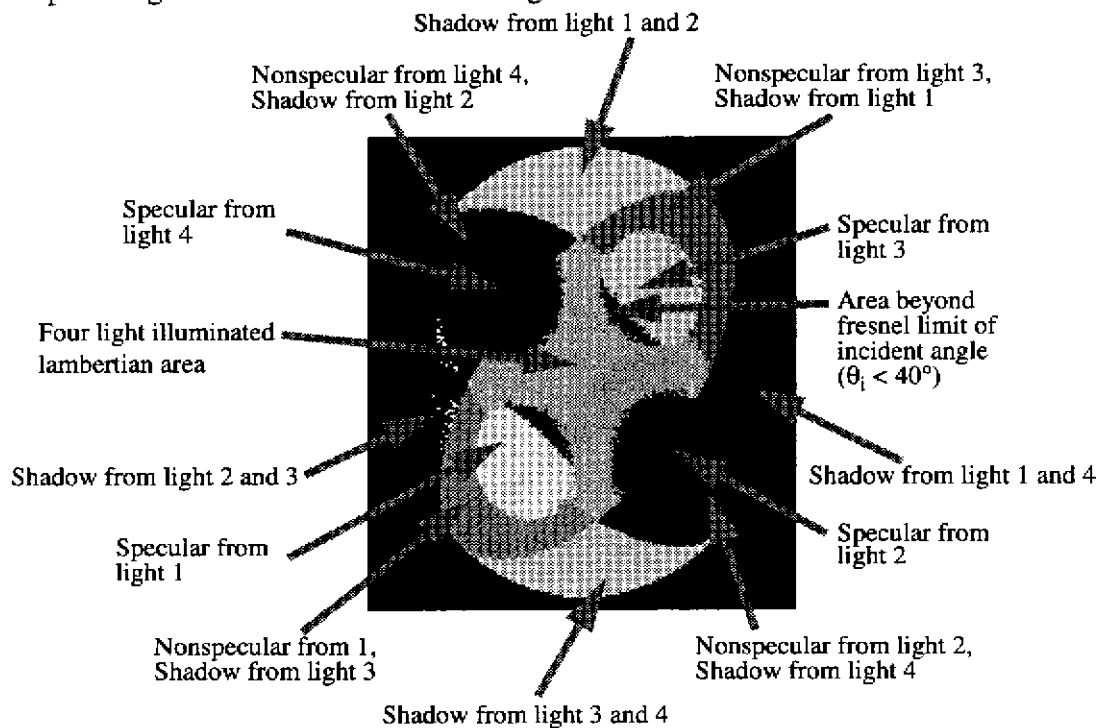


Fig. 6-8. Segmentation for synthetic sphere.

The needle map produced from the four intensity images is:

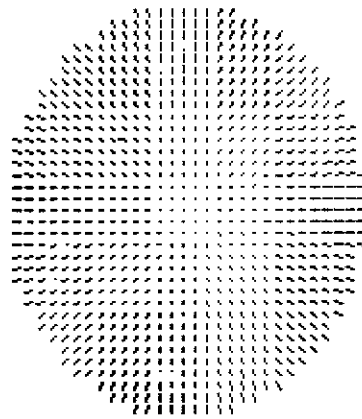


Fig. 6-9. Needle map for synthetic sphere.

The specular intensity, B, specular sharpness, K, and the offset, Offset, extracted for the four specular spots is:

	Offset	B	K
Specular from S1	-0.5	48.5	15.9
Specular from S2	-3.6	51.2	14.6
Specular from S3	-0.3	48.4	16.0
Specular from S4	-0.5	48.3	15.9
Average Values	-1.2	49.1	15.6

The plot of intensity versus incident angle for light source two is:

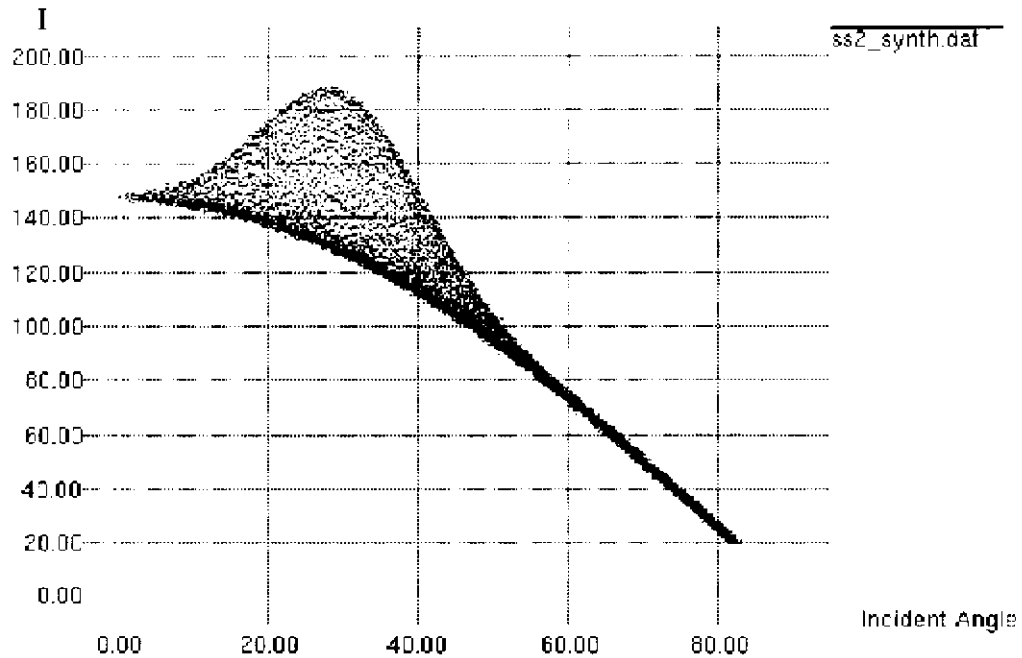


Fig. 6-10. Intensity vs. incident angle for synthetic sphere.

If our data follows the simplified Torrance-Sparrow model, a plot of  $\ln(D*N_z)$  versus  $\alpha^2$  should be linear. This can be seen from:

$$D = B \left( \frac{\exp(-K\alpha^2)}{N_z} \right)$$

$$\ln(DN_z) = (-K\alpha^2) + \ln(B)$$

The plot of  $\alpha^2$  versus  $\ln(D*N_z)$  for light source two is:

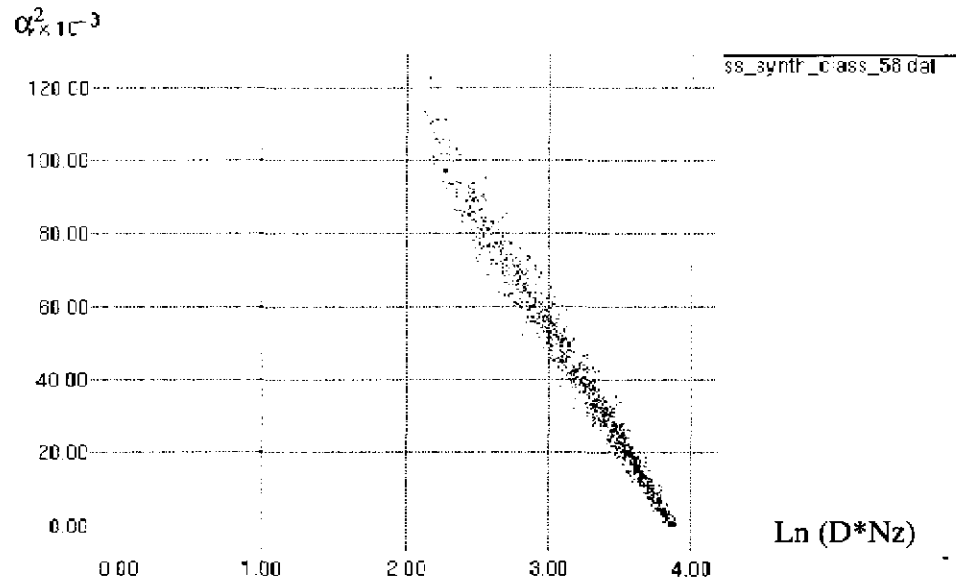


Fig. 6-11.  $\alpha^2$  versus  $\ln(D*N_z)$  for synthetic sphere.

## 6.4.2 Experimental Results

The experimental results consist of images of two objects, a specular painted sphere and a plastic helmet. Both objects exhibit hybrid reflectance. In addition, images of a specular plastic bottle are included. The bottle exhibits a specular spike. So, it does not conform to our reflectance model assumptions, but we are able to extract the bottle's shape.

### 6.4.2.1 Experimental Setup

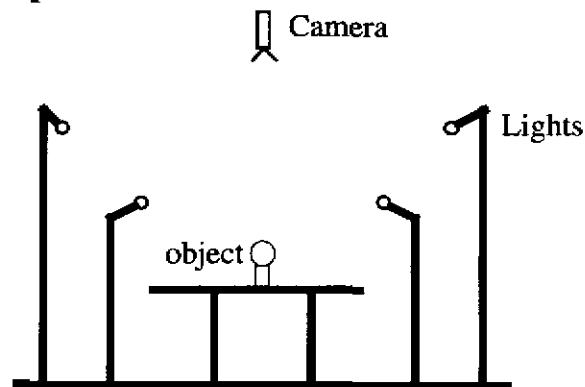


Fig. 6-12. Experimental Setup

A ceiling mounted, Sony XC-57 camera, with an 85 mm Nikkor lens, was used. The camera

to object distance was approximately 2.5 meters. Four ECA, 250 watt, light bulbs were mounted on light stands. The bulb to object distance was approximately 2.6 meter

### 6.4.2.2 Painted Specular Sphere

Four images of a painted, 12.7cm diameter, sphere were taken. Light source directions were determined to be:

	Sx	Sy	Sz
Light source one	-.541	.681	.494
Light source two	.661	.588	.466
Light source three	.592	-.632	.499
Light source four	-.631	-.555	.541

Raw image data was linearized, and normalized

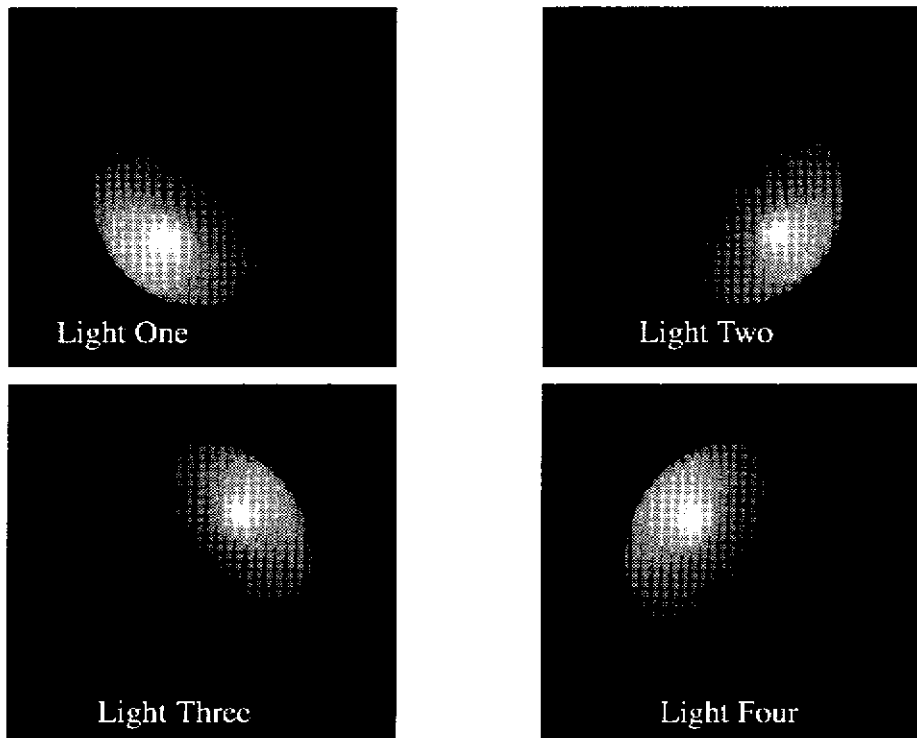


Fig. 6-13. Painted sphere images.

The pixel segmentation for the above images is:

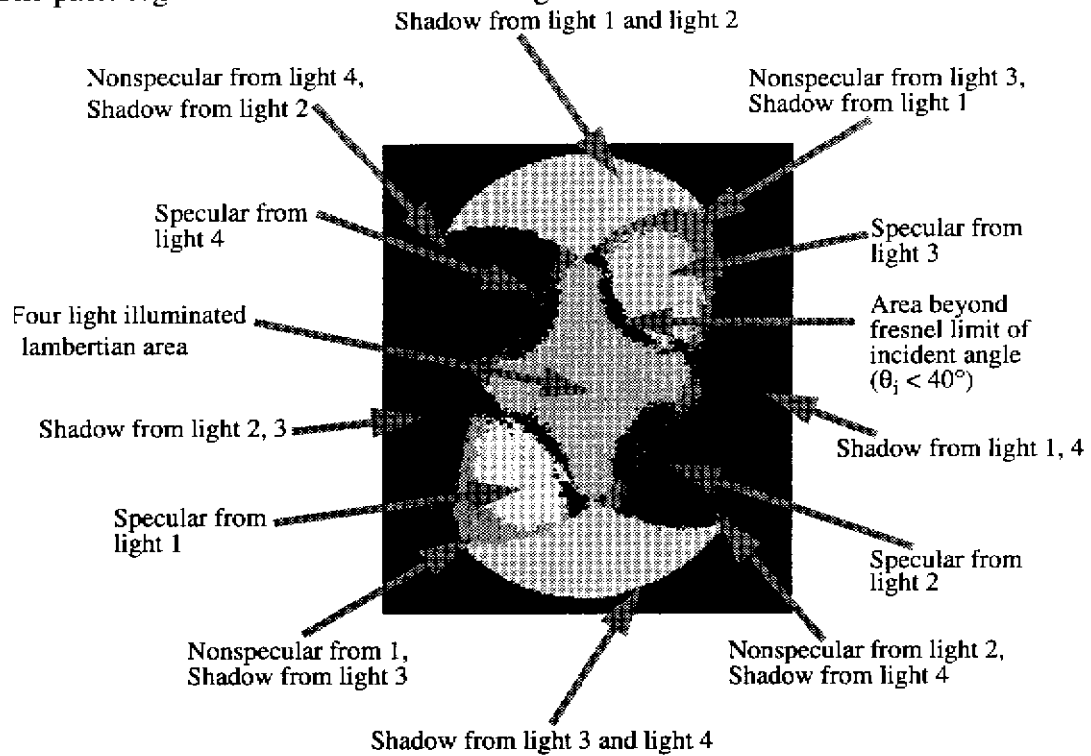


Fig. 6-14. Segmentation for painted sphere.

The needle map, using the extracted lambertian albedo =139.8, produced from the four intensity images is:

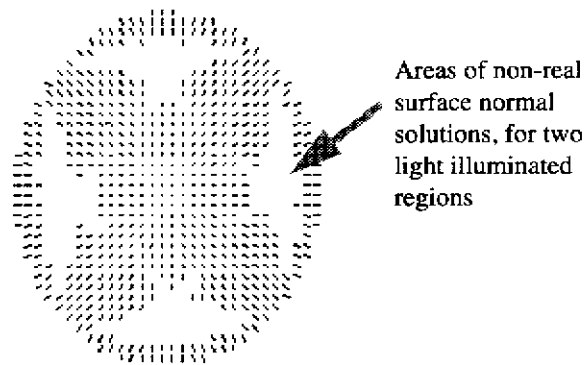


Fig. 6-15. Needle map for painted sphere

If we increase the lambertian albedo by the Offset, we are able to extract the surface normals

in the two light illuminated regions.

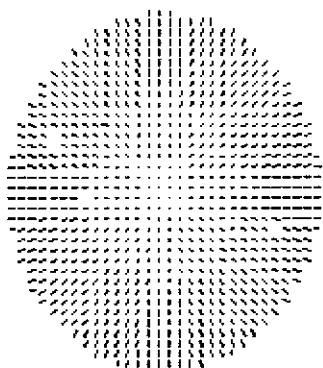


Fig. 6-16. Needle map for painted sphere

The specular intensity, B, specular sharpness, K, and the offset, Offset, extracted for the four specular spots is (The extracted lambertian albedo,  $\rho$ , is 139.8.)

	Offset	B	K
Specular from S1	10.1	43.5	16.7
Specular from S2	8.2	55.1	17.0
Specular from S3	14.6	45.8	21.2
Specular from S4	15.1	39.9	22.8
Average Values	12.0	46.1	19.4

The plot of measured intensity versus incident angle for light source three is:

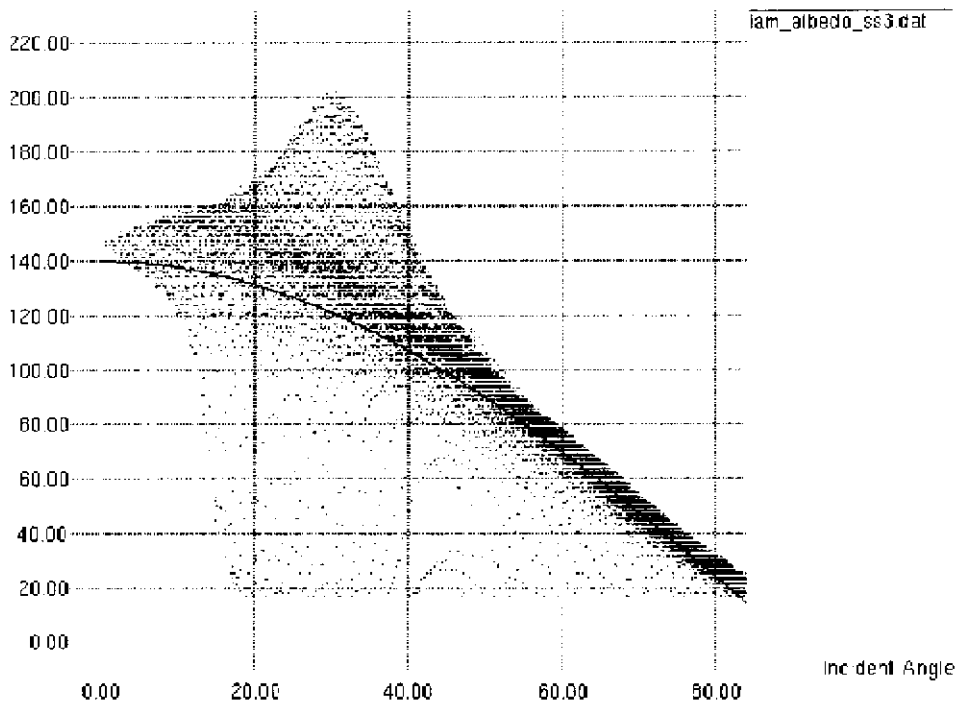


Fig. 6-17. Measured intensity vs. incident angle for painted sphere for S3

The plot of the intensity versus incident angle using the extracted values of B, K, and Offset for the specular spot due to light source three is (For this plot, since the area of interest is the specular lobe, the lambertian albedo is the sum of Offset and  $\rho$ ):

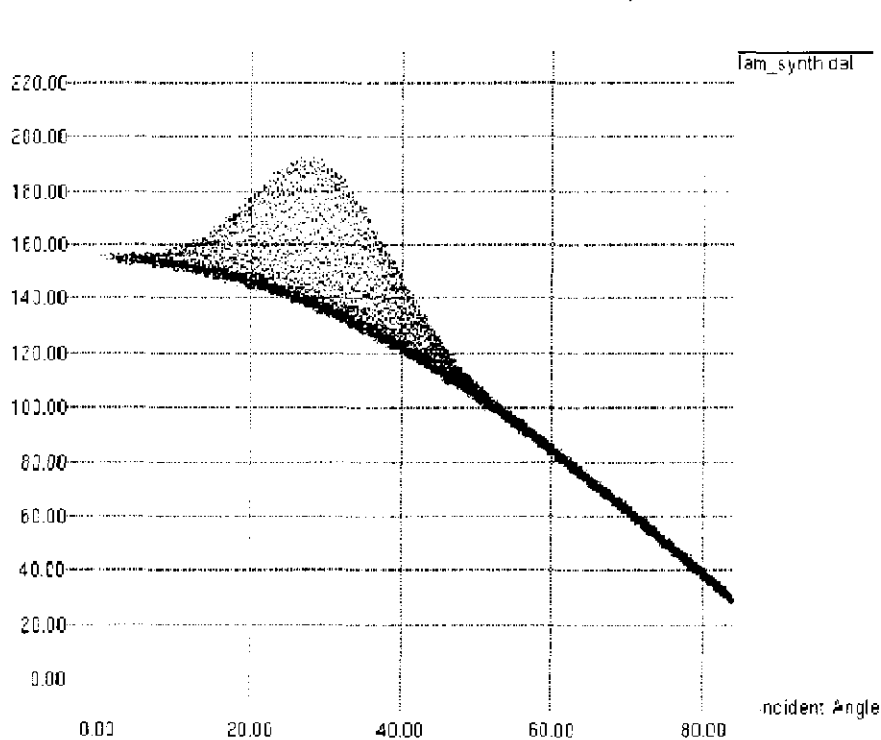


Fig. 6-18. Intensity vs. incident angle for painted sphere using extracted parameters for S3.

The plot of measured intensity versus incident angle for light source two is:

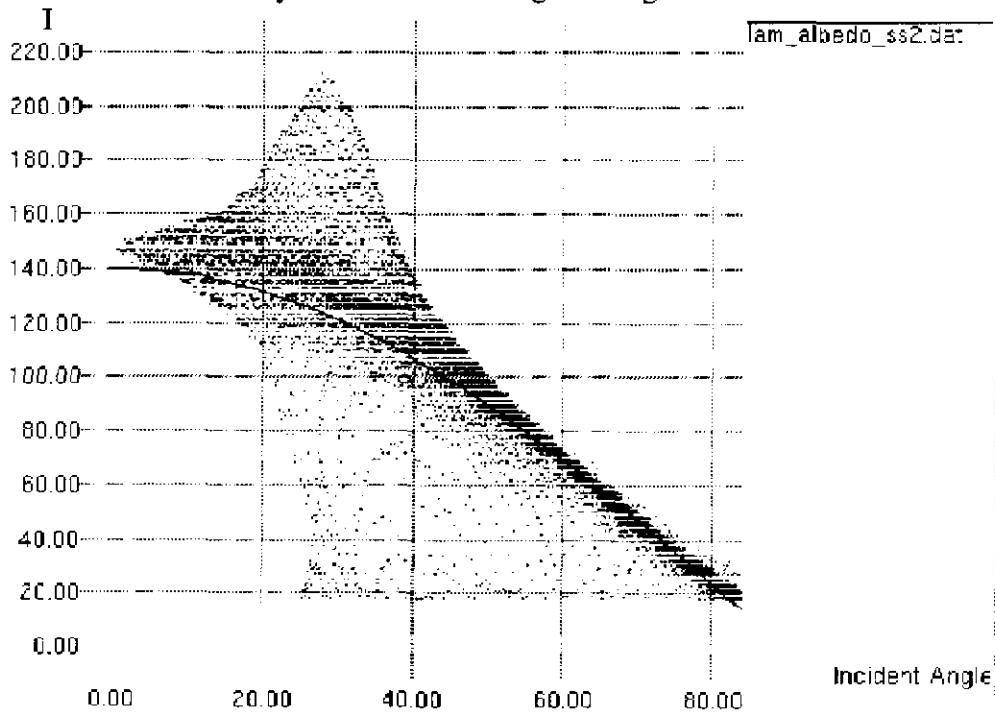


Fig. 6-19. Measured intensity vs. incident angle for painted sphere for S2

One should note the difference in magnitude between the lambertian albedo's cosine curve near the specular part of the intensity plot, and the intensity data.

The plot of the intensity versus incident angle using the extracted values of B, K, and Offset for the specular spot due to light source two is (For this plot, since the area of interest is the specular lobe, the lambertian albedo is the sum of Offset and  $\rho$ ):

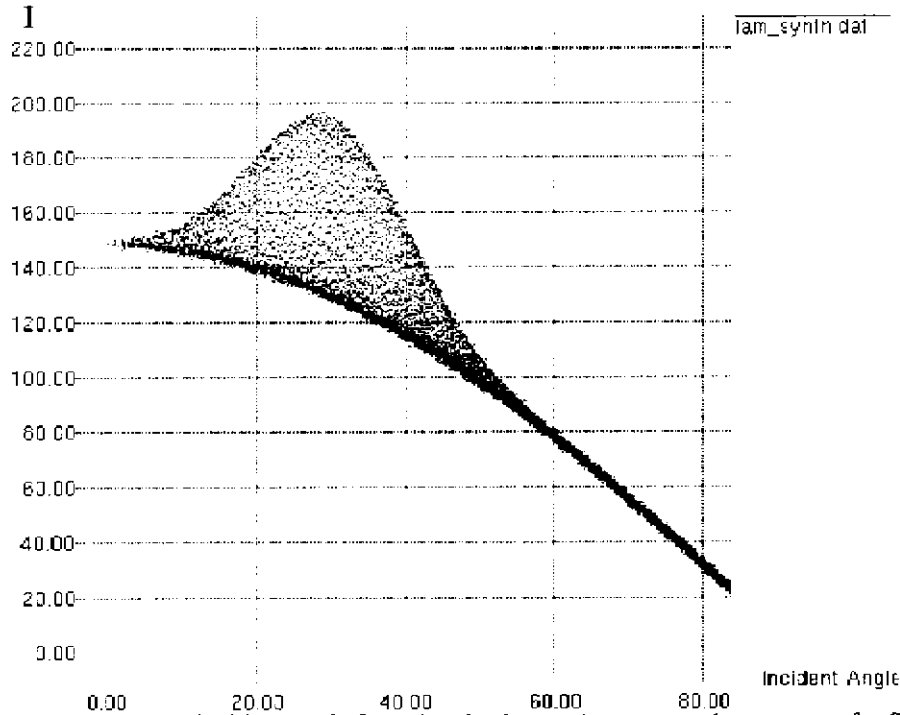


Fig. 6-20. Intensity vs. incident angle for painted sphere using extracted parameters for S2.

The plot of  $\alpha^2$  versus  $\ln(D*Nz)$  is:

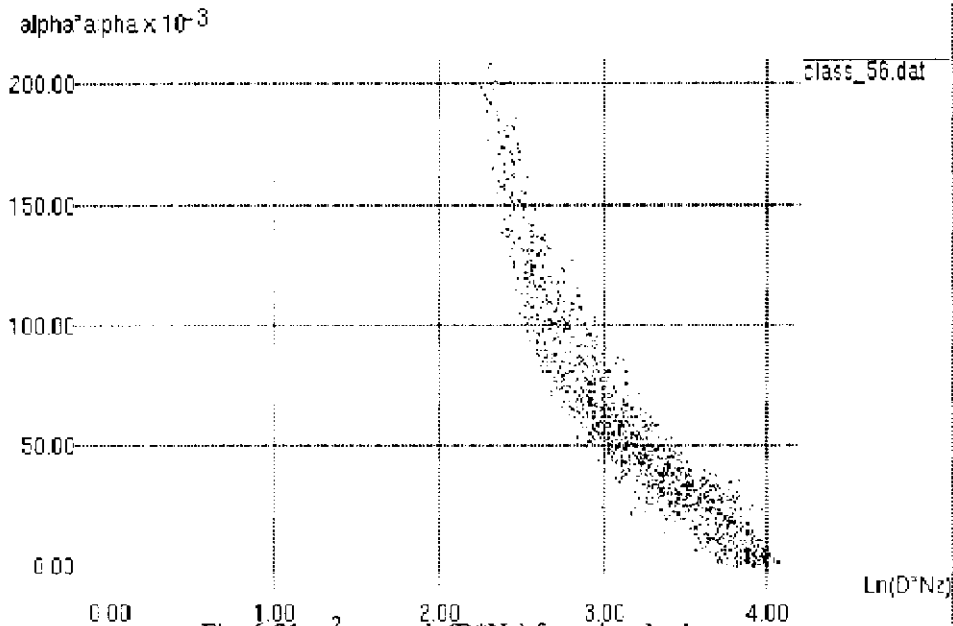


Fig. 6-21.  $\alpha^2$  versus  $\ln(D*Nz)$  for painted sphere.

One should note the nonlinearity of the plot. This is caused by the Offset term of our model. When we compensate for the Offset, the plot becomes linear.

The plot of  $\alpha^2$  versus  $\ln[(D-Offset)*Nz]$  is:

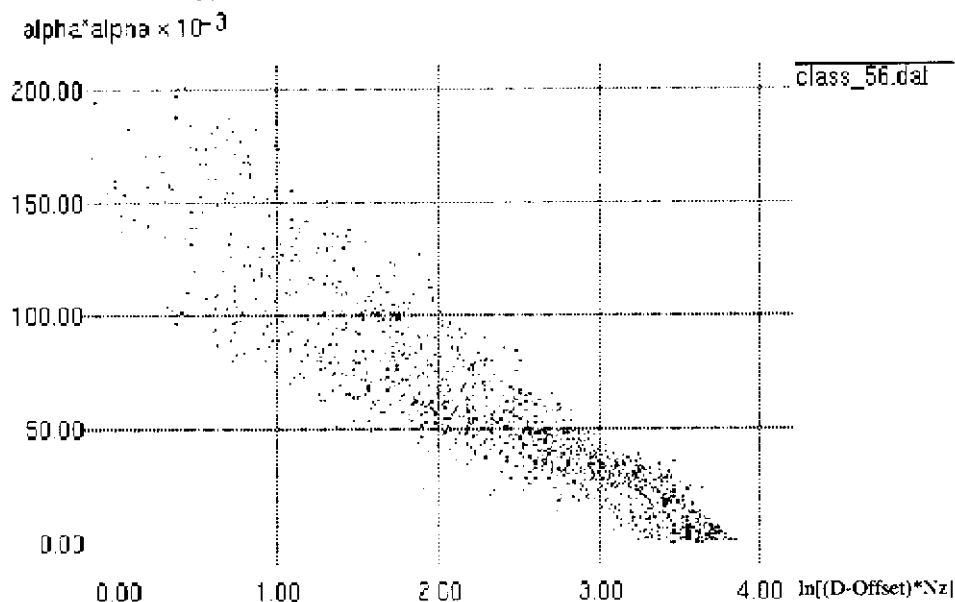


Fig. 6-22.  $\alpha^2$  versus  $\ln[(D-Offset)*Nz]$  for painted sphere.

We compared the ideal surface orientations for the sphere with the surface orientations produced by our algorithm. For the four light illuminated region the mean orientation error was 2.5 degrees, with a standard deviation of 2.0 degrees. For the three light illuminated region the mean orientation error was 2.5 degrees, with a standard deviation of 1.3 degrees. For the two light illuminated region the mean orientation error was 12.8 degrees, with a standard deviation of 10.0 degrees.

#### 6.4.2.3 Plastic Helmet

Four images were taken of a plastic helmet using the following light source directions:

	Sx	Sy	Sz
Light source one	-.523	.661	.539
Light source two	.605	.588	.537
Light source three	.601	-.587	.542
Light source four	-.581	-.621	.526

The four images contain interreflections due to concavities in the surface of the helmet. Since our model does not include interreflection, we manually segmented the images to

eliminated any areas where interreflection might occur.

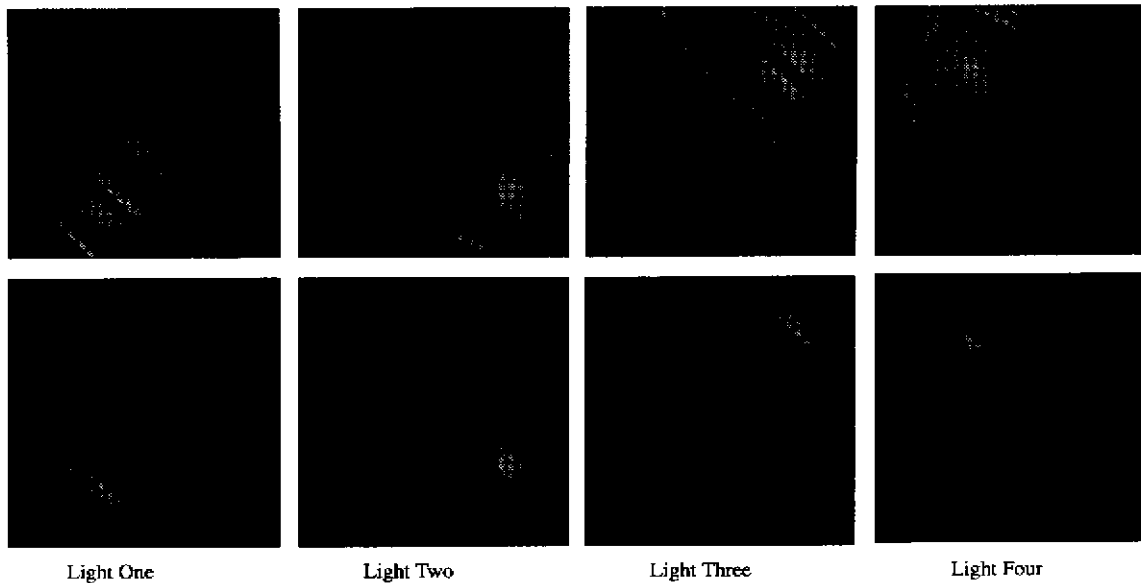


Fig. 6-23. Plastic helmet images and manually segmented plastic helmet images.

In addition to interreflection, the plastic exhibited a small specular spike. Due to the averaging nature of the pixels in the CCD array, most of the images did not show the spike. However, the image due to light source number two did show the spike. The spike's presence caused the gradient descent fit to not converge, for light source number two's specular lobe. To compensate for the any spike in the other images, we increased the specular threshold in the four light illuminated area to:

$$\tau_{dev} > 18 \sqrt{\left(\frac{\partial}{\partial I1} R1 + \frac{\partial}{\partial I1} R2\right)^2 \sigma_i^2 + \left(\frac{\partial}{\partial I2} R1 + \frac{\partial}{\partial I2} R2\right)^2 \sigma_i^2 + \left(\frac{\partial}{\partial I3} R1 + \frac{\partial}{\partial I3} R2\right)^2 \sigma_i^2 + \left(\frac{\partial}{\partial I4} R1 + \frac{\partial}{\partial I4} R2\right)^2 \sigma_i^2}$$

With these modifications to our algorithm, we were able to extract the specular lobe's characteristic's for light source one, three, and four

	Offset	B	K
Specular from S1	-2.1	36.5	8.4
Specular from S3	-6.4	49.9	10.1
Specular from S4	-8.1	41.5	8.3
Average Values	-4.2	42.6	8.9

The pixel segmentation for the above images is:

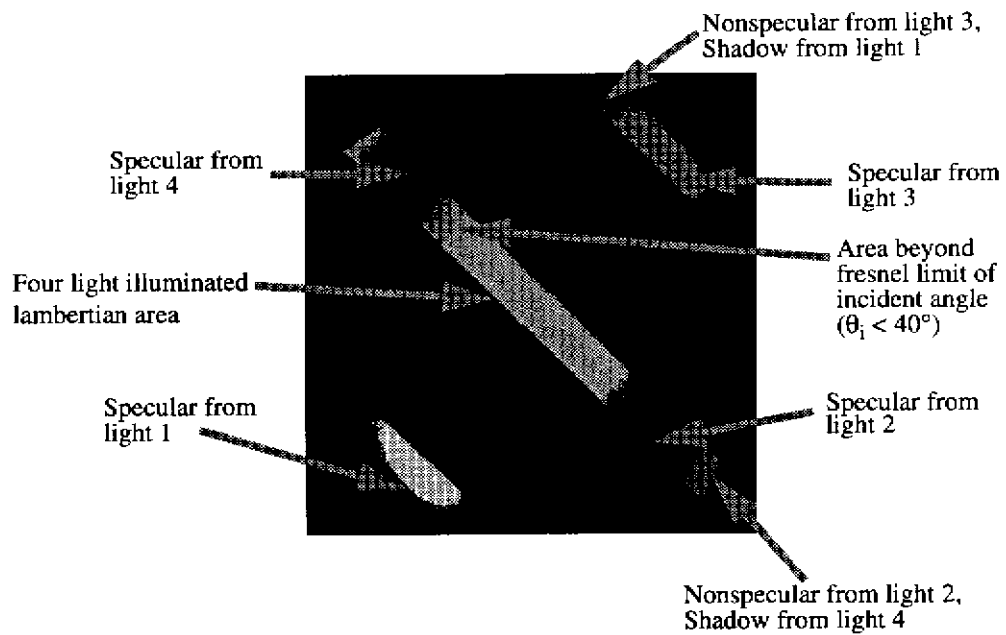


Fig. 6-24. Segmentation for plastic helmet.

The needle map produced from the four intensity images is:

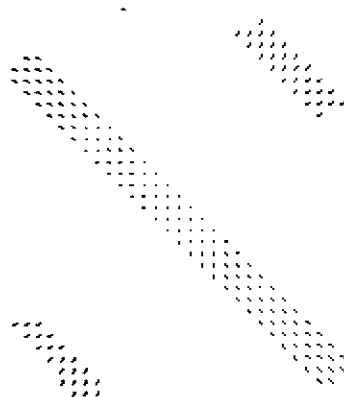


Fig. 6-25. Needle map for plastic helmet

The plot of  $\alpha^2$  versus  $\ln(D*Nz)$  for light source four is:

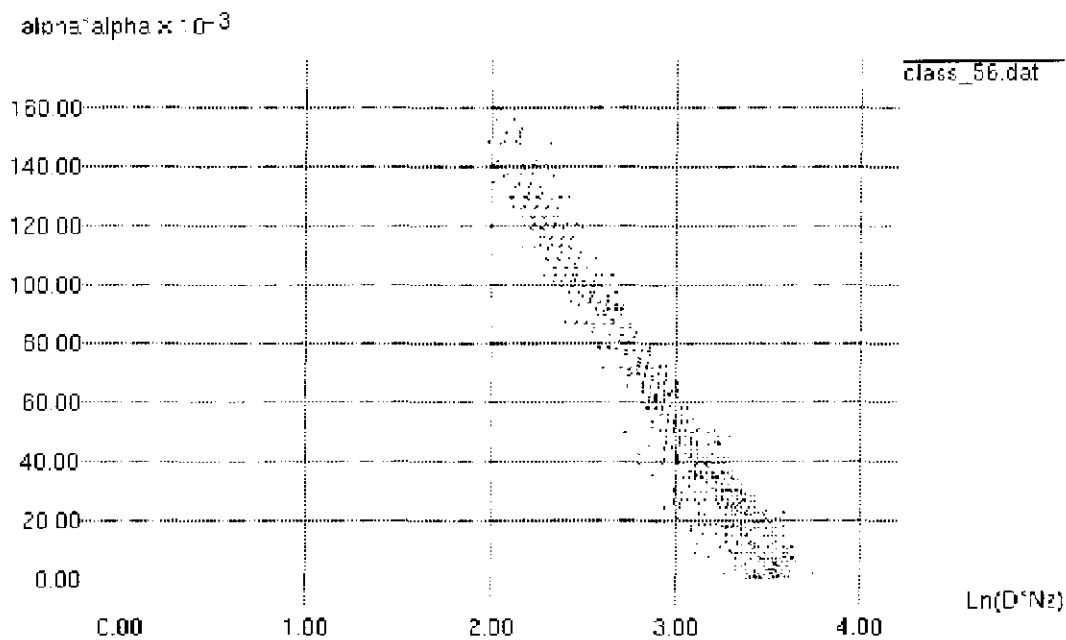


Fig. 6-26.  $\alpha^2$  versus  $\ln(D*Nz)$  for plastic helmet.

#### 6.4.2.4 Plastic Bottle

Four images were taken of a plastic bottle. The bottle exhibits a strong specular spike. This prevents us from recovering the specular intensity and specular sharpness of the bottle. However, we are able to recover the shape of the bottle.

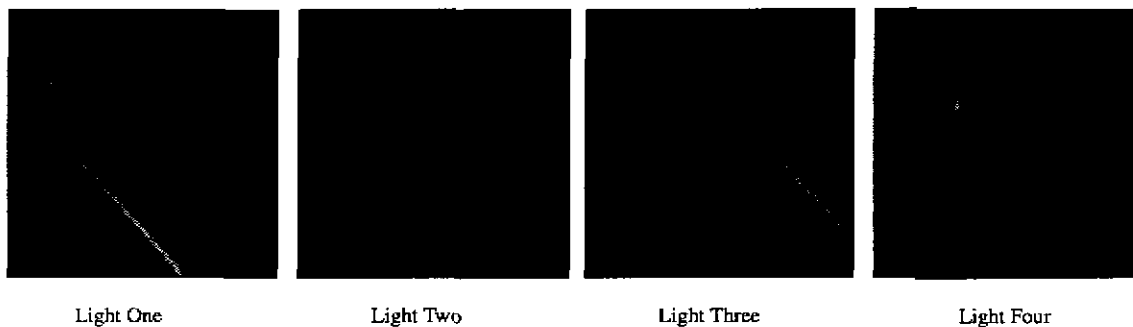


Fig. 6-27. Images of plastic bottle.

The pixel segmentation of the four intensity images is:

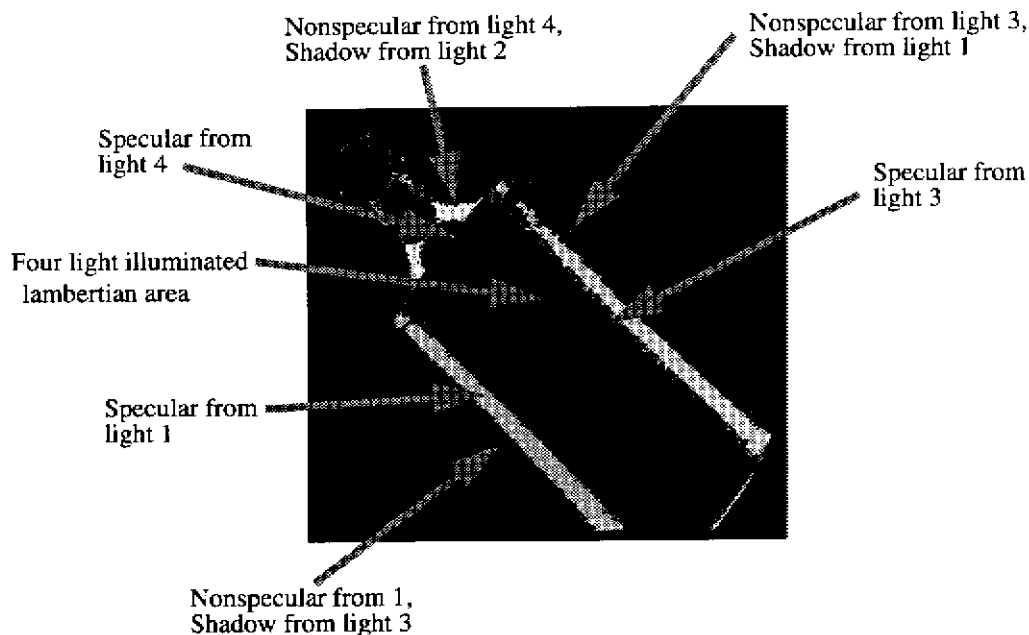


Fig. 6-28. Segmentation for plastic bottle.

The needle map produced from the four intensity images is:

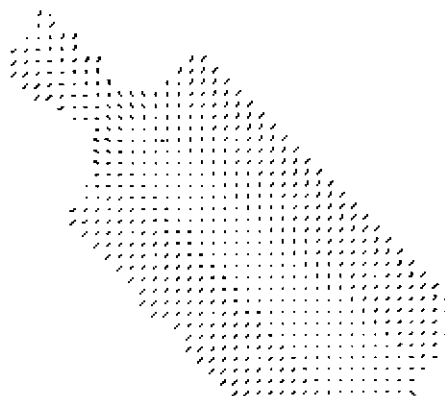


Fig. 6-29. Needle map for plastic bottle.

## 6.5 Conclusions

This chapter discussed the illumination of surfaces that exhibit a hybrid reflectance. We developed a method for extracting the shape, specular intensity, and specular sharpness of these surfaces. The work includes three important parts: determination of shape, segmentation of pixels into specular and nonspecular pixels, and determination of specular intensity/specular sharpness. Coleman and Jain's work for performing segmentation in areas illuminated by four lights, was improved by making the segmentation statistically meaningful. We

developed methods for recovering shape and for performing statistical segmentation in regions illuminated by three lights. We also developed methods for recovering shape in regions illuminated by two lights. The methods produced reasonable results on synthetic and real images. We recovered the shape, specular intensity, and specular sharpness of several hybrid objects, and we have recovered the shape of objects that contain moderate to large specular spikes.

# Chapter 7

## Conclusions

This thesis explored illumination planning for photometric measurements. We studied how illumination affects the reliability of surface orientation measurements in the presence of intensity noise for the following: lambertian surfaces, rough lambertian surfaces, specular spike surfaces, and specular lobe objects. We investigated how to determine the shape and reflectance parameters of hybrid surfaces by imposing constraints on illumination, and we explored the reliability of specular lobe reflectance parameter estimation in the presence of intensity noise.

### 7.1 Summary

The work on the reliability of surface orientation measurements in the presence of intensity noise showed that for each photometric function there are light source configurations that produce high reliability and light source configurations that produce low reliability. We showed that the shape of the error surfaces is related to the shape of the photometric function, the stability of the system of photometric equations, and the signal/noise ratio of our measurements. While, considering these three factors separately, gave some insight into the error surfaces, it is still important to remember that the error surfaces are a function of a system of photometric equations. These factors act together, and cannot be uncoupled without altering the very system we are studying. So, in some real sense, the error surfaces are the only truthful representation of each system's behavior.

#### 7.1.1 Illumination of Lambertian Surfaces

First we explored illumination planning for 2D discrete lambertian normals. We showed how the shape of the error surface, for one normal, was related to the shape of the lambertian intensity function, the stability of the lambertian system of equations, and the signal/noise ratio of the measurements. Then, we developed a 3D illumination planning system that determined how to efficiently illuminate a specified set of faces on a convex polyhedral object. The planner conducted a statistical simulation to predict how much uncertainty we could expect in our measurement of surface orientation for a candidate light source configuration. The plans were implemented using an array of light sources and a camera mounted

on a PUMA robot. The experiments showed that the planner's predictions were accurate.

We then extended the convex lambertian methodology to simple 2D and 3D lambertian concavities. We realized that for illumination planning purposes, the concavity could be treated as a non-interreflecting shape equal to the pseudo shape. We developed an illumination planner that planned illumination for a concavity composed of two rectangular faces, and we conducted experiments on a 3D lambertian concavity which validated our planner's predictions. Finally, we examined the effect of source position error on the measurement of lambertian surface orientation. We found through a graphical analysis that the orientation error, in 2D, when both light sources are on opposite sides of the normal, is limited by the magnitude of the source position error.

### **7.1.2 Illumination of Rough Diffuse Surfaces**

Rough diffuse surface models are much more general than the pure lambertian model. We examined 2D illumination for these surfaces. The shape of the rough diffuse error surfaces, for small values of  $\sigma$ , was close to the lambertian error surface. However, as the roughness of the rough diffuse surface increased, and the intensity profile deviated more from the lambertian intensity profile, the error surfaces showed greater differences. We developed a 2D illumination planner that planned illumination for a given surface orientation, and we conducted experiments that validated the planner. This work showed that the methods developed in the lambertian chapter could be successfully extended to non-lambertian surfaces, and to higher dimensionality reflectance functions.

### **7.1.3 Illumination of Specular Spike Surfaces**

In order to illuminate specular spike surfaces, we utilized spherical extended light sources. We showed that the shape of the specular spike error surface was closely related to the shape of the extended light source intensity function, which is substantially different from the lambertian intensity function. We developed a 2D illumination planner that planned illumination for a given surface orientation, and we conducted a series of experiments on polished metal objects that validated the planner.

### **7.1.4 Illumination of Specular Lobe Surfaces**

We examined the illumination of specular lobe surfaces from two perspective. First we examined how illumination affects the determination of surface orientation, in the presence of intensity noise, when the specular lobe reflectance parameters are known. Secondly, we examined how illumination affects the determination of the specular lobe parameters, in the presence of intensity noise, when surface orientation is known. We developed 2D illumination planners for both problems.

### **7.1.5 Illumination of Hybrid Surfaces**

We investigated illumination planning for hybrid surfaces from a slightly different perspective. Instead of finding the optimal light source positions to determine surface orientation, or reflectance parameters, given a certain amount of intensity noise, we examined how con-

straints on light source placement could allow us to determine both the shape and reflectance parameters of a hybrid object. We developed methods for recovering shape and for performing statistical segmentation in regions illuminated by three and four lights. We also developed methods for recovering shape in regions illuminated by two lights. We recovered the shape, specular intensity, and specular sharpness of several hybrid objects.

## 7.2 Contributions

We have shown that the light source configuration affects the reliability and simplicity with which a photometric measurement can be made. We have also shown that the light source configuration affects what parts of an object are illuminated. Specifically:

1. We developed techniques for measuring the sensitivity of surface orientation to intensity noise for: lambertian surfaces, rough lambertian surfaces, specular spike surfaces, and specular lobe surfaces.
2. We developed illumination constraints that allow the shape and reflectance parameters of hybrid surfaces to be determined using point light sources.
3. We showed that the methodology of combining object models with accurate sensor noise models and reflectance models allows the accurate prediction of measurement reliability.
4. We showed that it is possible to conduct statistical photometric measurements.

## 7.3 Future Directions

The study of illumination planning is in an early state. Certainly, more research is needed on how illumination affects intensity based computer vision algorithms. We started the exploration of illumination planning for photometric measurements. There are parts of the problem space that we did not explore. In the table below we list the problem space for the four photometric models. The “X” indicates what we have researched.

Photometric Model	Surface Orientation Measurement Error Source		
	Intensity Noise	Source Position Error	Viewer Position Error
lambertian	X	X	
rough diffuse	X		
specular spike	X		
specular lobe	X		

In addition to the potential errors listed above, the rough diffuse model has a potential source of error in the reflectance parameter,  $\sigma$ . The specular spike model has a potential source of error in the extended light source parameter,  $H$ . The specular lobe model has potential sources of error in the specular parameters,  $B$  and  $K$ .

We explored constraints for illuminating hybrid surfaces, but we did not explore a systematic method for achieving an illumination configuration. This is a combinatorial analysis problem. For each candidate light source position, certain parts of the object will be specular and certain parts of the object will be lambertian. The planner would have to find combinations of light sources that allow shape and specular parameter estimation to be conducted in an efficient manner. There might be a large number of candidate light source configurations that could accomplish both tasks. A metric to compare configurations is needed.

Modeling the effect of light source configurations on the photometric measurement of surface orientation, in the presence of intensity noise, is a big step towards understanding how reliable such a measurement can be. In order to make accurate photometric measurements possible, a number of additional error sources need to be examined. Three major assumptions are that the irradiance of the object is uniform, the incident light is parallel, and viewing is orthographic. In general, due to finite object size, finite source size, finite object to source distances, and perspective effects, these assumptions are violated. In theory, this can be modeled if one precisely knows the geometry of the illumination, camera optics, and object configuration. However, I have not seen anyone solve this problem at a level of detail that would explain the photometric variation across a simple scene. This is a prerequisite for reliably detecting defects in objects using photometric techniques.

Incorporating factors that affect object irradiance and sensor irradiance, such as source radiance, source to object distance, and aperture, into the planner would be a worthwhile extension.

Another research direction is extending the "sensor noise model/CAD model" sensor planning paradigm to additional sensors such as range finders. In one sense, the noise characteristics of the CCD are very easy to model. The noise is repeatable and is primarily due to shot noise. Sensors like range finders are much more complicated. Further research may be necessary to model these sensors.

# Appendix A

## Light Source Direction and Normalization

### A.0.1 Light Source Directions

The accuracy of the light source directions is very important. We have tested a number of techniques. The simplest technique is to use the brightest point on the surface of a lambertian sphere. The normal of the brightest point is coincident with the vector pointing to the light source. Although the method is simple to implement, it is sensitive to noise.

A second method is to fit the lambertian reflectance function to the 100 brightest pixels of a lambertian sphere. Since the data around the peak of the cosine is flat, the fit is not very stable. If the number of points (the threshold used to select the points) changes, the light source direction will change. A more stable fit can be obtained by using points extending from the brightest part of the cosine, to the shadow area of the cosine. This fit will be stable. If the threshold is changed, within reasonable amounts, the light source direction will not change.

Light source directions are calculated by performing a least square fit to the intensity data of a lambertian sphere. The least squares formulation contains a residual term. This term allows the dark current value of the camera to be recovered.

The intensity at each point on the lambertian sphere is:

$$A = \rho (S_x N_x(i, j) + S_y N_y(i, j) + S_z N_z(i, j))$$

The total error over the entire image between the measured intensity,  $E(i, j)$ , and the intensity given by the lambertian model, using our solution for  $(S_x, S_y, S_z, D)$ , where  $D$  is the residual, dark current term, is:

$$P = \sum_{i, j} [E(i, j) - S_x N_x(i, j) - S_y N_y(i, j) - S_z N_z(i, j) - D]^2$$

We want to find the minimum of the error with respect to  $(S_x, S_y, S_z, D)$ . This happens when:

$$\frac{\partial P}{\partial S_x} = 0 = \sum_{i,j} N_x(i,j) (E(i,j) - S_x N_x(i,j) - S_y N_y(i,j) - S_z N_z(i,j) - D)$$

$$\frac{\partial P}{\partial S_y} = 0 = \sum_{i,j} N_y(i,j) (E(i,j) - S_x N_x(i,j) - S_y N_y(i,j) - S_z N_z(i,j) - D)$$

$$\frac{\partial P}{\partial S_z} = 0 = \sum_{i,j} N_z(i,j) (E(i,j) - S_x N_x(i,j) - S_y N_y(i,j) - S_z N_z(i,j) - D)$$

$$\frac{\partial P}{\partial D} = 0 = \sum_{i,j} E(i,j) - S_x N_x(i,j) - S_y N_y(i,j) - S_z N_z(i,j) - D$$

This set of four equations can be solved directly for  $S_x$ ,  $S_y$ ,  $S_z$ , and  $D$ .

Another method for determining light source positions is to build a fixture that precisely locates each light source. This method was used, in chapter 2, for the array of light sources. In chapter 3, in two dimensions, we used a precisely aligned rotational stage to locate light sources. In chapter 4, we located the extended light sources by fitting the intensity distribution of each extended source to our model. The method is similar to the lambertian method discussed above.

### A.0.2 Image Intensity Normalization

Light source radiances need to be normalized because light source radiances are usually not equal. The most common technique uses the brightest pixel in the image as a normalizing factor. This technique is susceptible to image intensity noise inaccuracies. Using a larger number of points makes this technique more robust. We can use a lambertian sphere as an object. After we have solved for the light source's direction, we can fit a cosine to a plot of intensity versus incident angle. The magnitude of the cosine is our normalization factor. In Fig. A-1. , is a plot of intensity versus incident angle for a lambertian sphere (using the extracted light source direction) and a best fit cosine (magnitude = 143).

A less sophisticated method, that we successfully used in chapters 2 and 3, was to visually align a lambertian plane perpendicular to each light source. The intensity of each light source was the average intensity of the center of the plane.

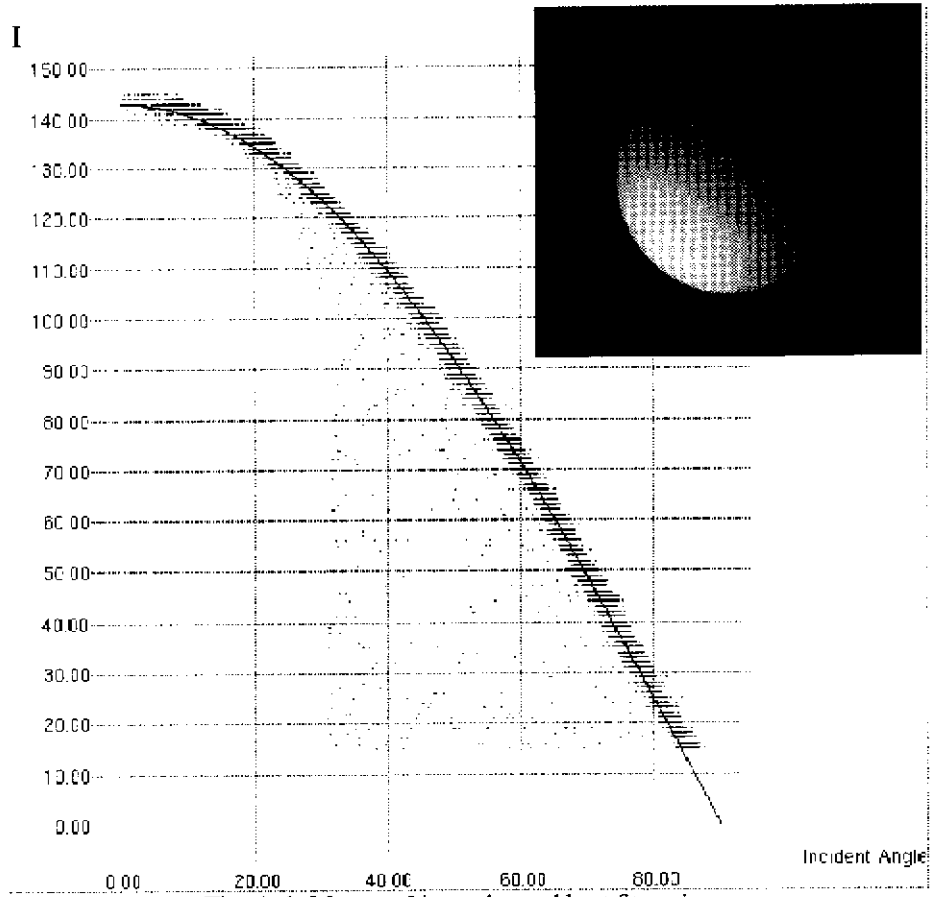


Fig. A-1. Measured intensity and best fit cosine.



## Appendix B

# Frames and Transformations for Puma, Camera, and Light Source Array

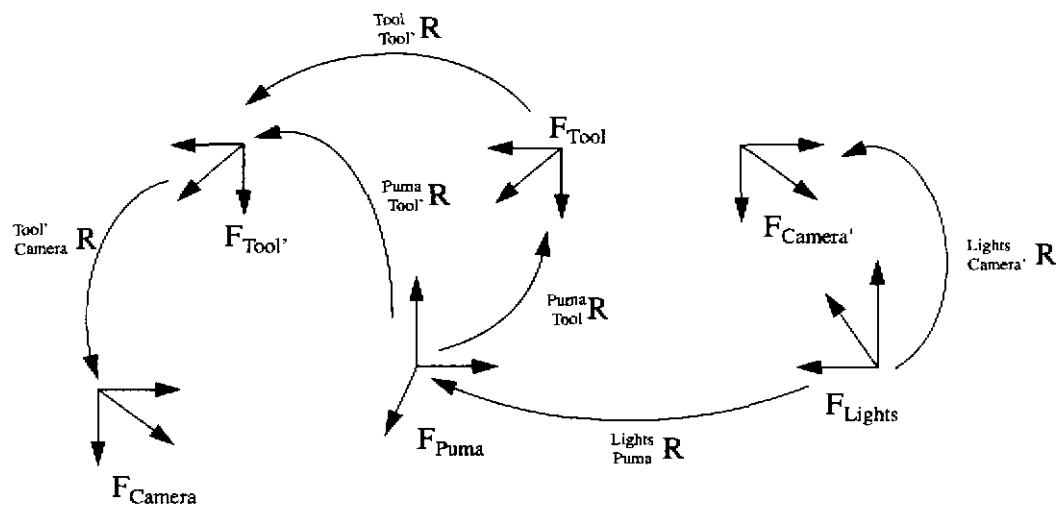


Fig. B-1. Frames for Puma, camera, and light source array

Many frames were used in the experimental setup for chapter 2. This section describes the frames and their relationships.  $F_{Lights}$  is the frame for the icosahedron holding the light source array.  $F_{Puma}$  is the frame for the Puma robot.  $F_{Tool}$  is the frame of the nominal Puma tool. This is specified when the Puma's "OAT" coordinates are equal to (0, 0, 0).  $F_{Camera'}$  is the frame of a virtual camera, at the desired viewpoint, looking at the object, at the center of the light source array.  $F_{Camera}$  is the frame of the real camera attached to the Puma's end effector.  $F_{Tool'}$  is the frame of actual tool frame.

The goal is to have  $F_{Camera'}$  aligned with  $F_{Camera}$ . We need to solve for  $R_{Tool/Tool'}$ .  $R_{Lights/Camera'}$  is known from the geometry of the icosahedron. Based on the icosahedron face that we want to view from, we can determine the orientation of the virtual camera. Given a desired viewpoint, specified in spherical coordinates by  $\theta$  and  $\phi$ ,  $R_{Lights/Camera'} = R_z(\theta)R_y(\phi)R_x(180)R_z(-90)$ .

This will make the +Z axis of the camera (optical axis of camera) point at the origin of the array of light sources. The +Y axis of the camera will point downward (not necessarily straight down), and the +X axis of the camera will be horizontal.  ${}^{Lights}_{Puma} R$  is known by solving for the transformation between the Puma robot and the light source array. This transformation was found by physically locating six points on the array of light sources with the end effector of the Puma robot. The locations of these points, in  $F_{Lights}$ , is known from the physical dimensions of the icosahedron structure, and the coordinates of these points, in  $F_{Puma}$ , are known from the Puma controller. The transformation was solved for by using the method of Hebert and Faugeras [Faugeras 86].  ${}^{Puma}_{Tool} R$  is fixed and is equal to  $R_x(-180)R_z(-90)$ .  ${}^{Tool}_{Camera} R$  is the transformation between the Puma's end effector and the camera. This was found by performing a hand/eye calibration procedure [Tsai 87] [Lenz 89]. Once these transformations are known, we can solve for the transformation between the Puma and the virtual camera:

$${}^{Puma}_{Camera} R = ({}^{Lights}_{Puma} R)^{-1} ({}^{Lights}_{Camera} R)$$

We want:

$${}^{Puma}_{Camera} R = {}^{Puma}_{Camera} R$$

or:

$$({}^{Puma}_{Tool} R) ({}^{Tool}_{Camera} R) = {}^{Puma}_{Camera} R$$

so:

$$({}^{Puma}_{Tool} R) = {}^{Puma}_{Camera} R ({}^{Tool}_{Camera} R)^{-1}$$

The transformation to go from the nominal tool frame,  $F_{Tool}$ , to the desired tool frame,  $F_{Tool'}$  is:

$$({}^{Tool}_{Tool'} R) = ({}^{Puma}_{Tool} R)^{-1} ({}^{Puma}_{Camera} R) ({}^{Tool}_{Camera} R)^{-1}$$

“O,A,T”, which the Puma needs, are the (-X),Y,Z Euler angles corresponding to  $({}^{Tool}_{Tool'} R)$ .

$$A = \text{atan2} \left( r_{00}, \sqrt{r_{12}^2 + r_{22}^2} \right)$$

$$T = \text{atan2} \left( \frac{-r_{01}}{\cos B}, \frac{-r_{00}}{\cos B} \right)$$

$$O = -1 \left( \text{atan2} \left( \frac{-r_{12}}{\cos B}, \frac{-r_{22}}{\cos B} \right) \right)$$

if  $A = \pm 90$

$$T = 0$$

$$O = -1 \left( \text{atan2} (r_{10}, -r_{20}) \right)$$

## Bibliography

- [Abrams 93] S. Abrams, P. K. Allen, K. A. Tarabanis, "Dynamic Sensor Planning", *1993 IEEE International Conference on Robotics and Automation*, pp. 605-610.
- [Batchelor 85] B. G. Batchelor, D. A. Hill, and D. C. Hodgson, "Automated Visual Inspection", IFS (Publications) Ltd., Bedford, U.K., 1985.
- [Batchelor 89] B. G. Batchelor, "A Prolog Lighting Advisor", *Intelligent Robots and Computer Vision VIII: Systems and Applications*, Bruce G. Batchelor, Editor, Proc. SPIE 1193.
- [Batchelor 90] B. G. Batchelor and F. M. Waltz, Editors, "Machine Vision Systems Integration", 1990, SPIE Optical Engineering Press, Bellingham, Washington.
- [Bevington 69] P. R. Bevington, "Data Reduction and Error Analysis for the Physical Sciences", McGraw-Hill, New York, 1969, pp. 56-65.
- [Bowyer 90] K. Bowyer and C. Dyer, "Aspect Graphs: An Introduction and Survey of Recent Results", *International Journal of Imaging Systems and Technology*, Vol 2, No. 4, 1990, pp. 315-328.
- [Christensen 94] P. Christensen and L. Shapiro, "Three-Dimensional Shape from Color Photometric Stereo", *International Journal of Computer Vision*, Vol. 13, No. 2, pp. 213-227.
- [Coleman 82] E. N. Coleman and R. Jain, "Obtaining 3-dimensional shape of textured and specular surfaces using four-source photometry", *Computer Graphics and Image Processing*, Vol. 18, No. 4, pp. 309-328, April, 1982.
- [Cormen 90] T. Cormen, C. Leiserson, R. Rivest, "Introduction to Algorithms", The MIT Press, Cambridge, MA, 1990.
- [Cowan 88] C. Cowan, "Automatic Sensor Placement from Vision Task Requirements", *IEEE Trans. on Pattern Analysis and Machine Intelligence*, Vol. 10, No. 3, pp. 407-416, May, 1988.
- [Cowan 89] C. Cowan, "Determining the Camera and Light Source Location for a Visual Task", *1989 IEEE International Conference on Robotics and Automation*, pp. 509-514.
- [Cowan 91] C. Cowan, "Automatic Camera and Light Source Placement Using CAD Models", *IEEE Workshop on Directions in Automated CAD-Based Vision*, June 1991, Maui, Hawaii, pp. 22-31.
- [Faugeras 86] O. Faugeras and M. Hebert, "The Representation, Recognition, and Locating of 3-D Objects", *The International Journal of Robotics Research*, Vol. 5, No. 3, pp.

27-52, Fall 1986.

- [Gigus 91] Z. Gigus, J. Canny, and R. Seidel, "Efficiently Computing and Representing Aspect Graphs of Polyhedral Objects", *IEEE Trans. of Pattern Analysis and Machine Intelligence*, Vol. 13, No. 6, pp. 542-551, June, 1991.
- [Golub 89] G. Golub and C. Van Loan, "Matrix Computations", The Johns Hopkins University Press, Baltimore, 1989, pp. 510-511.
- [Goral 84] C. Goral, K. Torrance, D. Greenberg, and B. Battaile, "Modeling the Interaction of Light Between Diffuse Surfaces", *Proceedings of SIGGRAPH 84*, Vol. 18, No. 3, pp. 213-221, July, 1984.
- [Gremban 92] K. Gremban and K. Ikeuchi, *International Journal of Computer Vision*, Vol. 12, No. 2-3, pp. 137-172.
- [Hager 88] G. Hager, "Active Reduction of Uncertainty in Multi-sensor systems", University of Pennsylvania, Philadelphia, Pennsylvania, Ph.D. Thesis, MS-CIS-88-47.
- [Hager 90] G. Hager, "Computational Methods For Task-Directed Sensor Data Fusion and Sensor Planning", University of Pennsylvania, Philadelphia, Pennsylvania, MS-CIS-90-38.
- [Healey 88] G. Healey and T.O. Binford, "Local Shape from Specularity", *Computer Vision Graphics and Image Processing*, Vol. 42, pp. 62-86, 1988.
- [Healey 94] G. Healey and R. Kondepudy, "Radiometric CCD Camera Calibration and Noise Estimation", *IEEE Trans. of Pattern Analysis and Machine Intelligence*, Vol. 16, No. 3, pp. 267-276, March, 1994.
- [Healey 92] G. Healey and R. Kondepudy, "CCD Camera Calibration and Noise Estimation", *1992 IEEE International Conference on Computer Vision and Pattern Recognition*, pp. 90 - 95.
- [Healey 91] G. Healey and R. Kondepudy, "Modeling and Calibrating CCD Cameras for Illumination Insensitive Machine Vision", *Optics, Illumination, and Image Sensing for Machine Vision VI*, Proc. SPIE 1614.
- [Hebert 85] M. Hebert and T. Kanade, "The 3D-Profile Method of Object Recognition", *1985 IEEE Conference on Computer Vision and Pattern Recognition*, pp. 458-463.
- [Heckbert 91] P. Heckbert, "Simulating Global Illumination Using Adaptive Meshing", Ph.D. Thesis, University of California, Berkeley, UCB/CSD 91/636, June, 1991.
- [Horn 1977] B. K. P. Horn, "Understanding Image Intensities", *Artificial Intelligence*, Vol. 8, No. 2, pp. 201-213, 1977.
- [Horn 1988] B. K. P. Horn, "Robot Vision", The MIT Press, Cambridge, Massachusetts,

1988.

- [Ikeuchi 81] K. Ikeuchi, "Determining the surface orientations of specular surfaces by using the photometric stereo method", *IEEE Trans. of Pattern Analysis and Machine Intelligence*, Vol. 3, No. 6, pp. 661-669, November, 1981.
- [Ikeuchi 88] K. Ikeuchi and T. Kanade, "Automatic Generation of Object Recognition Programs", *Proceedings of the IEEE*, Vol. 76, No. 8, pp. 1016-1035, August, 1988.
- [Ikeuchi 91a] K. Ikeuchi and J. Robert, "Modeling Sensor Detectability with the VANTAGE Geometric/Sensor Modeler", *IEEE Trans. of Robotics and Automation*, Vol. 7, No. 6, pp. 771-784, December, 1991.
- [Ikeuchi 91b] K. Ikeuchi and K. Sato, "Determining Reflectance Parameters of an Object Using Range and Brightness Images", *IEEE Trans. of Pattern Analysis and Machine Intelligence*, Vol. 13, No. 11, pp. 1139-1153, November, 1991.
- [Kiuchi 93] T. Kiuchi and K. Ikeuchi, "Roughness and Shape of Specular Lobe Surfaces using Photometric Sampling Method", *1993 IEEE International Conference on Computer Vision and Pattern Recognition*, pp. 765- 766.
- [Koshikawa 79] K. Koshikawa, "A Polarimetric Approach to Shape Understanding of Glossy Objects, *1979 International Joint Conference on Artificial Intelligence*, pp. 493-495.
- [Jiang 91] X. Y. Jiang and H. Bunke, "On Error Analysis for Surface Normals Determined by Photometric Stereo", *Signal Processing*, Vol. 23, pp. 221-226, 1991.
- [Kemotsu 93] K. Kemotsu and T. Kanade, *1993 IEEE International Conference on Robotics and Automation*, pp. 128-134.
- [Koenderink 79] J. J. Koenderink and A. J. van Doorn, "The Internal Representation of Solid Shape with Respect to Vision", *Biol. Cybernetics*, Vol. 32, pp. 211-216, 1979.
- [Kriegman 90] D. Kriegman and J. Ponce, "Computing Exact Aspect Graphs of Curved Objects: Solids of Revolution", *International Journal of Computer Vision*, Vol. 5, No. 2, pp. 119-135.
- [Kumar 91] B. Kumar, J.C. Robert, R. Hoffman, K. Ikeuchi. and T. Kanade, "*Vantage, A Frame Based Geometric Modeling System Programmer/Users Manual V2.0*", CMU-RI-TR-91-31, December 1991.
- [Lenz 89] R. Lenz and R. Tsai, "A New Technique for Fully Autonomous and Efficient 3D Robotics Hand/Eye Calibration", *IEEE Trans. on Robotics and Automation*, Vol. 5, No. 3, pp. 345-358, June, 1989.
- [Murase 94] H. Murase and S. K. Nayar, "Illumination Planning for Object Recognition Using Parametric Eigenspaces", *IEEE Trans. of Pattern Analysis and Machine Intel-*

*ligence*, Vol. 16, No. 12, pp. 1219-1227, December 1994.

- [Nayar 90a] S. K. Nayar, A. C. Sanderson, L. E. Weiss, D. D. Simon, "Specular Surface Inspection Using Structured Highlight and Gaussian Images", *IEEE Trans. on Robotics and Automation*, Vol. 6, No. 2, pp. 208-218, April, 1990.
- [Nayar 90b] S. K. Nayar, K. Ikeuchi, T. Kanade, "Determining Shape and Reflectance of Hybrid Surfaces by Photometric Sampling", *IEEE Trans. on Robotics and Automation*, Vol. 6, No. 4, pp. 418-431, August, 1990.
- [Nayar 90c] S. K. Nayar, K. Ikeuchi, T. Kanade, "Shape from Interreflections", *International Journal of Computer Vision*, Vol. 6, No.3, pp. 173-195, August 1991.
- [Nayar 91a] S. K. Nayar, K. Ikeuchi, T. Kanade, "Surface Reflections: Physical and Geometrical Perspectives", *IEEE Trans. of Pattern Analysis and Machine Intelligence*, Vol. 13, No. 7, pp. 611-634, July, 1991.
- [Nayar 91b] S. K. Nayar, "Shape Recovery using Physical Models of Reflection and Interreflection", Dept. of Electrical and Computer Engineering, Carnegie Mellon University, Pittsburgh, Pennsylvania, Ph.D Thesis, May 1991.
- [Niepold 87] R. Niepold, S. Sakane, T. Sato, and Y. Shiraii, "Vision Sensor Set-up for a Hand-Eye System Using Environmental Model", *SICE 87*, pp. 1037-1040.
- [Oren 95] M. Oren and S. K. Nayar, "Generalization of the Lambertian Model and Implications for Machine Vision", *International Journal of Computer Vision*, Vol. 14, No. 3, pp. 227-251, April 1995.
- [Oliver 65] B. M. Oliver, "Thermal and Quantum Noise", *Proceeding of IEEE*, Vol 53, pp. 436-454, May 1965.
- [Plantinga 90] H. Plantinga and C. Dyer, "Visibility, Occlusion, and the Aspect Graph", *International Journal of Computer Vision*, Vol. 5, No. 2, pp. 137-160.
- [Press 90] W. Press, B. Flannery, S. Teukolsky, W. Vetterling, "Numerical Recipes in C", Cambridge University Press, New York, 1990, pp. 490 - 494.
- [Ray 83] R. Ray, J. Birk, and R. Kelley, "Error Analysis of Surface Normals Determined by Radiometry", *IEEE Trans. of Pattern Analysis and Machine Intelligence*, Vol. 5, No. 6, pp. 631-645, November, 1983.
- [Rosenbach 61] J. Rosenbach, E. Whitman, and D. Moskovitz, "Essentials of Trigonometry", Ginn and Company, New York, 1961.
- [Sakane 87] S. Sakane, M. Ishii, and M. Kakikura, "Occlusion avoidance of visual sensors based on a hand-eye action simulator system: HEAVEN", *Advanced Robotics*, Vol. 2, No 2, pp. 149-165.

- [Sakane 90] S. Sakane, T. Sato, and M. Kakikura, "Automatic Planning of Light Source Placement for an Active Photometric Stereo System", *1990 IEEE International Workshop on Intelligent Robots and Systems*, pp. 559-556.
- [Sakane 91] S. Sakane and T. Sato, "Automatic Planning of Light Source Placement and Camera Placement for an Active Photometric Stereo System", *1991 IEEE International Conference on Robotics and Automation*, pp. 1080 - 1087.
- [Silver 80] W. M. Silver, "Determining Shape and Reflectance Using Multiple Images", S.M. Thesis, Dept. of Electrical Engineering and Computer Science, MIT, Cambridge, Massachusetts, June, 1980.
- [Solomon 96] F. Solomon and K. Ikeuchi, "Extracting the Shape and Roughness of Specular Lobe Objects Using Four Light Photometric Stereo", *IEEE Trans. on Pattern Analysis and Machine Intelligence*, Vol. 18, No. 4, pp. 449-454, 1996. © 1996 IEEE.
- [Solomon 95] F. Solomon and K. Ikeuchi, "An Illumination Planner for Convex and Concave Lambertian Polyhedral Objects", *1995 IEEE Workshop on Physics-Based Modeling in Computer Vision*, pp. 100-107. © 1995 IEEE.
- [Solomon 95] F. Solomon and K. Ikeuchi, "An Illumination Planner for Convex Lambertian Polyhedral Objects", *1995 IEEE International Conference Robotics and Automation*, pp. 1719 - 1725. © 1995 IEEE.
- [Solomon 92] F. Solomon and K. Ikeuchi, "Extracting the Shape and Roughness of Specular Lobe Objects using Four Light Photometric Stereo", *1992 IEEE International Conference on Computer Vision*, pp. 466-471. © 1992 IEEE.
- [Solomon 92] F. Solomon and K. Ikeuchi, "Inspecting Specular Lobe Objects using Four Light Sources", *1992 IEEE International Conference Robotics and Automation*, pp. 1707 - 1712. © 1992 IEEE.
- [Sparrow 78] E. M. Sparrow and R. D. Cess, "Radiation Heat Transfer", McGraw-Hill, New York, 1978.
- [Stewman 87] J. Stewman and K. Bowyer, "Aspect Graphs for Convex Planar-Face Objects", *IEEE Workshop on Computer Vision*, Miami, Florida, 1987.
- [Strang 88] G. Strang, "Linear Algebra and Its Applications", Harcourt Brace Jovanovich, New York, 1988.
- [Tagare 1991] H. Tagare and F. de Figueiredo, "A Theory of Photometric Stereo for a Class of Diffuse Non-Lambertian Surfaces", *IEEE Trans. on Pattern Analysis and Machine Intelligence*, Vol. 13, No. 2, pp. 133-152, 1991.
- [Tarabanis 90] K. Tarabanis, R. Tsai, and P. Allen, "Satisfying the Resolution Constraint in the "MVP" Machine Vision Planning System", *Proceedings DARPA Image Understanding Workshop*, Pittsburgh, P.A., September 11-13, 1990.

- [Tarabanis 91] K. Tarabanis, R. Tsai, and P. Allen, "Automated Sensor planning for robotic vision tasks", *1991 IEEE International Conference on Robotics and Automation*, pp. 76-82.
- [Tarabanis 95] K. Tarabanis, P. Allen, and R. Tsai, "A Survey of Sensor Planning in Computer Vision", *IEEE Journal of Robotics and Automation*, Vol. 11, No. 1, pp. 86-104, February, 1995.
- [Torrance 67] K. Torrance and E. Sparrow, "Theory for Off-Specular Reflection from Roughened Surfaces", *Journal of the Optical Society of America*, No. 57, pp. 1105-1114, 1967
- [Tsai 87] R. Tsai, "A Versatile Camera Calibration Technique for High-Accuracy 3D Machine Vision Metrology Using Off-the-Shelf TV Cameras and Lenses", *IEEE Journal of Robotics and Automation*, Vol. RA-3, No. 4, pp. 323-344, August, 1987.
- [Tsai 89] R. Tsai and K. Tarabanis, "Occlusion Free Sensor Placement", Yorktown Heights, NY: T.J. Watson Research Center, RC 14593, March 1989.
- [Woodham 78] R. J. Woodham, "Reflectance Map Techniques for Analyzing Surface Defects in Metal Castings", Ph.D. Thesis, Artificial Intelligence Laboratory, MIT, Cambridge, Massachusetts, June, 1978.
- [Woodham 90] R. J. Woodham, "Surface Curvature from Photometric Stereo", University of British Columbia, Computer Science Technical Report 90-29, October 1990.
- [Wolff 87a] L. Wolff, "Spectral And Polarization Stereo Methods Using A Single Light Source", *1987 IEEE International Conference on Computer Vision*, pp 708-715.
- [Wolff 87b] L. Wolff, "Shape from Polarization Images", *1987 IEEE Workshop on Computer Vision*, pp. 79-85.
- [Yi 89] S. Yi, R. Haralick, and L. Shapiro, "Automatic Sensor and Light Source Placement for Machine Vision", University of Washington, Seattle, Washington, CS-89-11-03.
- [Yi 94] S. Yi, R. Haralick, and L. Shapiro, "Error Propagation in Machine Vision", *Machine Vision and Applications*, Vol. 7, pp. 93-114, 1994.